Penetration of fastener projectiles into construction materials

Gang Zhou

How to cite:

Zhou, Gang (1988) Penetration of fastener projectiles into construction materials. Doctoral thesis, Durham University.

PENETRATION OF FASTENER PROJECTILES INTO CONSTRUCTION MATERIALS

by

GANG ZHOU

being a thesis submitted in partial fulfilment
of the requirements for the degree of Doctor of
Philosophy in the University of Durham, UK

September 1988

ABSTRACT

The normal impact penetration of both projectile and fastener into soils, rocks, and concrete at low velocities has been investigated using theoretical, experimental, and numerical approaches under axisymmetric conditions. The projectile penetration theory is developed on the basis of the existing cylindrical cavity expansion theory with target materials approximated by compressible locking behaviour in a hydrostatic state and elastic-plastic, linear strain-hardening behaviour in a shear state. This theory is one-dimensional with respect to wave propagation in a radial direction. Impact penetration experiments have been performed using a cartridge-operated tool firing the steel fasteners into sandstone and concrete targets. The associated pull-out problem has also been studied. Damage to both fastener and target caused by the impact penetration is assessed using an optical microscope. Finite element programs have been employed to investigate the penetration process of the projectile, and eventually to simulate the process of fastener penetration. The dependency of the penetration process on impact velocity, projectile nose shape, projectile-target interfacial friction, and target material properties have been studied for a variety of impact conditions. Comparisons of results obtained from all three approaches are made for cases in which data are available. Agreements reached are reasonably good.

ACKNOWLEDGEMENTS

The work presented in this thesis has been carried out in the University of Durham. The author expresses his gratitude to his supervisors, Professor P.B.Attewell and Dr. J.M.Wilson of the School of Engineering and Applied Science, University of Durham, for their invaluable discussions, assistance, and instruction during the past three years.

The author would also like to thank the following :

Mr. A.Brown, Technical Manager (North) of Hilti (Great Britain) Ltd. for supplying the cartridge tool and its accessories;

Professor M.J.H.Sterling of the School of Engineering and Applied Science, University of Durham. for providing access to the VAX computer facilities of his research group;

Newcastle Computing Laboratory for providing assistance in computing; and

Professor S.Reid and Mr. P.Tennant of the Applied Mechanics Division, Department of Mechanical Engineering, UMIST, for performing the measurements of the fastener velocities.

The author is also indebted to Dr. T.V.Parry, Mr. C.B.McEleavey, Mr. S.Richardson, Mr. A.Swann and Mr. B.P.Scurr for their assistance in experiments and in preparation of thin sections, to Ms J.Smart for her assistance in the taking and preparation of photographs, to Mr. R.G.Hardy of the Department of Geological Sciences, University of Durham for carrying out X-ray diffraction and fluorescence analyses on samples, and to secretarial staff of the School of Engineering and Applied Science for their help and co-operation during the preparation of this thesis.

The author also expresses his gratitude to the British Council and its staff members in Newcastle upon Tyne for financial support and assistance in overcoming problems during the past four years, and to the Education Section of the Embassy in London and Consulate General in Manchester of the People's Republic of China for their valued assistance and concern.

Finally, the author would like to thank his parents, sisters and their families for their concern and enthusiastic encouragement.

TABLE OF CONTENTS

LIST OF ILLUSTRATIONS

LIST OF TABLES

CHAPTER 1 INTRODUCTION

1.1 Introduction

The subject of impact and penetration has long been of interest to scientists from the areas of mechanics, physics, geophysics, metallurgy, material science, and engineering. Galileo was among the first to observe the difference between the static and dynamic behaviour of metals. Robins and Euler contributed the earliest work for the investigation of dynamic penetration. Since then the subject has been studied using empirical relations based on experimental results. Only from about the time of the Second World War was considerable research in analytical methods initiated and has continued to this time. More recently, with the advent and sophistication of large high-speed digital computers, research work on this topic has been greatly enhanced. Many analytically intractable or grossly tedious problems have been tackled and solved, and considerable progress made. Thus, the subject has now been extensively explored.

In areas involving impact and penetration the terminology is often scattered, and sometimes confusing. In the present context, some fundamental and phenomenological terms are defined for this thesis. The term *impact* is defined as the description of all phenomena associated with the physical process involved in the collision of two or more objects whose masses must be taken into account. Thus *impulsive* or *explosive* loading is excluded from impact because one of the striking objects does not possess the characteristics of a solid. The *target* is normally defined as any object or structure to which either impact or impulsive loading applies. Some impacts of practical interest produce a distinct local contact phenomenon when the striking object enters the surface of a target. This process results in the embedment of the striking object into the target and the formation of crater, providing physical emphasis to the meaning of penetration.

Thus, *penetration* may be defined as the entrance of a striking object into a target without completing its passage through the body. In contrast, *perforation* implies the complete piercing of target by the striking object. The penetration process can develop into perforation if targets are sufficiently thin. If the striking object rebounds from the impacted surface or penetrates along a curved trajectory, emerging through the impacted surface with a reduced velocity, the process is termed a *ricochet* .

The impact, penetration and perforation of striking bodies into metallic and non-metallic targets have now received widespread attention. Although military interest has and continues to be the important motivation for development and research in this area, the increasingly severe demands for safe, cost-effective design and dynamic behaviour of materials in short duration loading require a thorough understanding of materials and structures subjected to impact and impulsive loading. These concern the following.

(1) Military technology in:

(i) terminal ballistics for the study of plate penetration and perforation by bullets and shells and for the design of lightweight armour systems;

(ii) military weapons for the vulnerability of military vehicles, aircraft and structures to impact and impulsive loading.

(2) Civilian technology in:

(i) design of the protection of space vehicles subject to meteroidal impact;

(ii) design of the safety of nuclear-reactor containment vessels;

(iii) transportation safety of hazardous materials;

(iv) erosion and fracture of solids subjected to multi-impacts by solid and liquid particles, e.g. turbine blades, percussive drilling machines, pile drivers and grinding wheels;

(v) crashworthiness of vehicles;

(vi) explosive metal forming and welding, and safe demolition of prestressed concrete structures;

(vii) earth penetrations, e.g. remote investigations of geological materials, underground explosion, installation of deep-sea tension anchors, and measurements of sea-ice thickness;

(viii) study of the dynamic behaviour of materials at high rates of strain;

(ix) study of problems associated with the use of fasteners (which is the topic of this thesis).

Due to the complexity and variety of the subject, the establishment of a unified treatment of impact and penetration has thus far been inhibited by the variety of deformation mechanisms which may predominate, depending on the velocity regime, the material characteristics and configurations of the colliding bodies. Among these factors, the impact velocity so significantly influences the phenomenon that it precedes any other considerations in classifying the impact process. A rational description of the material response and deformation mechanisms then has to be confined to a specific velocity range. There is a number of existing classifications of the impact process as a function of the initial impact velocity. However, they are orientated to different purposes of applications. It is inappropriate directly to adopt any of these. Instead, referring to many classifications, especially those given by Backman and Goldsmith (1978) and by Zukas et al (1982), the following classification is considered more suitable to the work described in this thesis.

0 — 50	m/s	free falling velocity
50 — 500	m/s	low velocity
500 — 3000	m/s	high velocity
> 3000	m/s	hypervelocity

Because the response and the deformation mechanisms of materials depend on a number of parameters in addition to impact velocity, the range limitations should only be regarded as reference points and not as precise transition velocities.

The phenomena of impact and penetration in fluids and gases are beyond the scope of this thesis. Only the original solid state is considered. A main rational treatment of solids is perhaps bounded at two extremes by the dynamics of elastic solids and of compressible fluids. The response and deformation mechanisms which occur within these two boundaries have comprised a limited number of individual processes often with one predominant. They can be local or gross deformations or coupled, to some extent, dependent on a specific velocity range. The failure modes of target materials may be characterized in several different ways dependent on target thickness, material characteristics (brittle or ductile) and shape of the striking object in addition to impact velocity. Most failure modes are closely related to the perforation of thin or intermediate targets. Frequent types are fracture, spalling, scabbing, plugging, front or rear petalling, fragmentation in brittle targets, ductile hole enlargement and cratering (or embedment)*. Illustration of these modes is provided by Backman and Goldsmith (1978) and by Brown (1986).

---

* In general, embedment implies that the striking object is captured within the body of the target and involves no mass loss or erosion. The latter condition is not necessarily true for cratering.

In the following sections of this chapter, attention is devoted to the historical review of some fundamental principles and general phenomena, covering the whole range of impact velocity, pertaining to the impact and penetration. The impact phenomena occurring in the free falling velocity and hypervelocity ranges are only briefly reviewed for the complete coverage of the subject, and are not intended to be comprehensive. The high velocity range will be reviewed and discussed in terms of stress wave propagation. The principal phenomena in these velocity ranges are discussed only in a general sense, the dominant process or mechanism in each range will be emphasized for its relation to the impact and penetration of interest in the following chapters of this thesis in order to facilitate analyses and understanding. This thesis primarily concerns itself with the deformation process and rational treatment of impact and penetration in the low velocity range (50 — 500 m/s). Various aspects and the state-of-art of the subject are thoroughly discussed in a number of excellent review articles by Hopkins (1961), Goldsmith (1963), Backman and Goldsmith (1978) and Jonas and Zukas (1978), and are treated in detail in three monographs by Goldsmith (1960), Johnson (1972) and Zukas et al (1982).

The major objective of work in this thesis is two-fold. First, the majority of investigations have been concerned with the normal impact and subsequent penetration into construction materials such as soils, rocks, and concrete in the low velocity range. Three general types of approaches, i.e. theoretical, experimental and numerical, have been used to analyse, interpret and to understand these phenomena. Some part of work is equally applicable to metal materials, and to the higher ranges of impact velocity. Second, some efforts have been directed to understanding of the nature of anchorage formed between projectile and target after impact, which determines the force, known as the 'pull-out' force, required to extract the embedded projectile. For clarity, all aspects of the proposed work are as follows.

(1) A comprehensive and historical review of some fundamental principles and general phenomena pertaining to impact and penetration is discussed, primarily in terms of stress wave propagation, which is the major task of the current chapter.

(2) Experiments of both impact penetration and pull-out are conducted on a laboratory scale. The mineralogical characteristics and mechanical properties of sandstone as a target are described and determined.

(3) Slices of sandstone before and after impact are examined using an optical microscope and the impacted projectile (fastener) is examined by scanning electron microscope.

(4) The fundamental theory of impact penetration for geological materials is developed on the basis of existing cavity expansion theory under the ideal conditions of the material mechanical behaviours.

(5) A suite of two-dimensional computer programs is employed to simulate both penetration and pull-out processes. Numerical examples are provided and comparisons are made with results available from other sources.

(6) Impact penetrations under identical conditions in more (mineralogically) plastically-deformed rock (a limestone) and concrete should ideally be attempted for comparisons of penetrations, fractures and resistances to pull-out in sandstone.

1.2 Elastic Wave Phenomena

The response of striking bodies on impact in the lowest velocity range (0 — 50 m/s) is primarily dominated either by elastic wave phenomena or by elastic contact deformations provided that there are no drastic differences in the shapes of the striking bodies and their physical properties. The elastic waves that are generated include longitudinal, tranverse and torsional waves, their propagations becoming more complex when the boundary conditions are imposed by various structure geometries. This present review is restricted to the simple case of longitudinal wave propagation produced by impact in a homogeneous, isotropic, linear elastic bar or rod. Other types of geometry such as beam, plate, shell and half-space are not considered. Further, tranverse strain, lateral inertia, body forces and internal friction (dissipative force) effects in the bar are generally neglected. The elastic deformation problems of contact will be discussed at the end of this section.

Because of the assumption of one-dimensional motion of elastic waves, solutions can be obtained only in a few simple circumstances. Although these solutions are quite simplistic, they prove to be very useful in understanding the complex physical impact phenomena and in assessing the use of more complex analytical schemes. Extensive treatment of elastic wave propagation in solids is provided in detail in a number of monographs by Kolsky (1953), Goldsmith (1960), Johnson (1972), Wasley (1973), Achenbach (1973) and Zukas et al (1982). An excellent review of developments in elastic wave propagation is given by Miklowitz (1960).

Pochhammer (1876) and, independently, Chree (1889) presented the first analytical solution of sinusoidal wave propagation in infinitely long elastic bars, based on a linear theory of elasticity (often called 'exact' theory). The solution based on the specific boundary conditions comprised expressions relating the frequency and wavelength of the vibrations to the radius and material properties of the bars. The expressions are often called frequency equations (or dispersion equations or propagation conditions) for longitudinal waves. This solution forms a basis for much of the work in this area. The frequency equations for longitudinal wave propagation were solved by Bancroft (1941), who presented the numerical values. Davies (1948) confirmed the Pochhammer-Chree solution experimentally. Because of the complexity in application of the exact solution and the inherent restrictions, the Pochhammer-Chree approach is never used in practice. Instead, a number of elementary and approximate methods have been developed for treating elastic waves generated under one-dimensional (bar) impact situations. There are two types of approximate methods. The first one includes treatments that involve extensions of and improvements to the elementary theory (to be discussed below) so as to obtain the approximate dispersion curves. In the second method, the approximate solutions are obtained to the exact frequency equations using power series techniques. These two approximate methods will not be discussed further, but for more information, the afore-mentioned books should be referred to, especially that by Wasley (1973).

For many impact problems, the elementary theory is often employed under the assumptions in addition to those mentioned above that each plane cross section of bar remains plane during the wave motion and the longitudinal stress over each plane is uniform. It gives results close to reality as long as the ratio of bar radius to wavelength transmitted is much less than unity.

Based on the elementary theory, the first analytical solution of the equations of motion was obtained by Skalak (1957) for two semi-infinite bars undergoing impact. Jones and Norwood (1967) extended Skalak's solution by taking the radial dependence of stresses and strains into consideration. In all these solutions, the resulting integrals are so complicated that the evaluation of these integrals has been accomplished only for relatively long durations and distances from the impact end. However, for the practical impact of finite bars in which short wave lengths are involved, no direct analytical solution is available due to the difficulty resulting from the incorporation of end conditions. Love improved the elementary theory by considering radial inertia. Using Love's approximate theory, Conway and Jakubowski (1969) analysed experimental results from the coaxial impact of identical short-length bars and found that the comparison between experimental and analytical results was in close agreement provided that the end loading was correctly controlled. It is considered that a more acceptable solution can be derived using computational methods. Bertholf (1967) presented the results of a numerical study of the finite-length bars subjected to continuous and step loading.

A different school of thought dealing with elastic impact phenomena comes from the theory of the local contact deformations introduced by Hertz in spite of the static nature in its derivation. This theory, neglecting wave phenomena, predicts the local deformations under the assumptions that two bodies in contact have continuous, non-comforming and frictionless surfaces, and are considered elastic half-spaces; the strains are also assumed to be small. Thus, it only serves as a guideline since its assumptions limit its applicability to an ideal situation which can hardly be sustained in practice. For further details and its various forms of predictive equations the following reference is recommended to Goldsmith (1960) and Johnson (1982, 1985).

1.3 Elastic-plastic Wave Phenomena in the Low Velocity Range

When the yield strengths of materials are exceeded, the analyses of impact phenomena in terms of elastic plastic and shock wave propagation are far more complicated than those involving purely elastic material behaviour. A general, unified solution of this kind of analysis does not exist, but solutions have been obtained in two special cases, namely uniaxial stress and uniaxial strain states. These represent the extreme bounds of material behaviour, encompassing most other states of stress, and they are the simplest conditions to treat in mathematics and to produce in experiments. An analysis in either case is carried out to understand the dynamic deformation mechanisms through wave theory, to determine dynamic properties of materials and to construct the material constitutive equations.

The existing theories that have been employed for predicting the propagation of uniaxial stress waves in metallic bars fall into three general categories : (1) the rate-independent theory using the static stress-strain curve, (2) the rate-independent theory using a single dynamic stress-strain curve. (3) the rate-dependent theory in the form originally proposed by Malvern (1951). In the case of the second category there still is argument about whether or not this theory should be regarded as the rate-independent theory. On the other hand, the theory that has constantly been used to describe stress waves in conditions of uniaxial strain developed from plate impact.

1.3.1 Uniaxial stress wave propagation

1.3.1.1 *Wave analysis by rate-independent theory*

The foundation of rate-independent (RI) theory of plastic wave propagation under uniaxial stress conditions was formulated by Donnell (1930) who studied the wave propagation of inelastic stress in a semi-infinite bar by extending the concept of elastic wave propagation. Considering an elastic plastic material having a static bilinear stress-strain relation independent of strain rate he found that two distinct wave fronts would propagate through the material. The velocity of each front has its own characteristic speed dependent on the respective moduli of the elastic and plastic regions, as shown in Figure 1.1. Major contributions to the development of this theory were made during the Second World War independently by von Karman and Duwez (1950) in the U.S.A., Taylor (1946) in England and Rakhmatulin (1945) in the USSR.

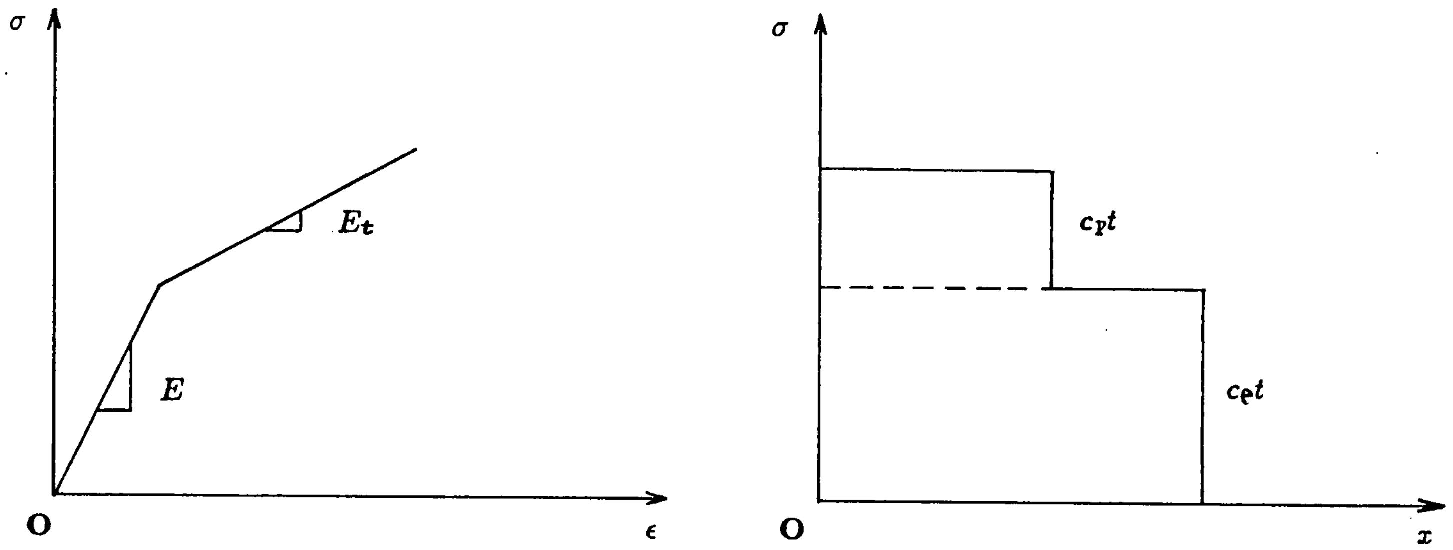

Figure 1.1 Stress–strain relation and wave profile for bilinear material

The theory was formulated on the basis of the following assumptions :

a) lateral inertia effects are negligible;

b) strain rate is neglected;

c) total strain (i.e. sum of elastic and plastic components of strain) in uniaxial stress is a single-valued function of stress;

d) the stress-strain curve is concave towards the strain axis (as shown in Figure 1.3).

The analysis is most simply made in terms of engineering (or nominal) stress and strain in the Lagrangian coordinate system. The complete solution can be schematically presented in Figure 1.2. Three distinct regions which show the strain, ϵ, along the axis of the bar at a given time, t, may be identified by reference to the original axial position, x, within the unstressed bar :

(a) from $x = 0$ to $x = c_p t$ the strain is a constant, ϵ_0 , and the plastic wave travels with front velocity c_p.

(b) between $x = c_p t$ and $x = c_\epsilon t$, there is variable distribution of strain between ϵ_0 and ϵ_Y (yield strain);

(c) for $x > c_\epsilon t$, i.e. ahead of the elastic wave, the bar is physically unstressed. It shows that there is a discontinuity in the strain at $x = c_\epsilon t$.

A powerful mathematical treatment for this type of wave propagation is the method of characteristics, the inherent complexities of which make further explanation difficult. Detailed information about this method can be found in monograph by Zukas et al (1982).

Predictions of the RI theory consist of two primarily distinct features. First is the presence of a plateau of constant strain near the impact end, which has

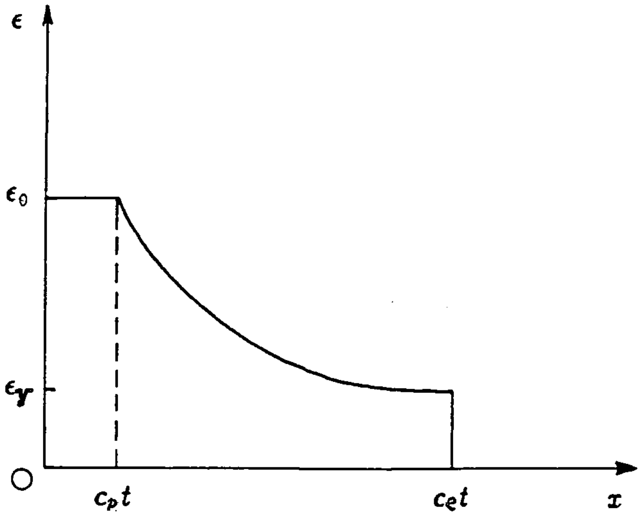

Figure 1.2 Strain distribution in bar

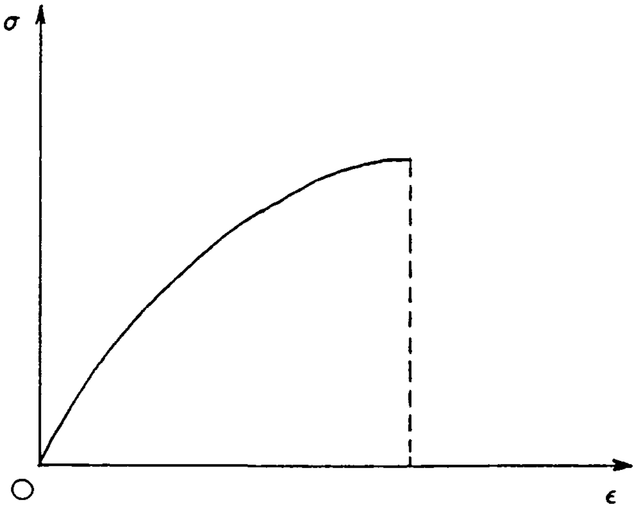

Figure 1.3 Stress-strain curve

been verified by a number of experimental investigations, primarily by Duwez and Clark (1947). Second, each small increment of plastic stress is expected to propagate at a characteristic velocity (which should be less than the elastic wave velocity) dependent on the tangent modulus or local slope of the static stress-strain curve. However, the experimental observations performed first by Bell (1951), on a bar which was prestressed into the plastic range statically or as the result of a prior pulse, show that both elastic and plastic waves are propagated at the elastic wave velocity. This point casts the most serious doubt about the validity of the RI theory, causes the major controversy about the necessity of including strain-rate effects in the constitutive model, and has generated nearly all of the experiments conducted in this area in the following three decades in order to explain this disagreement. However, it is reported that the predictions made with a single dynamic stress-strain curve agree very well with experimental results.

Another remarkable feature of the RI theory is the concept of a critical velocity beyond which instantaneous failure will occur at the impacted end. For the stress-strain curve as shown in Figure 1.3, at the ultimate strength of the material the speed of plastic wave propagation is zero. It implies physically that the energy of impact cannot propagate away from the impact end because of the zero velocity of additional strain and thus instantaneous failure occurs.

For the material behaviours considered so far in the RI theory, the stress-strain curve is concave toward the strain axis only. Thus it excludes the formation of shock waves. In practice, however, some materials (e.g. nickel-chrome steel, rubbers, concrete, soils and rocks) have the form of idealized mechanical behaviour as shown in Figure 1.4 indicating concavity toward the stress axis. Since the slope governing the wave speed is an increasing function of strain, higher strain increments will travel faster than lower strain increments

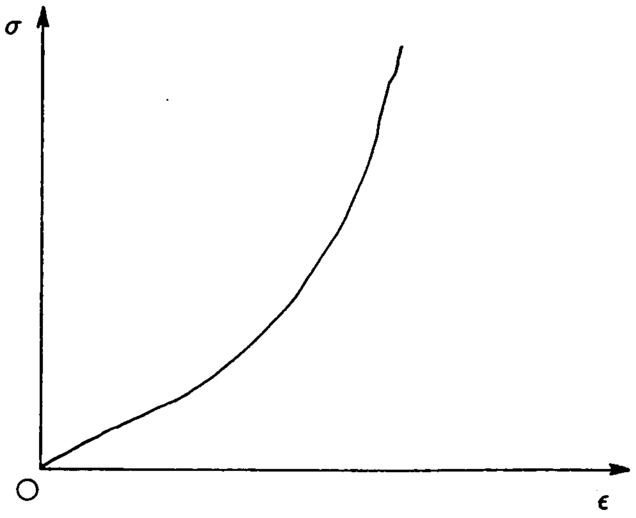

Figure 1.4 Stress-strain curve for a locking material

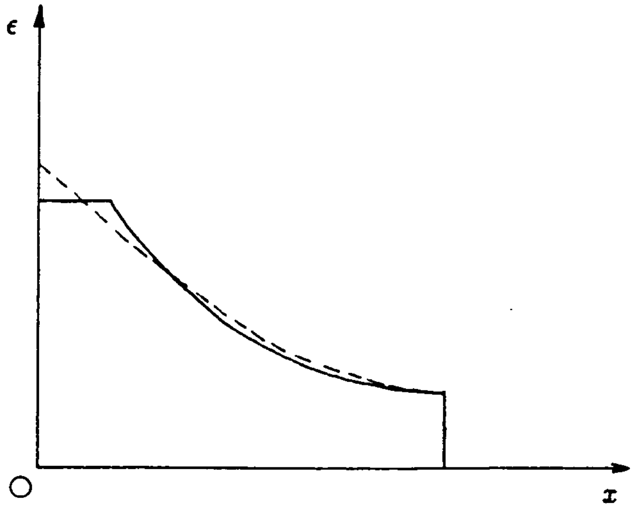

Figure 1.5 Comparison of strain distribution in bar produced by RI theory (solid line) and by RD theory (broken)

and must eventually overtake them. Because of the physical impossibility of having a higher strain increment without a lower strain increment, the stress waves would coalesce to form a shock front (this topic will be discussed in a subsequent section). Materials having this type of the mechanical behaviour are often designated as locking media (Further discussion about this is given in next chapter).

This basic theory of one-dimensional plastic wave propagation is generated only under the condition that the applied load acting at the end of a semi-infinite bar is non-decreasing (i.e. increasing or constant). If, after a certain time, the applied load decreases (or is entirely removed) resulting in elastic unloading, then the interactions of loading-unloading waves have to be considered, and if the bar is finite in length, waves will be reflected completely. One of the first of this type of problems was presented by Lee (1952).

1.3.1.2 *Wave analysis by rate-dependent theory*

It has been noted in the discussion in the subsection above that many materials behave quite differently under static and dynamic loading, showing rate sensitivity, and also that some aspects of wave propagation phenomena are not very well explained by the RI theory, especially the observed problem of the plastic wave propagation with elastic wave velocity. The disagreement between the prediction of the RI theory and experiments has been attributed to the strain rate effects, so that it is apparent that a rate-dependent consideration is required in the formulation of a constitutive equation for a proper description of material behaviour.

Ludwik (1909) postulated a logarithmic dependence of stress on strain rate. This relation of the form $\sigma = \sigma_1 + b\ln(\frac{\dot{\epsilon}_r}{d})$ has been the basis of numerous proposed constitutive equations to describe rate effects. Sokolo$\overset{v}{\wedge}$sky (1948) first treated wave propagation in elastic viscoplastic material without strain hardening using a similar strain-rate dependent relation. The most commonly used form of rate-dependent theory was proposed by Malvern (1951a, 1951b) for the dynamic behaviour of materials, namely

$$\sigma = f(\epsilon) + b\ln(1 + d\dot{\epsilon}_p) \tag{1.1}$$

where $f(\epsilon)$ is the stress from a quasi-static stress-strain curve in which ϵ is the total strain, $\dot{\epsilon}_p$ is the plastic strain rate and the superposed dot denotes the time derivative, and b, d are constants. This expression can be rewritten in the form

$$\dot{\epsilon}_p = \frac{1}{d}[\exp(\frac{\sigma - f(\epsilon)}{b}) - 1] \tag{1.2}$$

which shows that the plastic strain rate is a function of the overstress, $\sigma - f(\epsilon)$, or the difference between the instantaneous stress and the value that would occur in a quasi-static test at the same value of strain. The Malvern law decomposes the total strain rate into an elastic and a plastic component and assumes that the elastic strain rate ($\dot{\epsilon}_e$) is related to the stress rate through Hooke's law. The plastic strain rate function is then taken in the more general form

$$E\dot{\epsilon}_p = g(\sigma, \epsilon) \quad \text{or} \quad E\dot{\epsilon} = E(\dot{\epsilon}_e + \dot{\epsilon}_p) = \dot{\sigma} + g(\sigma, \epsilon) \tag{1.3}$$

This formulation implies that a material is brought to a state of incipient plastic flow after a given amount of elastic strain, independent of the elastic strain rate, but, because the plastic flow requires sufficient time to become appreciable, the additional strain beyond the static yield strain is at first mainly elastic (Malvern 1951a,b).This explains the propagation of stress increments at the elastic wave velocity in a prestressed bar since time is required for flow to occur.

The predictions from the rate-dependent theory were found to be sensitive to the assumed boundary conditions. The existence of a constant strain plateau could be confirmed provided that the constant stress boundary condition was used at the impact end. In contrast, early calculations by Malvern assuming a constant-velocity boundary condition failed to display this feature. However, it was shown later from the strain-rate solutions of Wood and Philips (1967) that the strain plateau always existed as time became very large, using the semi-linear rate-type theory for either constant stress or constant velocity boundary conditions.

Most research in the literature has employed the semi-linear form of the RD theory proposed by Malvern, in which the plastic strain rate is a function of stress and strain. One apparent prediction of this formulation is that the incremental wave velocity is the elastic wave velocity as observed in numerous experiments assuming there is no instantaneous plastic response.

The RD theory of Malvern is readily solved using the method of characteristics. For further details concerning this method, see Zukas et al (1982). An alternate approach to the method of characteristics for solving plastic wave propagation problems is a finite element or finite difference computer program. However, analytical treatment still provides a great deal of insight. Because neither the RI nor the RD theories give really close agreement with the experimental strain rate records it appears that further study, both experimental and analytical, is needed. A microscopic description of material deformation provides a promising approach for treating an incremental elastic viscoplastic, strain hardening behaviour with strain rate effects based on dynamic dislocation concepts. For further information an article by Taylor (1965) is recommended.

A major controversy between the RI and RD theories appears to involve the necessity of incorporating strain-rate effects into the constitutive equations for impacts in bars or rods and mathematical simplicity. The discrepancies are most apparent near the impact end and at earlier times as shown in Figure 1.5. However, the numerical study performed by Wood and Philips (1967) showed that the strain plateau near the impact end could always be expected to appear using the RD theory as long as sufficient duration time was maintained, and they demonstrated that the RD solutions asymptotically approach solutions obtained from the RI theory as time increases.

Since the lateral or radial motion of material is neglected, and the rate effects occuring most are significantly close to the impact end, the validity of the RD theory was questioned by Cristescu (1972) on the grounds that the complex three dimensional stress state near the impact end cannot be described by a one-dimensional wave theory.

Both the RI and RD theories were generalized by Lubliner (1964) in a theory of plastic wave propagation formulated on the basis of a general quasi-static constitutive equation. He showed that both theories were special cases of a generalized theory and showed conditions under which one or the other is valid.

1.3.2 Uniaxial Strain Wave Propagation

Because of the low-amplitude stress levels and relatively long time duration obtained from the uniaxial stress wave studies on long bars or rods, a number of problems were encountered in attaining high-amplitude stresses and determining dynamic properties of materials. Thus it has become necessary to make use of experimental configurations involving a uniaxial strain condition, such as plate impact, to produce high stress levels and high strain rates offering the simplicity of a one-dimensional analysis.

In these configurations, a plane wave can be generated by impacting a flat plate, the lateral dimensions of which are large compared to the distance travelled by the longitudinal waves or where appreciable lateral displacements are not possible. A description of the one-dimensional or uniaxial strain state is then valid for the motion of the central portion of the plate. This leads to one component of displacement or strain in the direction of wave propagation, and a three-dimensional state of stress. It is not necessary to assume neglect of lateral inertia, as is the case for uniaxial stress. The effects of thermo-mechanical coupling are neglected. Because of the lateral constraints, the stresses necessary to cause large plastic deformation are extremely high, often several orders of magnitudes above the yield stress of the material under an impact or explosive loading condition. Shock wave studies where the thermal pressure (that generated by shock waves causes the temperature rise of the material more than its volume change) is important are reviewed in next section. Here, for the stress regime where the elastic or cold pressure (that depends only on the density change or specific volume and is equal to the total pressure and specific internal energy at absolute zero temperature) is dominant and where material strengths and rigidity behaviour must be taken into account, analysis can often be made with the help of an elastic-plastic model.

The continuum theoretical analysis of elastic-plastic waves of uniaxial strain was first treated by Wood (1952), who emphasized the importance of hydrostatic compressibility in determining the nature of a wave.. Morland (1959) presented a systematic investigation of wave propagation treating elastic and plastic waves and the formation of shock waves. Fowles (1961) obtained some of the first experimental results verifying, in a general way, the predictions of the elastic-plastic model. The subject was also examined by Wasley (1973). A comprehensive treatment was provided by Nicholas (see Zukas et al, 1982) who extended a method of Wood to allow for variations in the elastic constants with increasing pressure. The approach taken below for the illustration of the analysis, though not rigorous, is presented because of its simplicity and because it provides insight and understanding of the situation, and requires minimum mathematical expertise.

The equations of motion and continuity are written in the familiar form for the uniaxial strain case :

$$\rho_0 \frac{\partial v_x}{\partial t} = \frac{\partial \sigma_x}{\partial x} \tag{1.4}$$

$$\frac{\partial \epsilon_x}{\partial t} = \frac{\partial v_x}{\partial x} \tag{1.5}$$

where $\sigma_x, v_x, \epsilon_x$ are the components of stress, particle velocity and strain in the direction of propagation, denoted by the Lagrangian coordinate x, ρ_0 the initial density, and t the time. If the density change is to be considered, particularly at high pressures, then mass conservation requires that

$$\epsilon_x = 1 - \frac{\rho_0}{\rho} \tag{1.6}$$

where ϵ_x is the compressive engineering strain.

The constitutive equation is needed to complete the formulation of the problem. It starts with separating strains into their elastic and plastic components, thus,

$$\begin{aligned} \epsilon_x &= \epsilon_x^e + \epsilon_x^p \\ \epsilon_y &= \epsilon_y^e + \epsilon_y^p \end{aligned} \tag{1.7}$$

where subscript y denotes any direction normal to the direction of wave propagation for an isotropic material, and superscripts e and p denote elastic and plastic components, respectively. The decomposition of total strain into elastic and plastic components requires that the total strains are small ($< 20\%$). Waves of finite strain, which occur under very high pressures, will be treated in the next section. Three basic assumptions are made concerning the stress-strain behaviour of the material : (1) the elastic strains are related to stresses through Hooke's law, (2) plastic flow is incompressible (i.e. plastic strains produce no change in density of the material), (3) strain-rate effects are not taken into account. From assumption (1), one has

$$\epsilon_x^e = \frac{1}{E}[\sigma_x - 2\nu\sigma_y] \tag{1.8}$$

$$\epsilon_y^e = \frac{1}{E}[(1-\nu)\sigma_y - \nu\sigma_x]$$

Assumption (2) can be expressed by

$$\epsilon_x^p + 2\epsilon_y^p = 0 \tag{1.9}$$

while the assumption of uniaxial strain condition requires

$$\epsilon_y = \epsilon_y^e + \epsilon_y^p = 0 \tag{1.10}$$

Combining (1.7), (1.8) and (1.9), the stress-strain relations in the elastic range are well known expressions.

$$\sigma_x = \frac{E(1-\nu)}{(1+\nu)(1-2\nu)}\epsilon_x = (K + \frac{4}{3}G)\epsilon_x \tag{1.11}$$

$$\sigma_y = \frac{\nu}{(1-\nu)}\sigma_x = (K - \frac{2}{3}G)\epsilon_x$$

where K is defined as elastic bulk modulus and G the shear modulus. For the material behaviour beyond the elastic region, plastic yielding occurs, and is defined by Mises-Hencky or the maximum shear stress criterion

$$\sigma_x - \sigma_y = Y(\epsilon_x^p) \tag{1.12}$$

where this has the same form as that for the uniaxial stress condition.

Hence, the stress-strain relation in the plastic range is expressed by

$$\sigma_x = K\epsilon_x + \frac{2}{3}Y(\epsilon_x^p) \tag{1.13}$$

The deviatoric stress remains constant, Y_0, in the simple case of an elastic perfectly-plastic material.

The yield point is defined by

$$\sigma_x = (\frac{K}{2G} + \frac{2}{3})Y_0, \quad \epsilon_x = \frac{Y_0}{2G} \tag{1.14}$$

and has been termed the Hugoniot Elastic Limit (HEL) as illustrated in Figure 1.6.

Equation (1.12) and Figure 1.6 show that the uniaxial strain curve (or stress Hugoniot) is parallel to the shock hydrostat (or pressure Hugoniot), and is offset from the hydrostat by an amount equal to two-thirds the yield stress, and that the stress is composed of a hydrostatic stress component and a contribution from the shear strength of the material. For low stresses the bulk modulus can be considered constant. At high stresses, the bulk modulus is generally an increasing function of stress that would lead to a concave-upwards stress-strain relation and to the formation of plastic shock waves. At sufficiently high stresses, the plastic shock waves can overtake the elastic precursor and form a single shock wave.

In practice, the loading wave is often reflected from the geometric boundaries, so resulting in the reduction of the stress levels. A wave of this type is called a rarefaction or release wave. The unloading process or path is usually referred to as a release adiabat, illustrated by curve BDE in Figure 1.7. In the uniaxial strain case the material unloads along an elastic release curve (section BD) until the difference in stresses is large enough to cause yielding in the reverse direction. Thereafter, the release curve is essentially that of a hydrostatically compressed material with the slope of the bulk modulus. When the stress unloads to zero, the material is still left with a compressive permanent strain. This results from lateral elastic stresses which are not relieved in this process

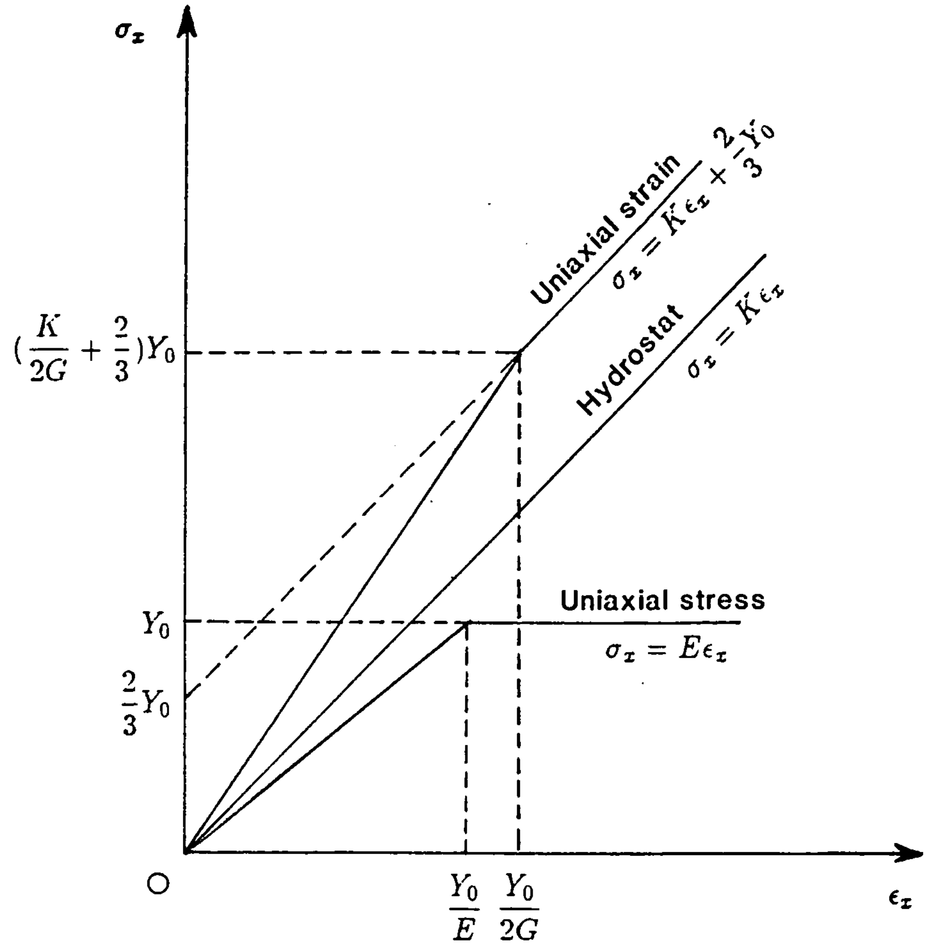

Figure 1.6 Stress–strain relations for elastic perfectly-plastic material behaviour

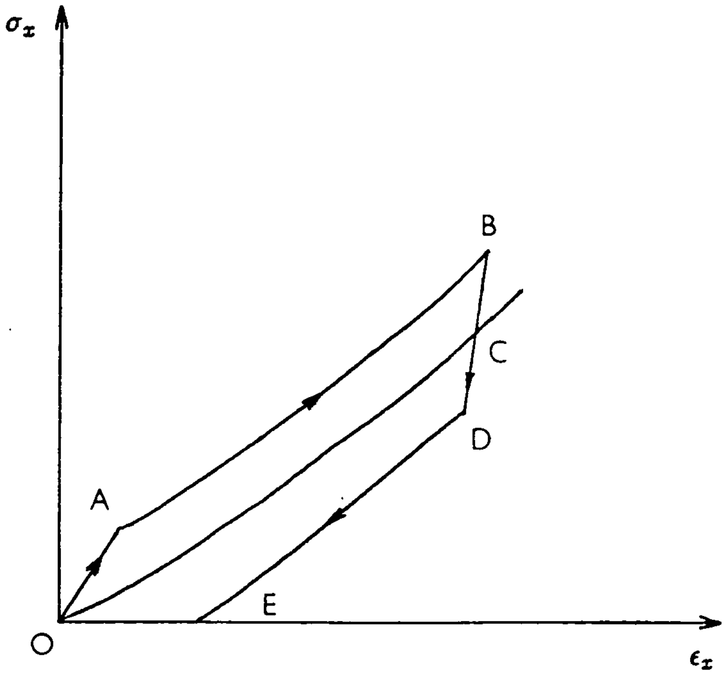

Figure 1.7 Stress–strain relation in uniaxial strain

and which maintain the material at the yield point. These lateral stresses can only be relieved by lateral expansion which is not allowed in this uniaxial strain analysis of elastic plastic wave propagation.

Because of both mathematical and physical complexities the above analysis for elastic-plastic wave propagation in uniaxial strain has been confined to the use of a rate-independent theory, analogous to the approach used extensively in uniaxial stress wave studies in long bars. As previously noted, the stress-strain relation in uniaxial strain is dominated by the hydrostatic behaviour that does not involve strain-rate effects because of the absence of shear stresses, particularly at higher pressures. Nicholas (1982) pointed out that higher strain rates are generally achieved experimentally at higher pressures, so that rate effects, even if more extensive at higher rates, are less significant in the overall stress-strain behaviour. Morever, the slope of the stress-strain relation governing the plastic wave velocity is insensitive to strain hardening or strain-rate effects because of the large contribution of the hydrostat. However, the discrepancies frequently found between predictions based on the rate-independent theory and experimental results suggest the involvement of rate effects in the uniaxial strain configuration. To identify effects of shear strength and strain-rate, experiments are commonly undertaken to observe either the attenuation of a plastic release wave or the amplitude of the elastic precursor at low stress levels where both elastic and plastic shock wave fronts exist. The decay of the elastic precursor with propagation distance is considered as some form of strain-rate effect or as an obvious manifestation of stress relaxation. Additional difficulties may occur in interpreting experimental data, but the current trend appears to favour strain rate-dependent analysis.

The variety and complexity of elastic-plastic phenomena make the development of a mechanical model of any observed behaviour a very difficult task.

Promising progress made in this area came with the application of concepts of dislocation mechanics. In dislocation theory, strain-rate effects and strain hardening are incorporated. Taylor (1965) first investigated the decay of the elastic precursor in detail based on this theory, and concluded that the decrease in amplitude of the elastic precursor with increasing propagation distance may be attributed to stress relaxation. In recent years, the microscopic phenomena adopted for explanations of deformation from a continuum-mechanical viewpoint have generated a number of dynamic theories of plasticity which, while still evolving, show great potential to progress in this area. Comprehensive reviews are provided by Cristescu (1968), and later by Campbell (1973).

As will be seen, elastic-plastic analysis assuming incompressible flow is a special case of compressible hydrodynamic theory. NeverthERLess investigations using this approach have proved to be extremely useful in attempting to understand certain physical situations.

In addition to the simple approach discussed above, a general continuum analytical theory of elastic-plastic waves has been developed by Lee and Liu (1967), who considered both finite elastic and plastic strains, and change in temperature due to thermomechanical coupling effects.

1.4 Shock Waves and Response

As impact velocities produce stress levels considerably in excess of the yield stress of the material, significant changes can be found in the bulk rigidity modulus and density. Shear strength, which can support only low shear stress at such stress levels, becomes a factor which has an almost negligible influence on the mechanical behaviour, whereas the compressibility affects the behaviour significantly so that the state of the solid material is characterized as if the material were a compressible fluid. Thus, stress waves propagating in solids can be considered in terms of the theory of hydrodynamics. The important implication from the increase of the bulk modulus is that high-amplitude stresses are propagated more rapidly than are lower-amplitude ones, and eventually overtake them to form a nearly vertical front. The continuous plastic wave front breaks down and a single discontinuous wave front develops to travel at a specific velocity. This wave front is termed a shock wave. It is more precisely defined as a finite stable, discontinuous or almost discontinuous wave in stress, density, particle velocity and entropy, having an amplitude exceeding the elastic limit of the material in which it is propagating. In fact, the shock front consists of a transition zone the thickness of which depends on the material. At higher pressures, the thickness of the shock front in solids is generally approximated by a surface during propagation while useful results can be obtained simply by applying the law of conservation of mass, momentum and energy across the shock front (Rankine-Hugoniot equations). Shock waves in solids are often generated by high-speed projectile impact or explosion on a material boundary. Scientific interest in them from military and non-military applications centres on their mathematical description, influence of dynamic material properties, determination of the constitutive equations or permanent damage caused by their passage.

Again, an exhaustive coverage of research contributions is not intended here, but a condensed review of the field is provided to give a simple illustration of the mechanical aspects of the shock waves and the major trends in their development. Only comprehensive reviews, or summaries and original works are cited here. Extensive treatment of the subject can be found in the monographs by Kolsky (1953), Goldsmith (1960), Cristescu (1967), Wasley (1973), Nowacki (1978) and Zukas et al (1982). Comprehensive, critical reviews are given by Duvall (1962), Doran and Lindre (1966), and Davison and Graham (1979).

Because of the significant influence of increasing compressibility and neglect of the shear strength of the material, the elastic-plastic analysis of wave propagation has been recognized to be inadequate in this pressure regime. A theoretical description of the phenomena has primarily been based on a compressible fluid behaviour. The propagation of shock waves and the deformation of the bodies involved must then be analysed by the relations governing compressible fluid flow, which consist of the nonlinear partial differential equations of continuity, motion and conservation of energy, and a constitutive equation specifying the relation between stress and density in a continuum. In addition, the equations of conservation of mass, momentum and energy across the shock front (i.e. so-called jump conditions) must be satisfied on the assumptions that the steady-state condition exists and the equilibrium of initial and final states is maintained. The effects of thermodynamic coupling is generally disregarded. For mathematical simplicity the analysis is often confined to the case of plane waves of infinite lateral extent, i.e. macroscopic uniaxial strain, as in elastic-plastic analysis. Hence, jump conditions are expressed as follows :

$$\frac{\rho_0}{\rho} = 1 - \frac{v}{c_s} \tag{1.15}$$

$$\sigma_1 - \sigma_0 = \rho_0 v c_s \tag{1.16}$$

$$e_1 - e_0 = \frac{1}{2}(\sigma_1 + \sigma_0)(V_{v0} - V_{v1}) \tag{1.17}$$

where c_s denotes shock velocity, σ, ρ, v, e and V_v are normal stress, density, particle velocity, specific internal energy and specific volume $(= \frac{1}{\rho})$, respectively, in which subscripts '0' and '1' denote the initial state ahead of the shock front and the final state behind it, respectively. The locus of final states behind the shock front can be uniquely determined for a given material by the initial state ahead of the shock. This locus in stress-volume plane is commonly referred as to a Rankine-Hugoniot equation of state, or simply a Hugoniot. As can be seen from

Equations (1.15) and (1.16), the Hugoniot can be determined by measurement of only two of the four variables, σ, v, c_s, ρ. These two variables are usually shock velocity which can be measured directly and particle velocity which cannot be directly measured for many metals. The particle velocity is then often obtained by the inference from the measurement of free-surface velocity. However, for materials such as rocks and ceramics, some sophisticated methods have been developed by Dremin and Adadurov (1964) to measure particle velocity directly.

As discussed above, at high pressures the mechanical behaviour of the solid in the absence of the shear strength is described using a hydrodynamic model as shown by curve I in Figure 1.8(a). However, when brittle materials are employed to study impact phenomena, strain rate effects are found by a number of investigators to be very important in the early period of loading. The materials no longer sustain any shear stress once yielding commences so that the final shock state lies on the hydrostat or shock Hugoniot as illustrated by curve II in Figure 1.8(a). The mechanical behaviour of this kind is often described by a model, called an elastic-hydrodynamic model. If pressures are lower, the shear strength of the material cannot be disregarded. A description of wave phenomena follows the elastic-plastic analysis reviewed in the last section.

At certain pressures and temperatures some solids can transfer from one crystalline structure to another. These changes are the so-called phase (polymorphic) transitions as illustrated in Figure 1.8(b). Due to this fact several shocks waves will appear, which propagate with distinct velocities. The shock wave is then no longer stable. Research into shock stability has been the subject of many investigations, but is beyond the scope of impact phenomena concerned in this thesis. The effects of shock waves on sandstone will be discussed in Chapter 3.

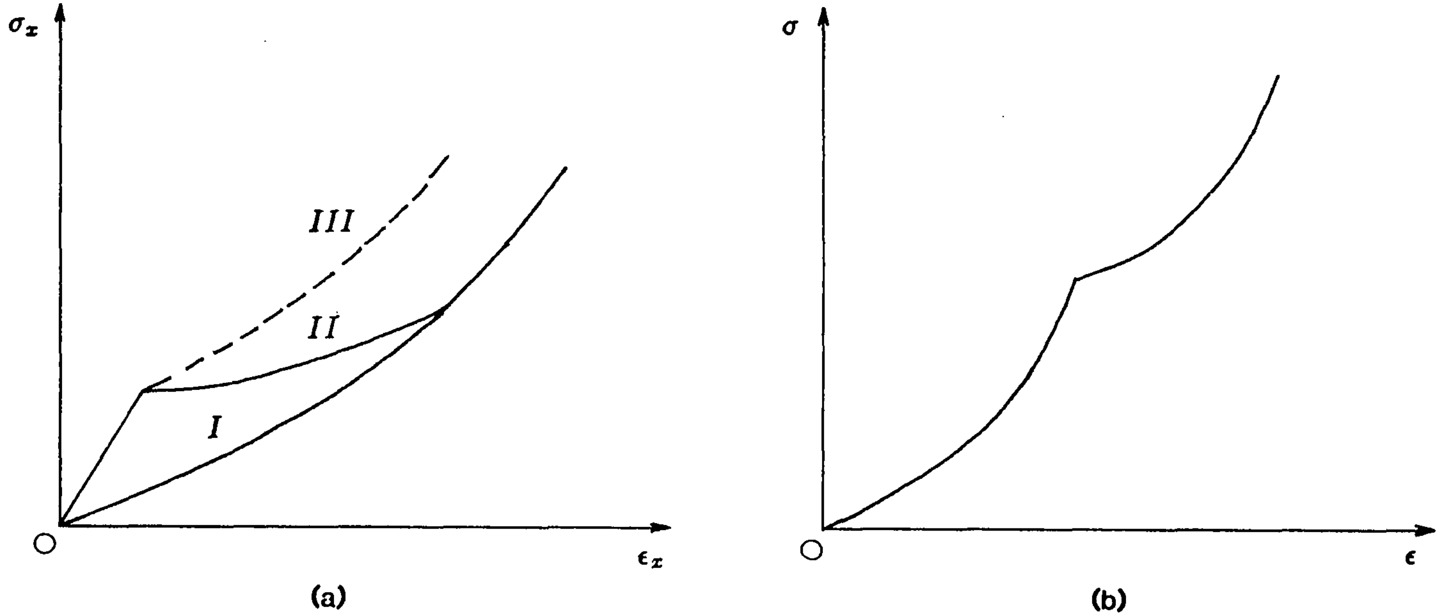

Figure 1.8 (a) Comparison of three stress–strain relations in uniaxial strain

(b) Illustration of the material phase transition

1.5 Hypervelocity Impact

In some physical situations such as the meteoroidal impact from the advent of space travel, jet penetration produced by a shaped charge (detonatable explosive device) and long rod or pellet penetration for terminal ballistic design, both the striking objects and targets are severely deformed either partially or completely because of the very high impact velocity, and many undergo a transformation from the state of a normal cohesive solid to that of a quasi-fluid. The large stresses induced by such impacts greatly exceed the yield strengths of materials so as to permit 'safe' neglect of material shear strength and compressibility. The impact velocity created in situations of this type is termed hypervelocity, the domain of which varies with projectile and target material combinations. It is at present favoured to take a velocity in excess of the elastic longitudinal wave velocity (c_e) as the lower bound and that less than thrice the plastic longitudinal wave velocity (c_p) as the upper bound (i.e. $c_e < V < 3c_p$, where $3c_p$ denotes the explosive limit).

Investigations into this velocity regime usually centre on the penetration history, factors affecting the penetration depth, wave propagation effects, damage of the striking object and terminal crater geometries on which the final prediction of penetration efficiency is based. A theoretical analysis of impact and penetration phenomena is often based on the hypothesis of steady, incompressible flows because of the complete deformation of the striking object and local target material. Opik (1936) developed the first theory of this type to study meteoroidal impact on a semi-infinite target while Birkhoff et al (1948) presented the penetration of jet-generation by a shaped charge on a semi-infinite target. Some extensions were made to account for the unsteady motion from the simple theory of Birkhoff. Although it has proved successful in application to limited problems, this simple theoretical approach as a whole is often criticized on the grounds of the absence of strength effects and the assumption of steady motion, resulting in the considerable deviations between experimental results and predictions. Consequently, the original hydrodynamic theory was modified to incorporate strength effects, first by Pack and Evans (1951), who also pointed out the three-phased process of cratering. A different model has been proposed by Grimminger (1948) who considers a rigid striking object for the meteoroidal impact. Similar treatment with a rigid portion of projectile in long rod penetration was also provided by Alekseevskii (1966) and by Tate (1967, 1969). As a result of this development, a compressible hydrodynamic theory is extensively introduced to investigate the various problems of hypervelocity impact.

In general, hypervelocity penetration involves three distinct stages : (a) when the striking object impacts the target surface a strong plane shock wave is initiated in both the striking object and target. A crater is then produced, and the interface between the striking object and target is moving relative to the shock wave; (b) after this first stage of impact the shock wave runs far ahead of the interface leaving the materials behind the shock unaffected so that the steady-state situation develops where the hydrodynamic analogy is applied. If the target is thick enough and the striking object long enough this intermediate stage will be the dominant phase of penetration; (c) when energy at the crater wall can no longer overcome the target material resistence or when the striking object is completely consumed then the termination stage results in crater formation or else failure occurs.

Taken overall, the penetration is clearly an unsteady process, especially in the initiating and terminating stages of the cratering process. In a more complete treatment these effects must be taken into account, leading to the introduction of elastic plastic considerations that can only be achieved using extensive computational codes such as DYNA, HEMP, EPIC and HELP. Such examples are provided by Pidsley (1984) and by Misey (1977). Morever, if rarefaction waves are involved as is the case in the finite target impact situation, then reflected waves and their interactions with incoming waves must be considered. This is especially true in thin plate impacts where observed phenomena are often examined from the viewpoint of shock wave propagation. Abundant contributions on this topic can be found in numerous monographs by Burke and Weiss (1971), and by Chou and Hopkins (1972).

Because of limited applicability to penetration mechanics and to problems concerned in the following chapters of this thesis, there will be no further discussion. There is a vast literature on this subject. Important work is covered quite comprehensively in a series of proceedings ranging from 1964 to 1969 and in a monograph edited by Kinslow (1970). Reviews and surveys are also given by Backman and Goldsmith (1978) and by Swift (1982).

Chapter 2 THEORY OF IMPACT PENETRATION

2.1 Introduction

Impact and penetration phenomena are extremely complicated. The interaction of projectile and target involve not only different materials and geometries at given impact conditions, but also various deformation mechanisms and damage patterns. Hence, much research work in this area has been experimental in nature, especially in early times. However, in order to quantify the phenomena the collected data are often either correlated with some algebraic equations leading to empirical or semi-empirical analytical relations to make predictions for the guidance of further experiments or are used to fit the equations generated by some analytical theory for predictive calculations.

A number of useful empirical equations have been developed which provide reasonable estimates of the penetration depth, based on the projectile and target characteristics for a variety of situations. However, some empirical parameters contained in these equations are not defined explicitly in terms of the target properties and the projectile characteristics. The numerical values of these parameters have to be evaluated from the separate penetration experiments. Thus, although some success has been achieved using these numerical equations, they may prove unreliable or else if reliable, their accuracy is limited to the range of test conditions for which they are deduced. A more basic approach has been introduced to treat one or two predominant aspect of physical phenomena (such as plugging, spalling, and cratering) by approximating the gross physical behaviour of the target material with a simple constitutive law. Once such a realistic constitutive law has been established, a boundary-value problem will be formulated using a group of governing differential equations with some simplifying assumptions. Further simplifying assumptions are usually made in the cause of obtaining a solution. The theory of dynamic expansion of a cylindrical cavity which will be developed in subsequent sections is one of such approaches in which material is approximated by a compressible locking behaviour in dilatation and bilinear elastic-plastic strain-hardening behaviour in shear. Unlike the empirical equations the resulting equations produced by the analytical approach do not contain empirical parameters that have to be determined from separate tests. For a complete solution of impact and penetration phenomena recourse must be made to a numerical approach using either the finite element or the finite difference computer programs which are the subject of Chapter 4 in this thesis. In the present chapter, attention is concentrated on (a) a brief review and discussion of existing empirical equations; (b) discussion on the mechanical behaviour of a locking medium; (c) the theoretical development of a cavity expansion using the locking approximation; (d) penetration theory adapted from the cavity expansion theory.

For different combinations of the projectile-target dimensions, analytical method used to attempt a solution can be quite different. The following context is confined to phenomena and the rational treatment of normal impact and penetration into a thick - semi-infinite target (i.e. the influence of a distal boundary on the penetration process is not present or is negligible). There is a vast amount of literature dealing with thin plate, intermediate and thick targets impact resulting in penetration and perforation. Considerable information can be found, among others, in articles by Goldsmith (1963), Zaid, El-Kalay and Travis (1973), Backman and Goldsmith (1978), Jonas and Zukas (1978) and Zukas et al (1982), and in monographs by Goldsmith (1960) and by Johnson (1972). A review paper given by Brown (1986) also covers many aspects of this topic.

2.2 Review and Discussion of Empirical Relations

In this section, efforts are made towards the assembly of empirical relations in areas such as cratering and penetration into target material in which the formulation of a rigorous theory has been inhibited by the complexity and variability of impact phenomena.

The empirical relations are closely related to certain types of material characterizations and impact conditions. The large number of parameters appearing in them make the impact and penetration process very complicated to understand, especially those parameters which are difficult to control. In general, these relations do not give any insight into the process described, but rather provide an overall effect over some parameter ranges. However, because of the complex nature of impact phenomena their value should not be underestimated, especially when the number of variables to be correlated is small.

Most empirical relations used in penetration mechanics were developed under the assumption that the target resistance (F) to penetration is a function of initial impact velocity. This assumption is often expressed mathematically by a power series as follows* :

$$F = a_0 + a_1 V + a_2 V^2 + \cdots \quad + a_n V^n \tag{2.1}$$

where a_n and V^n are positive constants and velocities, respectively. However, in practice only the first three terms are actually found to have physical meanings. Thus, Equation (2.1) is truncated at second order to be the following empirical expression, the very well known as force law.

$$F = a_0 + a_1 V + a_2 V^2 \tag{2.2}$$

Through Newton's second law of motion, the following equation for projectile motion after impact is immediately obtained :

$$-m\frac{dV}{dt} = a_0 + a_1 V + a_2 V^2 \tag{2.3}$$

---

* It should be mentioned that a_0 in this section denotes a constant and its utility is confined within this section. The appearance of a_0 anywhere else in this thesis will denote the initial cavity radius as shown in Appendix B.

where m, t are projectile mass and time, respectively. The empirical prediction equations are then derived by integrating this motion equation with the axial resistance force given in the above force law. In the above equation, the terms on the right-hand side have been interpreted to associate with material strength, frictional effects and the acceleration of target material, respectively.

Because of a limited understanding of the penetration process and obviating mathematical difficulty, one or two constants in Equation (2.3) are often assumed to have no effect on the penetration process in order to make the final relations capable of prediction as a simple engineering tool. That is, most empirical relations are special cases of the above equation as will be seen in what follows.

One of the earliest known penetration equations was proposed by Robins and Euler, who assumed that the resistance to penetration was a constant proportional to the cross-sectional area of the projectile. Poncelet later modified the Robins-Euler assumption by considering that the resistance is a function of impact velocity in addition to the material strength. Since then, a number of empirical relations have been developed based on more or less different versions of the force law and with varying degrees of success. Among others, the following assumptions and their resulting prediction equations are quite well known and representative :

Robins and Euler

$$-m\frac{dV}{dt} = a_0 \tag{2.4}$$

$$Z_f = \frac{m}{2a_0}V_0^2 \tag{2.5}$$

where Z_f, V_0 are the final depth of penetration and the initial impact velocity, respectively.

Poncelet

$$-m\frac{dV}{dt} = a_0 + a_2V^2 \tag{2.6}$$

$$Z_f = \frac{m}{2a_2}\ln(1 + \frac{a_2}{a_0}V_0^2) \tag{2.7}$$

Resal

$$-m\frac{dV}{dt} = a_1 V + a_2 V^2 \tag{2.8}$$

$$Z_f = \frac{m}{a_2}\ln(1 + \frac{a_2}{a_1}V_0) \tag{2.9}$$

Petry

$$-m\frac{dV}{dt} = a_0 + a_2 V^2 \tag{2.10a}$$

$$Z_f = \frac{mgk}{A}\log(1 + \frac{V_0^2}{20000}) \tag{2.10b}$$

where g, k and A are gravitational acceleration, constant and the cross-sectional area of a projectile.

Allen, Mayfield and Morrison (1957a,b)

$$-m\frac{dV}{dt} = a_2 V^2 \quad \text{for} \quad V_0 > V > V_c \tag{2.11a}$$

$$-m\frac{dV}{dt} = a_1 V^2 + a_0 \quad \text{for} \quad V_c > V > 0 \tag{2.11b}$$

$$Z_f = Z_c + \frac{a_1}{2}\ln(1 + \frac{a_1}{a_0}V_c^2) \tag{2.12}$$

where Z_c is critical penetration depth at critical velocity V_c.

Young (1969) *

$$Z_f = 13.4N\psi\sqrt{\frac{mg}{A}}\ln(1 + \frac{V_0^2}{465}) \quad V_0 < 61 \quad \text{m/s} \tag{2.13a}$$

$$Z_f = 0.257N\psi\sqrt{\frac{mg}{A}}(V_0 - 30.5) \quad V_0 \geq 61 \quad \text{m/s} \tag{2.13b}$$

where N, ψ are soil constant and nose shape factor, respectively.

Chisholm, Peleze and Pugh (1962, see Wang, 1971) **

$$-m\frac{dV}{dt} = a_0 + a_1 V \tag{2.14}$$

---

* Young derived his equations using a best fitting technique, so the assumed force is not available.

** Equations(2.15) and (2.16) giving the respective penetration depths have been derived by the author.

$$Z_f = \frac{m}{a_1}(V_0 - \frac{a_0}{a_1})\ln(1 + \frac{a_1}{a_0}V_0) \qquad (2.15)$$

Fuchs**(**1963**)

$$-m\frac{dV}{dt} = a_0 + a_1V + a_2V^2$$

$$Z_f = \frac{m}{a_2}[\ln(1 + \frac{2a_2}{a_1}V_0) - \frac{V_0}{V_0 + \frac{a_1}{2a_2}}] \qquad (2.16)$$

for ${a_1}^2 = 4a_0a_2$.

It can be noted that Petry's equation (2.10) has virtually the same form as Poncelet's, and differs only in the constants which have been evaluated.

In the above discussion, almost all empirical equations have been derived on the basis of a force law, i.e. the resistive force is a function of impact velocity. However, Wang (1971), and Murff and Coyle (1973) employed different expressions for low velocity projectile penetration by assuming that the resistance to penetration is a function not only of impact velocity but also of projectile depth (i.e. displacement in the direction of penetration), which is expressed in the following form :

Wang (1971)

$$-m\frac{dV}{dt} = a_0 + a_2V^2 + b_1Z \qquad (2.17)$$

where Z, b_1 are displacement in the direction of penetration and a constant, respectively.

Murff and Coyle (1973)

$$-m\frac{dV}{dt} = a_0 + a_1V + b_1Z \qquad (2.18)$$

The complicated resulting prediction equations were obtained and were reported to give fairly reasonable results for the ranges of conditions considered.

2.3 Mechanical Behaviour of Materials with Locking Characteristics

In this section, the constitutive relations of the locking materials are described and their characteristics are discussed for the formulation of the cavity expansion theory. A material subjected to dynamic loading (impact or impulsive) will experience deformation. Before the yield limit of a material is reached the material experiences elastic deformation, its linear stress-strain relation being governed by Hooke's law. Beyond the yield limit, plastic deformation occurs. A stress-strain relation in this range deviates from (the extension of) Hooke's linear law, and can be described in a number of rather different ways depending on the characterization of a material. Thus, to facilitate analysis and understanding it is necessary to distinguish materials in terms of their mechanical behaviours in order to to make it possible to characterize their stress-strains relation sufficiently and accurately. A material may be loosely classified as 'soft' or 'hard' according to its strengths. Whatever it is termed, its true mechanical behaviour may always be idealized by two straight lines giving a stress-strain curve which is independent of strain-rate effects, as illustrated in Figure 2.1.

For a 'soft' material in the plastic regime as qualitatively shown by line OAB in Figure 2.1, an increase in deformation results in a decrease in stress * and the material does not support any stress greater than the yield stress. This process of deformation coincides with the behaviour of 'strain-softening 'materials which are often encountered in civil engineering practice. Such 'softening' behaviour is unstable, and then may transit to a stable state with increasing strain to sustain a residual stress. However, if it is assumed to have no significant difference between yield stress* and residual stress of a material then it can be conceived that the deformation proceeds unlimited at an approximately constant state of stress once the yield limit has been reached. Hence, there exists an extreme case of the mechanical behaviour of a 'soft 'material, as indicated by line OAC.

---

* It should be noted that for this class of materials, a material loses its resistance with the increase of deformation only after its ultimate strength is reached. If there is no significant difference between yield strength and ultimate strength of material, the ultimate strength is omitted in Figure 2.1.

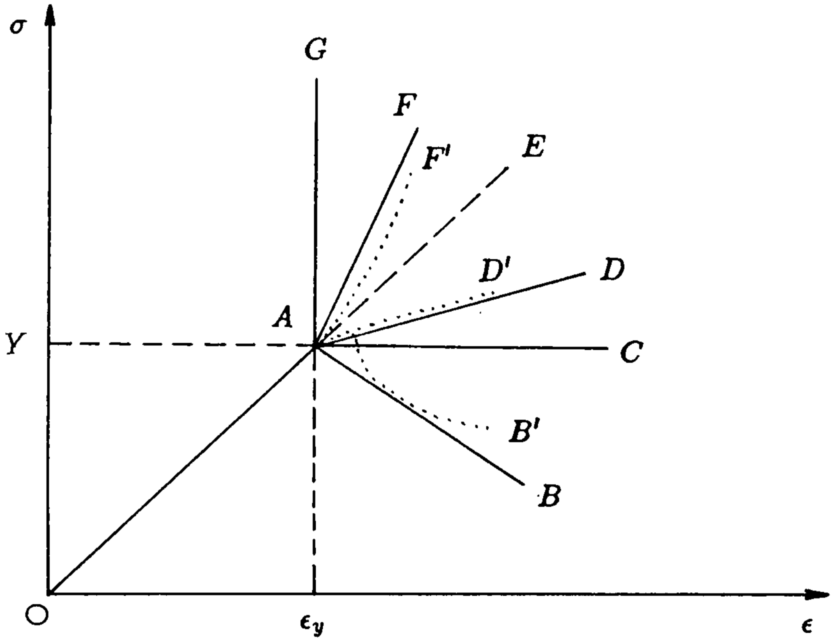

Figure 2.1 Stress–strain relation

In general, the material with this type of stress-strain relation is commonly called an ideal plastic or elastic perfectly-plastic material. In this case here, that state of constant stress rather serves as a limiting condition. The analysis and understanding of this 'soft' material are very useful. However, emphasis in this section is placed on the other class of materials discussed in the subsequent text.

In contrast with 'soft 'material described above, there exists a 'hard 'material with its mechanical behaviour bounded between an elastic perfectly-plastic and ideal 'locking' state, the former being taken as a lower extreme case of the range, and the latter being considered as an upper extreme case of the range, as indicated by line OAG in Figure 2.1. It may be noted from Figure 2.1 that in this class of materials the material resistance to deformation always increases with the proceeding deformation. However, there are two distinct situations depending on the slope of stress-strain curve in this range and leading to two rather different ways of analysis and understanding the material behaviour. It is apparent that if the slope of stress-strain curve is smaller than Young's modulus (i.e. $0 < E_t < E$), the slope governing wave speed is a decreasing function of strain, stress waves corresponding to their slopes have speeds less than the elastic wave velocity. As the deformation proceeds, stress waves propagate slower and slower and the distance between elastic and plastic wave fronts increases steadily, so excluding the formation of shock wave. Thus, the solid with (average tangential modulus less than Young's modulus ($0 < E_t < E$) is commonly called an elastic-plastic strain-hardening material, as shown by line OAD in Figure 2.1. If the slope of the stress-strain curve is greater than Young's modulus (i.e. $E < E_t < \infty$) then the slope governing wave speed is an increasing function of strain. Stress increases faster than strain does until deformation nearly ceases, so leading to a state in which material is said to be locked. In other words, the distance between elastic and plastic waves fronts diminishes gradually until the two fronts coalesce to form a shock front, as illustrated by curve OAF' and ideally by line OAF in Figure 2.1. The material with a tangential modulus greater than Young's modulus and having a locking tendency is termed a locking material. (A more complete definition will be given in the following appropriate paragraphs.) If the slope of stress-strain curve is approaching infinity, the upper extreme case of the locking material is obtained, indicated by line OAG in Figure 2.1. Up to now the locking materials have been distinguished from the strain-softening and strain-hardening materials in terms of their mechanical behaviours. The important properties of locking materials are hereafter discussed with emphasis being placed on their stress-strain relation related to the cavity expansion theory and penetration theory which will be followed.

The use of porous materials and artificially foamed solids in structural applications, of soils in soil dynamics and geophysics, has gained widespread attention during the past three decades. For instance, lightweight distended metallic foams have been employed as either outcasings or interfacial layers or core materials to protect structures from impact and shock waves, and geological materials have been either targets or engaged in earth penetration studies. Materials such as these and those like nickel-chrome steel, rubbers, ice and snow are examples of locking (or compactable) materials. The dynamic behaviour of these locking materials under impact or impulsive loading and in particular, phenomena relating to the constitutive relationships and the propagation of shock waves through them have required thorough understanding and analysis.

The concept of locking in a material can be described in the following way. Consider a material with the initial density ρ_0 in the non-deformed state subjected to a compressive loading. With the increase of this loading material undergoes deformation until a certain level of pressure (P_c - critical pressure) is reached, and then the density of material jumps to a limiting value characteristic of the material, (or called locking density). Once this limiting density has been reached, the material is said to be locked, no or almost no further increase of the density is possible during any subsequent increase in loading. During unloading the density remains constant and equal to the limiting density reached during loading, as illustrated in Figure 2.2. It is assumed that the material has only two states, i.e. the elastic (segment OA) and the locking plastic (segment BC), and that the transition from the elastic to plastic occurs only on the shock wave front instantaneously as shear yielding takes place at $P = P_c$ in which a viscosity effect is not taken into account. Because the shock front is approximated by a surface, the density change is manifested by a jump. In the elastic range, the material is incompressible and reversible deformation follows Hooke's law, while in the locked plastic range at $P > P_c$, the material again is incompressible, and behaves as a rigid body. A residual volumetric deformation is produced (line CBD) after the material is unloaded, or in other words, the material is compacted. During yielding the deformation is converted to the plastic work. As one knows, the influence of the hydrostatic stress on plastic work is insignificant in the yield of metals. Such an assumption appears not to be quite true for porous materials and geological materials. In this case it is more plausible to assume that the plastic work increases with an increase of the hydrostatic stress. In spite of this, the effect is regarded as being substantially insignificant.

Described above is a general model of locking mechanical behaviour in a material. A number of special cases further simplify this general model to facilitate analytical formulation in wave propagation problems. These are discussed in subsequent text.

The concave-upward (toward the stress axis) stress-strain curve as illustrated in Figure 1.4 was first reported by White and Griffis (1948) and the locking concept appeared in the paper by Ishlinskii et al (see Cristescu, 1967), who studied soil deformation caused by an underground explosion. The work of above authors was further developed by Zvolinskii (1960). Prager (1957a,b)

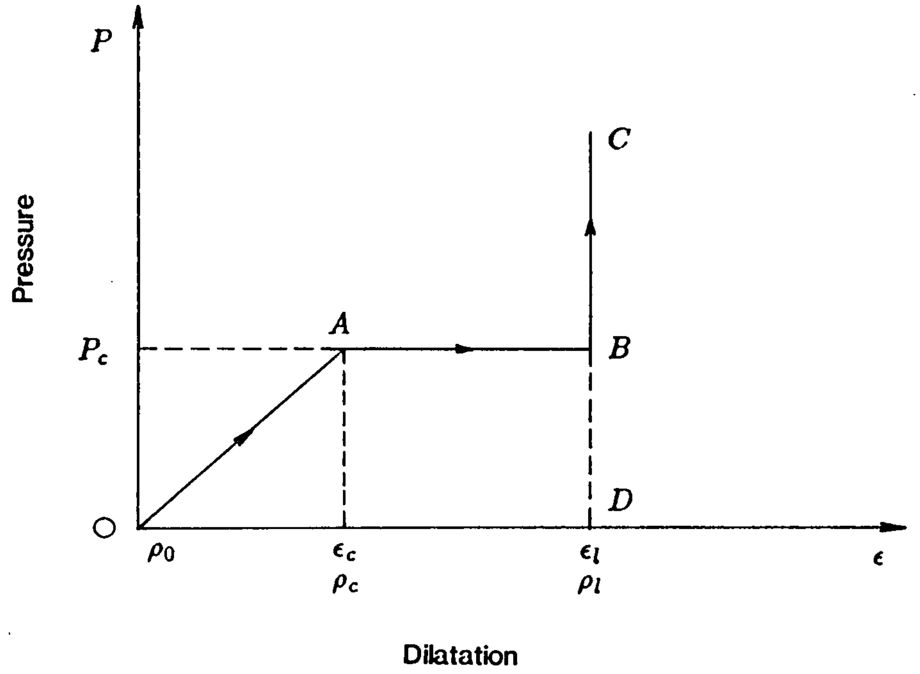

Figure 2.2 Stress–strain relation in a locking material

discussed one of special cases with a material model termed ideal locking and proposed a general theory for this class of materials which presentsa critical condition beyond or under which locking can or cannot occur. Further, Sun and Philips (1969) developed a more complicated general theory which contained three locking conditions. However, these general theories have been developed only for static problems. The propagation of spherical waves in a plastic locking material was also treated by Salvadori et al (1960) who attempted closed solutions with additional simplifying assumptions. Hanagud (1964, 1966) considered, in an analytical way, problems of expansion of a spherical cavity in a locking material and studied the constitutive equations of this type of materials. Scott and Pearce (1975) employed this model to investigate soil compaction by impact. The propagation of an impulse in a viscous simple locking material was discussed by Miles (1961). Based on the general model of a locking material as shown in Figure 2.2, there is a number of special cases which are very useful and offer simple analysis and understanding.

(1) Ideal locking model, $\epsilon_c = \epsilon_l$

Since the material of a certain initial density does not offer at first very much resistance to compression, when the material is compressed and its volume is reduced there is a resulting increase in density. Once its limiting density is approached, the material becomes incompressible in the manner of a rigid body, as shown by curve OCD in Figure 2.3(a), and can be idealized by line OAB. This material model is termed the ideal locking material. It is noted that after yield the material density does not experience a finite jump (no energy is dissipated during this process). There will further be two special cases from this model which will be discussed in the subsequent text.

(2) Rigid plastic locking model, $\epsilon_c = 0$

In contrast to the ideal locking model, the material in the present situation

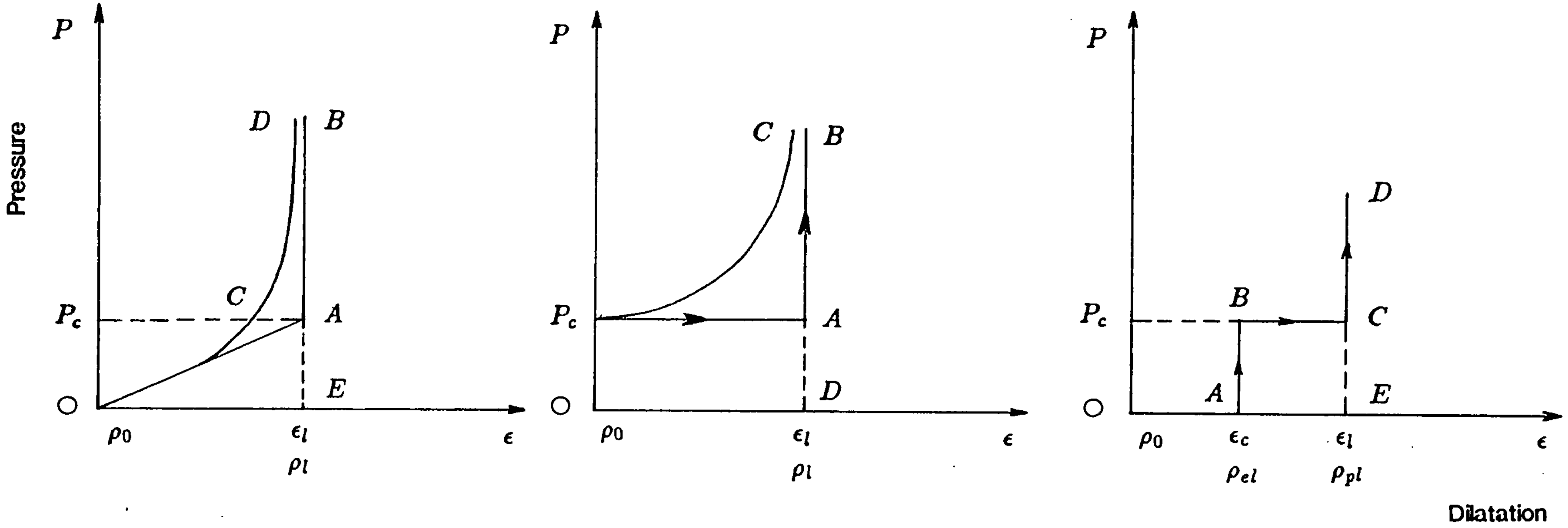

(a) (b) (c)

Figure 2.3 Pressure–volumetric strain relations in locking materials does not produce any deformation until the yield stress is attained, and then the material density immediately reaches its limiting value with a concomitant jump, so leading to some irreversible deformation, as shown in Figure 2.3(b).

(3) Elastic locking and plastic locking model, $\epsilon_c \neq \epsilon_l (= 0)$, $\epsilon_c = \epsilon_{el}$

Since a wave discontinuity exists at the interface of a stress-free state and an elastic state, a shock front can then be expected. Hence a finite jump in density (also in stress) is assumed from the stress-free to elastic states. However, if this leading shock front is relatively weak, the elastic locking density (ρ_{el}) may approach the initial density. Then this model is virtually same as the second special case, i.e. rigid plastic locking model. In spite of this, this model as shown in Figure 2.3(c) has been widely accepted as a more general example of the two-state behaviour of locking materials, and is extremely useful in the formulation of the cavity expansion theory.

In certain circumstances, the ideal locking model does not describe the material behaviour accurately. There are two such cases to be discussed below. First, when a large finite deformation problem is involved and the initial pressure * of compressive loading considerably exceeds the yield limit of a material, the elastic stresses can be safely neglected resulting in an extreme case of idealization. The material with this type of behaviour in volumetric deformation is called the simple locking model, as illustrated in Figure 2.4(a) (it can be easily followed by setting $P_c = 0$ in Figure 2.3(a)). This simplified model is very useful when used to analyse the mechanical behaviour of plastic materials, such as soft soils. Second, when the pressure is increased greater than the yield limit and the limiting density of the material has been reached, any further increase in pressure will still produce deformation. This material behaviour, in which the

---

* It is assumed that before the material has sufficient time to yield, the pressure has risen to a level which is considerably greater than the yield limit.

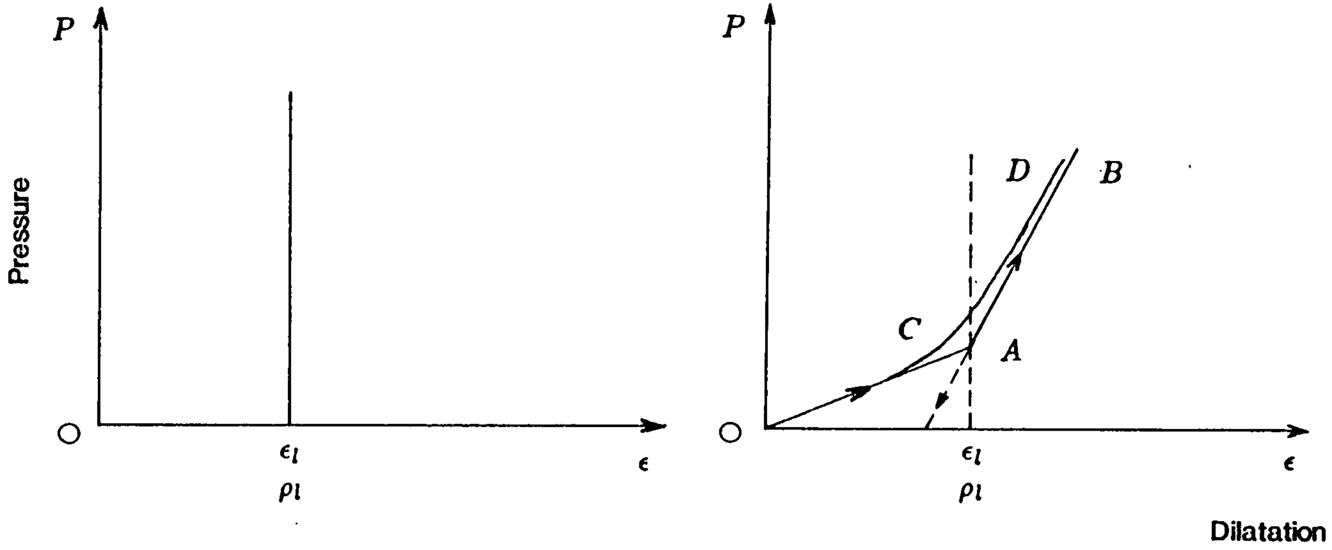

(a) (b)

Figure 2.4 Pressure–volumetric strain in simple locking and non-ideal locking materials density can increase beyond the locking value, is called the non-ideal locking model, as shown in Figure 2.4(b). As the pressure is reduced to zero, the residual volumetric strain is still very large compared to the small elastic recovery, and at present the increase in pressure to generate a small increase in density is much greater than it is in the elastic state.

2.4 Cavity Expansion Theory

There is wide variety of problems in solids involving either spherically symmetric or axisymmetric inelastic deformation when subjected to dynamic loading. Interest in these problems stems from various motivations. For example, the deep underground explosions by high-explosive charges have been investigated in the past half century for military, geophysical and mining applications and the safe design of pressure vessels and walled structures is another long-standing problem in industry. Deep metal punching and gun barrels are also closely connected with the present topic. Finally, impact and penetration into soil, rock, concrete and metal by shaped-charge jets, and projectiles or other striking objects have offered some good examples. In all the above cases of this class of problems there is a common feature in their deformations. This is that the deformation of materials has an approximate pattern of either spherical symmetry (underground explosions, pressure vessels, walled structures and penetration by hemi-spherical projectiles) or cylindrical symmetry (deep metal punching, gun barrels and penetration by shaped-charge jets and sharp-nosed projectiles) by envisaging the expansion of a formed cavity. Henceforth, the deformation of all solids exhibiting this feature is described as a cavity expansion, and a solution development for this cavity expansion is termed cavity expansion theory.

The dynamic expansion of spherical or cylindrical cavities in solids has been studied by many researchers. The first theoretical investigation of the cavity expansion with spherical and cylindrical shapes was provided by Bishop, Hill, and

Mott (1945) to approximate the solution of a quasi-static indentation process of a rigid punch in a semi-infinite medium. Hill (1950) discussed many aspects of the expansion of a spherical shell and a cylindrical tube in his monograph. The quasi-static expansion of a spherical cavity in metals was also treated by Chadwick (1959) who studied a similar case in ideal soil which obeyed the Coulomb yield criterion and flow rule. A dynamic solution for spherical expansion was later obtained by Hopkins (1960) who also incorporated the effect of material strain-hardening.

There is extensive Russian work relating to the cavity expansion problem, especially the problem of an underground explosion in soils. Because this work has its own complicated feature (e.g. the presence of moisture and degree of water saturation) it requires a separate treatment. No attempt is made here to summarize their work. For detailed information, a survey article given by Zvolinskii, Pod'Yapolskiy and Flitman (1973) should be consulted. It is apparent that the cavity expansion problems not only are of the practical importance, but also stimulate the academic interest in a variety of diverse fields. In this section, attention is deliberately confined to a general theory of a cylindrical cavity expansion with geometry as illustrated in Figure 2.5 and with material behaviour described by ideal locking compressibility under hydrostatic stress (as stated in the last section) and elastic-plastic, linear strain-hardening under shear stress, as illustrated in Figure 2.6.

The theory of dynamic expansion of a cylindrical cavity in an ideal compressible locking, elastic-plastic strain-hardening material is developed in Appendix A. This theory depicts the expansion of a uniform cavity of instantaneous radius $r(t)$ to the projectile radius in a semi-infinite material subjected to conditions of plane strain. The effect of material compressibility is approximated by means of an instantaneous locking assumption whereby the material experiences locking in both elastic and plastic states such that transition from the elastic to plastic

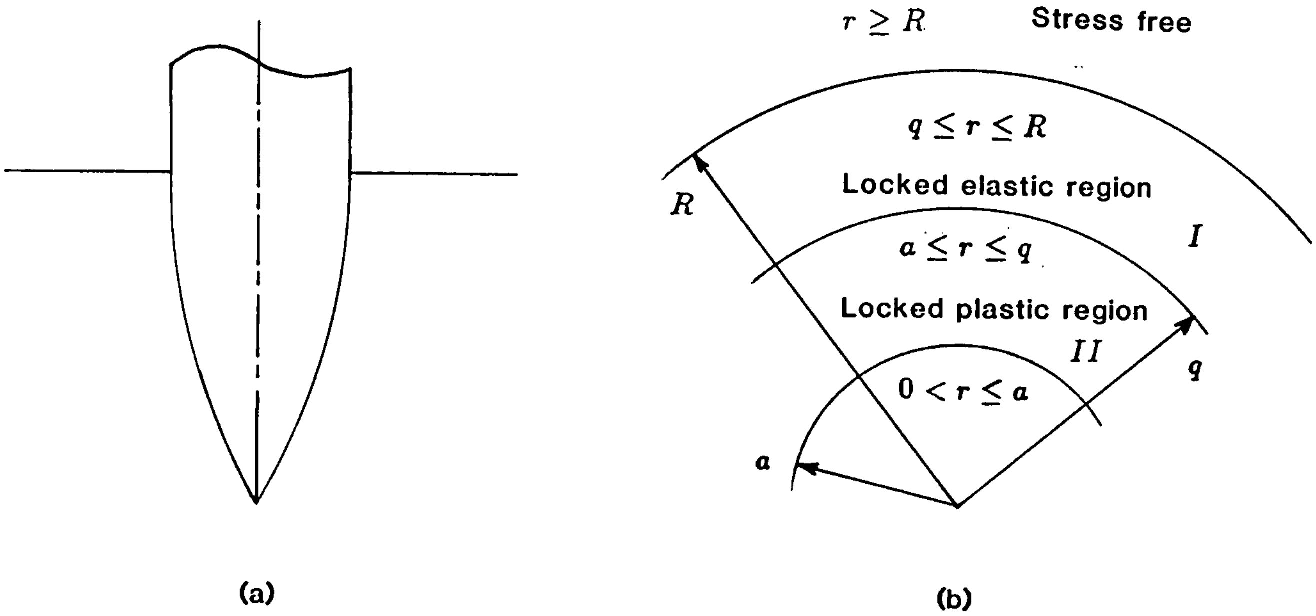

(a)

(b)

Figure 2.5 Geometry of cylindrical cavity expansion in a locking elastic–plastic material

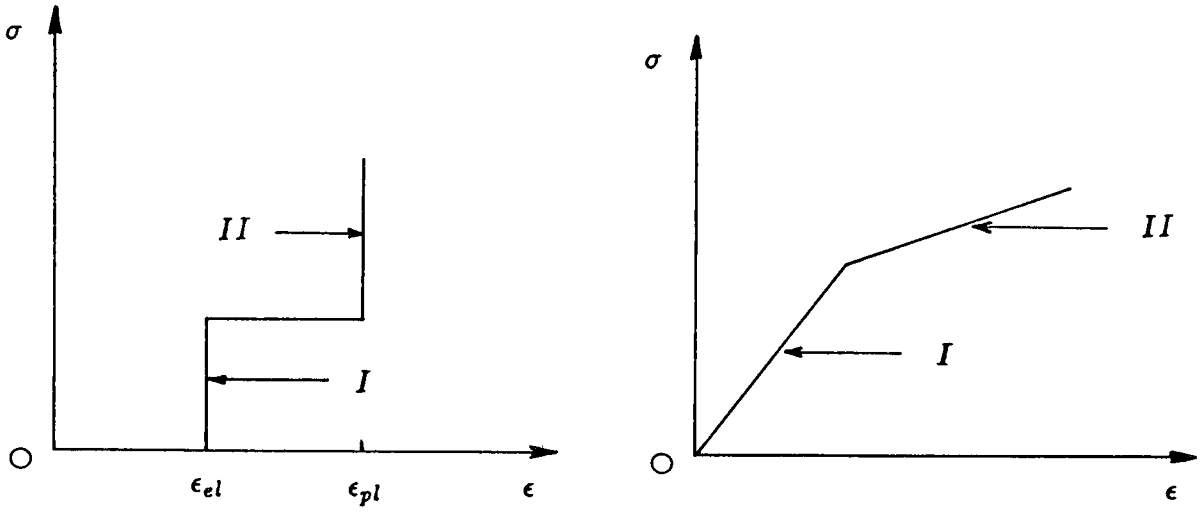

(a) Dilatation

(b) Shear

Figure 2.6 Stress–strain relation for a locking elastic–plastic material states is accomplished by a finite volumetric strain. As discussed in Section 2.4, the locking strains are a function of the instantaneous average dynamic pressure. The material in shear is described by bilinear elastic-plastic strain-hardening behaviour. Only in-plane stresses are considered. The exact solution of this theory is obtained from an equation of motion for the cylindrical expansion of the material having the mechanical behaviour stated above, and with the conservation laws of mass and momentum applied to the expanding boundaries of the locked elastic and locked plastic regions. Because of its complexity in order to make predictions as a practical engineering tool, an approximate solution is introduced to reduce it to a simpler form by using certain assumptions. According to Equation (A.66), the cavity pressure or local compressive normal stress to enlarge a cavity is determined for an assumed velocity field in the material adjacent to the cavity as

$$\begin{aligned} p(t) &= \frac{E}{3}(1-e^{-2\beta}) - \frac{Y_1}{2}\ln\alpha_2 + \frac{E_t}{3}\ln\alpha_2\ln(1-\sqrt{\alpha_2}) \\ &\quad -\frac{2}{3}E_t\sum_{n=1}^{\infty}\frac{(-1)^{n-1}}{n^2}[\alpha_2^{-\frac{n}{2}} - (\alpha_2^{-\frac{1}{2}}-1)^n - 1] + \frac{\rho_0}{2}\dot{a}^2 - \frac{\rho_2}{2}(\dot{a}^2 + a\ddot{a})\ln\alpha_2 \\ &= p_s + p_d \qquad (2.19) \end{aligned}$$

where

$$\begin{aligned} p_s = {} & \frac{E}{3}(1-e^{-2\beta}) - \frac{Y_1}{2}\ln\alpha_2 + \frac{E_t}{3}\ln\alpha_2\ln(1-\sqrt{\alpha_2}) \\ & -\frac{2}{3}E_t\sum_{n=1}^{\infty}\frac{(-1)^{n-1}}{n^2}[\alpha_2^{-\frac{n}{2}} - (\alpha_2^{-\frac{1}{2}}-1)^n - 1] \end{aligned} \qquad (2.20a)$$

in which α_2, β and Y_1 are defined in Equations (A.41b), (A.20) and (A.29) and

$$p_d = \frac{\rho_0}{2}\dot{a}^2 - \frac{\rho_2\ln\alpha_2}{2}(\dot{a}^2 + a\ddot{a}) \qquad (2.20b)$$

It is apparent that this cavity pressure consists of the separate contributions due to quasi-static deformation (or the shear resistance), p_s and dynamic pressure (or inertia), p_d, respectively. It is also noted that the quasi- static part of the pressure is determined by the constitutive properties of the surrounding material, i.e. the Young's modulus E, strain-hardening modulus E_t, yield strength Y, initial and locked plastic densities, ρ_0 and ρ_2. The dynamic part of the pressure is determined by the radial position, velocity and acceleration of the cavity wall.

Comparing the above results with those obtained from the dynamic expansion of a spherical cavity under similar conditions, as discussed by Hanagud and Ross (1971), it is obvious that their solutions differ only with respect to the constant terms. Thus, no attempt will be made to develop a similar theory for the dynamic expansion of a spherical cavity. In the above discussion, the developed theory is based on the homogeneous and isotropic material assumption. However, some materials have an apparent layered structure. Bernard and Hanagud (1975) developed a theory of dynamic expansion of a spherical cavity for such materials.

The present theory yields the material displacement front separating an outer elastic region from an inner plastic region, and which implies a condition that the tensile stress is less than the material strength. This implication excludes consideration of the formation of cracks at the elastic-plastic interface and elastic front.

2.5 Penetration Theory

In the preceding section, the cylindrical cavity expansion theory developed in Appendix A is discussed. This theory forms the basis of the present penetration theory which will be discussed subsequently in this Section. The results from the cavity expansion theory will be directly applied to the penetration problem.

By means of an ad hoc analogy, Goodier (1965) first extended the dynamic expansion theory of a spherical cavity to the penetration of a rigid spherical projectile into an incompressible elastic-plastic, strain-hardening material. Hanagud and Ross (1971) modified the cavity expansion theory to account for the target compressibility by means of the ideal locking approximations. Bernard and **Hanagud (1975), Bernard** (1976) further developed the cavity expansion theory to concentrically layered compressible material and used that as the basis of a projectile penetration theory for layered targets. In their work, a nose shape other than hemispherical was considered and the theory of penetration at non-zero obliquity was also proposed. Realizing that the penetration of porous materials by a rigid sharp-nosed projectile may be better described by the dynamic expansion of a cylindrical cavity, Norwood (1974) proposed a corresponding analysis for the penetration problem in a state of plane strain. Quite recently, Forrestal, Longcope and Norwood (1981a, 1981b), Longcope and Forrestal (1981, 1983), **Forrestal and Longcope** (1982), Norwood and Sears (1982), and Forrestal (1983, 1986) developed a series of penetration models based on the cylindrical cavity expansion theory by employing a variety of different constitutive relations for either plastic or elastic-plastic geological materials. In their work, the similarity solutions were obtained and the formations of the radial cracks at the elastic-plastic interface and the elastic-stress free boundary were taken into account (Forrestal and Longcope, 1982; Forrestal, 1983, 1986). **Butler (1975) and Rohani (1975) also treated this problem.**

At present, the following fundamental assumptions are made for the validity of the present penetration theory :

(1) the projectile is assumed to be completely rigid;

(2) the projectile impacts normal to the surface of target (i.e. at zero obliquity) and remains normal to it at all times;

(3) the target is initially stress-free and at rest;

(4) the target material is homogeneous and isotropic;

(5) the entire initial kinetic energy is transformed into the permanent deformation of the target and shock waves;

(6) the influence of the temperature change in the target is very localized and so heat conduction is neglected;

(7) there is no energy source within the system;

(8) body forces are neglected.

Assumptions (3), (4), (6), (7) and (8) are retained from the cavity expansion theory. There are also two assumptions made for the projectile-target interaction as follows :

(9) the nose surface of a projectile is in complete contact with the target when the penetration depth is greater than the nose length.

(10) after the penetration depth is greater than the nose length, only normal stress exists on the nose surface of the projectile (i.e. the friction effect is negligible).

It is not unreasonable to assume that the motion of the target material is mostly radial because of the sharp nose of projectile. To explain this point clearly, it is advantageous to use some observed evidence from penetration experiments. It was observed from the surface of the impacted fastener as described in Section 3.4.2 that the severe abrasion occured mostly at the nose surface, especially near the tangential point to the aft cylinder (fastener shank), yet adhesion of the target material to the aft body was due to the elastic recovery. This seems to suggest that the penetration of a sharp-nosed projectile in the target is the result of radial pushing action of the nose portion of the penetrating projectile. A cylindrical projectile with a conical nose travelling at velocity V_z at time t is first considered, as shown in Figure 2.7(a). It is assumed that V_z is a small velocity increment so that its higher order terms are negligible (this implies physically that the target particle acceleration has only a small effect on the projectile loading). Thus, the following relation exists since the projectile

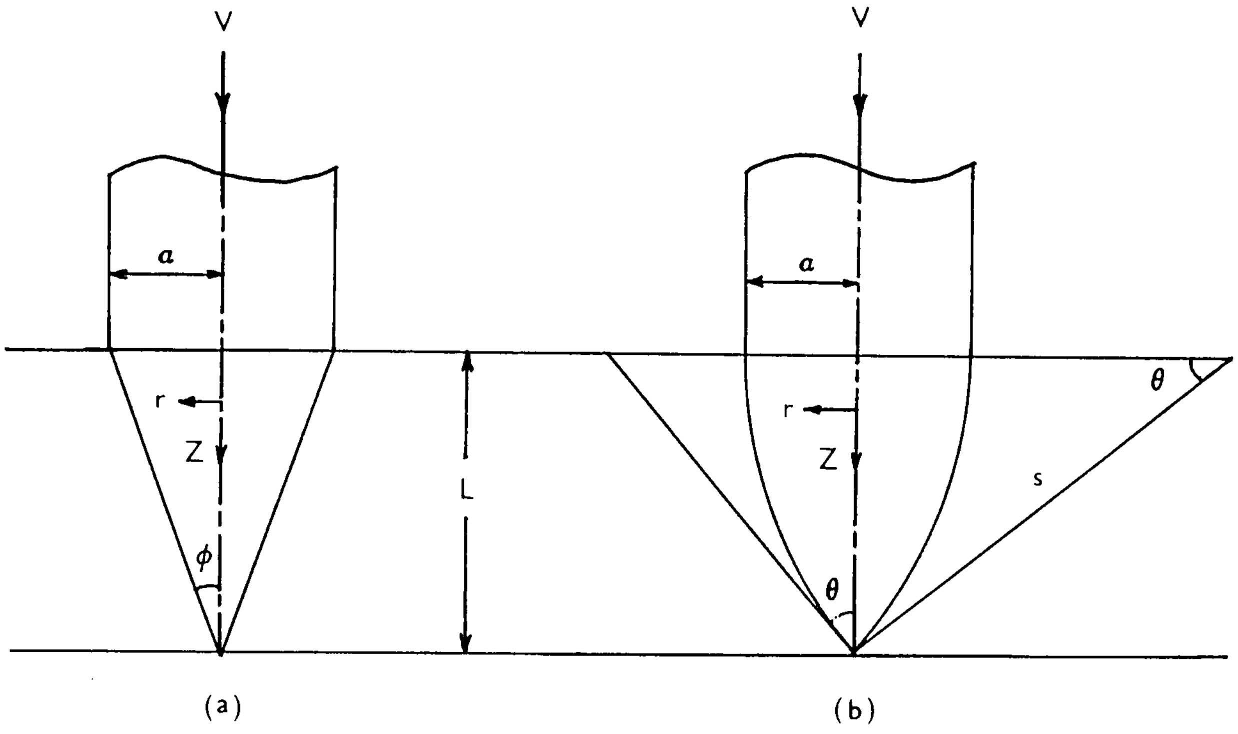

Figure 2.7 Geometries of conical and ogival noses

is a rigid body :

$$a = tV_z \tan\phi, \qquad V_z = \dot{Z} \tag{2.21}$$

where Z denotes the penetration depth at time t. Then Equation (2.19) becomes

$$p(t) = p_s + BV_z^2 \tag{2.22}$$

where

$$B = \frac{(\rho_0 - \rho_2 \ln\alpha_2)}{2}\tan^2\phi \tag{2.23}$$

Now, consider the work-energy relation, i.e. the total plastic work performed on the surrounding material by the initial kinetic energy in a small element.

$$dU = p(t) \cdot dS \cdot dr \tag{2.24}$$

where dS is the surface area of the instant cylindrical cavity at radius r ($0 < r < a(t)$). Hence $dS = 2\pi r dZ$ and the plastic work at the cavity surface (i.e. the axial resisting force) for that unit thickness (dZ) becomes

$$\frac{dU}{dZ} = \int_0^a 2\pi p(t) r dr = p(t)\pi a^2 = p(t)A \tag{2.25}$$

where A is the cross-sectional area of the projectile. Subject to assumptions (5) and (6), the change of the kinetic energy is equal to the plastic work performed on the cavity, that is, in conjunction with Equation (2.22)

$$-\frac{d}{dZ}(\frac{1}{2}mV_z^2) = \frac{dU}{dZ} = Ap(t) = A(p_s + BV_z^2) \tag{2.26}$$

with the initial and final conditions

$$V_z = V_0, \quad Z = 0; \qquad V_z = 0, \quad Z = Z_f \tag{2.27}$$

Equation (2.26) is integrated to give the impact velocity - penetration depth relation as

$$Z = \frac{m}{2AB}\ln(\frac{p_s + BV_0^2}{p_s + BV_z^2}) \tag{2.28}$$

As the velocity of the projectile is reduced to zero, then the final depth of penetration is obtained as

$$Z_f = \frac{m}{2AB}\ln(1 + \frac{B}{p_s}V_0^2) \tag{2.29}$$

It is interesting to note that Equation (2.29) is of the same form as empirical Equations (2.7) and (2.10).

Alternatively, the resulting equation for rigid body motion of a projectile with mass m can be used to give the total axial resisting force by integrating the normal stress over the nose surface of projectile. Thus, for cylindrical projectiles having conical noses,

$$m\ddot{Z} = -F_z = -\int_{Z=0}^{Z=L} p(t) \cdot \sin\phi dA(Z) \tag{2.30}$$

where $dA(Z) = 2\pi\frac{\tan\phi}{\cos\phi}ZdZ$. Integration of the right-hand side of Equation (2.30) in conjunction with Equation (2.21) and $\dot{a} = \dot{Z}\tan\phi$ leads to

$$m\ddot{Z} = -p(t)\pi a_0^2 = -[p_s + \frac{(\rho_0 - \rho_2\ln\alpha_2)\tan^2\phi}{2}\dot{Z}^2 - \frac{1}{2}\rho_2 a_0\ln\alpha_2\ddot{Z}]\pi a_0^2 \tag{2.31}$$

which is solved for the penetration-projectile velocity relation replacing $\dot{Z}$ with V_z

$$Z = \frac{M}{2AB}\ln(\frac{p_s + BV_0^2}{p_s + BV_z^2}) \tag{2.32}$$

where

$$M = m - \frac{1}{2}\rho_2 a_0\ln\alpha_2 \tag{2.33}$$

As the projectile velocity drops to zero, the final penetration depth is then obtained as

$$Z_f = \frac{M}{2AB}\ln(1 + \frac{B}{p_s}V_0^2) \tag{2.34}$$

It is found by comparing Equation (2.28) with Equations (2.32) and (2.33) that if the second term, so-called added mass or dirt cone, in the right-hand side of Equation (2.33) is neglected, then Equation (2.32) will be exactly the same as Equation (2.28). Because the added mass, $\frac{1}{2}\rho_2\pi a_0^3\ln\alpha_2$, is usually far smaller then the projectile mass, neglecting the added mass term seems to be reasonable and implies that the effect of the target acceleration is negligible.

For cylindrical projectiles with ogival noses as shown in Figure 2.7(b), a similar procedure as above applies. The ogive shape is assumed to be an arc of a circle with radius s and is tangent to the cylindrical aft body. Its locus is described by

$$r = a - s + \sqrt{s^2 - Z^2}, \quad Z = V_z t, \quad 0 < r \leq a \tag{2.35}$$

By replacing $a, \dot{a}, \ddot{a}$ in Equation (2.19) with $r, \dot{r}, \ddot{r}$ the pressure at the cavity surface becomes

$$p(t) = p_s + C(Z)V_z^2 \tag{2.36}$$

where

$$C = \frac{\rho_0}{2} \cdot \frac{Z^2}{s^2 - Z^2} - \frac{\rho_2}{2}\ln\alpha_2[\frac{s^2(s-a)}{(s^2 - Z^2)^{\frac{3}{2}}} - 1] \tag{2.37}$$

It should be noted that in the above equation C is a complex function of variable Z instead of a constant. Thus, the axial resisting force is given by

$$F_z = \int_0^L 2\pi p(t)(a - s + \sqrt{s^2 - Z^2})\tan\theta dZ \tag{2.38}$$

The integration for rigid body motion of a projectile is then given by

$$m\ddot{Z} = -F_z \tag{2.39}$$

which is solved to give the penetration depth as

$$Z = \frac{m}{2AC_2}\ln(\frac{C_1 p_s + AC_2 V_0^2}{C_1 p_s + AC_2 V_z^2}) \tag{2.40}$$

$$Z_f = \frac{m}{2AC_2}\ln(1 + \frac{AC_2}{C_1 p_s}V_0^2) \tag{2.41}$$

where

$$C_1 = \frac{2\pi L}{\cos\theta}[a\cos\theta - L + \frac{L}{\sin\theta}(\frac{\theta}{2} + \frac{1}{2}\sin\theta\cos\theta)] \tag{2.42}$$

$$C_2 = \frac{2L}{a^2\cos^2\theta}(a - \frac{L}{\sin\theta})[\frac{\rho_0}{2}(\ln\frac{\sin\theta - \cos\theta + 1}{\sin\theta + \cos\theta - 1} - \sin\theta) - \frac{\rho_2}{2}\ln\alpha_2(\tan\theta - \frac{a}{L}\frac{\sin^2\theta}{\cos\theta} - \sin\theta)]$$

$$\frac{2L^2}{a^2\sin\theta\cos^2\theta}[\frac{\rho_0}{2}(\frac{\theta}{2} - \frac{1}{2}\sin\theta\cos\theta) - \frac{\rho_2}{2}\ln\alpha_2((1 - \frac{a}{L}\sin\theta)\ln\frac{\sin\theta - \cos\theta + 1}{\sin\theta + \cos\theta - 1} - (\frac{\theta}{2} + \frac{1}{2}\sin\theta\cos\theta))] \tag{2.43}$$

From the variation of the half-nose angle in the coefficient C_2 in above equation it can be observed that as this angle approaches $\frac{\pi}{2}$, which is the case of a semi-spherical nose, the depth of penetration approaches zero. This implies physically that the axial resisting force becomes infinity and produces an infinite expansion, which is not allowed.

At this stage, it should be pointed out that in the foregoing analysis when the total resisting force is calculated it has been assumed that the cavity pressure or the compressive normal stress on the projectile nose surface or the cavity surface is constant for a given velocity. In other words, the normal stress is independent of the nose shape. Thus, the stress distribution on the nose surface is spatially uniform. This assumption appears to be plausible for the quasi-static part of the normal stress, but obviously it is questionable for the distribution of the dynamic pressure over the nose surface. Goodier (1965) proposed a cosine spatial variation of dynamic pressure around the spherical nose of a projectile so that the maximum pressure is obtained at the tip (or stagnation point) of the projectile nose and zero normal pressure at the base of the projectile nose. Bernard and Hanagud (1975) considered the spatial variation of dynamic pressure over the ogival and conical projectile noses in terms of a nose shape factor. No further consideration will be given in this thesis to this problem. For more details, the above references should be consulted.

The major objectives of a theoretical study into impact penetration are to find the resisting force or pressure exerted on the surface of the penetrating projectile and the penetration depth. The axial resisting forces obtained are expressed in Equations (2.31) and (2.38) for conical and ogival noses of projectiles, respectively, and the final depths of penetration are correspondingly given in Equations (2.34) and (2.41). Examining these equations some principal criteria in the design of impact penetration can be justified as follows :

(a) The analytical results show that the axial resisting force increases with the increase of projectile radius and impact velocity; the ignorance of target inertia overestimates the resisting force and underestimates the penetration depth.

(b) The results also show that the final depth of penetration increases as the impact velocity increases and that either a denser or a longer projectile is expected to penetrate into a target more deeply. The increase of projectile diameter reduces penetration.

It has been shown in the preceding analysis that the projectile penetration theory can be developed approximately on the basis of the cavity expansion theory. However, because of this crude analogy, the predictions from the present penetration theory may represent only the overall features of the projectile-target interaction which offers a complex physical phenomenon in practice. This theory has not been verified in experiments; hence further efforts should be made to assess its applicability and accuracy by comparative numerical examples. Moreover, it should be re-emphasized that the motion of the target material was assumed only radial in the development of this theory, the effect of frictional force acting on the nose surface was neglected and the influence of the aft body of the projectile has not been taken into account. This latter point implies that a gap may exist between the surface of the projectile aft-body and the surrounding materials, and may have some effect on the penetration process of the projectile. The rate-independence behaviour in shear was assumed. These considerations, together with the non-zero obliquity impact and penetration into layered targets, provides some important areas which merit further investigation.

Chapter 3 EXPERIMENTAL STUDY OF IMPACT PENETRATION

3.1 Introduction

The experimental study of impact penetration described in this thesis consists of three parts. The first part is the penetration experiment which comprises a cartridge-operated fixing tool firing a fastener into a cylindrical target with the initial impact velocity measured separately. Without perforation the fastener is embedded in the target which is relatively large. In the second experimental part the embedded fastener is pulled out from the target at a constant rate in order to investigate the bonding mechanism formed during penetration. The last part is the microscopic pre- and post-impact examination of the fastener and target.

In this and subsequent chapters, the term 'fastener' is used to denote the specific device which is the projectile fired from the cartridge tool. The term 'projectile' is a generic term and is used elsewhere in the thesis in this sense. If not stated expressly, the use of fastener elsewhere implies direct connection to experiments described in this Chapter. The distinction so made is just for maintaining this device as it is to avoid confusion.

3.2 Penetration Experiments

3.2.1 Description of apparatus

The penetration experiments were performed using a cartridge tool firing a fastener into a target which consists of a sandstone core encased in reinforced concrete. The cartridge tool and accessories were provided by Hilti (GB) Ltd. The cartridge tool of type DX450, as shown in Figure 3.1(a), is a powder-actuated tool based on a co-acting piston principle, designed for fixing work in the construction industry. This co-acting piston principle means that the

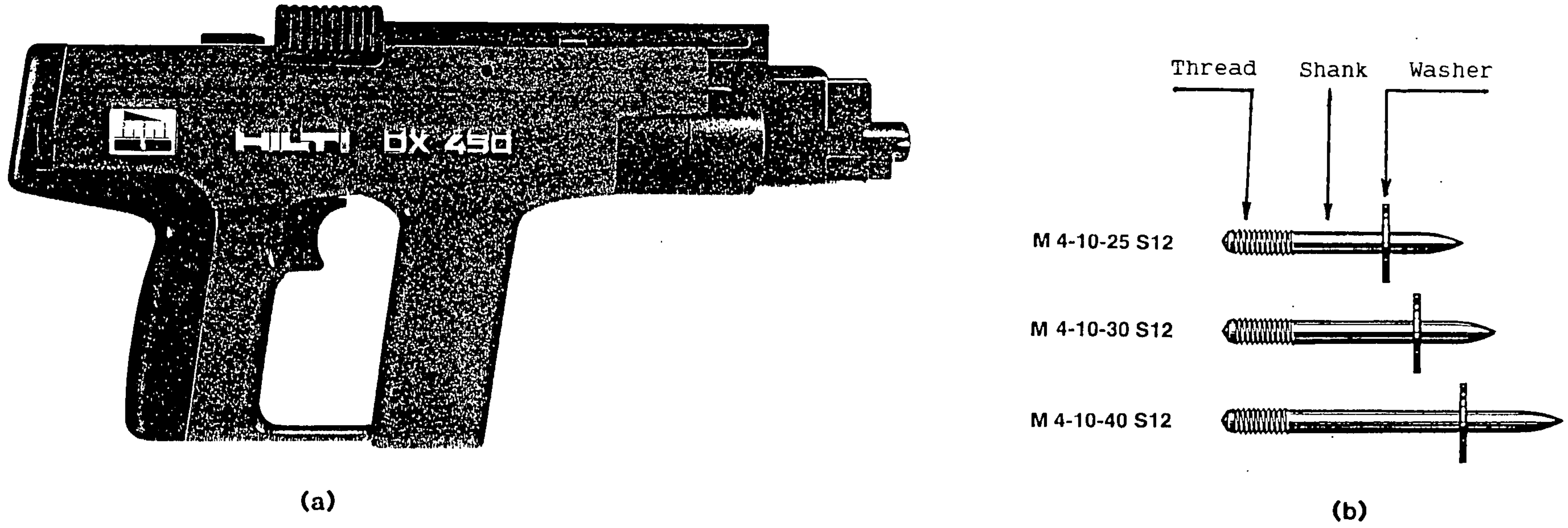

(a)

(b)

Figure 3.1 (a) DX450 cartridge tool (b) Screw fasteners piston and fastener are accelerated together inside the tool and have the same velocity at the time the fastener strikes the target material. Because there is no immediate resistance to this co-action, so only the mass inertia of the fastener and piston act. The cartridges are supplied by the manufacturer in two strengths; red (medium–high power) and black (extra–high power). The driving power of the tool can be varied by means of a power regulator (a thumb wheel) in which the setting as selected is shown on a scale by an indicator. This is controlled by the volume of the gas expansion chamber in the piston guide, which can be enlarged or reduced by the thumb wheel through a regulating pin. The largest and smallest volumes correspond to the lowest and highest power regulator settings, respectively. Using the DX450 tool with the red cartridge, the lowest and highest power settings give a kinetic energy ranging from 120 Nm to 320 Nm, respectively according to technical information provided by Hilti. Referring to BS 4078:1966, this tool is thus categorized as a high power tool.

A wide range of fasteners may be purchased for use with the tool. Only three types of fasteners as shown in Figure 3.1b were chosen for use in all the penetration experiments. After preliminary tests the red cartridge (calibre 6.8/11 M) was selected for all experiments. The type M4-10-25S12 fastener was chosen for the first part of penetration experiments. Types M4-10-30S12 and M4-10-40S12 were taken for the second part experiments. The fasteners have an ogival nose with the nose apical angle of 45^o degrees. Besides the no minal diameter of 3.5 mm, the rest of their dimensions is indicated in the type specifications as shown in Figure 3.1(b) in which the second, third and last numbers (i.e. the number after the letter S) denote the lengths of thread and fastener shank, and the washer diameter in mm, respectively. The washers are attached to the shanks of both sizes of fasteners about 11 mm and 14 mm from the ballistic point, respectively and act as a penetration retarders. Their effects on the penetration process will be discussed in Section 3.2.4. All fasteners are of the same material in which a zinc layer is coated over the work-hardened mild steel. The mechanical properties of fastener available is shown in Table 3.1a, and the physical properties are shown in Table 3.1b.

Table 3.1a Mechanical properties of fastener

Mass g	Uniaxial tensile strength GN/m^2	Shear strength GN/m^2	Bending strength GN/m^2
3.1	2	1.28	3

Table 3.1b Physical properties of fastener

Type	M4-10-25S12	M4-10-30S12	M4-10-40S12
Weight	3.1g	4.0g	4.1g
Total length	35 mm	40 mm	50 mm
Shank length	25 mm	30 mm	40 mm
Thread length	10 mm	10 mm	10 mm
Washer diameter	12 mm	12 mm	12 mm
Washer location	11 mm	13 mm	14 mm

The target cores were made from cylinders of Staindrop sandstone 150 mm high and 100 mm diameter cored from large sandstone blocks. Around the core was cast a reinforced concrete case having an outer diameter of 150 mm. The concrete was allowed to cure for a minimum of 28 days at room temperature. The mineralogical composition by weight of the sandstone was determined by X-ray diffraction and X-ray fluorescence methods. The results are shown in Table 3.2. It can be noted from this Table that the sandstone is silica-cemented and the quartz grains are the major component. The grain sizes of the quartz in the intact sandstone slide were determined, using a Vickers microscope model-55, to be in a range from 0.03 to 0.38 mm, having an average grain size of 0.175 mm. The size distribution of quartz grains was analysed using a computer program by dividing grain sizes into eight ranges from 0 to 0.4 mm with an increment of 0.05 mm. The results are illustrated by a bar graph in Figure 3.2. This Figure shows that the quartz grains spanning in the range from 0.15 to 0.25 mm occupy about 85 % of the total quartz volume and about 75 % of the total components in sandstone. Moreover, these quartz grains were observed to have a random distribution in sandstone, showing no macroscopically specific structure. Thus, it is apparent that the sandstone is, mineralogically and structurally, a relatively simple rock in which mineralogy and structure are assumed not to add complexity to the process of impact penetration. The mechanical properties of Staindrop sandstone are summarised in Table 3.3. A number of plain concrete cylinders were tested to give an average uniaxial compressive strength of 23 MN/m^2. Thus, the reinforced concrete used in making the casing for the target should be expected to have a higher compressive (or tensile) strength. The effect of the casing was to inhibit radial cracking of the sandstone in regions remote from the impact and to simulate the condition pertaining in a semi-infinite sandstone block.

3.2.2 Experimental procedure

The arrangement of penetration experiments on the laboratory specimens is shown in Figure 3.3. Initially, twelve tests were conducted using the DX450 tool fitted with a spall stop attachment (type 45/S4) and the M4-10-25S12 fastener. The spall stop attachment with a diameter of 70 mm produces sufficient area

Table 3.2 Mineralogical composition of sandstone

Sample no.	Quartz %	Kaolinite %	Feldspar %	Muscovite and Illite %	Total %
1	85	8.1	3	2	98.1
2	86	9.3	<5	-	100
3	84	7.8	3	-	94.8
4	90	5.5	<5	-	100
5	86	8.6	5	<3	102.1

Note :

(1) Results of quartz and kaolinite come from XRF chemical and X-ray diffraction analyses with automatic computer control.

(2) Results of feldspar, muscovite and illite are determined by the linear regression method with X-ray diffraction recording charts using the statistical program, MIDAS.

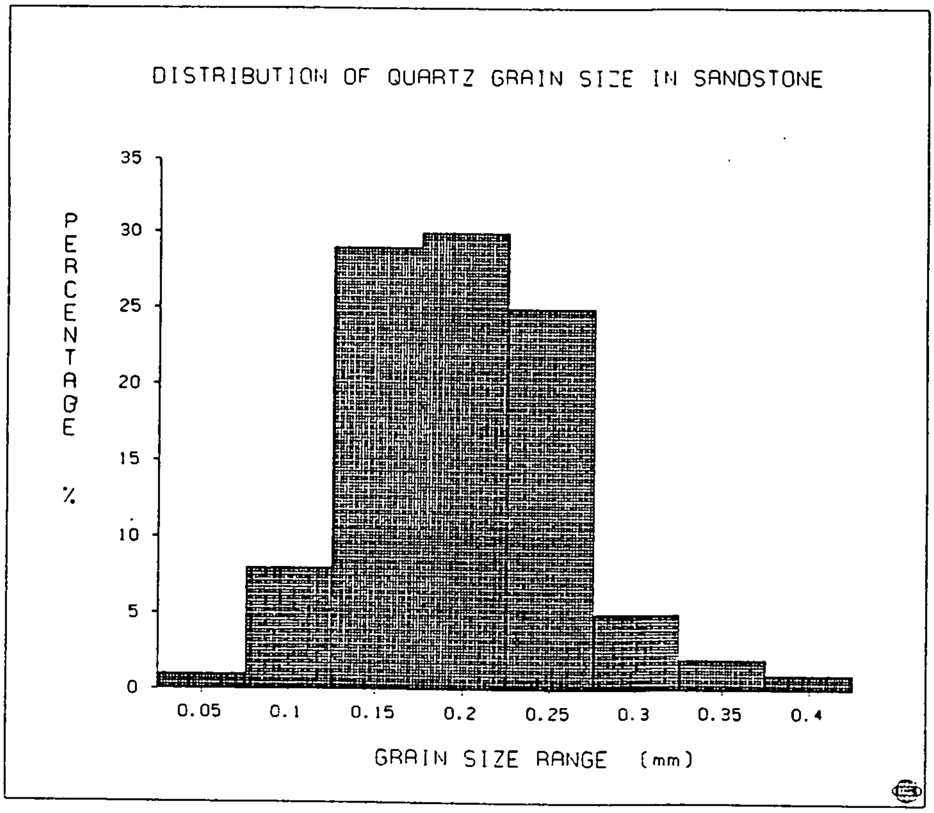

Figure 3.2 Distribution of quartz grain sizes in sandstone

Table 3.3 Mechanical properties of sandstone

Density, kg/m^3	2130
Young's modulus, GPa	13.62
Poisson's ratio	0.2
Bulk modulus, GPa	7.5
Shear modulus, GPa	5.68
Uniaxial compressive strength, MPa	45.0
Uniaxial tensile strength, MPa	4.55
Porosity, %	18

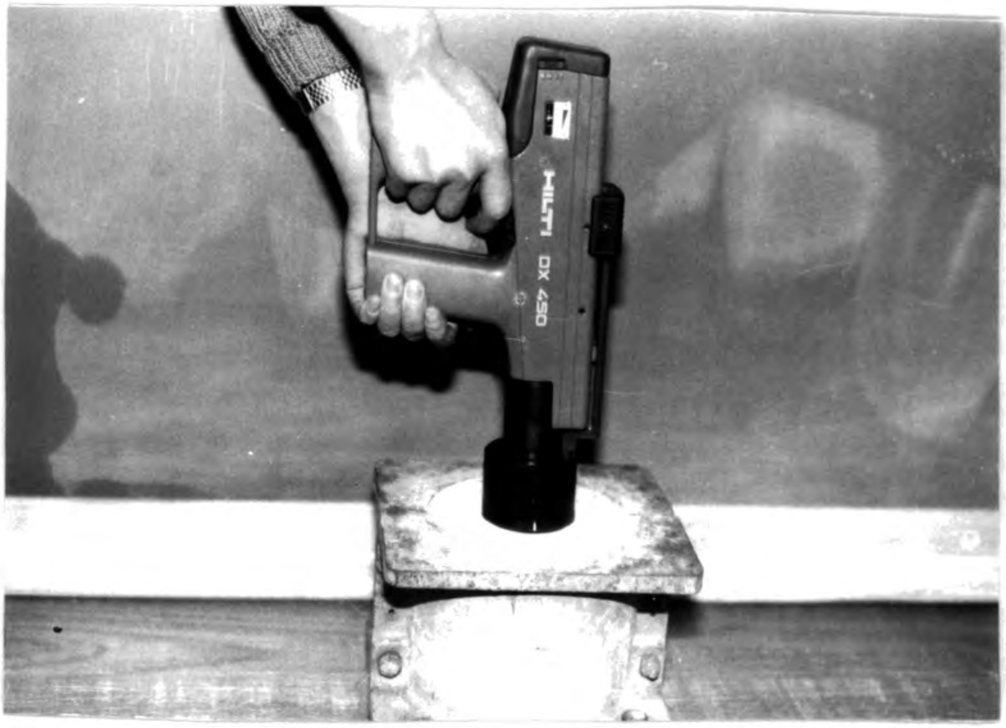

Figure 3.3 Experimental arrangement for penetration test

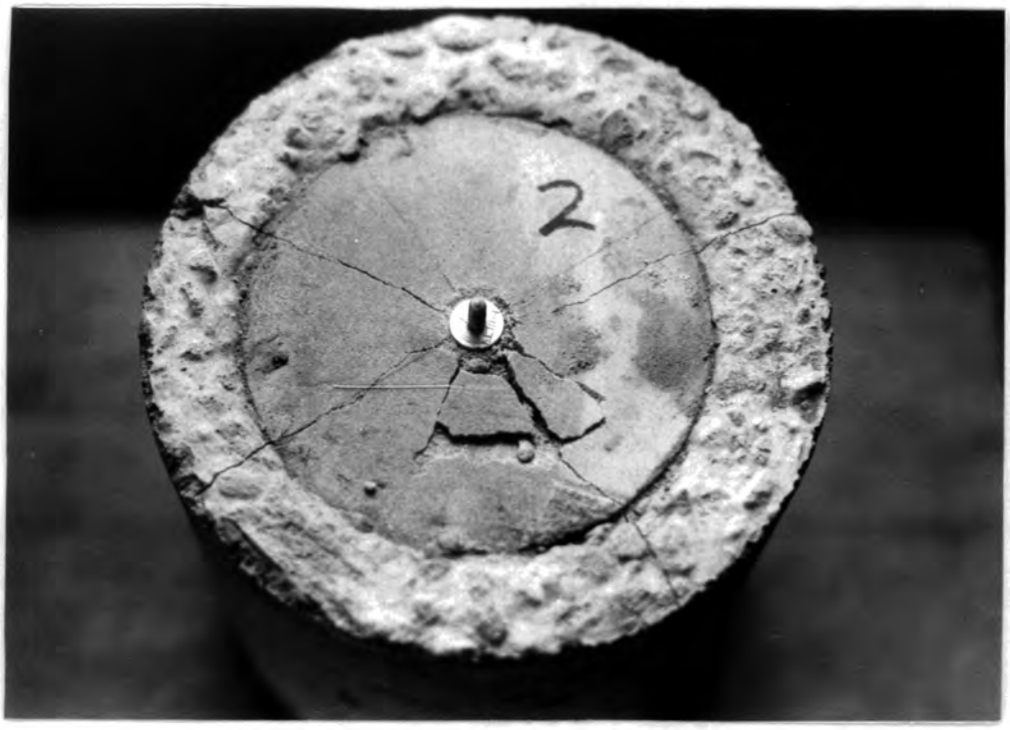

Figure 3.4 Impacted specimen

to stabilize the tool at right angles to the target surface. The geometric centre of the target surface was marked to ensure axisymmetric penetration. In the tests the power regulator settings were varied between 1.5 and 2.5 at intervals of 0.25. These corresponded to impact velocities ranging from approximately 61 m/s to 71 m/s according to test results carried out under contract to Durham University by the Applied Mechanics Division of the Department of Mechanical Engineering at UMIST (Tennant, **1987 ; 1988**). A typical specimen after impact viewed from above is shown in Figure 3.4 in which axisymmetric penetration is manifested by a reasonable symmetric distribution of fracture pattern. The penetration depth for each test was measured from the length of shank protruding above the target surface. (In some of the tests the protruding portion of the fastener was not at normal inclination to the target surface). The results of experiments are summarised in Table 3.4a. Diagrammatic presentation of these experimental results is shown by curve I in Figure 3.5 in which the penetration depth of the fastener is plotted against the power regulator setting. The curve shows clearly that the depth of penetration approaches a limiting value of 25 mm (shank length) as the setting of the power regulator approaches 2.5. This limit results from the washer encountering the threshold portion of the fastener shank with also a possible resulting rapid increase in resistance towards the final stages of penetration. This leads to the choice of the use of a fastener with the larger shank length in later penetration experiments.

Thus, fasteners with the larger sizes, i.e. types M4-10-40S12 and M4-10-30S12, and with the higher power settings (i.e. greater than 2.0), were used to investigate deeper penetrations. It can be seen from Table 3.1b that these two types of fasteners have the shank lengths of 40 mm and 30 mm, respectively, and the former only has mass 0.1 gram more than the latter. Moreover, these types of fasteners have masses little more than 1 gram greater than that for type M4-10-

Table 3.4a Results of penetration experiments on sandstone targets

Test number	1	2	3	4	5	6	7	8	9	10	11	12
Fastener mass, g	3.1	3.1	3.1	3.1	3.1	3.1	3.1	3.1	3.1	3.1	3.1	3.1
Power setting	1.5	1.5	1.5	1.75	1.75	2.0	2.0	2.0	2.25	2.25	2.5	2.5
Penetration depth, mm	14.15	20.0	20.1	20.94	22.0	22.6	24.0	24.3	24.33	24.6	24.3	24.86
Initial impact velocity, m/s *	61	61	61	63.5	63.5	66	66	66	68.5	68.5	71	71

* Initial impact velocity was measured separately; for further information see Section 3.2.3.

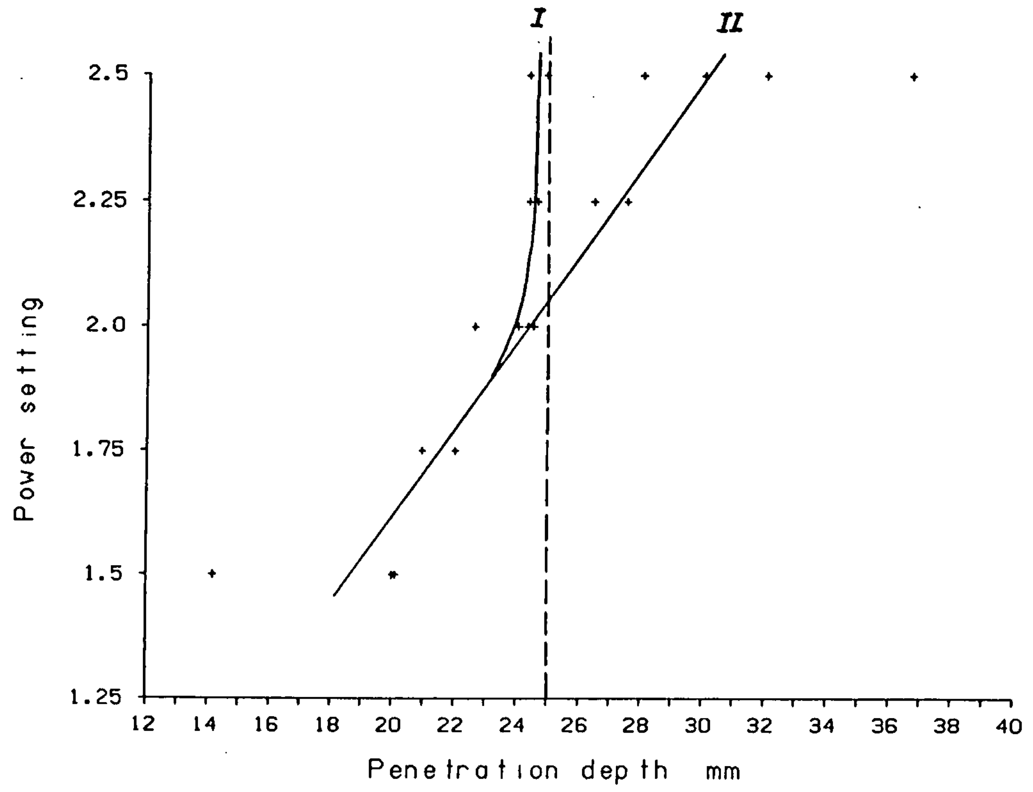

Figure 3.5 RELATION BETWEEN POWER SETTING AND PENETRATION DEPTH FOR SANDSTONE TARGETS

25S12. The effect of this increase in mass is considered negligible when compared with the 120 gram piston. To this end, seven tests were conducted following the same experimental procedure. However, severe bending of fastener shanks was often encountered in tests using type M4-10-40S12 with the power setting of 2.0 and less. Thus, type M4-10-40S12 fasteners were only used with a power setting of no less than 2.25, and type M4-10-30S12 fasteners were used with a power setting of no more than 2.25. The results obtained from penetration tests are presented in Table 3.4b. By combining these results with those obtained at the power setting of less than 2.25 in Table 3.4a, a realistic relationship between the power setting and the penetration depth for the sandstone targets is produced, as shown by curve II in Figure 3.5. It is clearly seen that the penetration depths achieved in the first part of the experiments using M4-10-25S12 fasteners with power settings greater than 2.25 are considerably underestimated because of a lack of sufficient shank lengths to allow further penetration. Especially, at the power setting of 2.5, the average penetration is reduced by 22 percent compared with the average penetration obtained at the same power level using type M4-10-40S12 fasteners.

For comparison, ten penetration experiments were also conducted on concrete targets in the same way. Concrete was mixed using aggregate, sand and cement at the ratio of 3:2:1 with the average aggregate size of 8 mm. Its average dry density was 2273 kg/m^3. The results obtained using types M4-10-40S12 and M4-10-30S12 fasteners are summarized in Table 3.5. Comparison of these results with those obtained from sandstone targets is shown in Figure 3.6. It is interesting to note that less resistance was encountered in concrete targets than in sandstone targets at the same level of power setting. This could result from the difference of target porosities between these two materials.

3.2.3 Impact velocity measurement

Table 3.4b Results of penetration experiments on sandstone targets

Test number	1	2	3	4	5	6	7
Fastener mass, g	4.0	4.1	4.0	4.1	4.1	4.1	4.1
Power setting	2.0	2.25	2.25	2.5	2.5	2.5	2.5
Penetration depth, *mm*	24.5	26.42	27.5	28.0	30.0	32.0	36.67
Initial impact velocity, m/s *	66	68.5	68.5	71	71	71	71

* Initial impact velocity was measured separately, for further information see Section 3.2.3.

Table 3.5 Results of penetration experiments on concrete targets

Test number	1	2	3	4	5	6	7	8	9	10
Fastener mass, g	4.0	4.0	4.0	4.1	4.1	4.1	4.1	4.1	4.1	4.1
Power setting	1.25	1.5	1.5	1.75	1.75	2.0	2.0	2.25	2.5	2.75
Penetration depth, *mm*	24.0	28.5	29.0	33.0	33.0	38.7	39.0	36.0	40.0	40.1
Initial impact velocity, *m/s*	58.5	61	61	63.5	63.5	66	66	68.5	71	73.5

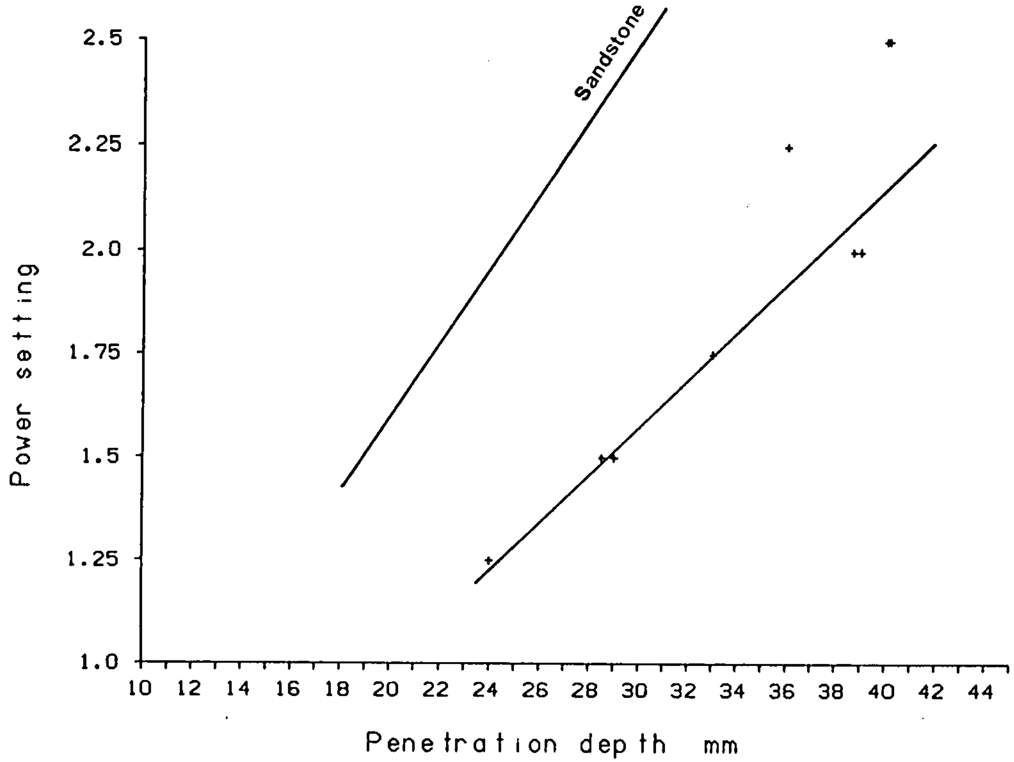

Figure 3.6 RELATION BETWEEN POWER SETTING AND PENETRATION DEPTH FOR CONCRETE TARGETS

The average impact velocities were determined by measuring the transit times over fixed distances. Passes of fasteners through these premeasured distances were detected by the interruption of light beams monitored by two pairs of high power LEDs with matching photodiodes and built-in amplifiers, in which their axes were oriented at 90° to each other. The detection system was checked prior to each test.

Two types of velocity were measured, namely the fastener-piston contact velocity and the subsequent free flight velocity. The results are represented in Figure 3.7 in which the velocity is plotted against the power regulator setting. It is interesting to note that the free flight velocity of a fastener is uniformly greater than the fastener-piston contact velocity by about 7 m/s. This is explained by the motion of a continuously accelerating piston. It should be pointed out that it is impossible to find out whether the piston is in contact with the fastener or not during penetration or part of the penetration during a normal fixing operation, but it is plausible to suggest that the fastener is being driven into the target material under such a condition. This coincides with the co-acting piston principle of the tool. Thus, in this Chapter as far as the impact velocity is concerned, the fastener-piston contact velocity is adopted, although measurements of other velocities are reported to be more reliable. The detailed results and discussion of testing are given in two Mechanical Engineering (A.M.Division) Reports (Tennant, 1987, 1988).

3.2.4 Washer effect test

In the preceding penetration experiments, the depths of penetration achieved at given impact conditions were controlled by both the target resisting force and the retarding effect of washer. In other words, the initial kinetic energies of fasteners were dissipated during not only the shank penetration but also during

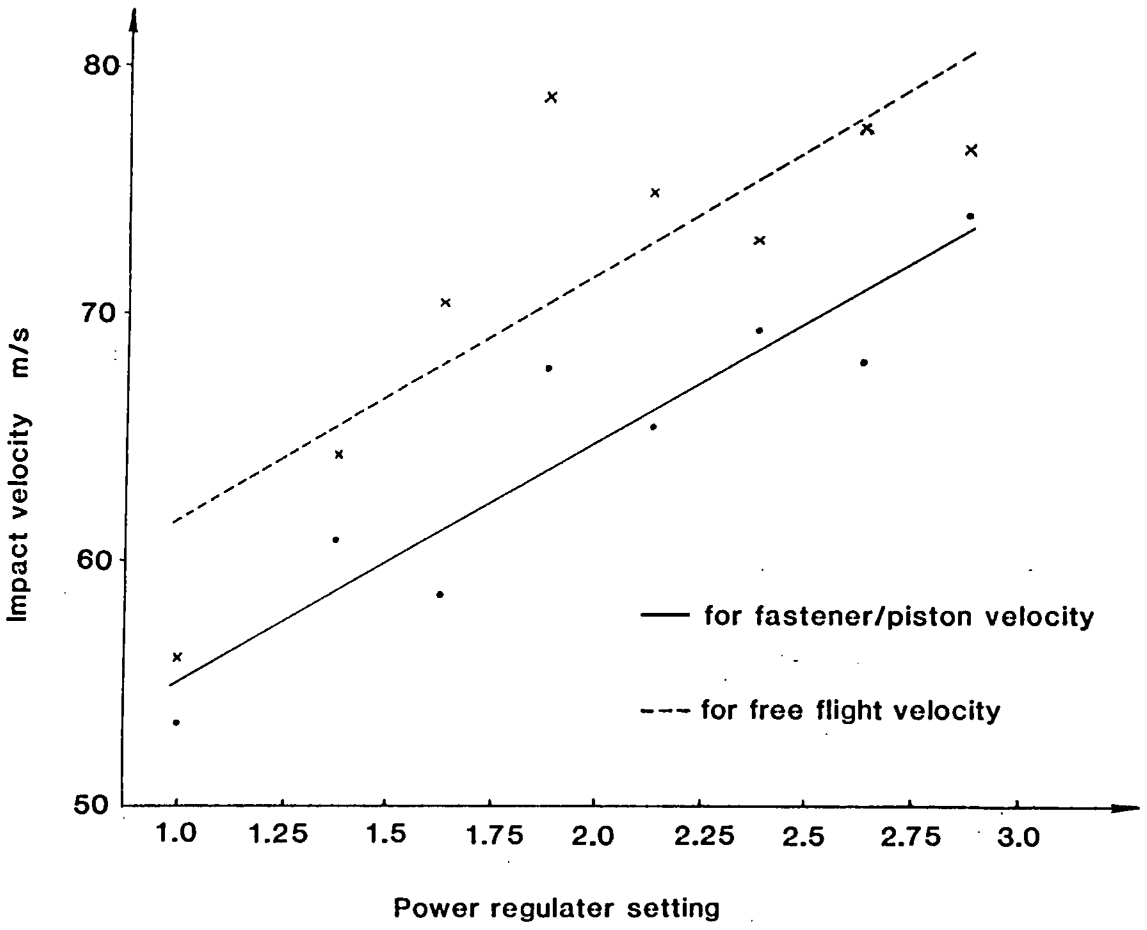

Figure 3.7 Relation between fastener velocity and power regulator setting

the process of the washer overcoming the strength of the material surrounding it and its subsequent frictional sliding on the shank surface. It can be easily imagined that after the washer comes into contact with the impact surface of target the penetrating velocity of fastener would suffer a sudden drop which may be significant. Thus, it would be important to estimate this retarding effect on the penetration process.

To this end, ten tests were conducted using an Instron Model 1195 universal testing machine under identical conditions. (These were undertaken using similar equipment to the pull-out tests described in the next section.) For this purpose, a simple hollow cylinder, having an inner diameter greater than the fastener shank diameter and a shallow socket on the top surface, was made. After calibration, each test was carried out simply by compressing down the threaded end with the washer resting in that shallow socket and with the fastener nose down in the hole of cylinder. The compression speed was 10 mm/min. The results obtained are presented in Table 3.6 with the average frictional force of 8.71 kN. A typical curve is shown in Figure 3.8.

The range of the initial impact kinetic energy can be obtained based on the impact velocity range mentioned in Section 3.2.2. Combining Table 3.6 with average maximum frictional force and residual frictional force of 8.71 kN and 3.25 kN, respectively, the washer effect on the impact kinetic energy is estimated and presented in Table 3.7. It shows that, at the displacement where the maximum frictional force is obtained, 7.6 % - 5.6 % of the initial impact kinetic energy is dissipated in overcoming this washer force, corresponding to velocities ranging from 61 m/s to 71 m/s and that at the limit of washer displacement (13 mm) where the residual frictional force is obtained, the dissipation of the kinetic energy increases up to 15 % - 11 %. It is obvious that the higher the impact velocity, the less is the kinetic energy loss due to the washer effect, which implies

Table 3.6 Washer frictional force tests

Fastener number	1	2	3	4	5	6	7	8	9	10	Average
Maximum frictional force, kN	9.38	9.5	10.8	11.2	6.43	8.15	8.18	9.2	7.0	8.25	8.71
Displacement at max. frictional force, mm	1.1	1.2	2.0	1.4	2.3	1.5	2.2	2.0	2.3	2.1	2.0
Residual frictional force, kN	2.5	2.7	2.7	4.0	4.1	2.4	4.4	4.5	2.0	3.7	3.5
Displacement at residual frictional force, mm	13	13	13	13	13	13	13	13	13	13	-

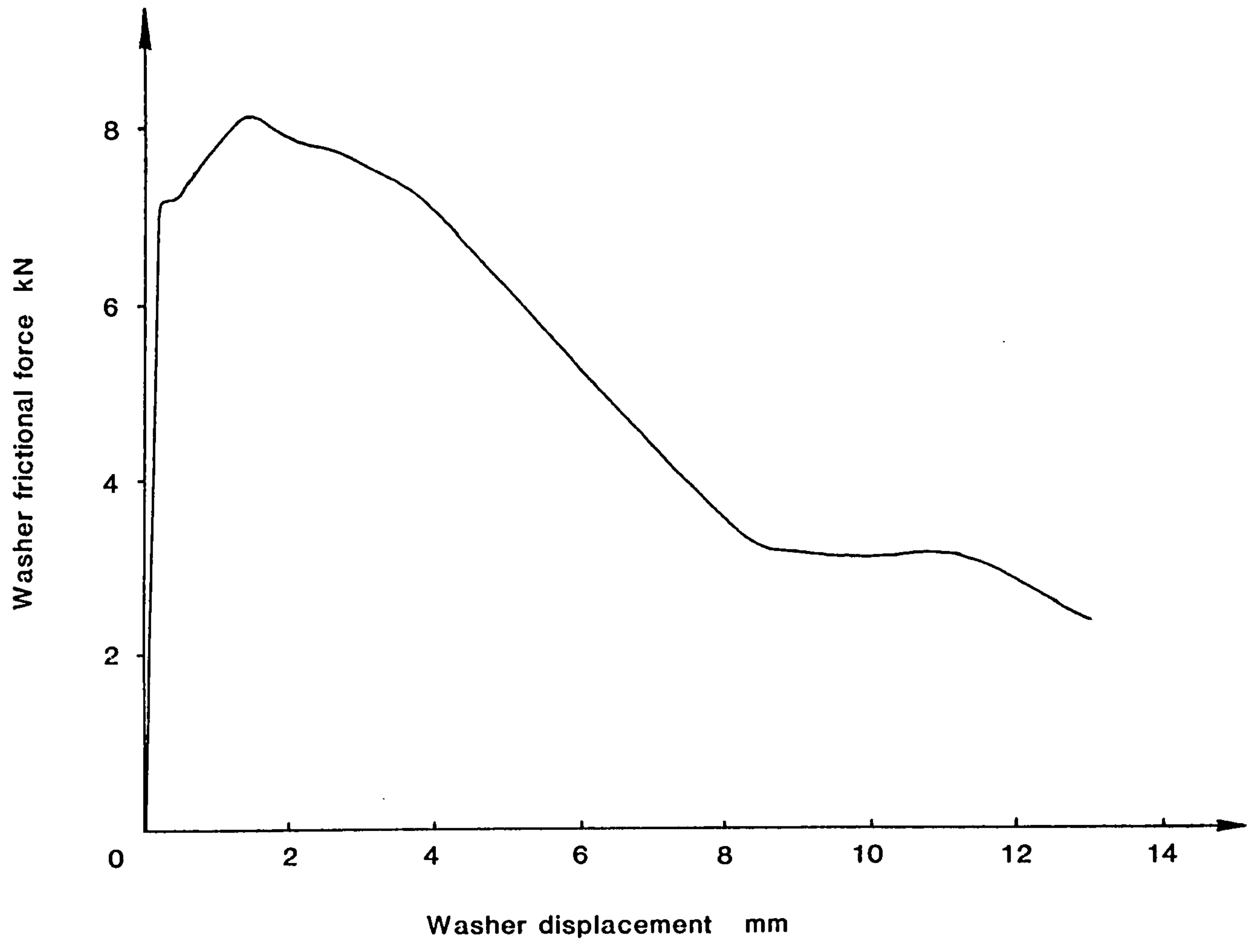

Figure 3.8 Typical test curve between washer frictional force and washer displacement

Table 3.7 Washer retarding effect on initial impact kinetic energy

Symbol	Range	Lower	Upper
1	Fastener mass + piston mass, g	3.1 + 120	3.1 + 120
2	Impact velocity, m/s	61	71
3	Initial kinetic energy, Nm	229	310.27
4	Washer displacement, mm	2 *	13 **
5	Average washer frictional force, kN	8.71	3.25
6	Washer kinetic energy, Nm	17.42	34.28
7	Ratio of 6 to 3, %	7.6	11
8	Ratio of 6^l to 3^u, 6^u to 3^l, %	5.6	15

* This denotes the washer displacement where maximum washer frictional force is obtained.

** This denotes the largest possible washer displacement.

l, u In row 8, these denote lower and upper ranges, respectively.

the apparent friction effect. Thus, it is evident that the washer has a significant effect on the fastener penetration, especially at relatively low power settings.

3.3 Pull-out Experiments

As the fastener comes to rest in the target at the end of penetration, an interfacial bond may have been formed between the fastener surface and the surrounding target material due to severe abrasion and adhesion occurring during the penetration. In other words, fastener will resist being pulled out in the manner of an anchor. To gain a better understanding of the bond development is not only itself an important research area which has attracted widespread attention but also a considerable contribution to the study of penetration. Of greater interest, is the bond (or fastening) strength, which is commonly measured by the pull-out force and is the maximum axial force necessary to withdraw the fastener from the target. Thus, the 'pull-out' test is such a procedure for characterizing this fastener-target interfacial bond strength, and provides quantitative information on the withdrawal process in terms of a pull-out force - displacement curve.

3.3.1 Description of apparatus

The pull-out test rig was made to fit into an Instron Model 1195 universal testing machine to facilitate the withdrawal of the embedded fastener from the target. The device consisted of a frame as shown in Figure 3.9a for clamping the specimen onto the moving cross head of the testing machine and a connector as shown in Figure 3.9b with a thread insert into which the fastener was screwed. This latter could be attached to a coupling of the fixed upper cross head of the machine by a removable pin. The testing machine was fitted with a strain-gauged load cell of 100 kN capacity and a chart recorder to measure the displacement of the cross head. A general operational view of the pull-out test is shown in

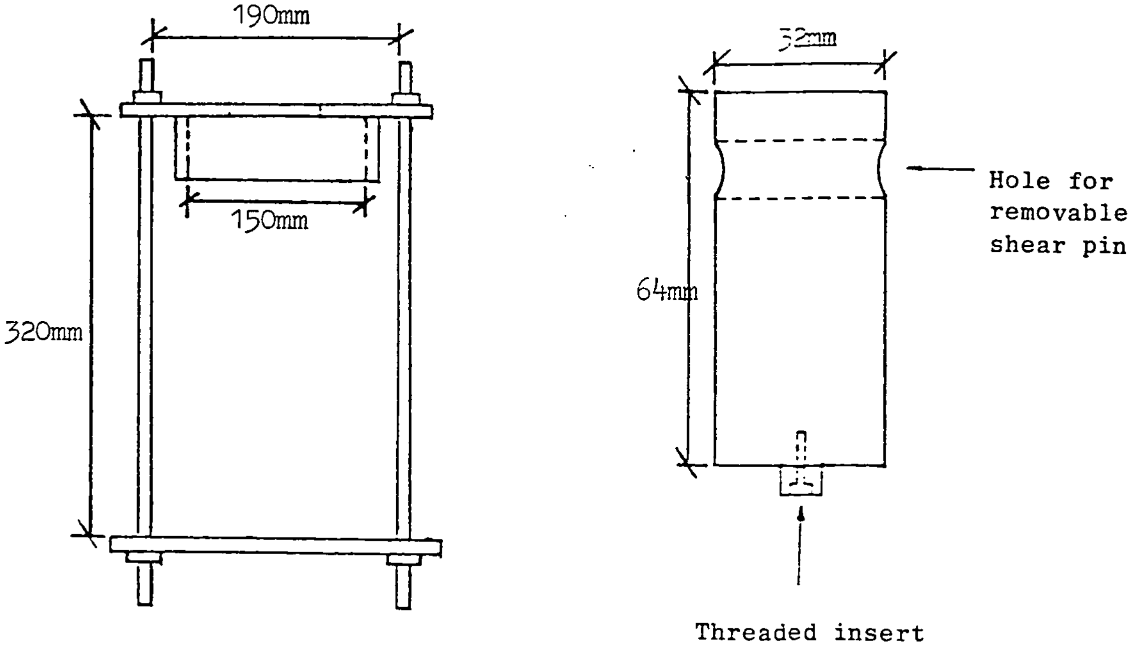

(a) (b)

Figure 3.9 Pull-out device (a) clamping frame (b) connector

Figure 3.10.

3.3.2 Experimental procedure

Before each test the testing machine was fully calibrated. The impacted target was then mounted onto the moving cross head using the clamping frame. The connector screwed onto the fastener thread was fitted into the coupling which was adjusted to ensure symmetric alignment of the specimen and the shear pin inserted. A tensile load was then applied to the fastener at a constant rate of 0.5 mm/min. The pull-out force as a function of cross head displacement was directly recorded on the chart plotter.

A total of twelve tests, using specimens from the penetration tests, was performed under identical conditions. A summary of the results is given in Table 3.8a which shows the maximum pull-out force of the fastener and the corresponding fastener displacement at the maximum resistance. Also shown are the data relating to the power level used during the firing of the fastener and its resulting penetration. This relationship is presented by curve I in Figure 3.11. It is seen that the maximum pull-out force increases with power regulator setting of the tool until the limiting penetration of just below 25 mm is achieved when the resistance is also limited. The pull-out force is very small at the lowest setting of the power regulator and the highest recorded value is 4.15 kN. Since the load cell capacity is 100 kN, which is far greater than the maximum pull-out force obtained, thus the motion of crosshead alone can be safely used to determine the displacement of the embedded fastener knowing the chart speed.

A typical curve of pull-out force against displacement (for specimen 10) for complete withdrawal of the fastener is shown in Figure 3.12. It is seen that a number of regions (I, II and III) can approximately be identified. Region I is the first part of the curve which may be due in part to initial slackness in the

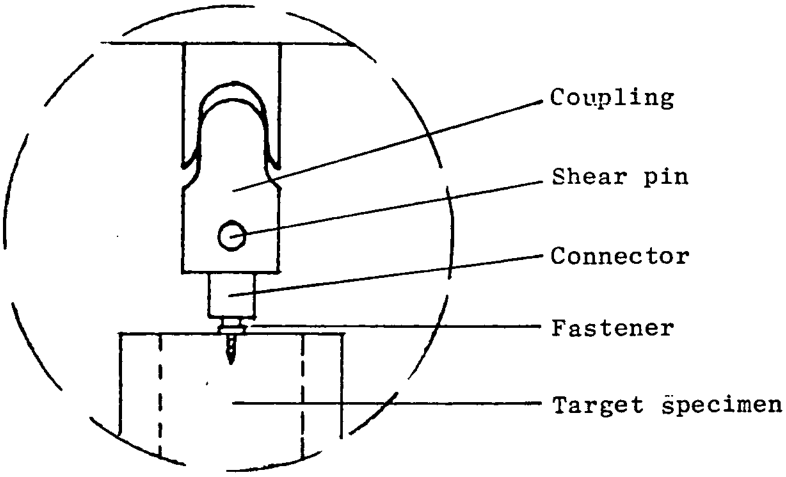

b. After connection (clamping frame not shown)

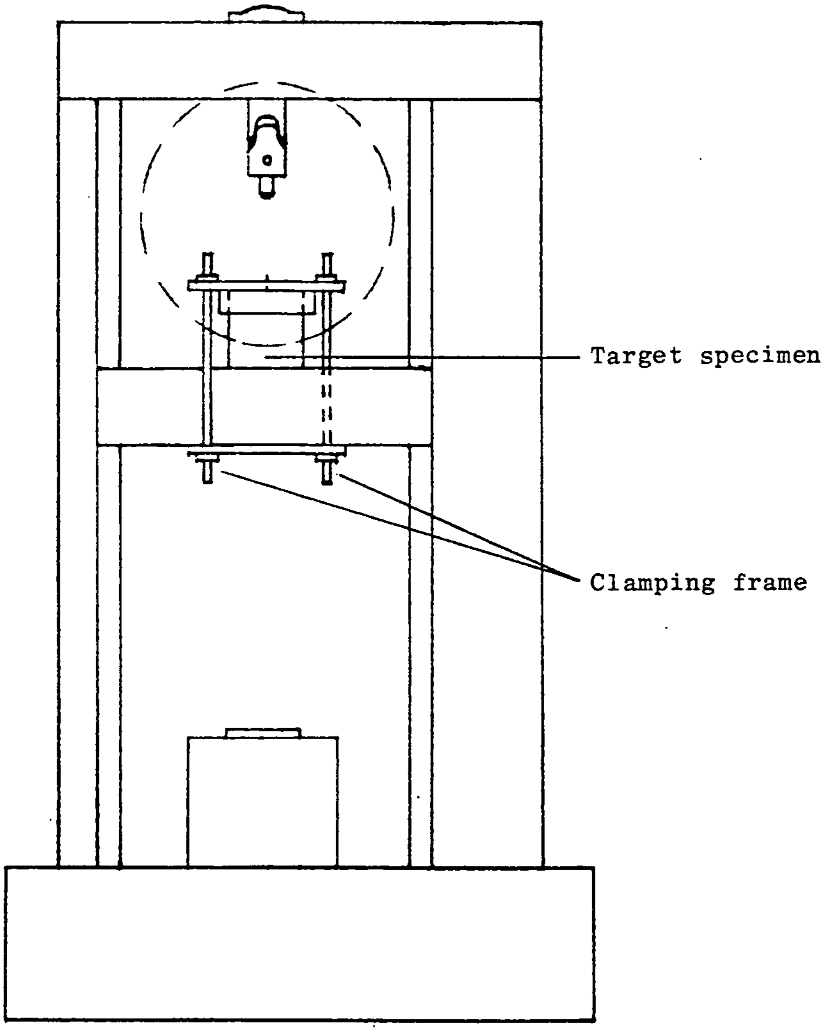

a. Before connection

Figure 3.10 Operational view of pull-out test

Table 3.8a Results of pull-out tests on sandstone targets

Crosshead speed : 0.5 mm/min Chart speed : 100 mm/min												
Specimen number	1	3	4	5	6	7	8	9	10	11	12	13
Power regulator setting	1.5	1.5	1.75	1.75	2.0	2.0	2.0	2.25	2.25	2.5	2.5	2.5
Penetration depth, mm	14.15	20.1	20.94	22.0	22.6	24.0	24.3	24.33	24.6	24.3	32.0	28.0
Maximum pull-out force, kN	0.5	1.95	2.06	2.2	2.23	2.35	2.8	3.0	2.92	2.95	3.35	4.15
Displacement at max. pull-out force, mm	0.09	0.16	0.3	0.4	0.445	0.385	0.2	0.31	0.61	0.374	0.56	0.5

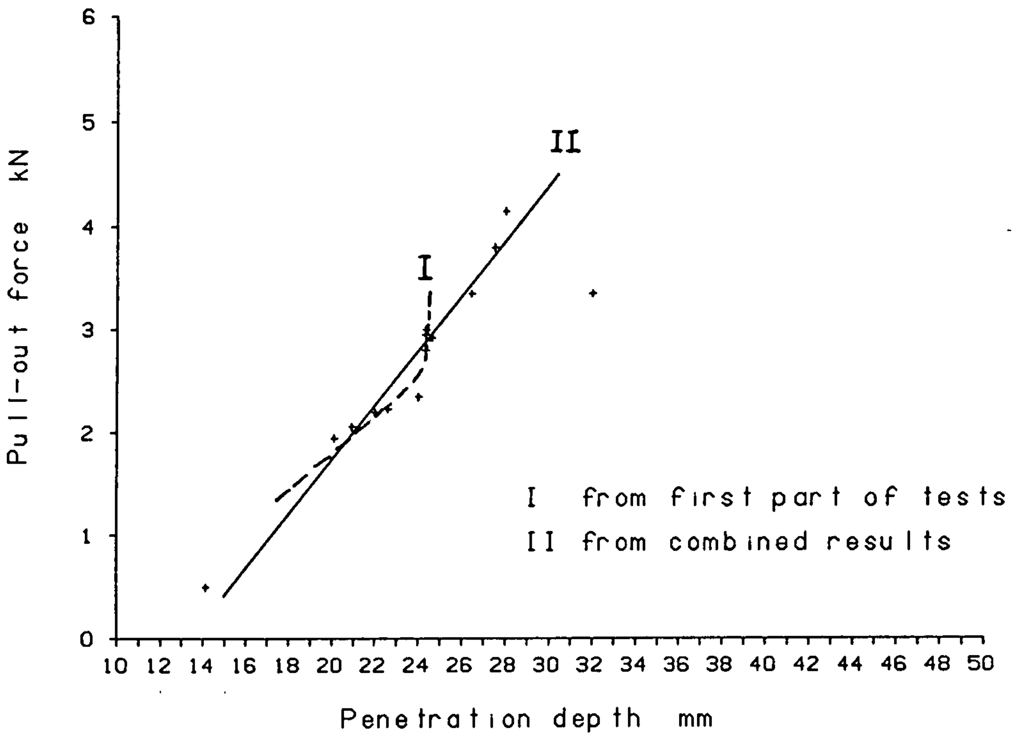

Figure 3.11 RELATION BETWEEN PULL-OUT FORCE AND PENETRATION DEPTH FOR SANDSTONE TARGETS

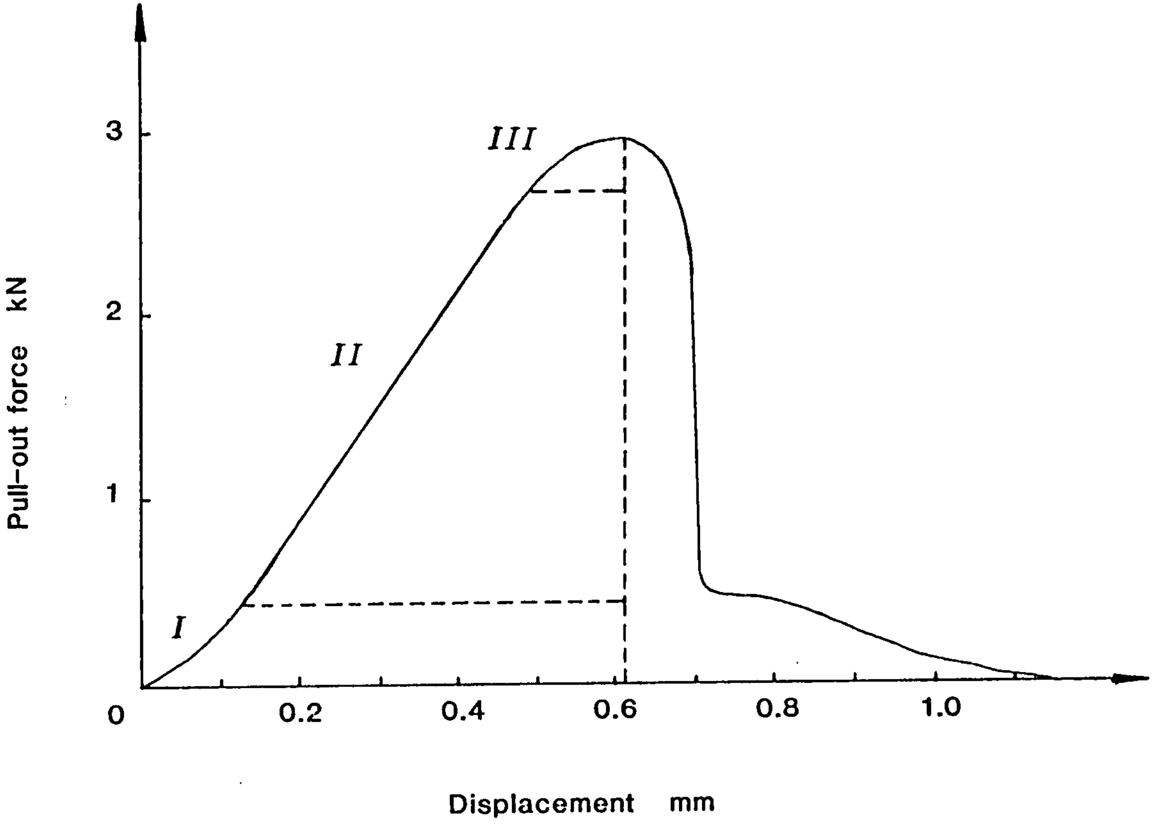

Figure 3.12 Typical pull-out curve

coupling and testing rig and due in part to the cracks formed during penetration closing up. In some cases in which curves show uneven start, the former reason is more likely. However, in the case illustrated in which the curve starts smoothly, the latter reason is more plausible. The fact that this region is very small indicates that most of cracks produced in that kinetic energy level are closed before the pull-out load is applied. Region II is a region of nearly linear behaviour. This region may be the result of sliding of surfaces once cracks have closed and the initiation of further cracks, but no debonding occurs. Region III exhibits the onset of complete loss of bond and shows an approach orwards the maximum pull-out resistance. It is interesting to note that the pull-out force does not fall right off after it reaches the maximum value. It seems to suggest that the pull-out load is resisted by both the interfacial bond strength governed by friction and the shear strength of target material. Once the shear strength of the target material is reached, friction reduces, so resulting in the debonding as indicated by a sudden drop in the pull-out resistance. If friction reduces sufficiently the fastener may be pulled out completely without shearing the surrounding target material. In other words, debonding should otherwise take place as the pull-out force reaches a maximum value. Moreover, if the pull-out force does not experience a sudden drop after the maximum value, it would suggest that the debonding process never actually take place. This implies that at least in this case the interfacial bond strength is stronger than the shear strength of target material. Observation of withdrawn fasteners shows that most fasteners have thick coatings, some of them even have a chunk of target material attached after they are pulled out, as shown in Figure 3.13. This strongly suggests that the large portion of what was recorded as the pull-out force at this situation is actually contributed by the shear strength of the target material. Under these circumstances, what had taken place during the pull-out is the conical shear

Figure 3.13 Withdrawn fasteners

failure as illustrated by a sketch in Figure 3.14 (this point will be supported later by Figure 3.16b). Therefore, the pull-out procedure, to certain extent, is not very well characterized using the present technique, and the pull-out force of the fastener is apparently underestimated. To improve results of these pull-out tests the clamping device has to be modified to fix an annular area directly around the fasteners. To this end, a steel ring having a thickness of 15 mm was made with the outer diameter of less than that of the target, and the inner diameter of 19 mm (which is slightly greater than the washer diameter). With this steel ring being inserted between the clamping frame and the target surface, the pull-out tests were performed following the same procedure. The results obtained using this new technique are presented in Table 3.8b, which also includes some previous results for comparison. It is seen from this Table (and also Table 3.9b for concrete targets) that the pull-out forces are more or less increased except in the case of test number 4 in which the target was fractured after the fastener penetration. Special attention should be drawn to two points. (a) If results obtained at the power setting of 2.0 are compared for two different techniques, the increase of the pull-out force is apparent. (b) It may be argued from the previous case that the increase of the pull-out force is expected because of the deeper penetration which results when the new technique is applied. However, if results from test numbers 2 and 3 are compared with that from number 12, then the improvement of the results is clearly justified. This is even more evident by results of pull-out tests for the concrete targets as described later. Combining these results with Table 3.8a, an improved relationship between the pull-out force and the penetration depth is obtained, as illustrated by curve II in Figure 3.11. Since the form of the pull-out force - displacement curve is dependent on a number of factors such as material strengths of both the embedded fastener and target materials, surface friction, penetration depth (i.e. contact area),

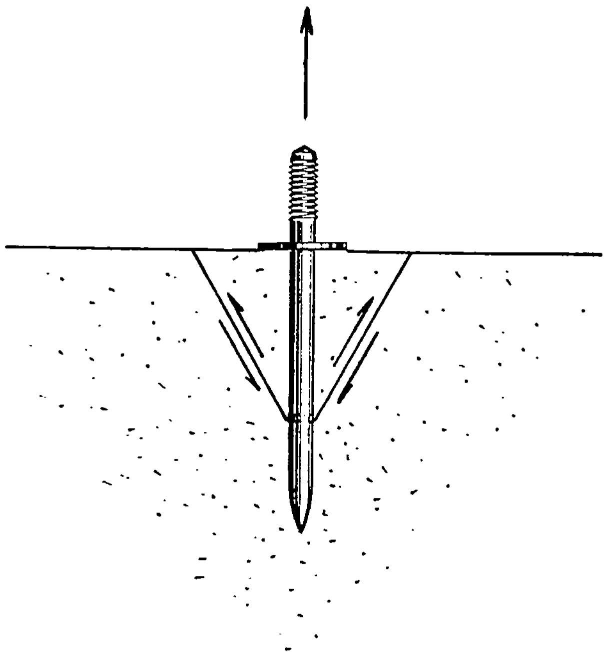

Figure 3.14 Shear failure in target during pull-out test

Table 3.8b Results of pull-out tests on sandstone targets

Test condition	New technique				Old technique			
Specimen number	1	2	3	4	6	7	8	12
Power regulator setting	2.0	2.25	2.25	2.5	2.0	2.0	2.0	2.5
Penetration depth, *mm*	24.5	26.42	27.5	36.67	22.6	24.0	24.3	32.0
Maximum pull-out force, kN	2.92	3.35	3.80	3.0	2.23	2.35	2.8	3.35

diameter of fastener and speed of pull-out during the test. among them, friction and shear strength of the target material are considered to have played dominant roles in the pull-out process at a constant rate.

It should be mentioned that during the process of fastener pull-out the fastener itself is in tension. Thus, with the value of the maximum pull-out force obtained during pull-out tests a simple calculation shows that the fastener elongation actually suffered is of the order of micron magnitude which is entirely negligible.

Also, it should be pointed out that the speed of pull-out can affect the apparent pull-out force of fasteners. This line of research remains to be further investigated.

The pull-out tests were also conducted on the concrete targets following the same experimental procedure. The results obtained are summarized in Table 3.9a. The relationship between the penetration depth and the maximum pull-out force is illustrated in Figure 3.15 in which the curve obtained from the sandstone targets is also plotted for comparison. It is seen that, in general, the deeper the penetration, the higher is the maximum pull-out force, and the latter increases more rapidly. Because of the higher penetration achieved in concrete targets than in sandstone targets, the larger pull-out forces are expected. Also, it was observed that although the tensile break of the target material near the surface adjacent to the fastener was frequently encountered after the pull-out test, the fasteners were relatively clean (i.e. the shank surfaces were revealed).

The new pull-out technique was also used on the concrete targets. Results obtained are given in Table 3.9b and also presented in Figure 3.15 by curve II. It is evident that compared with curve I in that diagram a considerable improvement in the pull-out tests has been achieved using this new pull-out

Table 3.9a Results of pull-out tests on concrete targets

Crosshead speed : 0.5 *mm/min* Chart speed : 50 *mm/min*					
Specimen number	4	5	6	8	9
Power regulator setting	1.75	1.75	2.0	2.25	2.5
Penetration depth, *mm*	33.0	33.0	38.7	36.0	40.0
Maximum pull-out force, k*N*	3.15	3.25	5.9	3.6	2.75 *

* Specimen number 9 was fractured subject to the impact penetration.

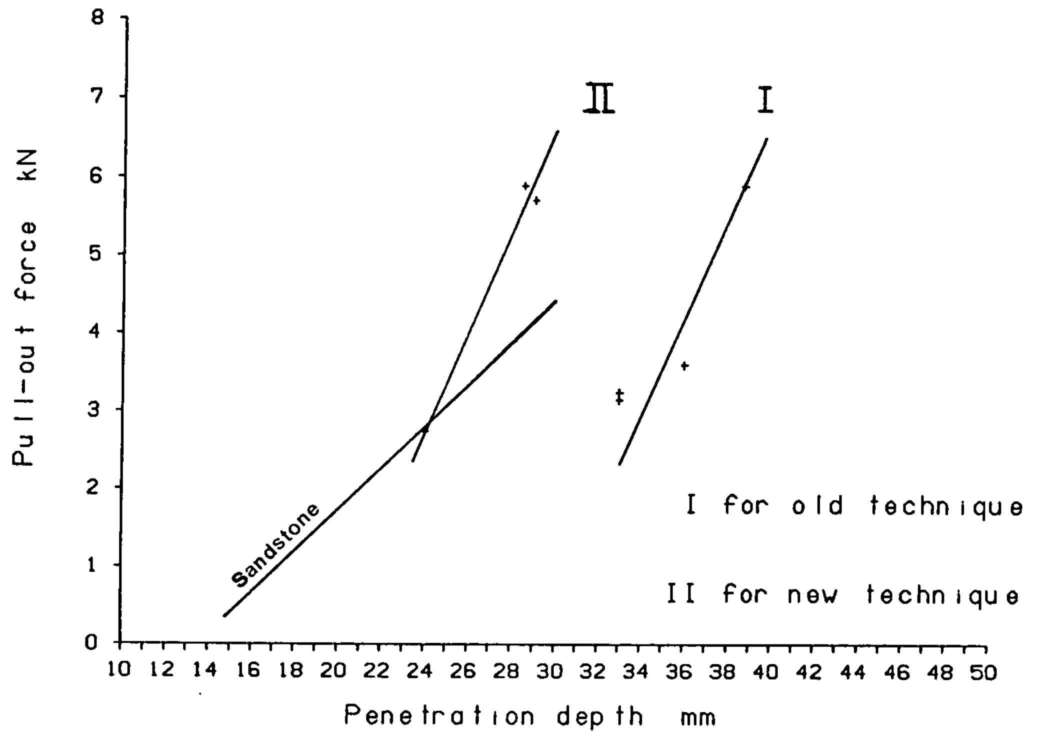

Figure 3.15 RELATION BETWEEN PULL-OUT FORCE AND PENETRATION DEPTH FOR CONCRETE TARGETS

Table 3.9b Results of pull-out tests on concrete targets

Crosshead speed : 0.5 *mm/min* Chart speed : 50 *mm/min*			
Specimen number	1	2	3
Power regulator setting	1.25	1.5	1.5
Penetration depth, *mm*	24.0	28.5	29.0
Maximum pull-out force, k*N*	2.75	5.9	5.72

technique.

3.4 Preparation and Examination of Slides

In order to understand and predict the behaviour of target material subjected to impact loading and also to support the pull-out mechanism described in the previous Section, it is necessary to describe the material response in terms of the impact effects on the microscopic structure – development of fracture and internal changes of deformations. The most common approach for this purpose is the examination of the impacted fastener and target which are usually made in the form of slides using optical microscope.

3.4.1 Preparation of slides

Two impacted targets were prepared for examination, the first one with the fastener removed from the target and the second one with the fastener embedded in the target. The same procedure of preparation was followed. However, extra caution was taken to avoid disturbing the fastener in the second sample because of the considerable difference of hardnesses between sandstone and steel during grinding.

To facilitate the preparation of the slides, the target material was first impregnated with resin in a pressurized triaxial cell which was intended to force the resin into voids and cracks in the sandstone so that minimal damage was occurred in the subsequent grinding stage. Resin comprising Araldite LY568, hardener HY932, accelerator DY219 and toluene thinner was coloured blue to enhance contrast for a better indication of internal changes. Once the resin had dried, a wet coring technique was used to remove a small core from the target, which was assumed to cover all the internal changes which were within a distance of five- to six-time the fastener diameter. The core was sectioned using a water-cooled diamond cutting wheel to produce comparatively thick slices, such that the normals to the forces on the slices were perpendicular to the direction of the axis of the target. The slices were ground and lapped sequentially with an abrasive powder of grit size 400 and 1000 microns, using a Production Lapping and Optical Polishing-LP30 machine, until the standard 30 to 40 micron thickness was obtained. Then, the slices were mounted on a glass slide for inspection using a transmitted light microscope.

3.4.2 Examination of slides

Figure 3.16a shows a general view of a thin section occupying an area of less than 40 $mm \times 40$ mm, which exhibits a fastener embedded in a sandstone target. Because of the larger size of target compared to that of fastener, most damage occurs around the fastener within the distance of ten times of fastener diameter except for macroscopic cracks running through the target radius in some cases in spite of the reinforced concrete surround. Figure 3.16b shows an enlarged view with the magnification of 10. For comparison, a thin section of intact sandstone is shown in Figure 3.17 in which the dark blue colour indicates the voids being infilled with the resin. Detailed observation of all these thin sections reveals that in addition to surface spalling and cratering, the damage comprises two regions : a grain pulverized region, surrounded by a cracked region. In the grain pulverized region which is a very thin layer having a varying thickness around the fastener shank, quartz grains are seen to be crushed and pulverized, as well as detached from the parent sandstone. Some features of this region are shown in Figures 3.18 to 3.20. In these Figures as well as the following Figures the direction indicated by an arrow denotes the penetration direction of the fastener. Figure 3.18 taken with a magnification of 14 shows an area at the front of the fastener tip, indicated by a dark 'triangle' region at the top of the figure. In addition to a network of cracks, two large cracks are visible propagating downwards along the two sides of the fastener shank. These

Figure 3.16a Photograph showing fastener embedded in sandstone

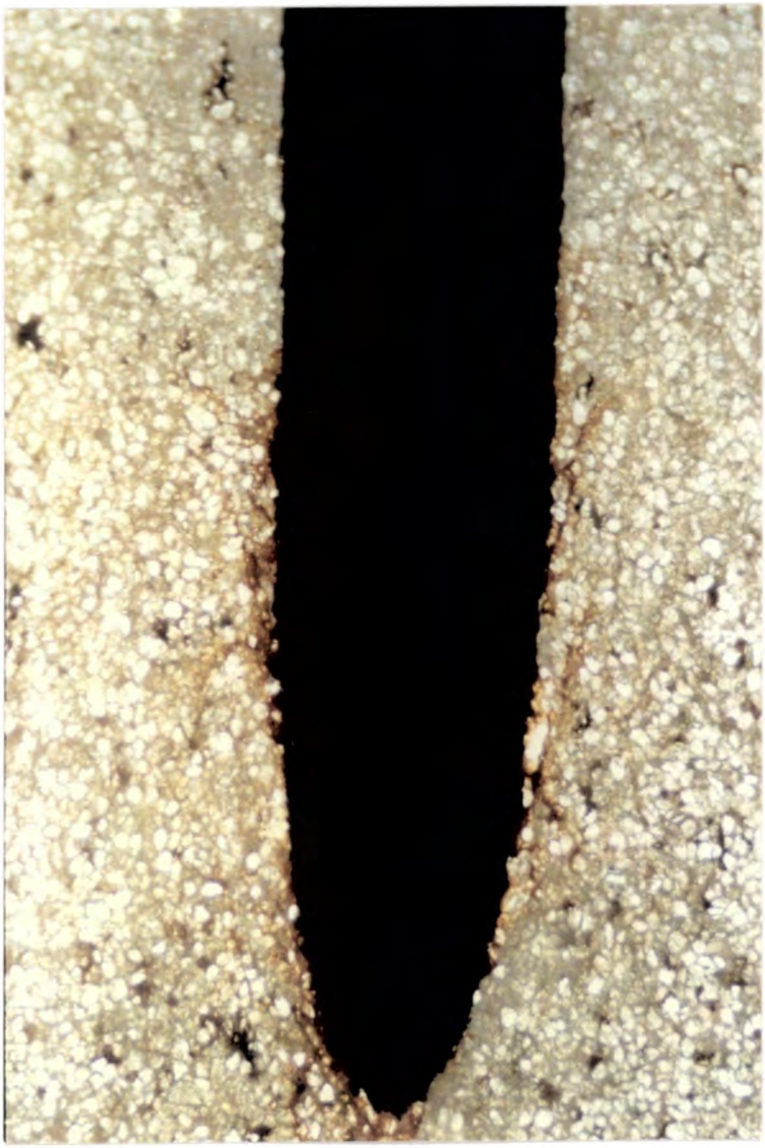

Figure 3.16b Microscope photograph showing detailed view of fastener

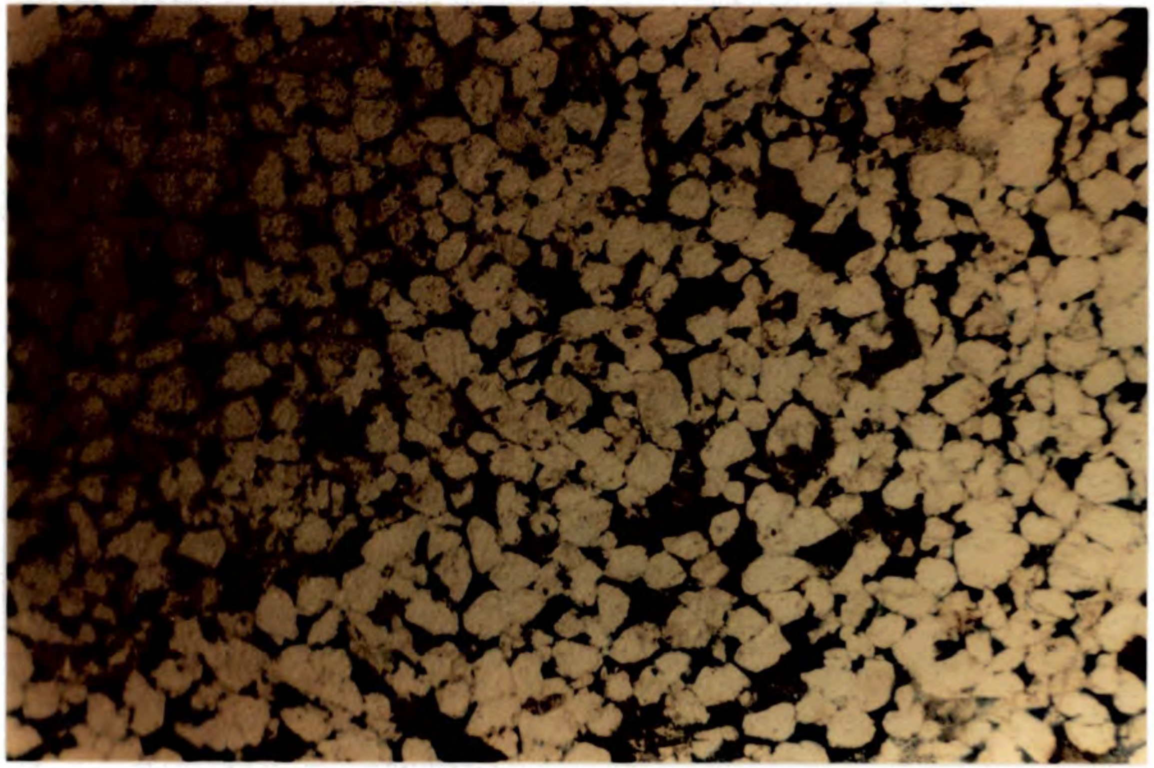

Figure 3.17 Microscope photograph of intact sandstone

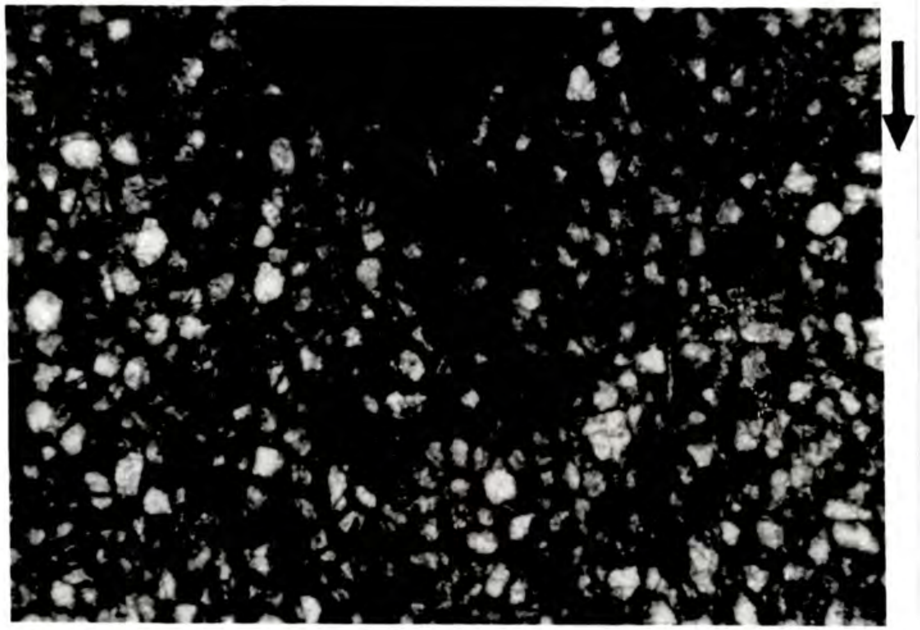

Figure 3.18 Microscope photograph showing grain pulverized region at the front of the fastener tip

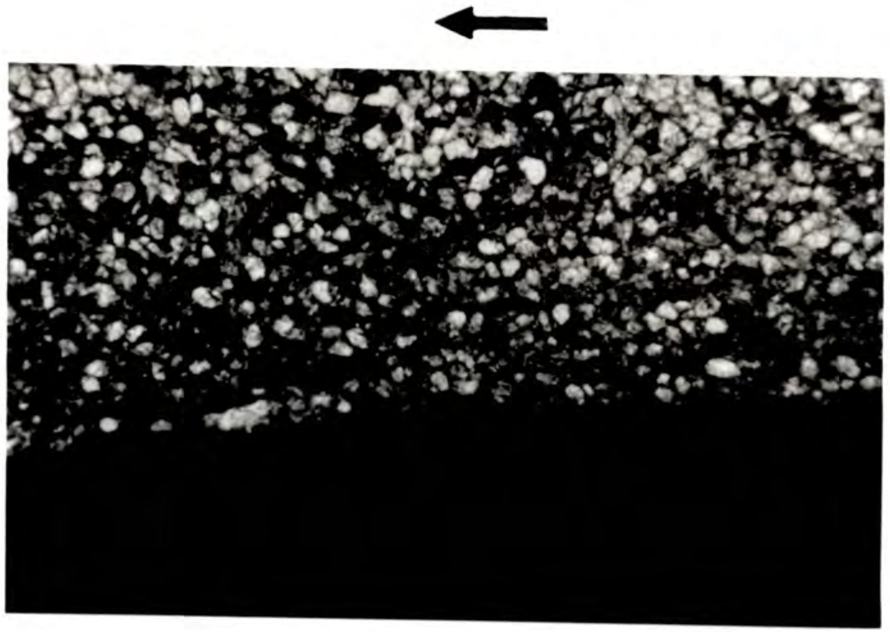

Figure 3.19 Microscope photograph showing grain pulverized region at one side of the fastener

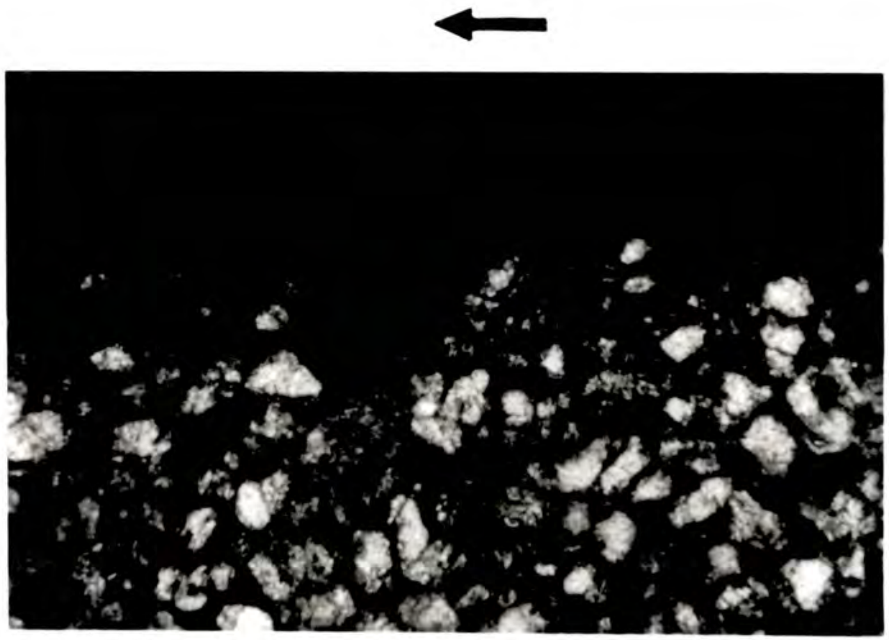

Figure 3.20 Microscope photograph showing grain pulverized region at the other side of the fastener

are most possibly caused by the shear action generated by the high difference between the principal stresses in the target. Figures 3.19 and 3.20 illustrate similar features, showing the two sides of the fastener with magnifications of 10 and 22, respectively, and in which some fractures are clearly visible in Figure 3.19.

In the cracked region, the dominant feature is the formation of cracks both within grains (transgranular or intragranular) and along grain boundaries (intergranular) as shown in Figures 3.21 and 3.22. Figure 3.21 taken with a magnification of 52 shows a tiny area (1.1 mm × 0.7 mm) which is just about 0.3 mm from the fastener shank. It can be observed that numerous transgranular cracks in the form of bands are propagating away from source. Figure 3.22a taken with the magnification of 20 shows the general view of a large crack contained in a slide which is sectioned perpendicularly (i.e. normal to the impact surface) at a distance of about 10 mm from the fastener surface. It is noted by observing along the penetration direction that the width of the crack reduces gradually and dies out at the depth of about 20 mm. With the higher magnifications of 30 and 20, respectively, Figures 3.22b and 3.22c show some detailed views of the tail region along the crack. It is seen that the path of crack follows mostly the grain boundaries giving a saw-tooth pattern because the strength of bond cemented quartz grains is much weaker than that of quartzs. Thus, the microstructure seems to have a strong influence on crack formation and propagation at a given impact.

During the impact penetration the fastener also suffered damage, but there is no gross deformation observed. The damage to the fastener is then primarily manifested by scratches on the fastener surface as shown in Figure 3.23. It is seen that most severe scratches occur on the fastener nose, and also that the remarkable difference can be observed between two impacted fasteners in which

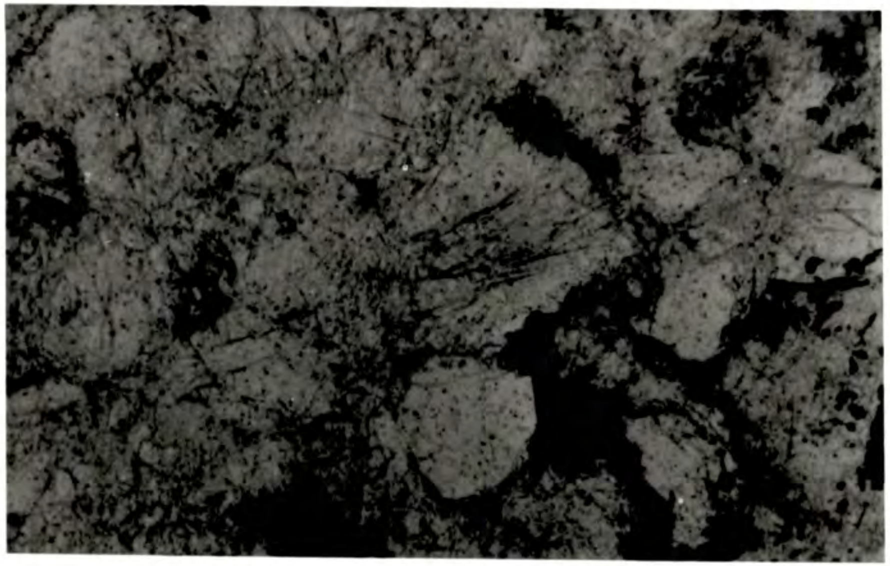

Figure 3.21 Microscope photograph showing transgranular cracks

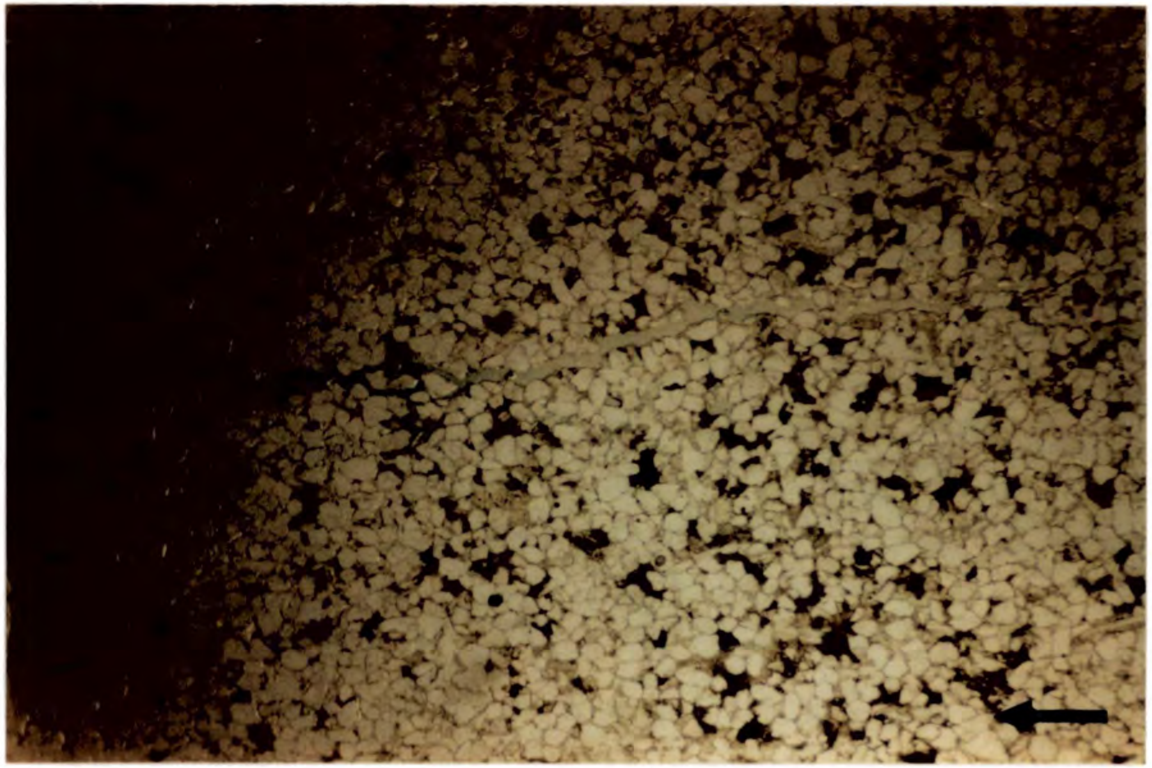

Figure 3.22a Microscope photograph showing a large crack

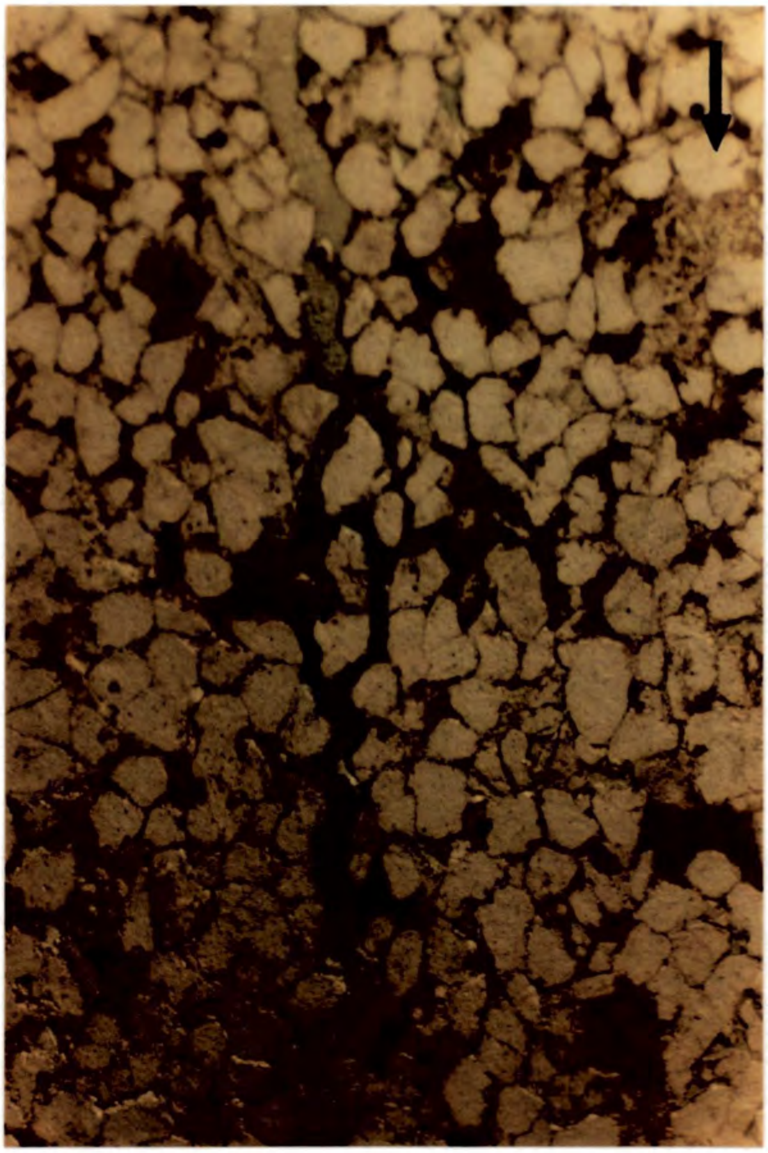

Figure 3.22b Microscope photograph showing detailed view of the crack

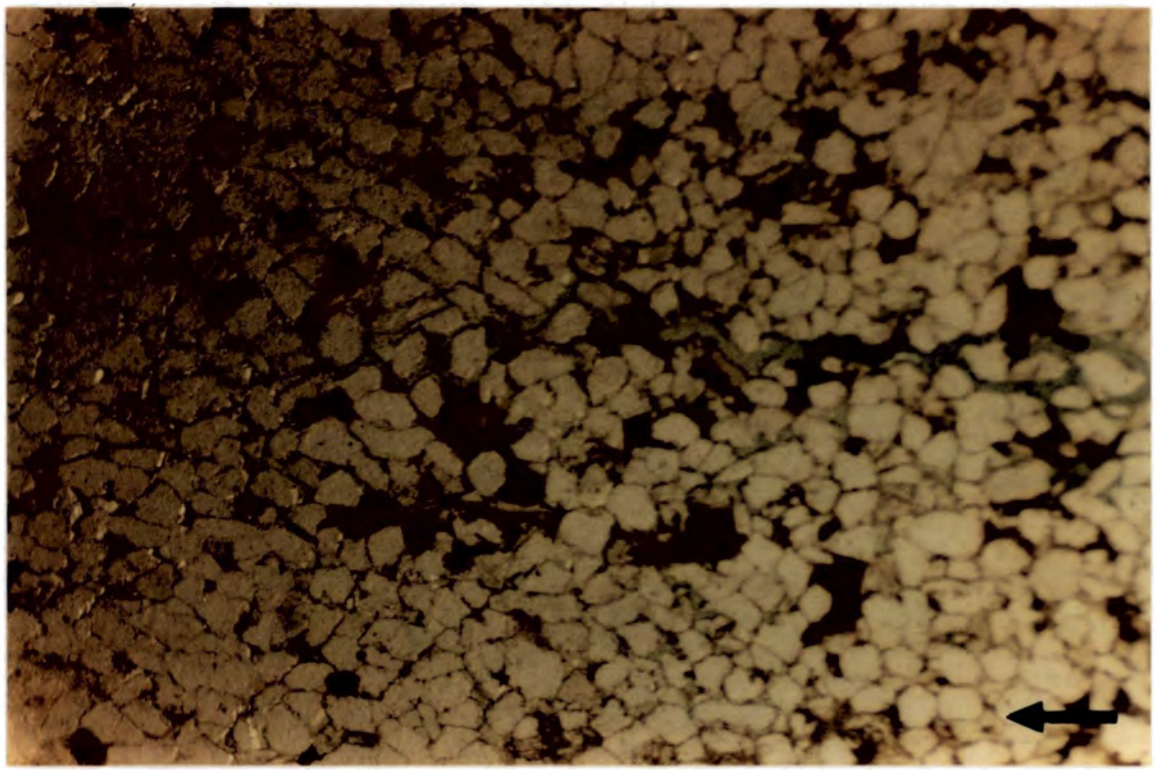

Figure 3.22c Microscope photograph showing detailed view at the tail of the crack

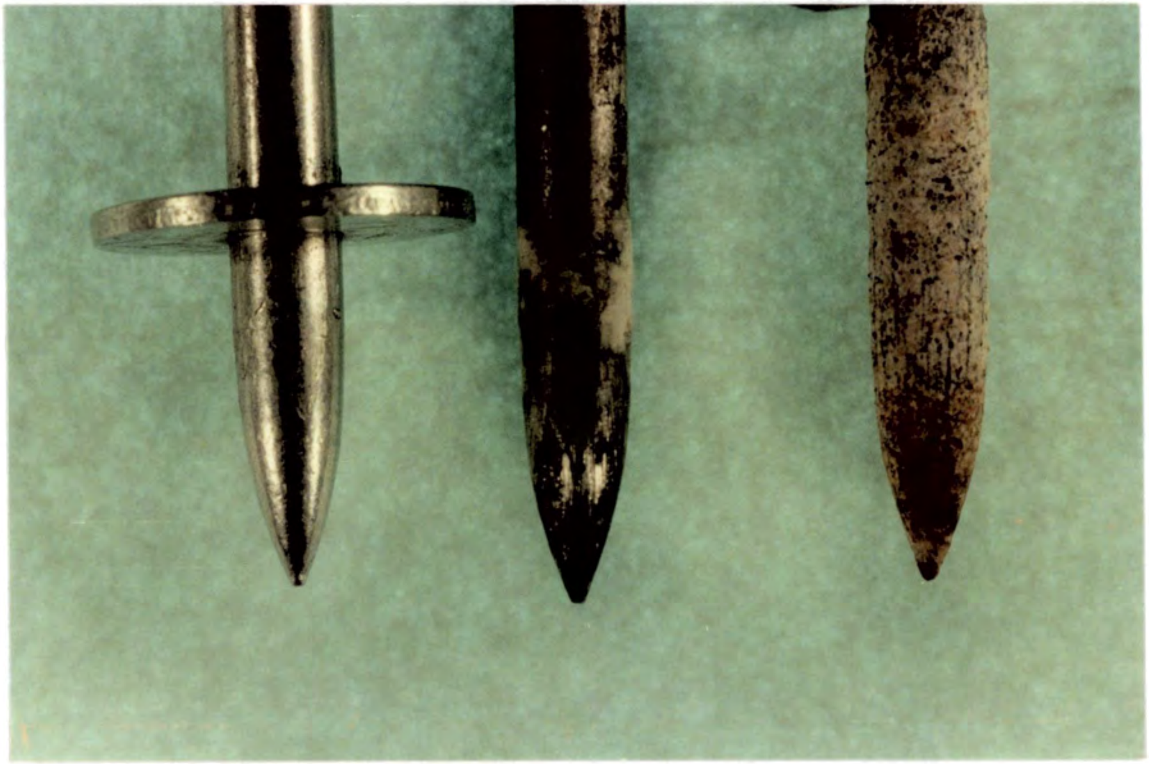

Figure 3.23 Photograph showing impacted and unused fasteners

the top fastener has a coating, while the one at the middle does not. For comparison, an unused fastener is also shown at the bottom of that Figure. This fastener surface damage can be noted from Figure 3.16b in which the fastener surface also exhibits a saw-like structure. From both Figures 3.16b and 3.23 it is noted that a brown colour is shown around and on the fastener surface. It seems to justify the conclusion that the temperature generated by the severe friction during penetration was so high that the kaolinite clay which cements the quartz grains in the sandstone was burned, and was sintered on the fastener surface. This phenomenon may contribute, to some extent, to the strength of the interfacial bond, and explain, on the other hand, the formation of the coating to the fastener.

The examination of these slides shows that a fine network of cracks (both inter- and transgranular) exists adjacent to the fastener. The tensile fractures occur around the fastener, as well as the shear failure, because of the high compressive and shear stresses produced by the impact penetration. It is also interesting to mention (see Figure 3.18) as a potential prediction that the large cracks at the front of the fastener may form a 'dirt cone' during penetration, and also may develop into a shear 'plug ' if the thickness of the target is sufficiently thin. As a final point to mention, it is worthwhile re-observing Figure 3.16b. Because the fastener surface, as discussed before, is interlocked with the adjacent target material, being manifested by the saw-like structure, and being enhanced by the sintering effect, so a strong interfacial bond is expected. If the fastener at this situation is being pulled out, the failure surface would develop along these tensile fractures which originate from the fastener-target interface and are rather weak. This point may very well support the pull-out results obtained previously and the shear failure mechanism in the target which are shown in Figures 3.13 and 3.14, respectively.

Chapter 4 COMPUTER SIMULATION

4.1 Introduction

Exact and approximate analytical solutions to the penetration event have been developed in the previous Chapter on the basis of idealizing the dominant physical phenomena of the target material. The resulting equations obtained for making predictions, similar to those in the authors's work cited in Chapter 3, are often relatively simple mathematical expressions. Although these equations are extremely useful as engineering tools within their proposed physical processes, the applications of these analytical solutions are limited in scope because of the simplifying assumptions introduced in their derivations. The most comprehensive approach to impact and penetration problems must then rely on numerical simulation using sophisticated computer programs to give a complete solution. Because less simplification or compromise is required in this approach, more accurate quantitative predictions are possible. Furthermore, the analyses of the results derived using these methods can provide a fundamental understanding of aspects of mechanical behaviour that are difficult, if not impossible, to obtain by alternative approaches. There are many commercial computer codes that are currently available for the analyses of impact and penetration. Zukas (1982) provides an excellent review of capabilities of these computer codes. Also, a summary and assessments of many computer codes are given by Reddy in Chandra and Flaherty(1983).

In most computer programs used for the investigations of impact and penetration phenomena the formulation begins with the conservation laws for mass, momentum and energy expressed in two or three dimensions. These conservation laws are coupled to the constitutive relationship. To carry out a computer simulation, the physical materials (continua) being modelled have to be represented by a discretized system. Two numerical techniques are usually used in the process of spatial discretization in computer programs. i.e. the finite difference and finite element methods. The complete assembly is then integrated step by step in time for realistic geometries and boundary conditions until the solution time of interest is exceeded.

In the finite difference method, the governing differential equations are directly approximated by replacing derivatives with difference quotients. In the finite element method, differential equations are first cast in variational form and then the solution is attempted in the form of a linear combination of algebraic polynomials defined over elements of the domain. A common feature of these two methods is the local separation of the spatial dependence from the time dependence of the dependent variables. The finite element method has advantage in handling complex geometry and boundary conditions.

Differential equations in either the finite difference or finite element method are generally derived using one of the two kinematic descriptions, Lagrangian and Eulerian. In the Lagrangian description, the computational grid is fixed within the material. Thus, the computational grid distorts with the deformation of the material. In the Eulerian description, the computational grid is fixed in space while material moves through the discretized space. Each of these two descriptions has its advantages and disadvantages dependent on various types of problems. Some hybrid schemes (coupled Eulerian-Lagrangian codes) have also been developed, showing promise in minimising inherent disadvantages of pure Lagrangian or Eulerian descriptions. (Generally, the Lagrangian description is used for material interfaces and outside of the contact region and the Eulerian description for the contact region.) In the temporal discretization, the governing differential equations are integrated either explicitly (using a second-order central difference scheme) or implicitly. The explicit time integration scheme is only conditionally stable. For valid computations the time step size must be kept below the critical value. However, implicit time integration is unconditionally stable, the price paid for this stability being the requirement to solve coupled equations at each time step leading to great complexity in the code and a increasing burden on computer resources.

4.2 Description of Computer Codes

4.2.1 Introduction

There are many different computer codes presently available to investigate impact and penetration problems. For example, Wilkins (1978) studied various metal impact deformation mechanisms using a Lagrangian finite difference program, HEMP. Sedgwick et al (1978) used a Eulerian finite difference program, HELP, to investigate a variety of metal impact phenomena. A series of studies of impact and penetration is provided by Johnson (1977, 1979a, b, 1986) who used EPIC. Thigpen (1974) treated rock penetration problems using TOODY, while using the same program Byers et al (1978) investigated soil penetration. Benson and Hallquist (1986) presented some computational results of diverse impact and penetration problems using DYNA. For the present numerical investigation carried out in this thesis, the computer codes DYNA2D and NIKE2D (2-dimensional versions of DYNA and NIKE) available in the public domain were used. However, emphasis of the code introduction was placed on DYNA2D. For full information about NIKE2D, its user's manual is recommended (see Hallquist, 1983b).

DYNA2D (Hallquist, 1984) is a two-dimensional finite element computer program developed at Lawrence Livermore National Laboratories (LLNL), California, USA for the analysis of dynamic problems involving large deformations of solids composed of inelastic materials. A preprocessor code MAZE (Hallquist, 1983a) and a post-processor code ORION (Hallquist, 1985) were used in conjunction with DYNA2D.

4.2.2 MAZE

The preprocessor, MAZE, has been developed as an input generator for DYNA2D. It can be used either interactively or with a command file. MAZE has three basic functions known as phases. The first is to provide a detailed computational mesh for the geometric configuration of the problem. The range of element types available can be combined to give a very good representation of practically any shape of structure. The second function is to define the interfaces and boundary conditions of materials, to define various loading and temperature conditions as well as to specify initial conditions and time parameters for computation. The results of these two phases can be viewed using a graphic display terminal for verification, and the computation mesh can be modified if necessary. In the third phase the constitutive models and material properties are coupled with the data prepared in two preceding phases to give output information for use as an input to the program DYNA2D. The range of material models includes materials with elastic, elastic plastic, hydrodynamic or viscoelastic behaviour and thermal, work hardening and strain-rate effects. A special facility for incorporating soil and crushable foam materials may be especially useful for dealing with concrete and geological materials like sandstone. All details of the MAZE program can be found in the user manual (Hallquist, 1983a)

4.2.3 DYNA2D

DYNA2D is a program developed for analysing problems involving the dynamic and hydrodynamic response of solids in axisymmetric and plane strain situations where large deformations and inelastic behaviour would be expected. This computer code is a vectorized two-dimensional explicit Lagrangian finite element program. The spatial discretization is achieved by the Petrov-Galerkin finite element method (FEM) with the use of 4-node solid elements. For axisymmetric problems using the Galerkin FEM, radial weighting causes centreline difficulties in large deformation calculations. However, the use of the Petrov-Galerkin FEM eliminates this radial weighting by weighting the momentum equations in the discretization by the product of the basis functions and the reciprocal of the radius. In the temporal discretization, the equations of motion are integrated by the central difference scheme. The stress is taken as constant over an element. All integrals for the constant stress quadrilaterals are integrated with a one-point quadrature scheme.

There are two important features which distinguish DYNA2D from other codes available for similar problems. These are a specialized contact-impact algorithm which allows gaps, friction and arbitrary slides between adjacent materials, and a rezoning facility. The contact-impact algorithm allows for a variety of methods of treating the interactions occurring at boundaries of bodies in contact or likely to come into contact. It requires designation of master and slave surfaces as input, in which each surface is defined by a number of nodal points. Each combination of the slave-master surface is termed a slideline (in two dimensions). For the proper definition of a slideline, a number of precautions should be considered. As the name implies, the slave-surface motion is dependent on the behaviour of the master surface, and the nodes in the slave surface are constrained to slide on the master surface after impact and remain on the master surface until a tensile force develops between the surfaces in contact. There are four types of slidelines available including (i) sliding only, (ii) tied sliding, (iii) sliding with voids (no tension interface), and (iv) sliding with voids and friction. Frictional forces are calculated using a Coulomb-type friction law and frictional coefficients may be specified. This interface treatment allows different materials to slide relative to one another, separate from each other if the tensile strength of the interface is exceeded, or collide with each other if previously separated.

Because of the large deformations involved in the impact and penetration process, the contact region of the computational mesh which moves with the deformed material is often severely distorted. Mesh elements become tangled and overlapped, resulting in computational inefficiencies and in inaccuracies and, in extreme cases, execution of the program ceasing. In this explicit Lagrangian method, the smallest element dimension controls the time step size of calculation. Hence as the distortion of the mesh increases, element sizes may decrease and the stable time step size is progressively reduced. It approaches zero for very large distortions leading to either the collapse of calculation or uneconomic impractical computation. Whenever such situations occur, recourse must be made to a built-in rezoning facility. Rezoning maps element quantities of the old grid onto the new grid such that conservations of mass, momentum and total energy, as well as the constitutive relationship, are satisfied. The new grid may be defined by the deletion of any number of mesh lines in both dimensions. Options are allowed to redefine positions of individual points, to equal or vary spacings along mesh lines and to reshape material boundaries. The overlay of the new and old grids and conservations of mass and momentum produce a density in each new element and a velocity for each new mesh point. Rezoning can be carried out interactively or automatically at given time intervals or in some suitable combination. Each time rezoning is done, conserved quantities are computed and printed for each material before and after rezoning to enable the user to see if the rezoned mesh is acceptable.

Both these facilities require some physical understanding of the penetration process and considerable experience if the program is to be used effectively.

Many incongruities arise from their misuse. Computations for certain impact and penetration problems take a long time and require a great deal of computer storage. DYNA2D provides a restart facility so that computations can be resumed after interruption. Input for DYNA2D may be generated using the preprocessor MAZE, or manually. Output is generated from DYNA2D for the post-processor code ORION in the form of restart, rezoning and binary plot files. All details about this code are given in the DYNA2D manual (Hallquist, 1984).

4.2.4 ORION

The output resulting from the computations is generally massive. Hence, to interpret and understand these output results for predictive purposes a post-processor code ORION must be relied on to provide visual displays of physical quantities of interest as well as tabulated information (printer output). ORION is capable of producing any physical quantity and time history in each coordinate direction for every nodal point or element in the modelled structure. It has the capability to plot the following features :

colour fringes

contour lines

vector plots

principal stress lines

deformed meshes and material outlines

time histories

reaction forces along constrained boundaries

interface pressure along slidelines

user specified labels.

ORION has two phases of operation, all but the time history plots being produced in phase one. All details of the commands used by ORION can be found in its manual (Hallquist, 1985).

4.3 Running the Program

The codes were mounted on two VAX computers, Micro VAX located in Newcastle and an 8600 housed in Durham. On both machines the programs ran under VMS and the amount of disc space available for this study was limited to 15 Mbytes and 25 Mbytes, respectively. The programs catered for a number of peripheral devices including monochrome and colour terminals and various plotters.

4.4 Simulations of Penetration Processes

The entire project of computer simulation consisted of three interrelated stages. These were the simulations of the projectile (or fastener shank) penetration, fastener penetration and fastener pull-out. The necessity of performing the projectile penetration at the initial phase was that

(i) it was a simplified problem,

(ii) it enabled familiarity with the program to develop without undue complexity,

(iii) it was a much studied problem; hence, comparison with other work would be possible,

(iv) it helped in a fundamental understanding of the penetration process.

In this Section, only simulations of penetration are presented and discussed. Fastener pull-out will be tackled in the next Section.

4.4.1 Projectile penetration

In practice, it is generally difficult to ensure normal projectile impact and to enforce the projectile to follow a normal path during subsequent penetration within the target because of the target packing structure and inhomogeneity. This is even true in some well-controlled laboratory penetration experiments. So, strictly speaking, it is more useful to have projectile impact at a small angle of obliquity (the angle between the normal to the target surface and the trajectory of projectile). For impacts normal to the target the angle of obliquity is zero. The two-dimensional code may provide some qualitative understanding of the penetration process for the plane strain condition, but generally this type of problem requires a three-dimensional treatment. However, such a treatment would increase tremendously the computational difficulty and require considerable computer resources. Also, for comparison with both theoretical and experimental work, the axisymmetric analysis in the numerical computation is of great advantage. Thus, in this Chapter, penetration simulation is confined to the normal impact penetration under an axisymmetric condition and with an assumption of the penetration path along the axisymmetric axis. The two-dimensional version of DYNA with its axisymmetric condition, which was previously described, was considered adequate to carry out this work.

The process of penetration was initiated with a projectile impacting the target at a given initial velocity and at zero obliquity. A long solid cylinder with an ogival nosetip was modelled as the projectile having a total length of 35 mm, and a diameter of 4 mm with calibre radius head (CRH) being 2.5 (an ogival nose has a circular shape which is defined by the parameter CRH, that is, the ratio between the arc's radius and the projectile diameter). The steel projectile was treated as an elastic plastic, strain hardening material having a Young's modulus of 209 GPa, a uniaxial yield stress of 1.2 GPa, a tangent modulus of

1.0 GPa and a density of 7800 kg/m^3. The finite element mesh was formed from 48 elements.

A cylindrical block was modelled as the target having both height and diameter of 150 mm. A total of 677 quadrilateral elements were used to form the computational mesh. Because constant-stress elements had been used in the formulation of DYNA2D, many small elements were necessary where the stress was expected to change rapidly. An area at a radius of 15 mm was then finely zoned to accommodate large potential plastic deformation since such deformation was expected to be localized. The area beyond this was coarsely zoned to conserve computational time because it was only intended to transmit wave effects or gross response. Due in part to this reason and in part to the small differences of material properties between sandstone and concrete, thus, the concrete case was not modelled for simplicity. A rigid body movement of target was inhibited by constraints on the far outer boundaries in the vertical direction. In this axisymmetric Lagrangian computation, target elements around the projectile were often severely deformed as the projectile entered the target. These elements were mostly compressed radially so that element sizes were greatly reduced if the element aspect was not large enough. These highly distorted elements controlled the time step size, resulting in considerable increase of problem cycles and computation time. Whenever this happened, frequent rezoning of target material in the vicinity of the projectile was required. Use of the rezoning facility not only added computation time but also introduced variability in the results dependent on the rezoning intervals and on the user's experience. To avoid this difficult situation and potential unreliability of results, and also to save on computation time, a tiny hole with a diameter of only 0.02 mm was introduced at the axisymmetric axis (or centreline) of the cylindrical target. However, the direct consequence of this assumption was the possibility for elements near the centreline to cross over radially, which was physically impossible. To compensate for this, a rigid wall was defined on the centreline. Penetration was achieved by expanding that hole. Ideally, the assumption that the introduction of a hole does not significantly change the states of stress and particle velocity in the target should be justified. The effect of the introduction of this central hole will be discussed in Chapter 5.

To impart the kinetic energy of the projectile to the target, a frictional slideline was defined along the outer boundaries of the projectile and target to accommodate their interaction. Friction was applied through the Coulomb-type friction law. A realistic frictional coefficient between the steel projectile and the Staindrop sandstone at the penetration condition was not available. Thus, a notional value was used in calculation with the best possible estimation (its effect on the penetration process will be discussed later). The slideline scale factor was increased by 15 times to reduce slideline overlap.

Two of the eleven available material models in DYNA2D were used for the target material in this analysis. These were the elastic plastic model, and soil and crushable foam model. Although it is suggested that the latter is more flexible and suitable to represent materials which have no regular characteristics like geological materials and concrete, the former one is easier to use and requires less user intervention. Thus the target material, sandstone, was first represented as an elastic plastic continuum, being fully determined by a density of 2130 kg/m^3, Poisson's ratio of 0.2, a Young's modulus of 13.62 GPa and a uniaxial compressive yield strength of 0.02 GPa.

The sandstone was also modelled using a pressure-dependent soil and crushable foam model. This material model required for input a pressure-volumetric strain relation and a yield strength-pressure relation. A pressure-volumetric strain relation was input in a tabular form. This determined the material compressibility of sandstone with a porosity of 18 %. When the stored maximum value of the volumetric strain was reached, unloading occurred elastically with a bulk modulus of 11.25 GPa from the corresponding point on the curve. This is assumed to be a tensile cutoff and the pressure after unloading was left at the cutoff value which was input. The relation used in this computation is shown in Figure 4.1. The deviatoric or yield strength-pressure relation used in this model is given by

$$J_2 = a_o + a_1 P + a_2 P^2 \tag{4.1}$$

where J_2 is the second invariant of the deviatoric stress tensor, P is pressure, and a_o, a_1 and a_2 are constants determined from experimental data. For a compressive triaxial test, the second invariant becomes

$$J_2 = \frac{(\sigma_1 - \sigma_3)^2}{3} \tag{4.2}$$

where σ_1 is the maximum compressive stress and σ_3 is the confining stress. Thus, the pressure-dependent yield criterion in this model is given by

$$\frac{(\sigma_1 - \sigma_3)^2}{3} = a_o + a_1 P + a_2 P^2 \tag{4.3}$$

This relation gives a general expression of Coulomb-type yield criteria. Obviously, the von Mises criterion is a special case obtained by setting $a_1 = a_2 = 0$ for the elastic-perfectly plastic material. Each of the three constants, a_o, a_1, and a_2 in above equation is a certain function of material strengths, and is determined by fitting experimental data into that equation. There is a range within which experimental data can reasonably be fitted, resulting in slight fluctuations of these determined constants. This implies that a slightly different fitting curve may be used. However, in the present calculation, a parabolic fitting curve with $a_2 = 0$ was used to represent the pressure-dependent yield behaviour, as shown

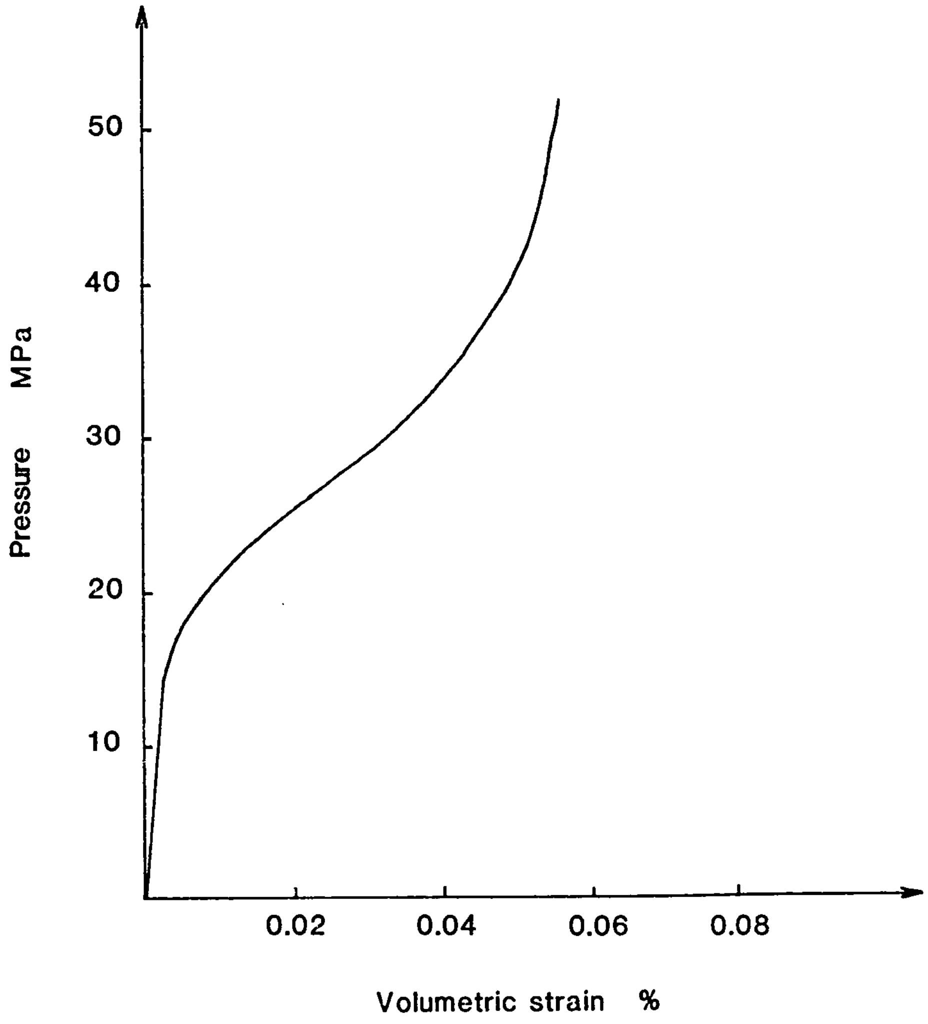

Figure 4.1 Pressure-volumetric strain relation for sandstone

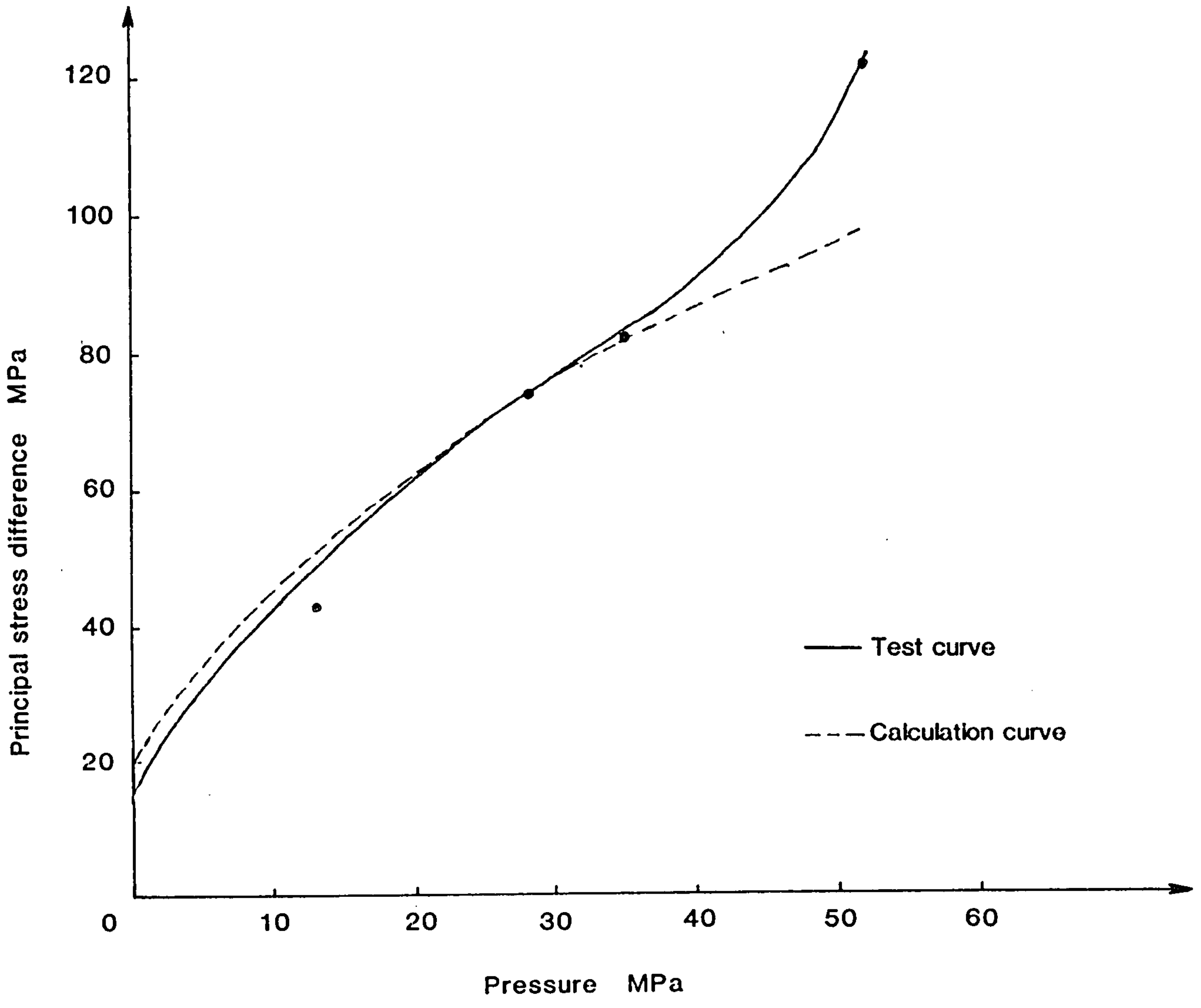

Figure 4.2 Yield strength-pressure relation for sandstone

in Figure 4.2. Input constants for yield criterion Equation (4.3) were as follows :

$$a_0 = 0.00133\ MPa, \quad a_1 = 60.27\ MPa, \quad a_2 = 0 \tag{4.4}$$

The computational results obtained using this model will be presented later.

The detailed examination of the computation results would be too lengthy to provide. Thus, only representatives which are sufficient to show the main features of system considered are presented. The impact velocity of 100 m/s was chosen to be low enough for the target material strengths to be important factors characterizing the penetration. Figure 4.3 shows a central portion of the entire configuration, i.e. the projectile-target contact region, at various times (0, 100 and 450 μs, respectively) after impact at the initial impact velocity of 100 m/s using the isotropic elastic-plastic model to approximate the target behaviour. It is seen that the deformation increases as time progresses over a period of 450 μs, and that the severe deformation and large displacement occur mostly in a relatively small region of target material. A lip is formed on the edge of the crater. Figure 4.4 exhibiting the contours of the maximum displacement illustrates that the target deformation extends only about 2.5 projectile diameters in the radial direction and 2.5 projectile diameters in the vertical direction when the projectile comes to rest Thus, the deformation front has approximately an outline of the shape of the projectile indicating apparent effects of friction and the nose shape of the projectile. The projectile motion is predicted mainly in terms of its deceleration, velocity, and penetration histories. Especially, the deceleration curve provides considerable information on the target resistance and material properties. Figure 4.5 shows the axial rigid body deceleration history of the projectile. It is seen that the projectile takes about 100 μs to encounter the highest resistance in the target, and this corresponds to the penetration depth of the projectile nose length. This resistance is maintained for about 250 μs, showing

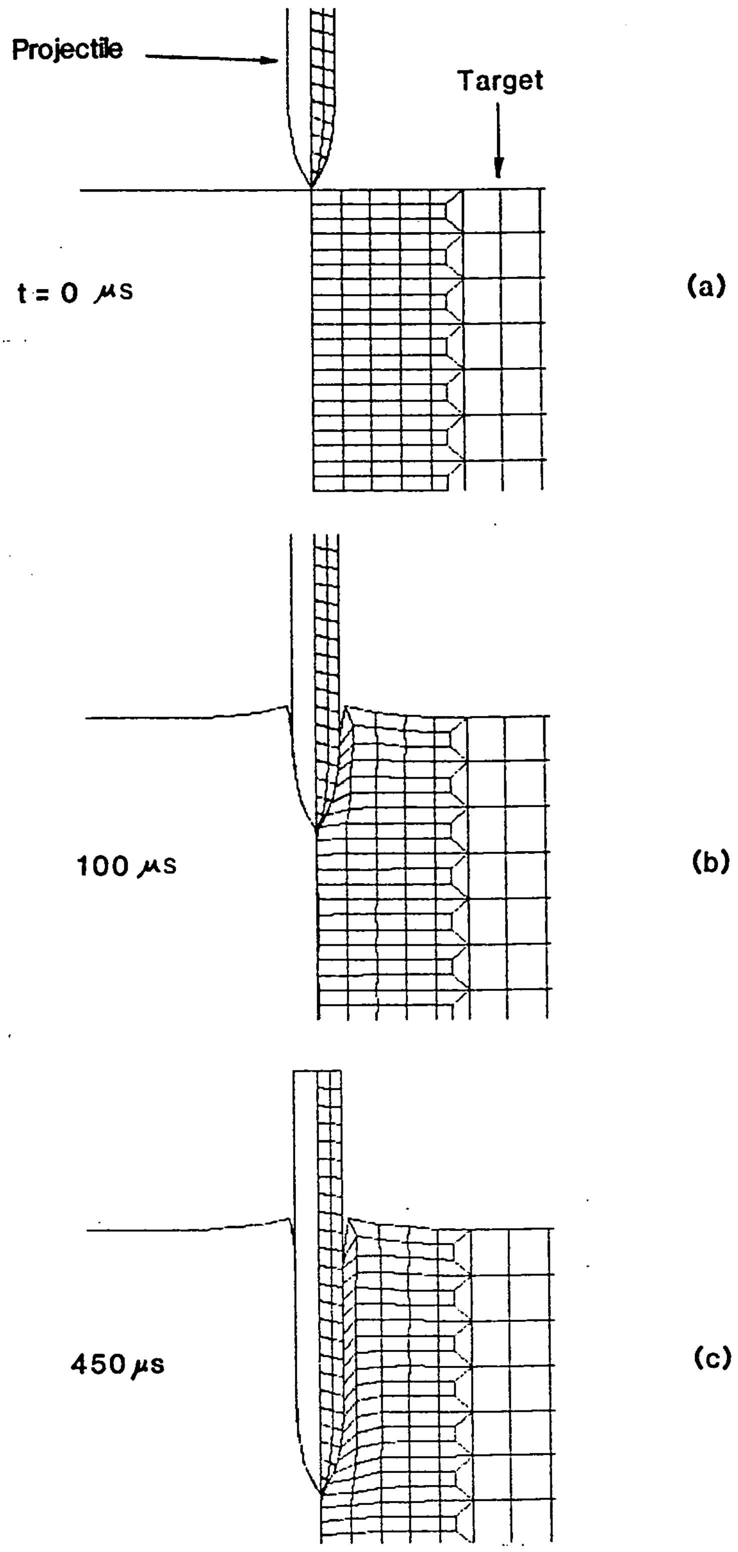

Figure 4.3 Configurations of projectile-target contact region at various times

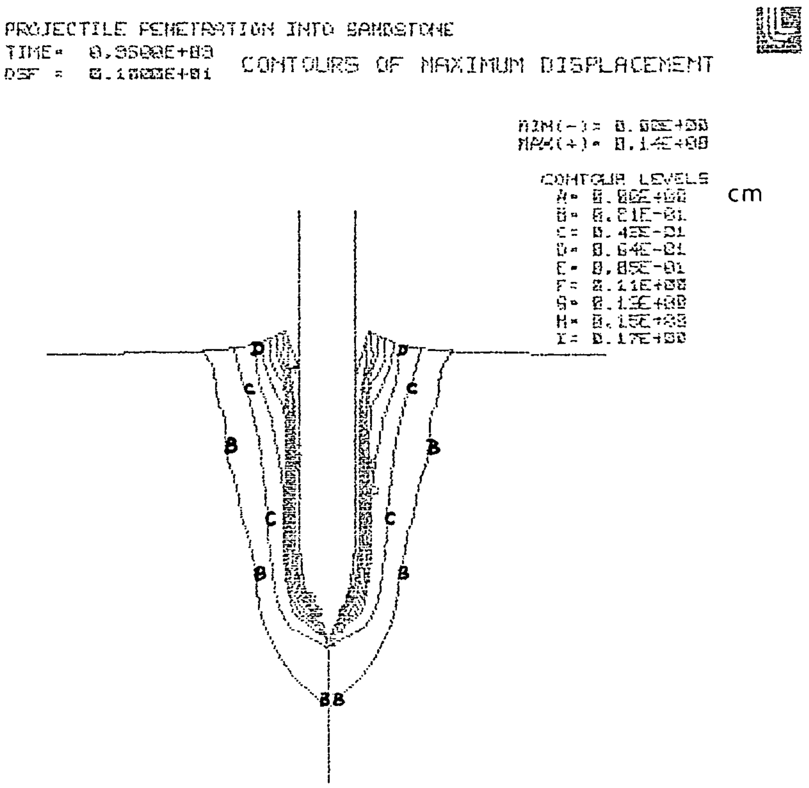

Figure 4.4 Contours of target displacement for 100 m/s impact

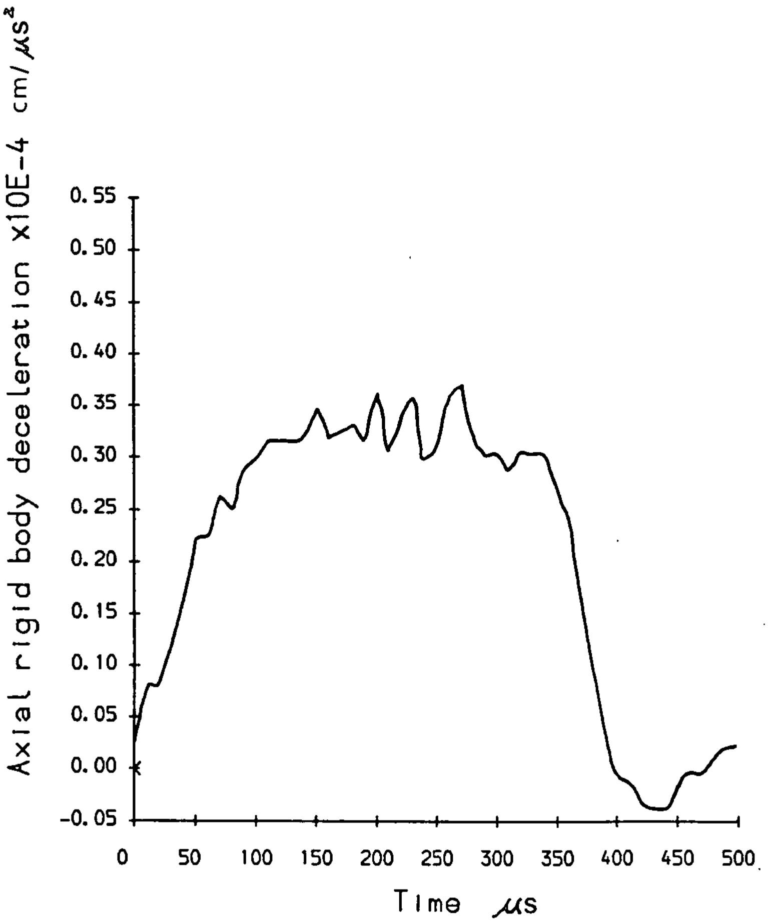

FIGURE 4.5 PROJECTILE DECELERATION HISTORY

steady motion before the projectile comes to rest. This is manifested by an approximate plateau at the deceleration value of 320 km/s^2 on the curve. It seems to suggest that once the yield strength is reached the target material develops plastic flow until most of the kinetic energy is dissipated, and also that the process of expelling the target material in front of the projectile contributes most resistance to penetration. Oscillations as seen along that plateau are attributed to stress wave effects. However, from the axial rigid body velocity history as shown in Figure 4.6 and the penetration history of the ballistic point in Figure 4.7 it is seen that the rigid body motion of the projectile is not affected by these effects. Also seen from these Figures is the fact that the penetration velocity decreases down to zero at about 360 μs and then the projectile rebounds at a velocity of about 5 m/s rather than resting at the maximum penetration depth. This may be attributed to the recovery of the kinetic energy imparted to the target as elastic strain energy. It will be shown later that as the impact velocity increases (up to 250 m/s) this rebound velocity approaches zero so implying that the kinetic energy imparted to the target exceeds the elastic strain energy. It is sometimes very useful to measure the penetration depth as a function of the impact velocity. This relation may provide a more comprehensive view of the projectile response and especially help to locate regions which offer the major resistance to penetration. Figure 4.8 obtained from an element located at the top of the projectile shows such a relation exhibiting a locus of the quarter of an approximate circle. In addition to the confirmation of the projectile rebound it illustrates the onset of the plastic flow which is manifested by the stair-like variation at region A.

Figures 4.9, 4.10 and 4.11 show axial and radial stresses and pressure contours, respectively. It can be seen that maximum stresses and pressure in the target occur near the nosetip of the projectile, and that the compression gen-

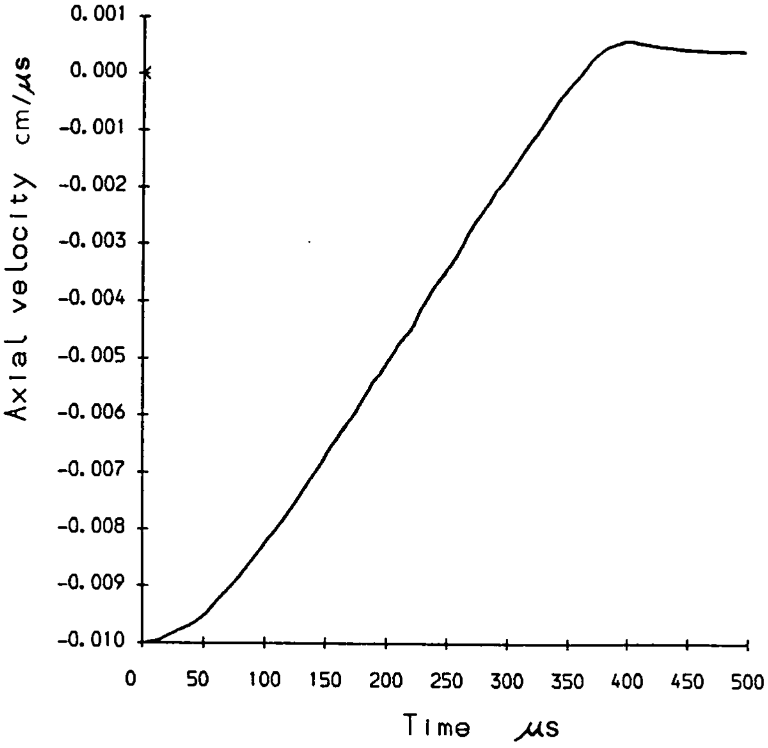

FIGURE 4.6 PROJECTILE VELOCITY HISTORY

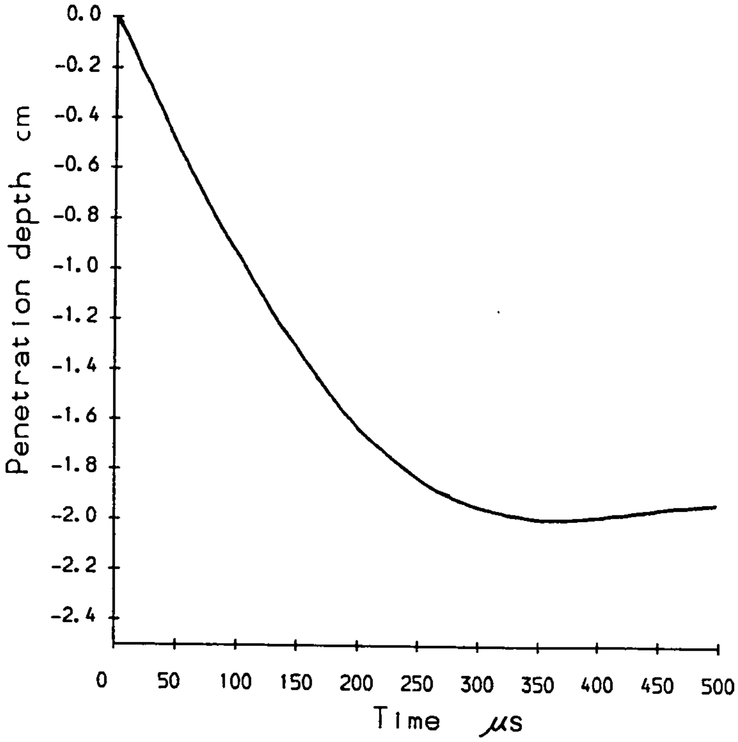

FIGURE 4.7 PROJECTILE PENETRATION HISTORY

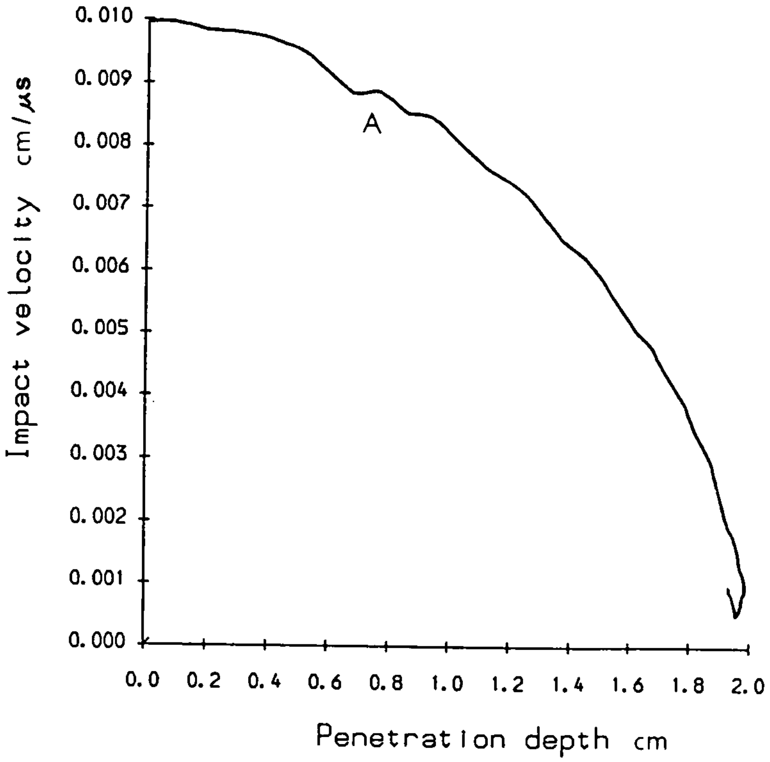

FIGURE 4.8 IMPACT VELOCITY - PENETRATION HISTORY

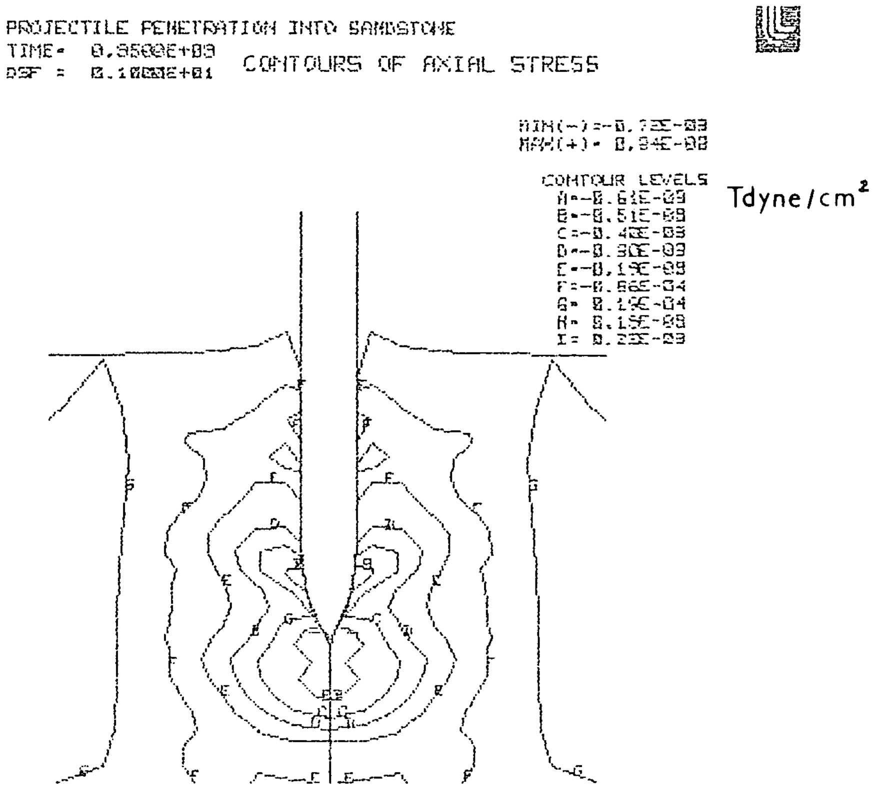

Figure 4.9 Contours of axial stress

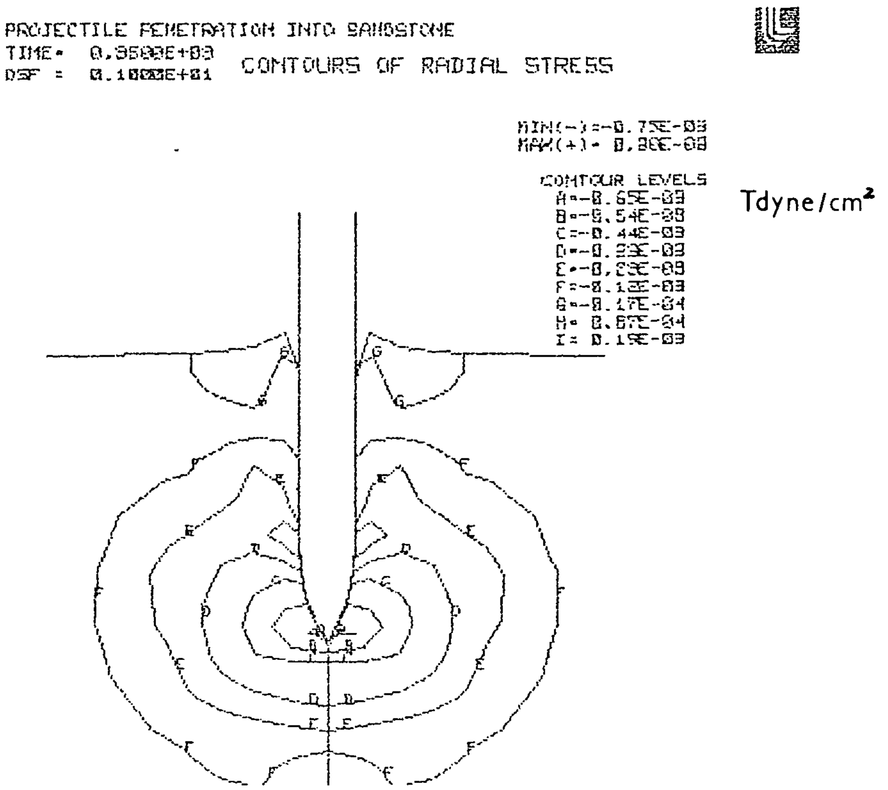

Figure 4.10 Contours of radial stress

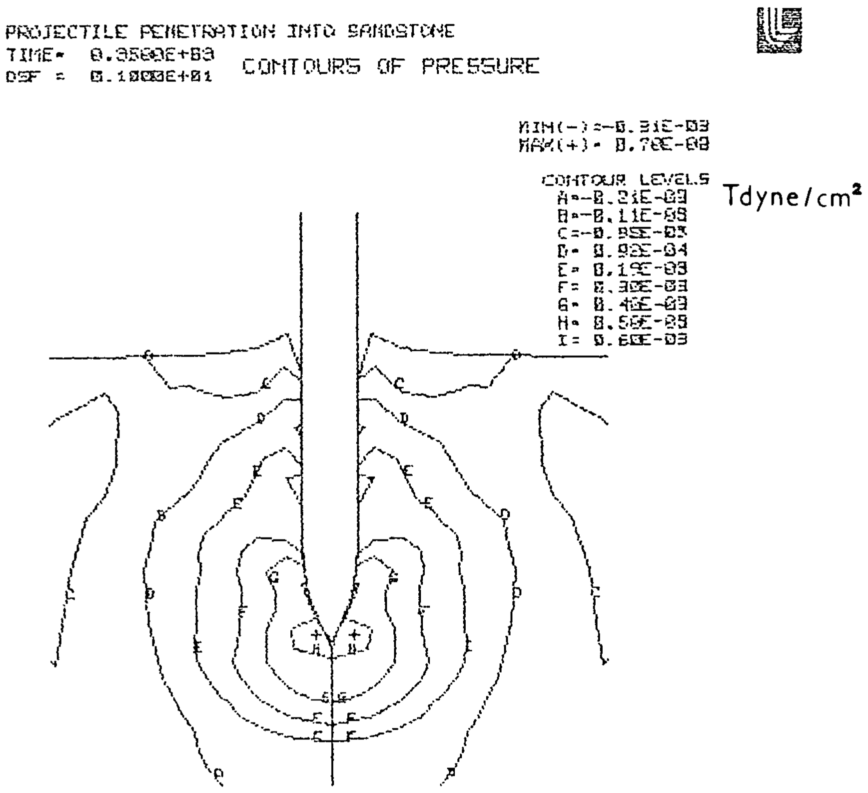

Figure 4.11 Contours of pressure

erated by impact is confined to a cylindrical zone having a radius of about 4 projectile diameters. It is also interesting to note from Figure 4.11 that a region near the impact surface around the projectile indicates the potential tensile failure (frontal petaling).

Figure 4.12 shows that the kinetic energy loss of the projectile (curve A) manifests itself primarily in the form of plastic work done in deformation of the target material. Only about 4 % energy imparted to the target material is associated with the particle motion.

In this calculation, a frictional slideline was used to treat interaction between the steel projectile and sandstone target. However, because a frictional coefficient between these materials under the penetration condition at an impact velocity of 100 m/s is not known, an assumed material value was adopted. It is generally considered that the dynamic frictional coefficient depends on the interface velocity and the normal stress state, and it decreases with the increase of the interface velocity. Gaffney (see Longcope, D.B. and Grady, D.E., 1978) measured the frictional coefficient between Dakota sandstone and steel using a rotating steel wheel technique in a velocity range of 10 to 30 m/s at a normal stress of about 40 MPa. Values ranging from 0.57 to 0.23 were obtained. Since the impact velocity in this calculation is much higher than the velocity range in which those results were produced, it seems plausible to assume that the dynamic coefficient of friction used in the present calculation is no more than 0.1 for the free-flight projectile penetration. The effect of friction with given frictional coefficient on the total penetration resistance is illustrated in Figures 4.13 and 4.14. It is seen that the penetration resistance increases with increasing surface friction, while the penetration depth and duration are all reduced accordingly. The degree of penetration depth and duration reduced by increasing the frictional coefficient from zero to 0.1 is calculated to be less than 20 percent

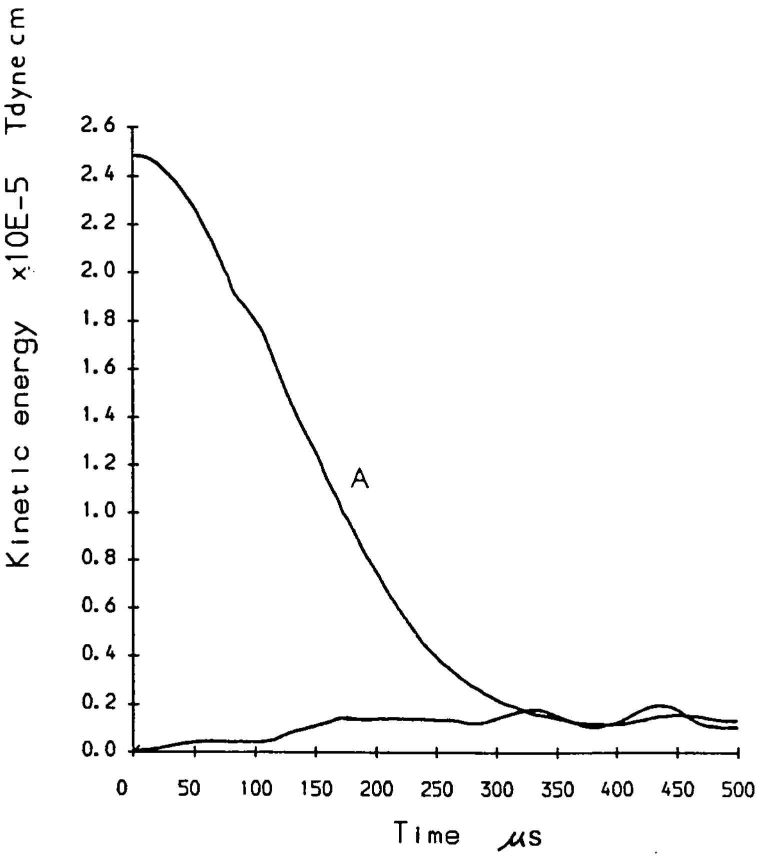

FIGURE 4.12 KINETIC ENERGY HISTORIES OF BOTH PROJECTILE AND TARGET

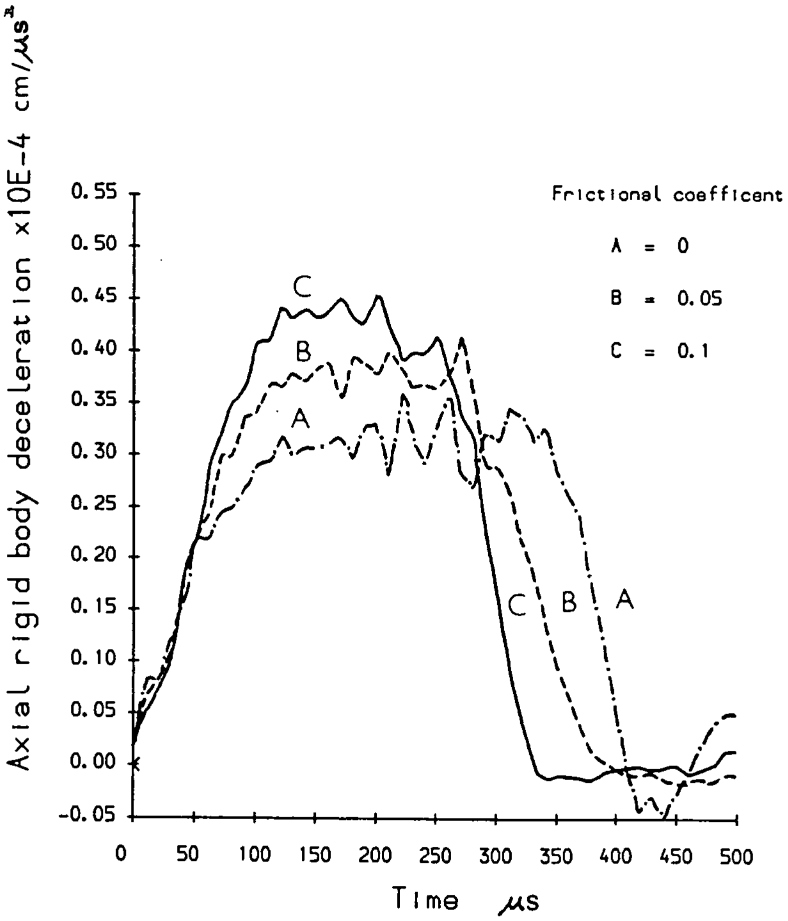

FIGURE 4.13 COMPARISON OF DECELERATION HISTORIES AT VARIOUS FRICTIONAL COEFFICIENTS

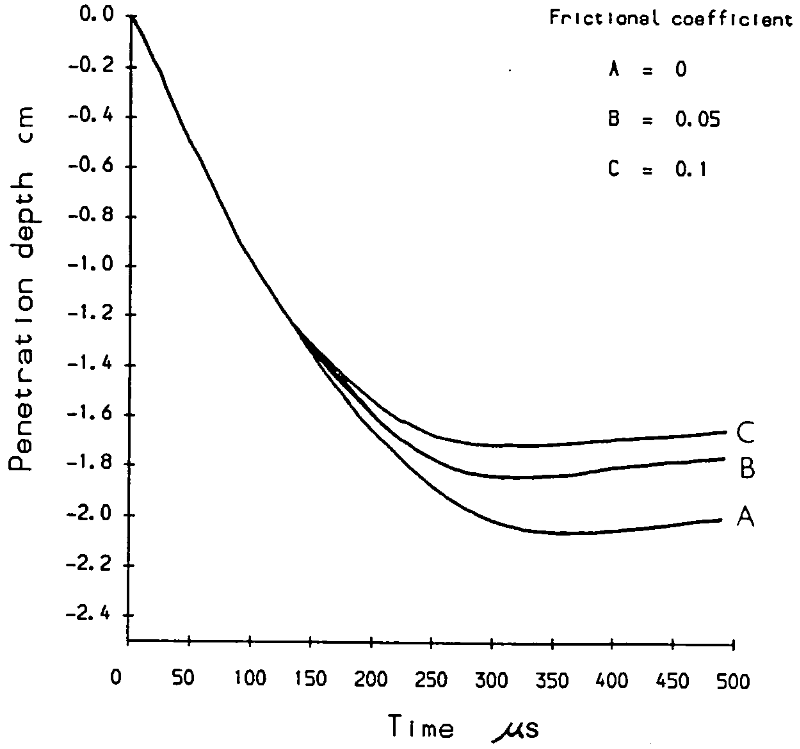

FIGURE 4.14 COMPARISON OF PENETRATION HISTORIES AT VARIOUS FRICTIONAL COEFFICIENTS

and about 80 μs, respectively. The direct consequence of incorporating a high frictional coefficient is the potential separation of the projectile-target interface which was reported in the literature. The present calculations performed with the highest frictional coefficient of 0.1 and the ogival nose of the 2.5 CRH reveal that separation does not take place in this application.

In the elastic plastic representation of the target material, it was expected that the yield strength and the hardening effect play important roles in the material behaviour since the constitutive relations of the geological materials and concrete are greatly affected by the confining pressure. Thus, although in previous calculations an elastic perfectly-plastic case was assumed, the influence of these strength parameters on the impact penetration merited some attention. To this end, the calculation (model II) was repeated using the larger yield strength of 45 MPa. Comparison with the previous model (I) is made in Figures 4.15 to 4.18. Results show the remarkable differences. The resistance to penetration is increased two-fold. The penetration duration and depth are reduced by 150 μs and by 40 percent, respectively. The most significant variation is found in the kinetic energy in which the target kinetic energy is increased by a factor of about 4 so that it amounts to the 30 percent of the initial kinetic energy of the projectile. To examine the sensitivity of penetration to the hardening effect, a hardening modulus with a magnitude of only 0.5 percent of Young's modulus was incorporated, and the calculation was repeated (with the previous value of yield strength, i.e. 20 MPa). Significant differences can be observed in Figures 4.19 to 4.21, showing comparisons with results obtained from the perfectly plastic model (I). It is seen that in addition to a 25 % reduction in the penetration depth, the most impressive difference lies in the deceleration histories in which the curve obtained from the elastic- plastic strain-hardening model shows a very sharp rise at a time of about 90 μs with a peak value of 588

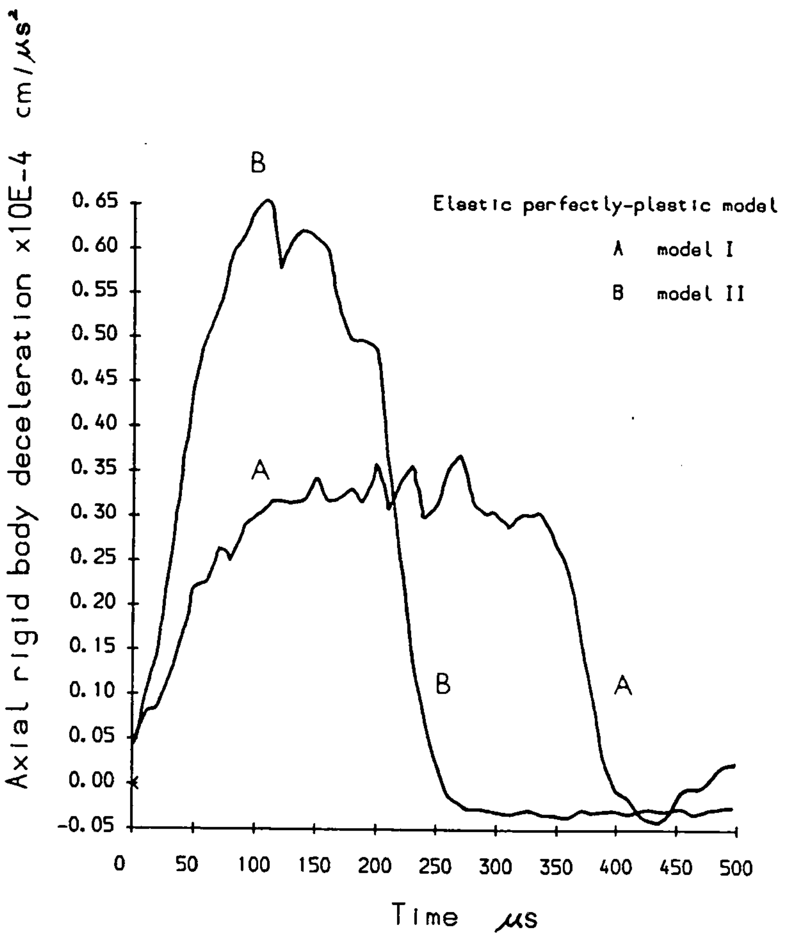

FIGURE 4.15 COMPARISON OF DECELERATION HISTORIES

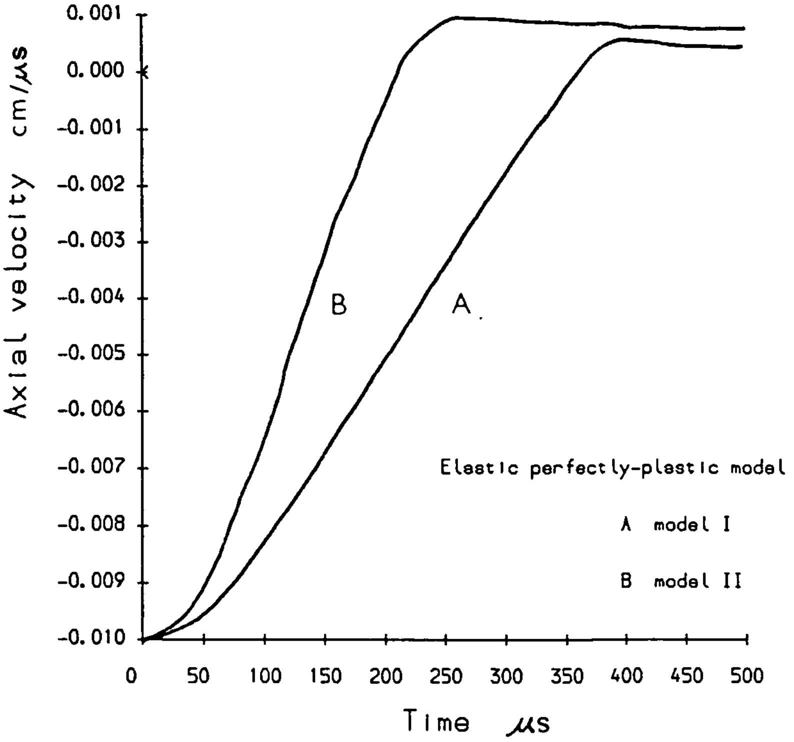

FIGURE 4.16 COMPARISON OF VELOCITY HISTORIES

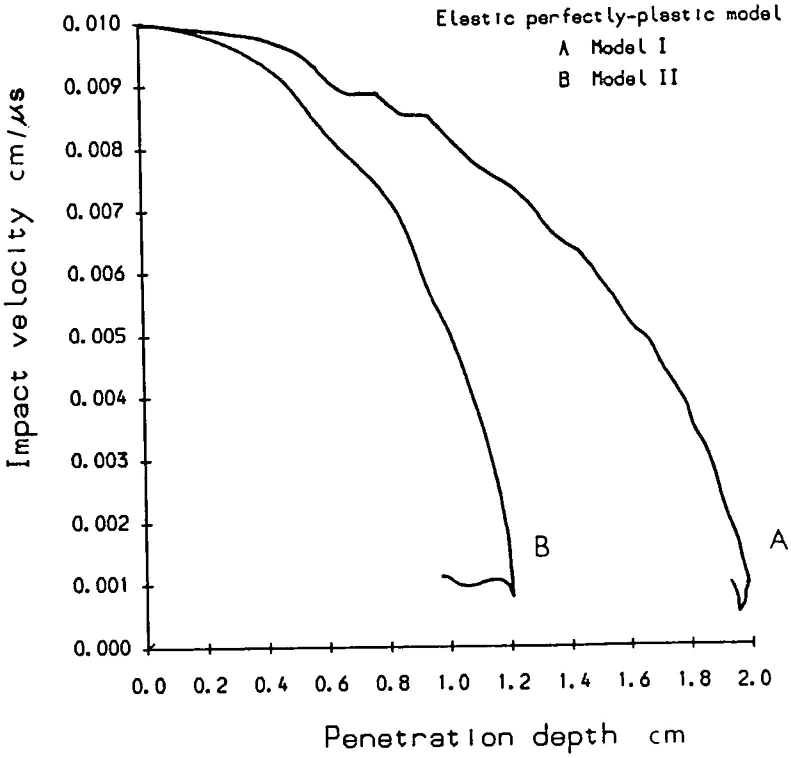

FIGURE 4.17 COMPARISON OF IMPACT VELOCITY - PENETRATION HISTORIES

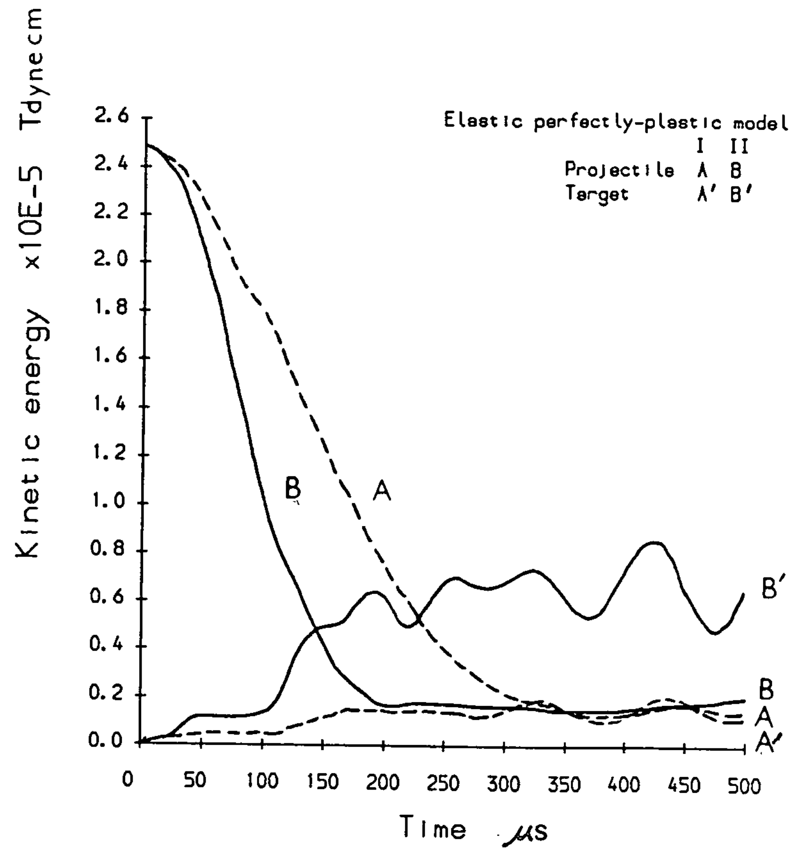

FIGURE 4.18 COMPARISON OF KINETIC ENERGY HISTORIES

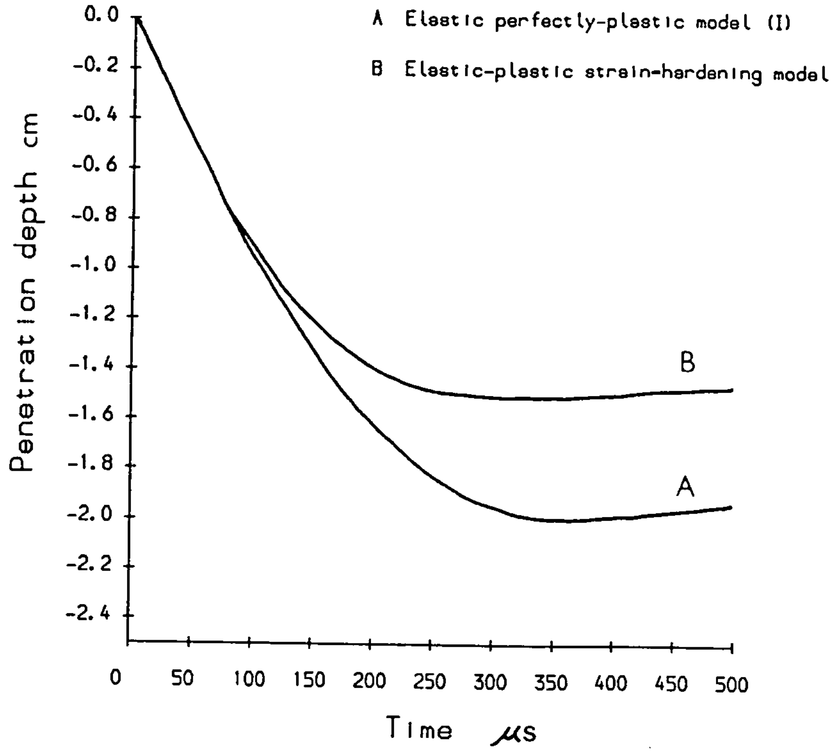

FIGURE 4.19 COMPARISON OF PENETRATION HISTORIES

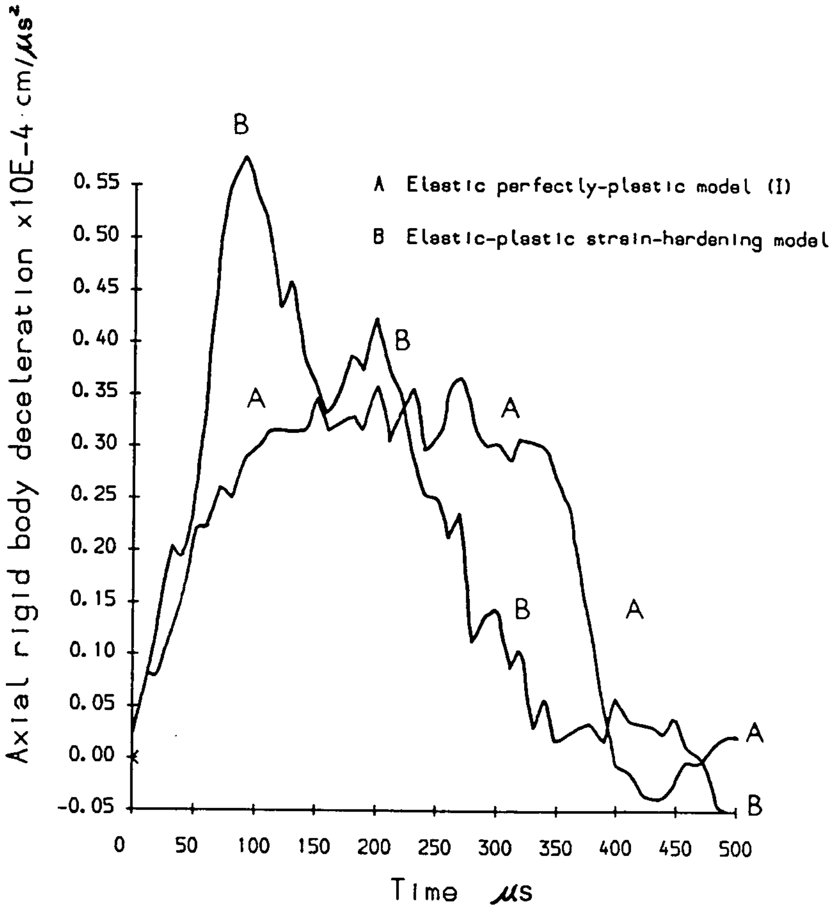

FIGURE 4.20 COMPARISON OF DECELERATION HISTORIES

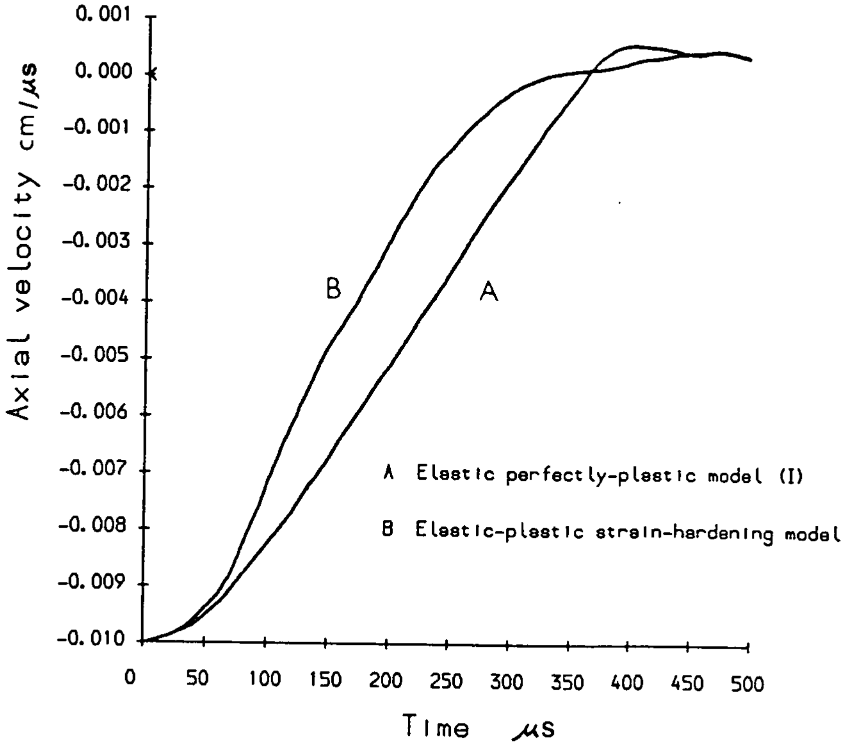

FIGURE 4.21 COMPARISON OF VELOCITY HISTORIES

km/s^2 (84 percent increase) and falls down very rapidly to zero. This curve shows no plateau (i.e. no plastic flow) as is seen in the perfectly plastic case, indicating, apparently, a hardening effect. It suggests, also as seen in Figure 4.21, that the hardening behaviour of the target material has significant influence on the depth of penetration and on the motion of the projectile. However, it has little effect on the duration of penetration.

As stated expressly in the previous chapters, the impact velocity and the nose shape of the projectile play dominant roles in the impact penetration event. Especially, the relation of the impact velocity to the penetration depth is always of great interest in this field. Therefore, the influence of these parameters over the impact penetration was investigated. The velocity range covered was from 50 m/s to 250 m/s. Calculations were performed using both the elastic perfectly-plastic (I) and the elastic-plastic strain-hardening models with a frictional coefficient of 0.1 at the projectile-target interface. The relation between the impact velocity and the penetration depth was established, as presented in Figure 4.22. It shows that two curves have the same general shape and that the penetration depth increased more rapidly than the impact velocity, so exhibiting a parabolic trend. A blunt projectile having a hemispherical nose with the CRH of 0.5 was chosen to investigate the nose shape. The penetration was performed at the identical impact condition. The contact region of the system is shown in Figure 4.23 at a time of 300 μs in which the separation of the projectile from the target is clearly observed. The penetration persisted for 220 μs, and the projectile reached a depth of only 11.5 mm which was 60 percent of that in the ogival-nose case. The relation between the projectile velocity and the penetration depth is illustrated in Figure 4.24 which shows that the nose shape is more effective in the early stage of penetration (i.e. embedment) and contributes a significant portion of the target resistance to penetration.

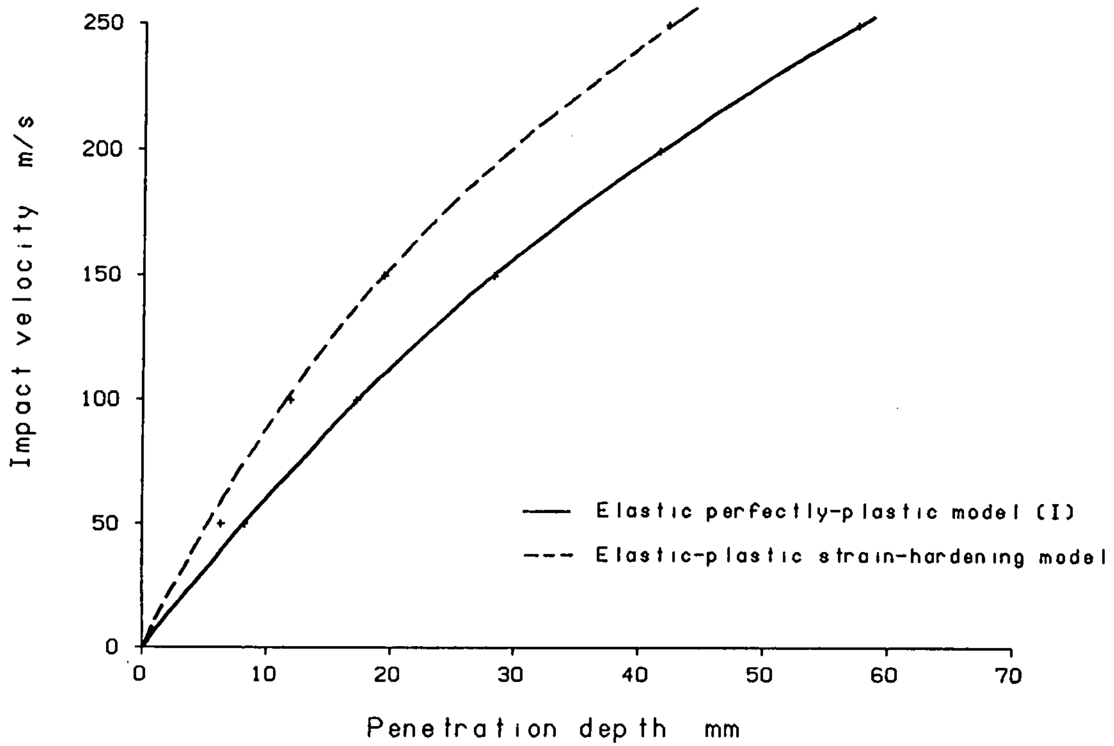

FIGURE 4.22 IMPACT VELOCITY - PENETRATION DEPTH RELATION

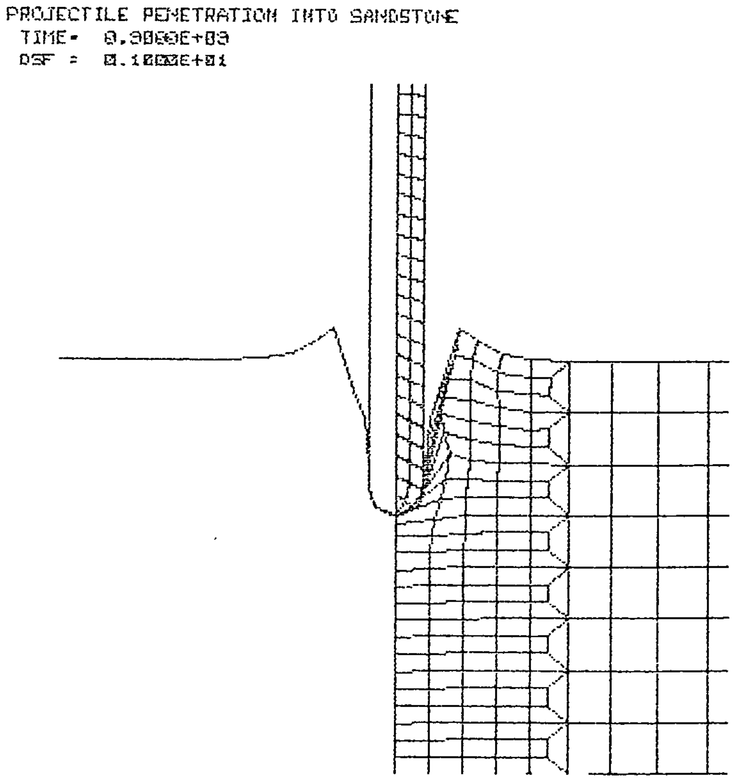

Figure 4.23 Configuration of projectile-target contact region for hemispherical-nosed projectile

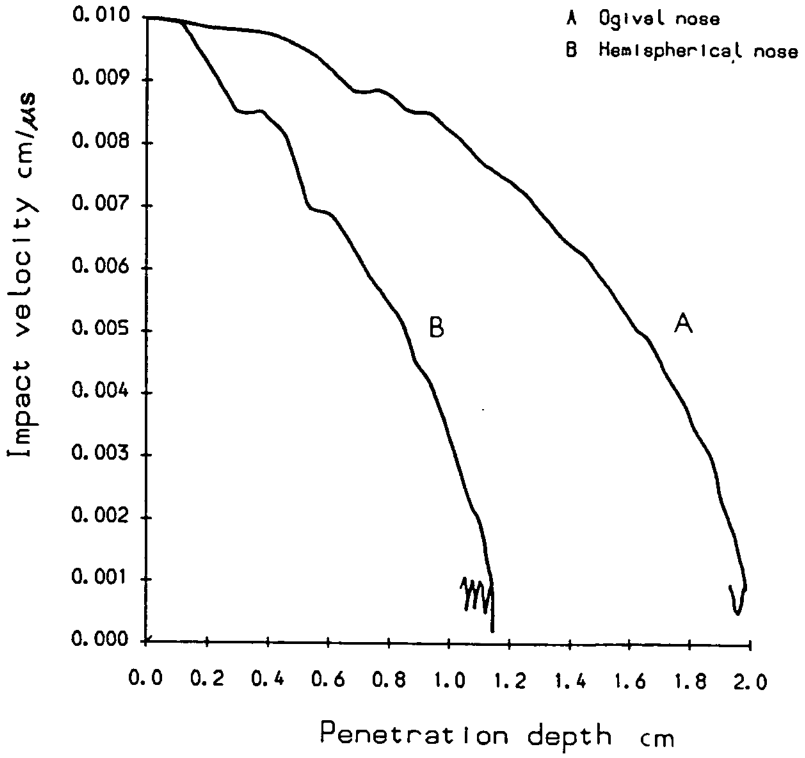

FIGURE 4.24 COMPARISON OF IMPACT VELOCITY - PENETRATION HISTORIES BETWEEN THE OGIVAL-NOSED AND THE HEMISPHERICAL-NOSED PROJECTILES

It is seen from the foregoing calculations that satisfactory results are obtained using the elastic-plastic (strain hardening) model to represent the target material. However, in the plastic deformation, the linear strain hardening behaviour is prescribed, which introduces a certain idealization of the material behaviour. This can be improved by using the soil and crushable foam model. Also, as an alternative, the calculation was performed using this model with the pressure-volumetric strain relation and yield strength-pressure relation described in Figures 4.1 and 4.2, respectively. The results obtained are compared with those of the elastic plastic model (I) in Figures 4.25 to 4.30. It is seen that the results produced by these two mo dels are in good agreement and that the slight disparity was expected because of the presence of the 5-percent volumetric strain in the latter model.

4.4.2 Fastener penetration

Based on the model developed for the projectile penetration in the preceding section, the penetration process of the fastener was simulated. Because the major difference between the projectile and the fastener is the presence of a washer on the fastener shank (or projectile) which acts as a penetration retarder, as illustrated in Figure 4.31. Simulation of the free-flight fastener penetration was attempted by incorporating the washer into the model of the projectile penetration.

The washer is made of the same material as the projectile, and was located about 11 mm from the ballistic point with the outer ring diameter of 12 mm. Only one solid element was used to represent the washer. Two extra slidelines were added to the model to define the washer sliding over the fastener shank and the washer-target impact. The process of the fastener penetration with an initial impact velocity of 100 m/s is illustrated in Figure 4.32, which exhibits

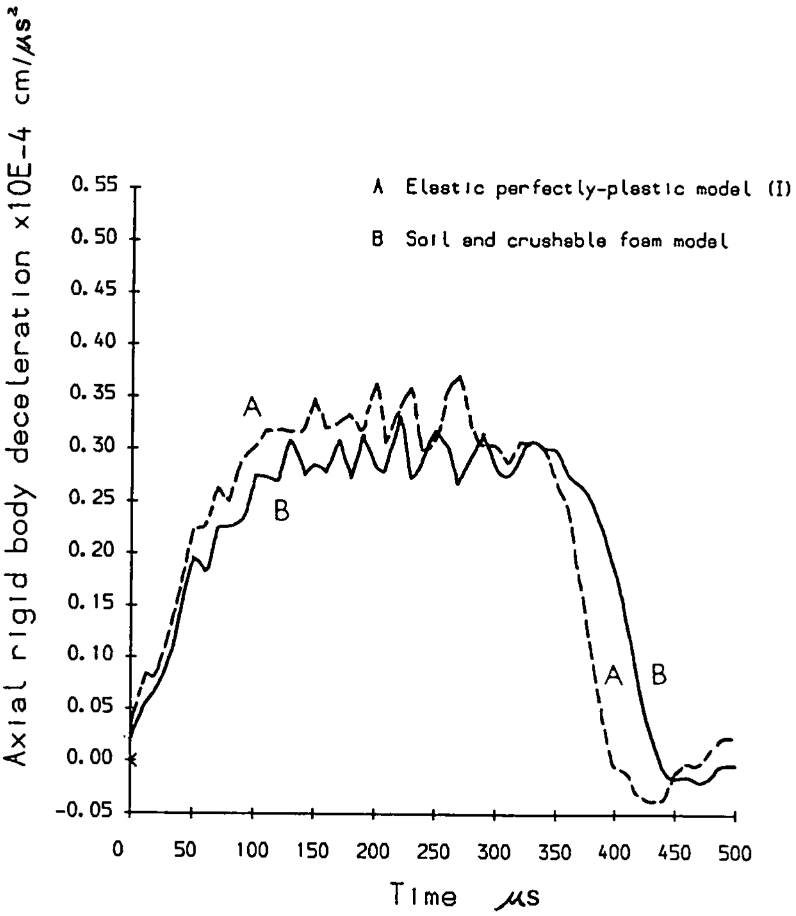

FIGURE 4.25 COMPARISON OF DECELERATION HISTORIES

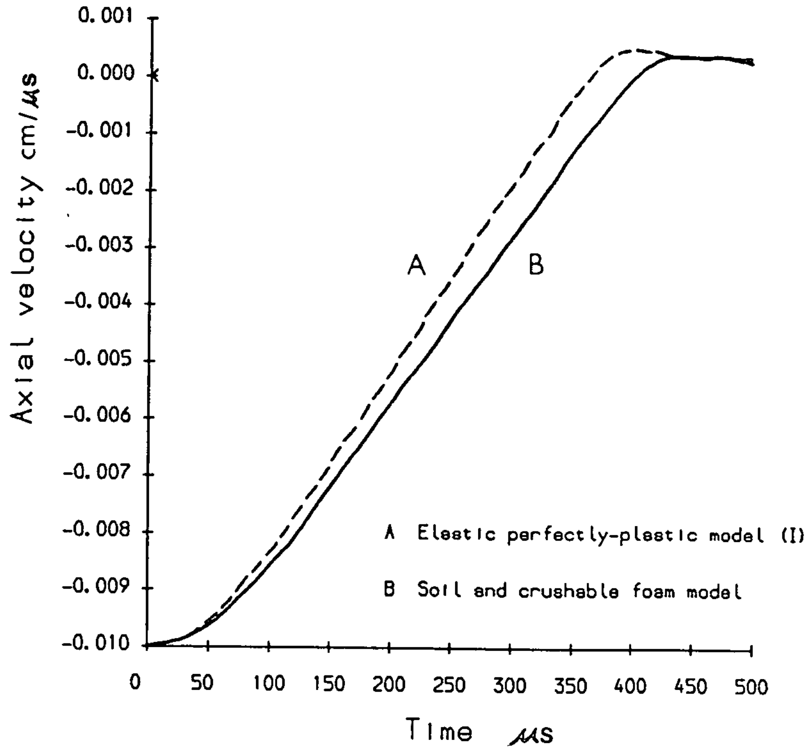

FIGURE 4.26 COMPARISON OF VELOCITY HISTORIES

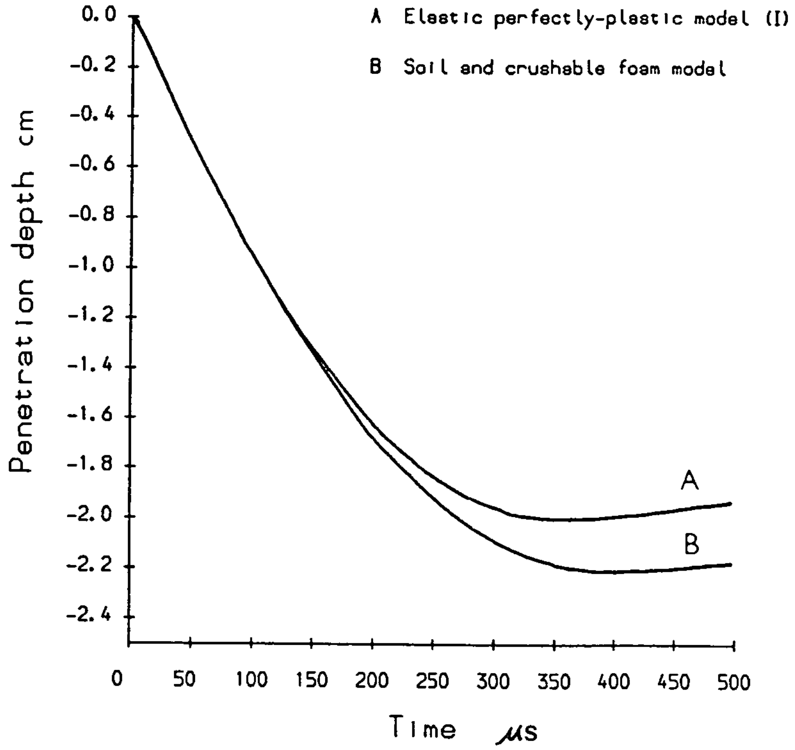

FIGURE 4.27 COMPARISON OF PENETRATION HISTORIES

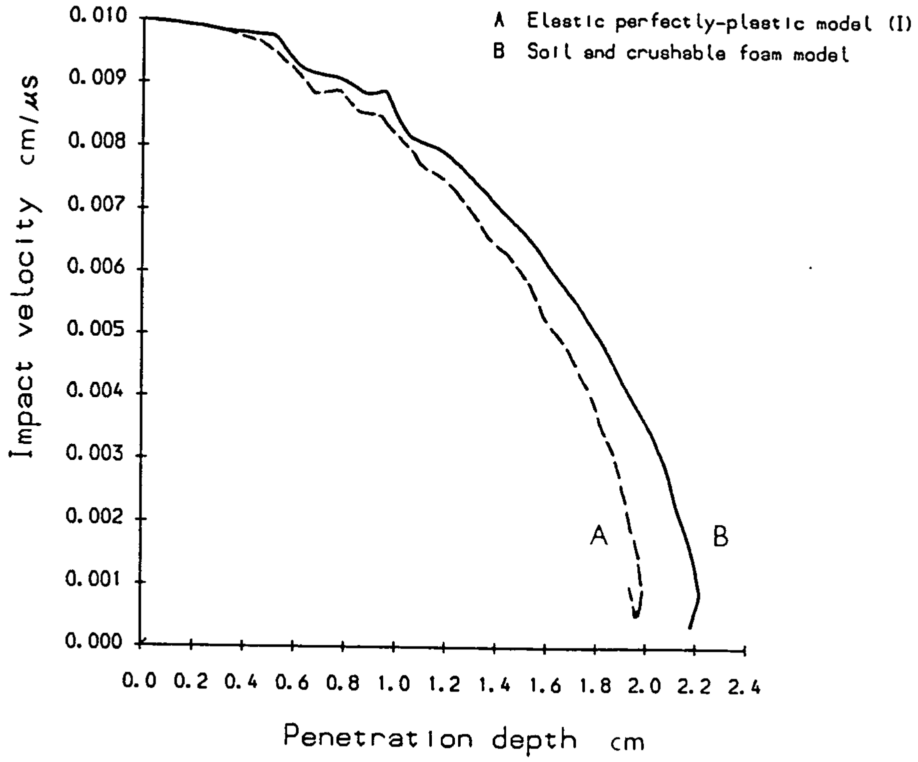

FIGURE 4.28 COMPARISON OF IMPACT VELOCITY - PENETRATION HISTORIES

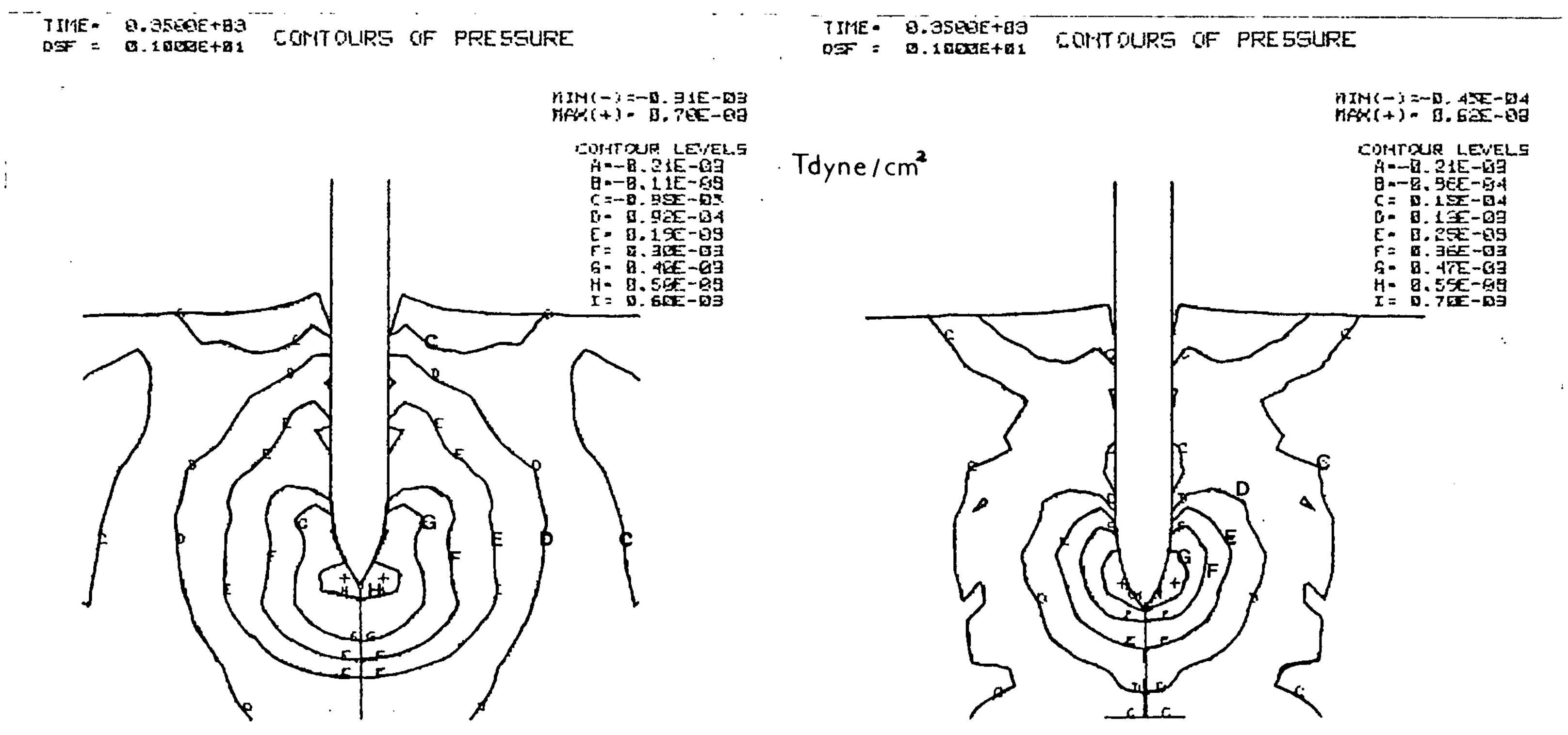

(a)

(b)

Figure 4.29 Comparison of pressure contours (a) From elastic perfectly-plastic model (I)
(b) From soil and crushable foam model

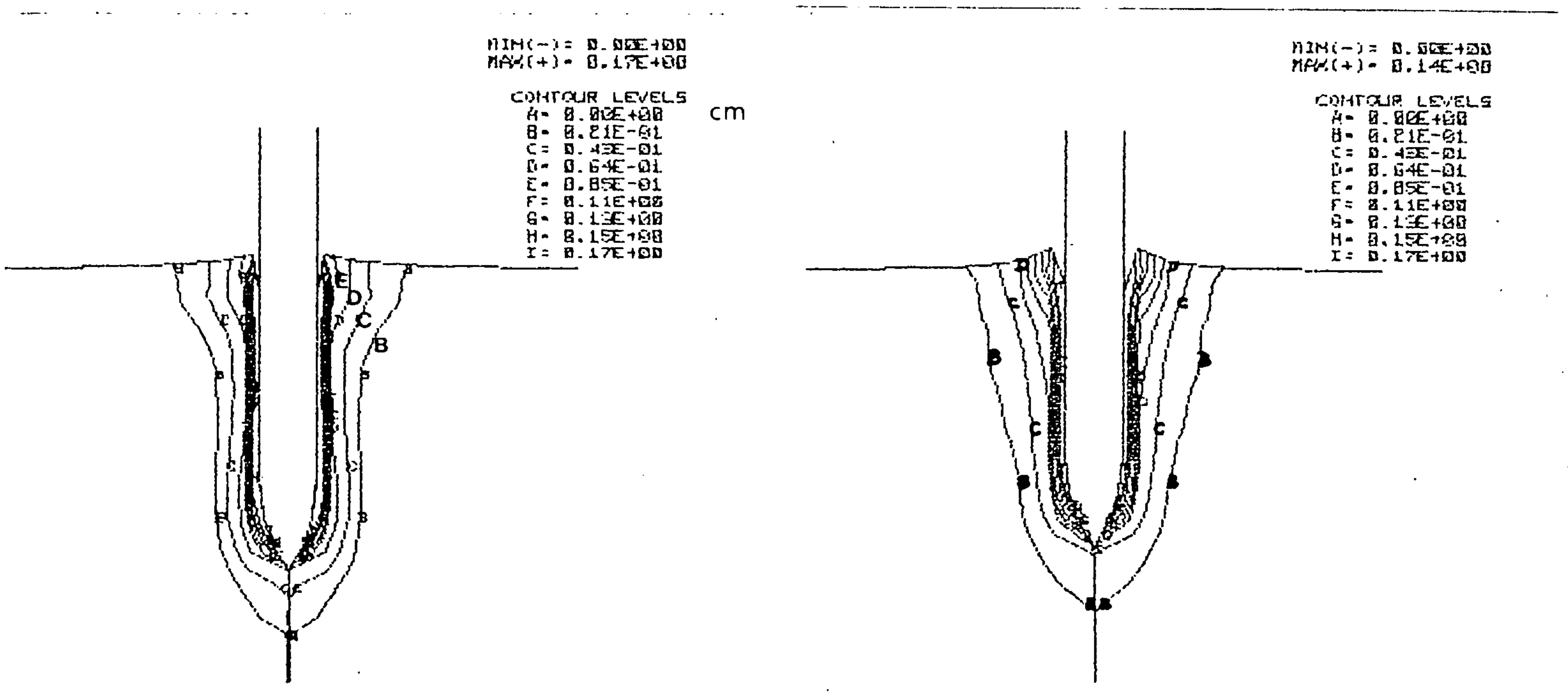

(a)

(b)

Figure 4.30 Comparison of displacement contours (a) From elastic perfectly-plastic model (I)
(b) From soil and crushable foam model

Projectile

Fastener

Figure 4.31 Comparison of projectile and fastener

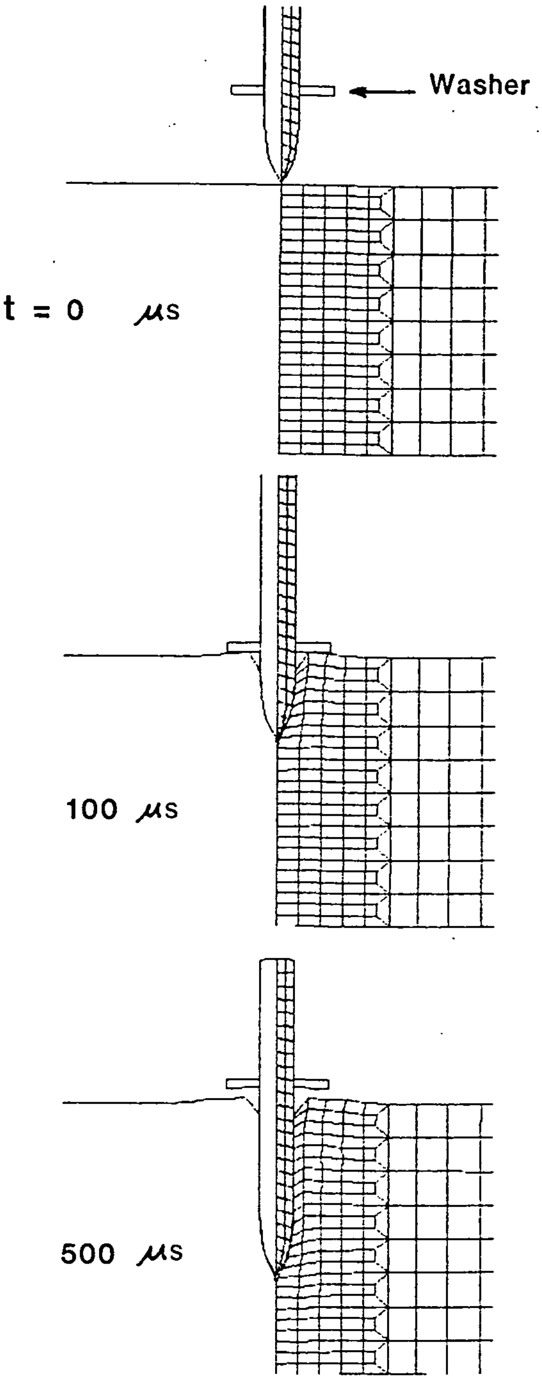

Figure 4.32 Configurations of fastener-target contact region at various times

the motion of the washer at various times. It is seen that at the end of the calculation the washer is about 1 mm above the impact surface. This agrees with observations in the penetration experiments described in the previous Chapter. The washer response is illustrated in Figures 4.33 to 4.35 in which it is seen that the retarding effect lasts for only about 50 μs. Figure 4.35 portrays the motion of the washer, which shows clearly that at 100 μs the washer impacts the target surface and then rebounds slightly. Only 1 mm reduction in the penetration depth was found, implying the insignificant effect of the washer retardation. It should be pointed out that in this calculation the washer-fastener shank friction is assumed to be only 20 percent of the fastener shank-target friction, and it is found that the former friction is very sensitive to the projectile motion. Furthermore, the present treatment incorporating the washer into the model was very crude. This problem might be better presented if a loading curve be employed to give a more refined control of the washer behaviour.

As described in Section 3.2.1, the actual process of fastener penetration is not that of a free-flight entry, but rather that the fastener is driven into a target by the piston. Thus, on the basis of the foregoing model, the fastener penetration simulation was further developed by incorporating the piston action. The piston is made of the same material as the fastener shank and the washer. It has a weight of about 120 grams, a diameter of 12 mm, and has a thread insert at the front having an inner diameter of 4 mm. The piston collar and the cartridge expansion chamber were not modelled because what it is required from the piston is just a propellent action. Three more slidelines were incorporated in the previous fastener penetration model to describe the piston-fastener interaction and the potential piston-washer impact. A frictional coefficient of 0.2 was used for the fastener-target interface. Contact between the fastener and the piston was defined as frictionless. The initial impact velocity was set to 62 m/s which

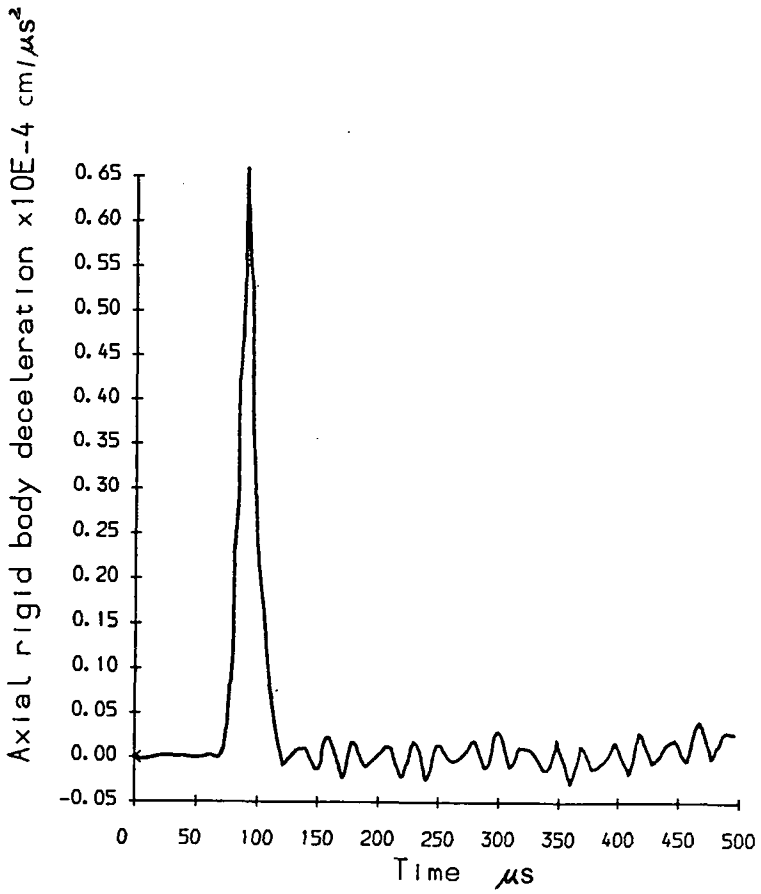

FIGURE 4.33 WASHER DECELERATION HISTORY

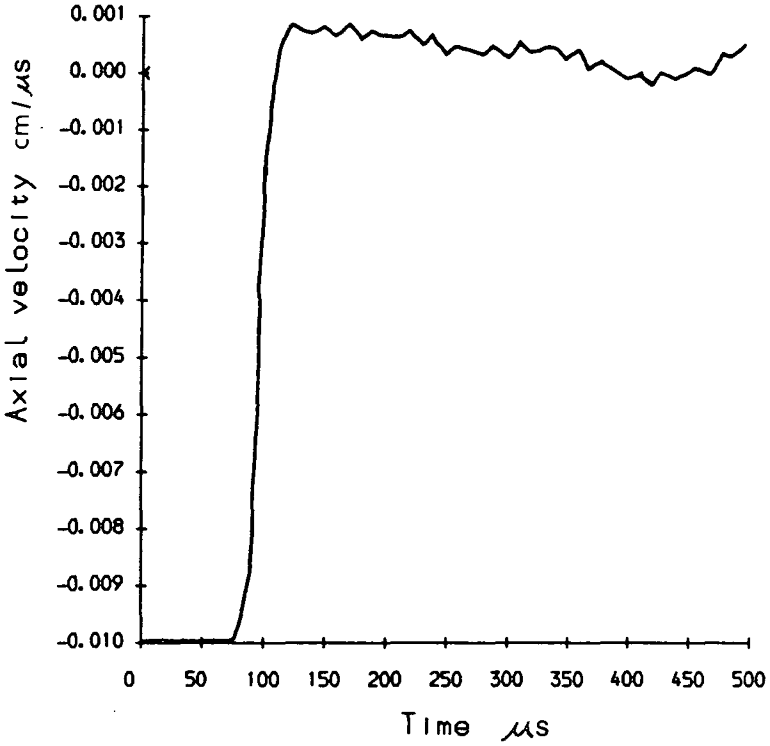

FIGURE 4.34 WASHER VELOCITY HISTORY

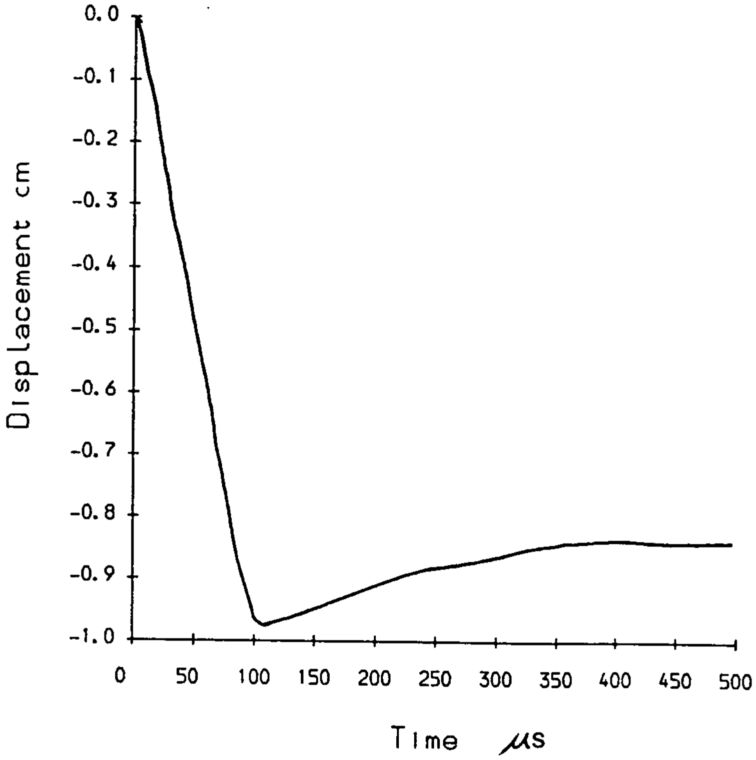

FIGURE 4.35 WASHER DISPLACEMENT HISTORY

corresponded to a power regulator setting of 2.5. Preliminary calculations which were not very successful revealed that the elastic perfectly-plastic representation of the target material using the previously defined values of material properties did not provide much resistance to the fastener penetration. A similar result was obtained with the elastic plastic representation incorporating a low hardening modulus. In both cases, the piston and the fastener over-penetrated the target and the washer became severely deformed, leading to numerical instability. As a consequence, the uniaxial compressive strength was used as the yield strength of the target material and a hardening modulus of 1 percent of the Young's modulus was also included. Four elements were employed to model the washer. Finally, the fastener shank length was increased up to 40 mm (to match the physical dimensions of M4-10-40S12 fastener) in order to avoid the mutual contact at the end of the piston, washer and target surface, which could affect the actual penetration of the fastener. The results of the modified calculation, in which the duration of impact increased to about 1.2 ms, are presented in Figures 4.36 to 4.47. Figure 4.36 portrays the motion of the fastener together with the piston at various times. In Figure 4.37, the piston deceleration history shows that the largest resistance was clearly encountered at about 750 μs although the curve oscillated considerably over its increase. This point was supported by the piston velocity history as shown in Figure 4.38, in which the turning region was evident corresponding to that time. Figure 4.39 shows a smooth increase of the piston displacement. The fastener motion in this process was dependent on the motion of the piston. This is reflected in the fastener velocity history which has a slight oscillation, as is shown in Figure 4.40, and is further supported by Figure 4.41 which exhibits this feature more explicitly. Figure 4.42 shows a penetration history of the fastener. The washer displacement could be observed in Figure 4.43. The action of the piston was so dominant in this process that

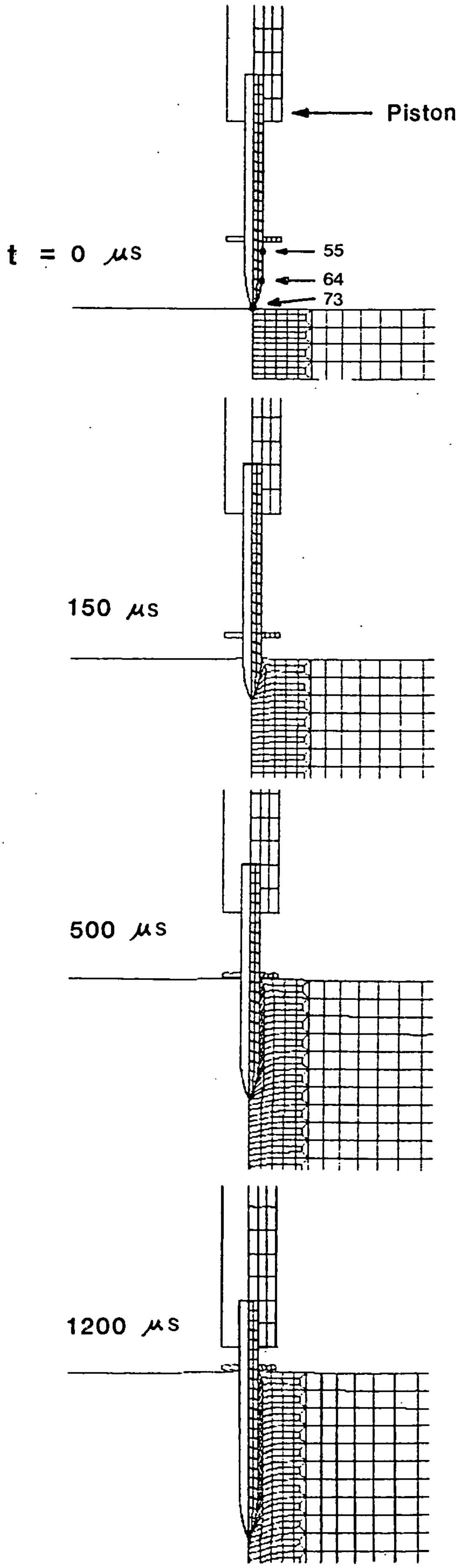

Figure 4.36 Configurations of fastener (with piston) target contact region at various times

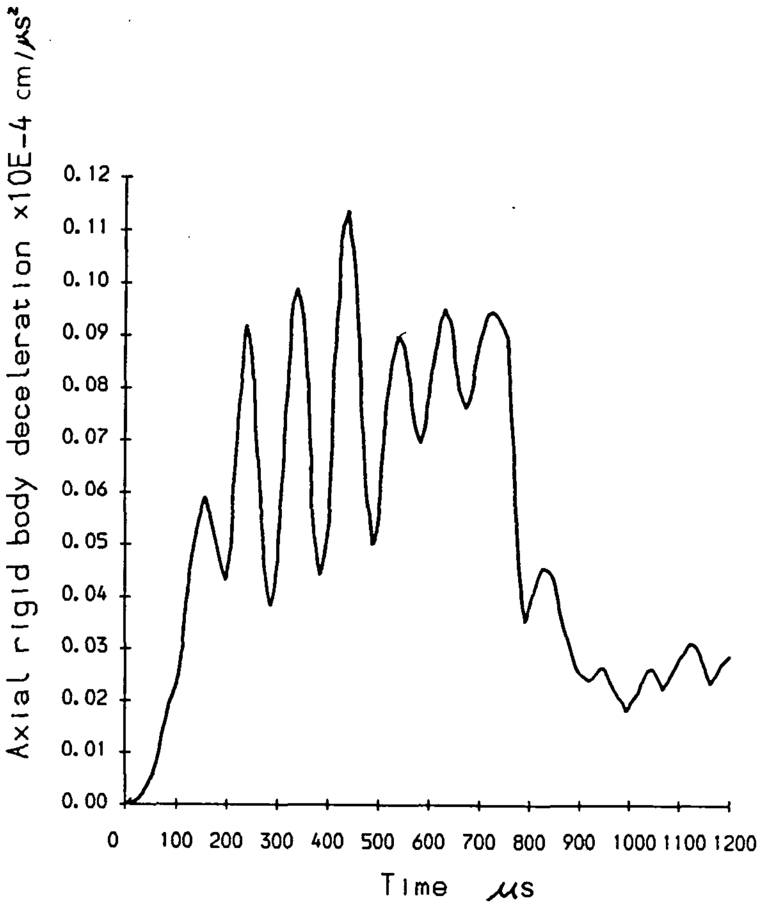

FIGURE 4.37 PISTON DECELERATION HISTORY

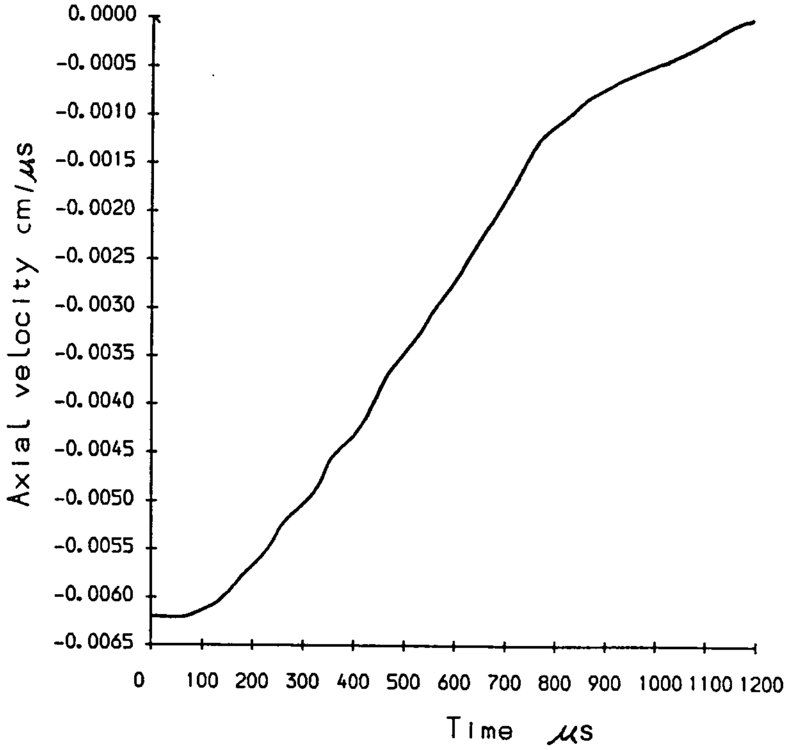

FIGURE 4.38 PISTON VELOCITY HISTORY

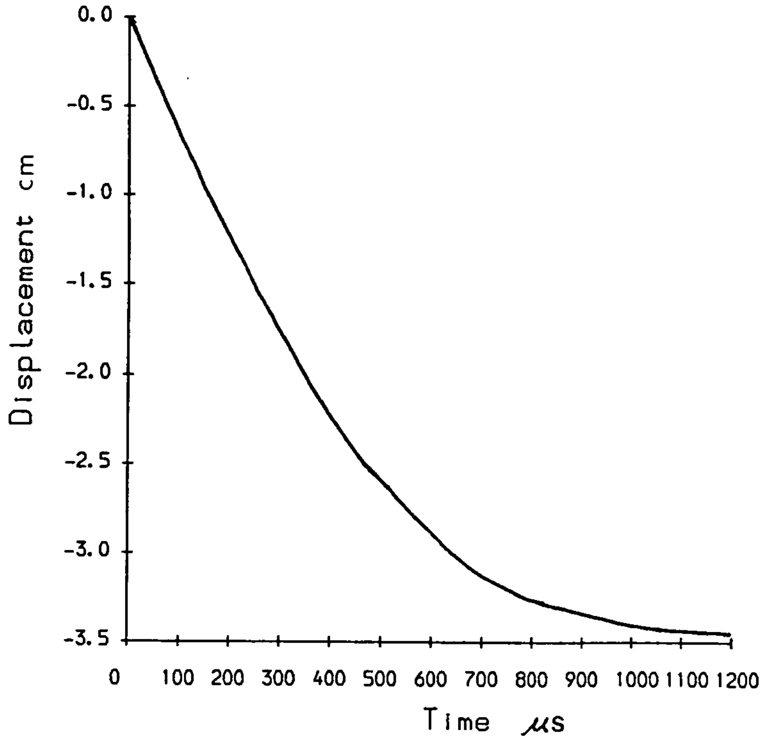

FIGURE 4.39 PISTON DISPLACEMENT HISTORY

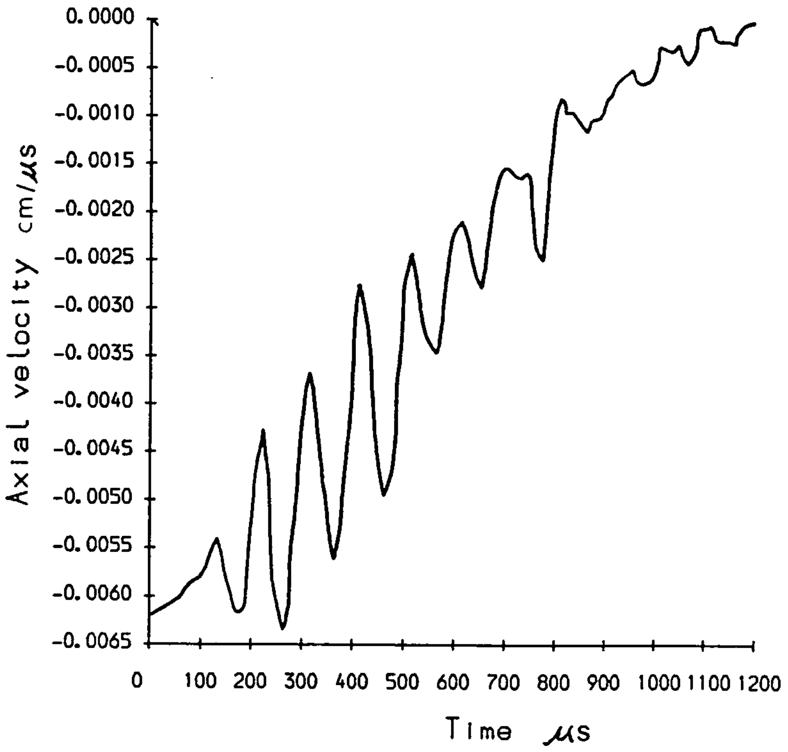

FIGURE 4.40 FASTENER VELOCITY HISTORY

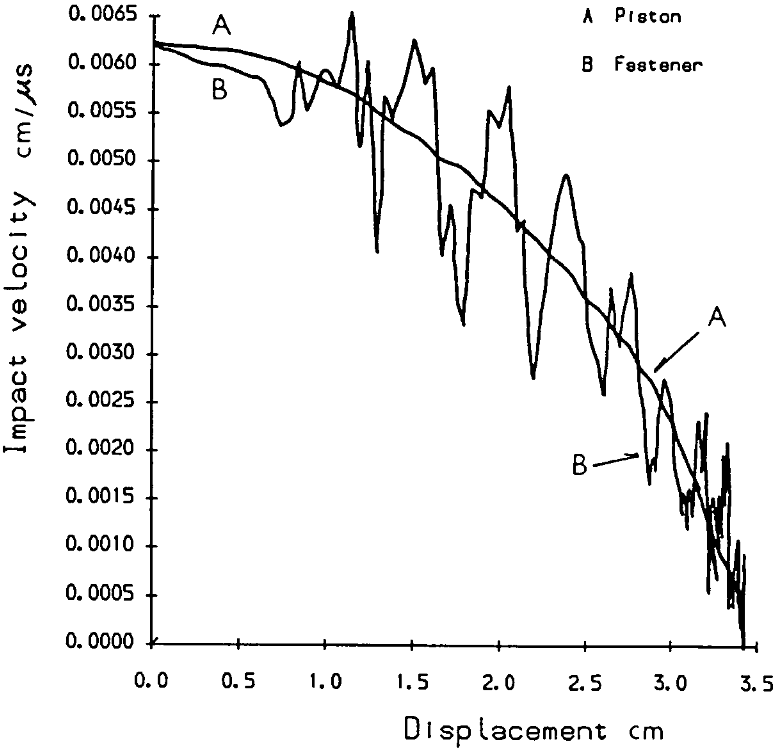

FIGURE 4.41 COMPARISON OF IMPACT VELOCITY - DISPLACEMENT HISTORIES

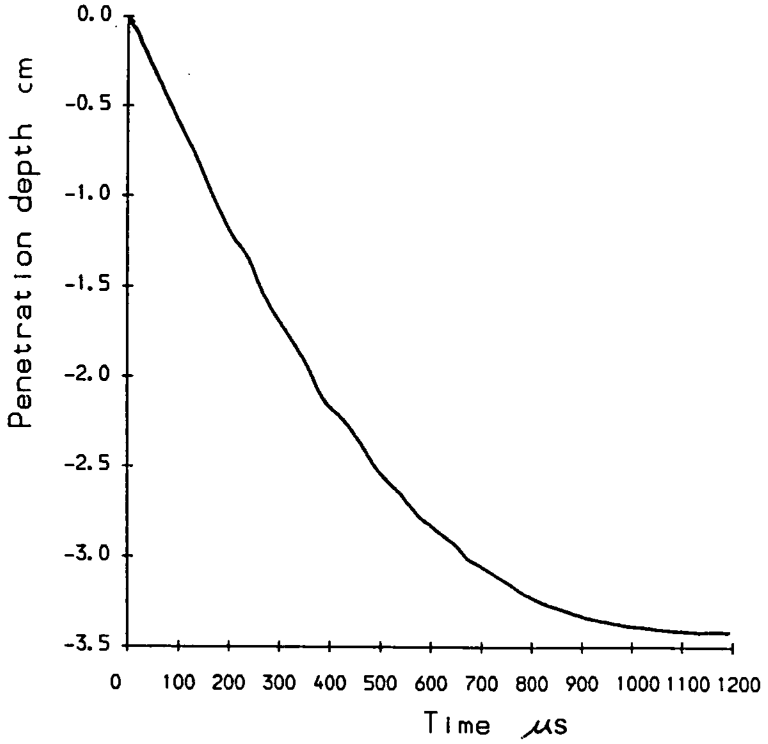

FIGURE 4.42 FASTENER PENETRATION HISTORY

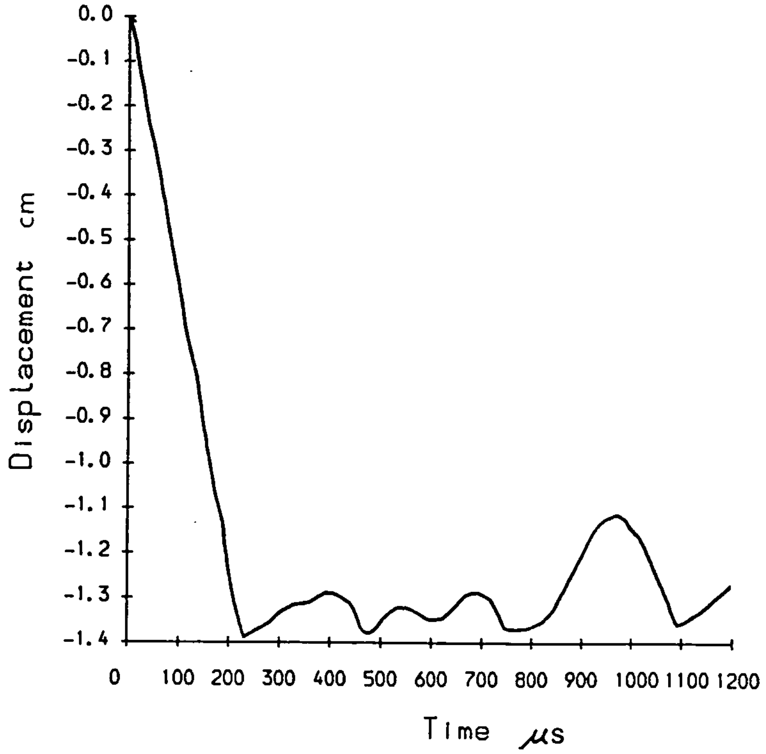

FIGURE 4.43 WASHER DISPLACEMENT HISTORY

the washer behaviour was actually negligible. This is explicitly seen in Figure 4.44 which also shows that the kinetic energy imparted to the target material constituted about 43 percent of the total initial kinetic energy.

In all the previous illustrations, only the responses for the individual materials in terms of various physical quantities have been examined. At present, the fastener-target interface behaviour is to be examined in Figures 4.45 to 4.47 which provide significant information about the fastener-target interaction. Figure 4.45 shows the history of the fastener-target interface force in the vertical direction. It is not surprising that its prediction has the same overall shape as that of the piston deceleration history and differs from the latter about a constant in magnitude. It is also observed in Figure 4.45 that after the peak resistance the curve shows severe oscillation. Figures 4.46a and b illustrate the axial interface force distribution in terms of three nodal points which were located at the tip, the turning region and the aft body of the projectile, respectively (see Figure 4.36). It is clearly seen that there was only a small portion of the axial resisting force distributed at the projectile tip and along the surface of the aft-body of the projectile. The largest portion of the axial resistance was distributed around the turning region of the projectile nose while the major shear stress was distributed on the tip of the projectile, as illustrated in Figure 4.47. It can be inferred that in moving along the projectile surface from the tip, the shear stress dies out.

For comparison with the experimental results, several calculations were performed with the initial impact velocity ranging from 49 m/s to 62 m/s, which corresponds to the power regulator setting on the cartridge tool of 1.5 to 2.5. The relation between the impact velocity and the penetration depth achieved is compared with the experimental curve in Figure 4.48. It is seen that the penetration depths predicted by computations are constantly greater than the

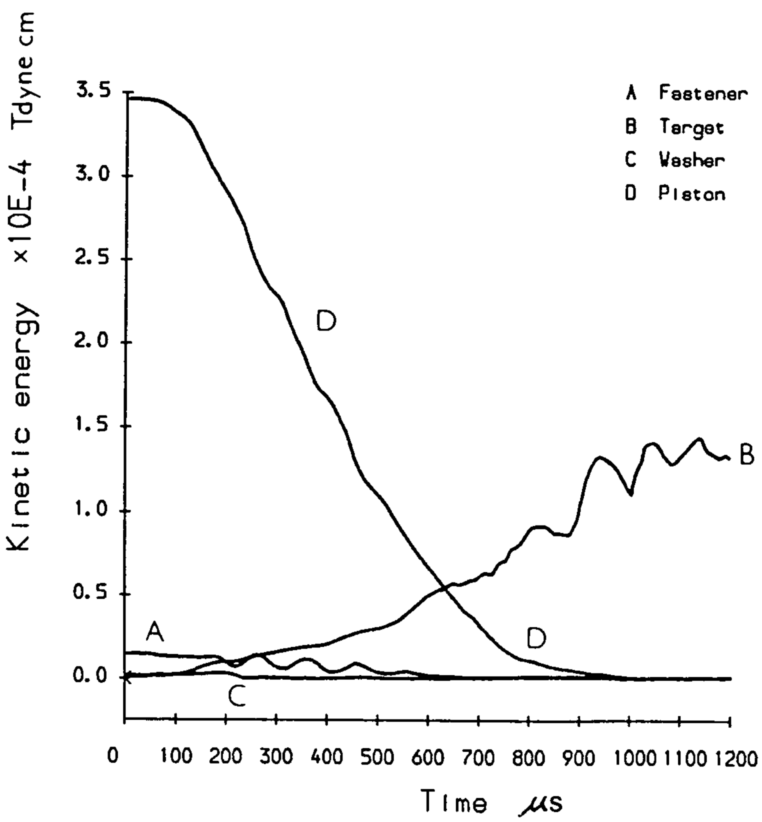

FIGURE 4.44 KINETIC ENERGY HISTORIES

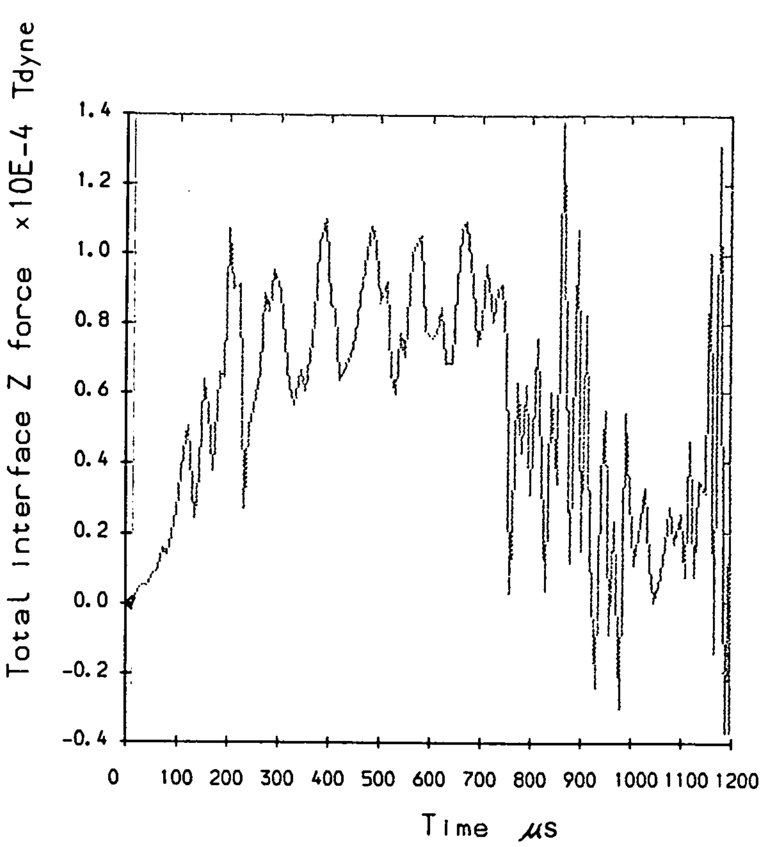

FIGURE 4.45 FASTENER-TARGET INTERFACE Z FORCE HISTORY

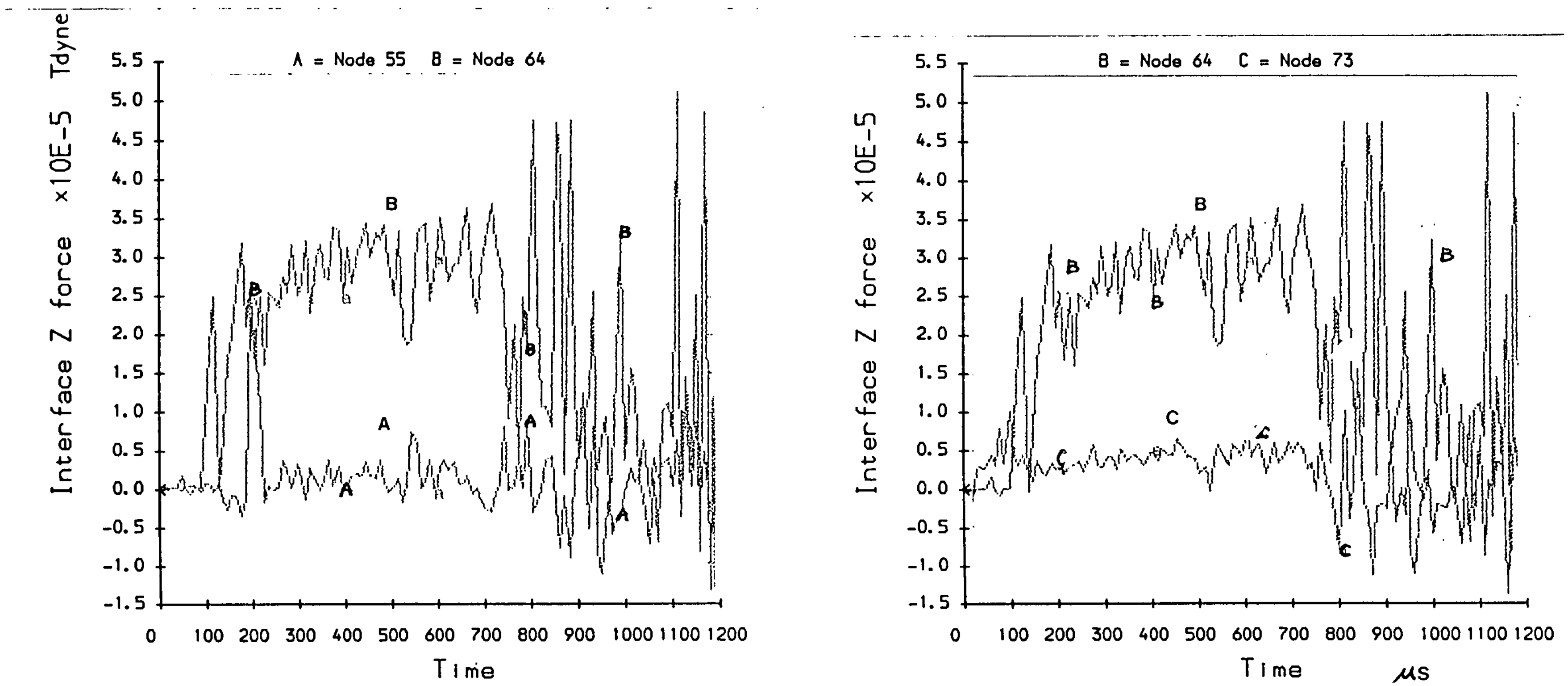

(a)

(b)

FIGURE 4.46a,b NODAL INTERFACE Z FORCE HISTORIES

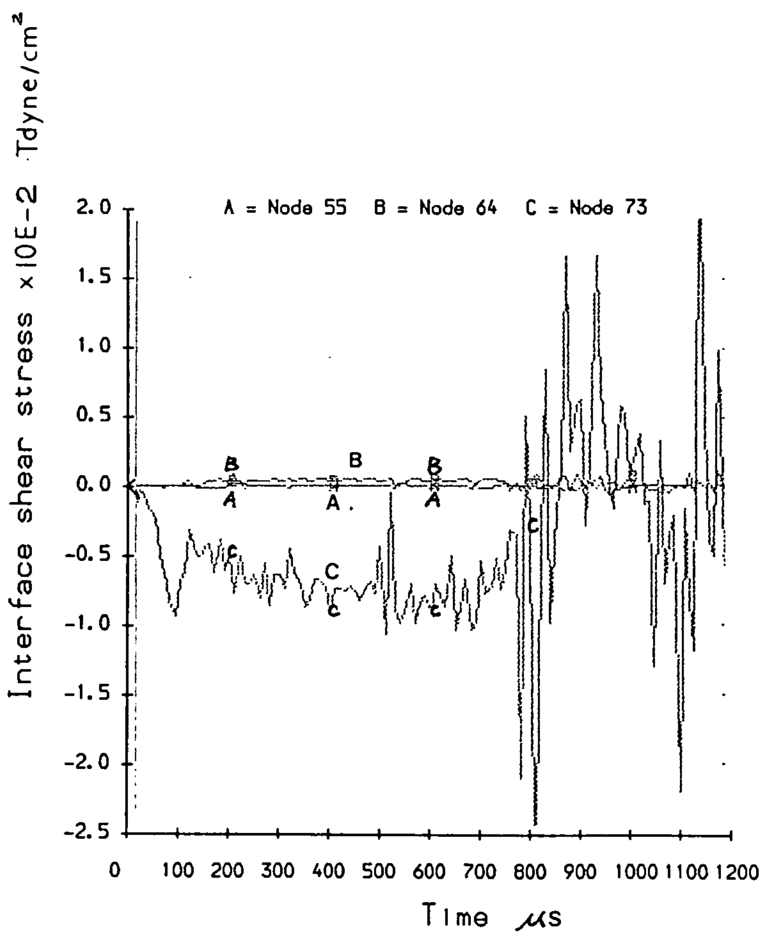

FIGURE 4.47 NODAL INTERFACE SHEAR STRESS HISTORIES

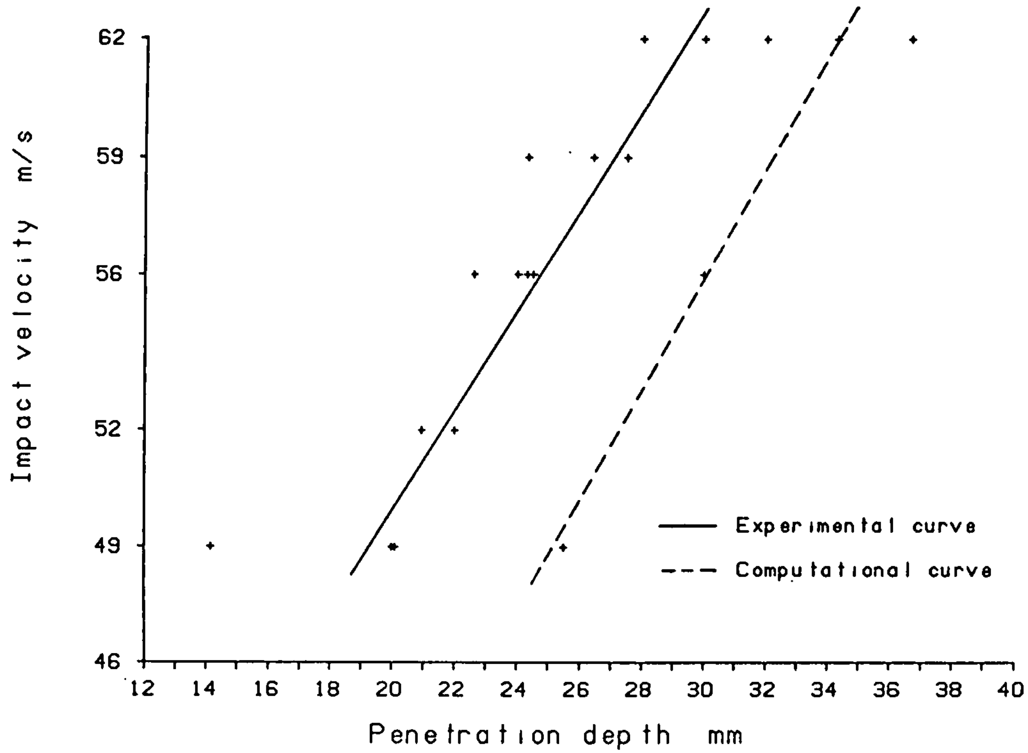

FIGURE 4.48 COMPARISON OF EXPERIMENTAL AND COMPUTATIONAL RESULTS

experiment values by about 20 percent.

In all the previous computations the steel strength was sufficient high so that the projectile and fastener were not deformed.

4.5 Simulation of Fastener Pull-out

The fastener penetration, resulting in the fastener coming to rest embedded in the target, was successfully simulated. The pull-out process, as described in Chapter 3, was attempted under similar conditions. Since the pull-out process is a quasi-static procedure, the time required to withdraw an embedded fastener from a target is of the order of a second. This makes it very difficult from both computational and economic points of view to use DYNA2D as a suitable program to carry out this work. Instead, an implicit finite element code, NIKE2D, was employed for this simulation. NIKE2D was developed by the same author as DYNA2D, and is also available in the public domain. This program is a fully-vectorized, finite-deformation, large strain, finite element code for analysing both the static and dynamic response of two-dimensional axisymmetric and plane strain solids. Full details about this program are contained in the user's manual (see Hallquist, 1983b).

The numerical procedure for performing the pull-out process was divided into two steps. To begin with, the projectile penetration was carried out using the dynamic analysis as previously described. With the projectile embedded in the target, the pull-out simulation was then performed by changing to a static analysis using the restart facility in which a loading condition can be redefined. Thus, the projectile penetration was modelled using the same computational model as DYNA2D. The results of the calculation are compared with those obtained using DYNA2D in Figures 4.49 to 4.53. It is seen that reasonably good agreement has been achieved.

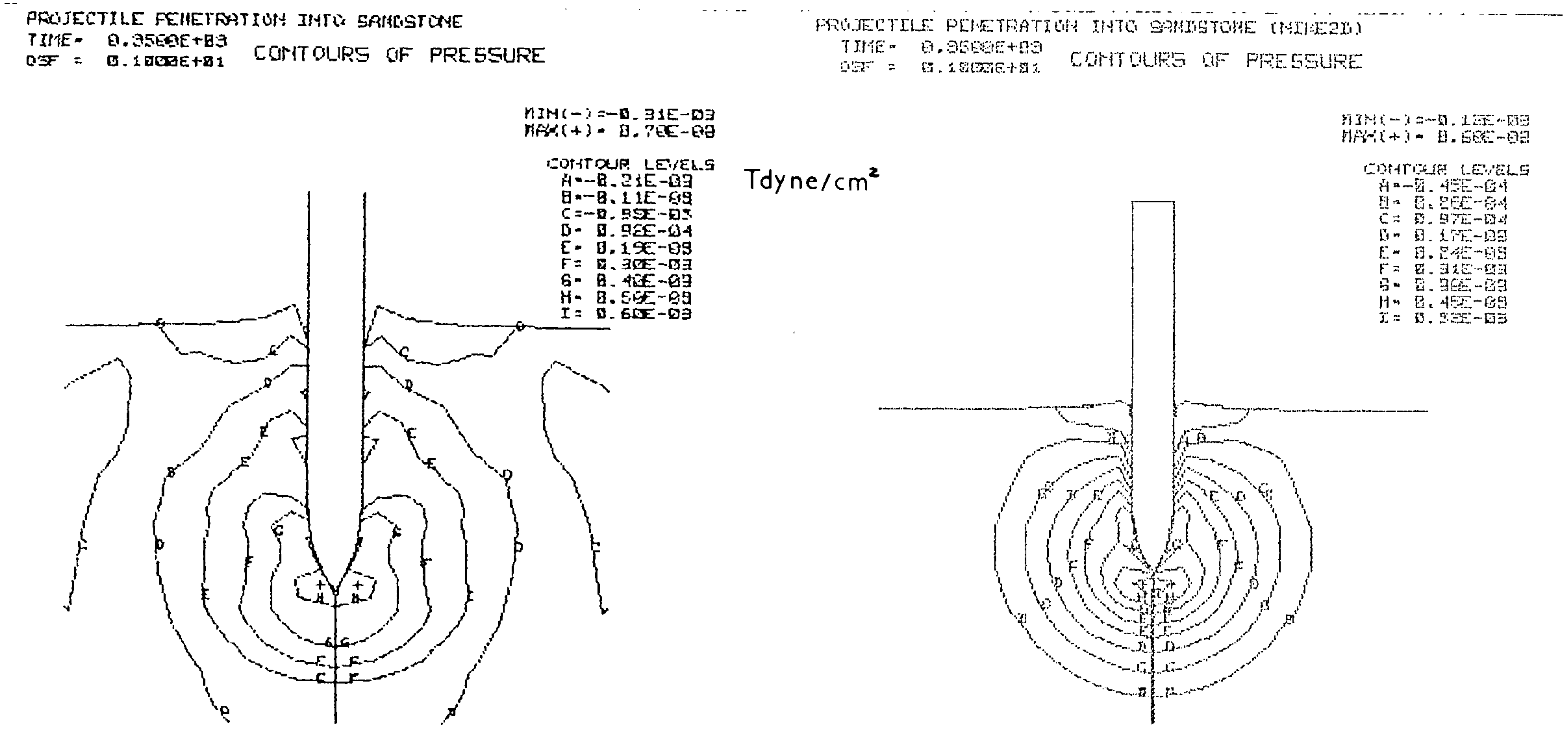

(a) (b)

Figure 4.49 Comparison of pressure contours (a) From DYNA2D (b) From NIKE2D

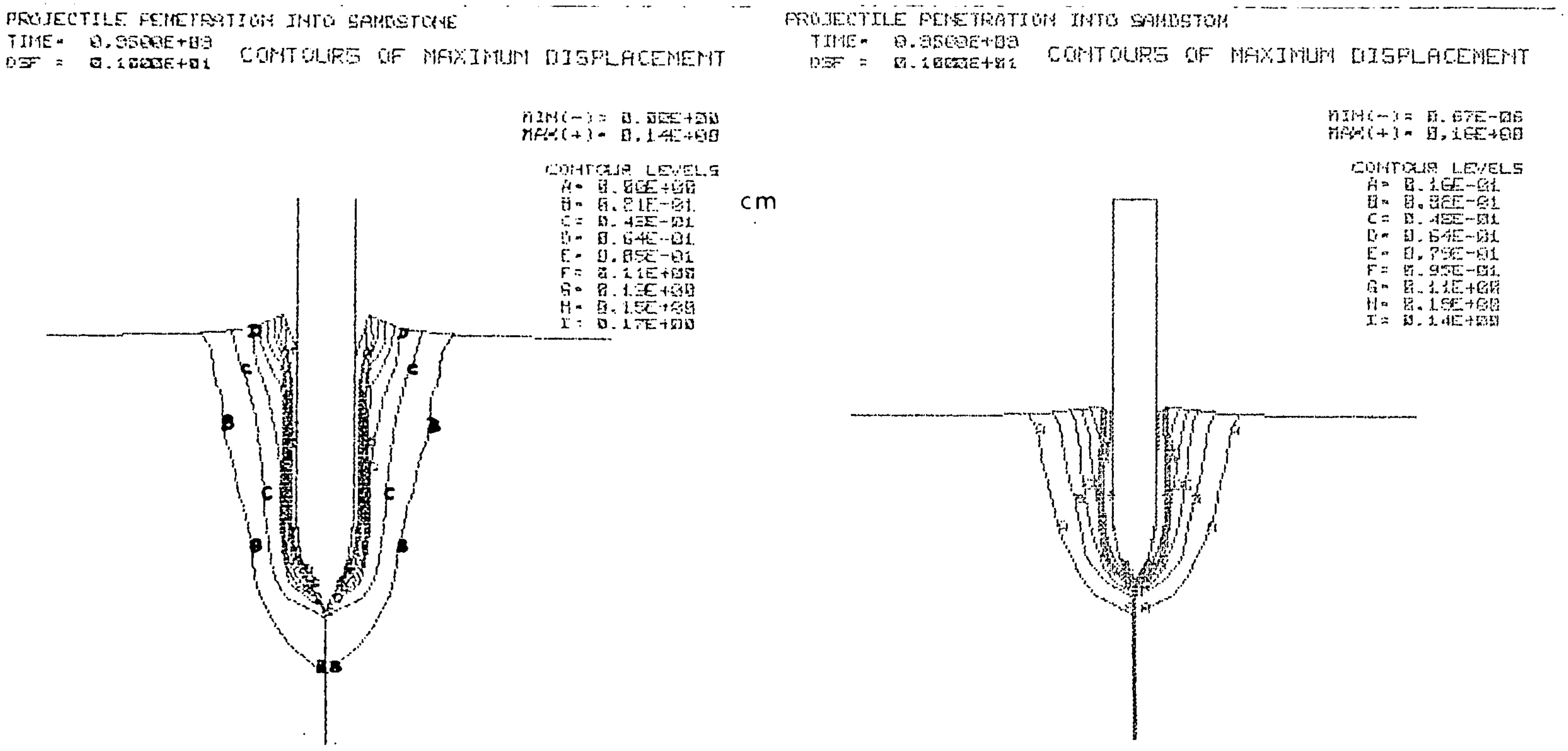

(a)

(b)

Figure 4.50 Comparison of displacement contours (a) From DYNA2D (b) From NIKE2D

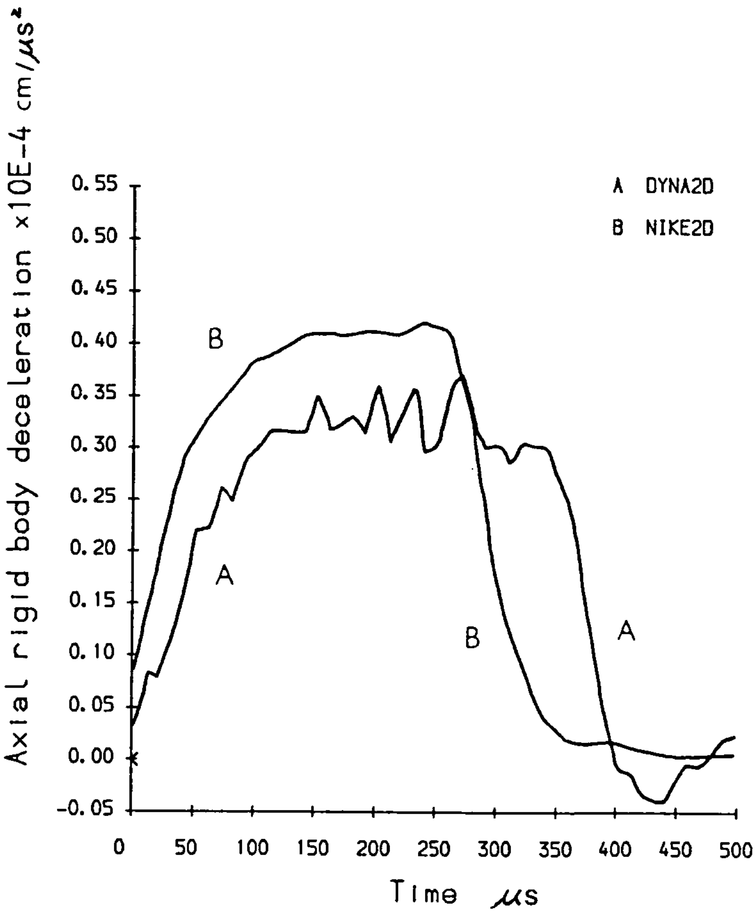

FIGURE 4.51 COMPARISON OF DECELERATION HISTORIES BETWEEN DYNA2D AND NIKE2D

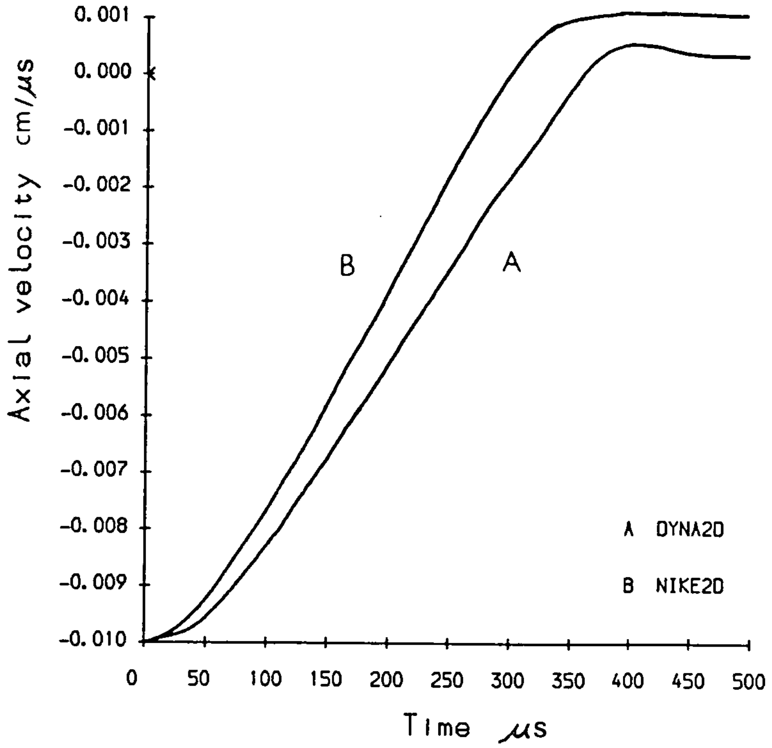

FIGURE 4.52 COMPARISON OF VELOCITY HISTORIES BETWEEN DYNA2D AND NIKE2D

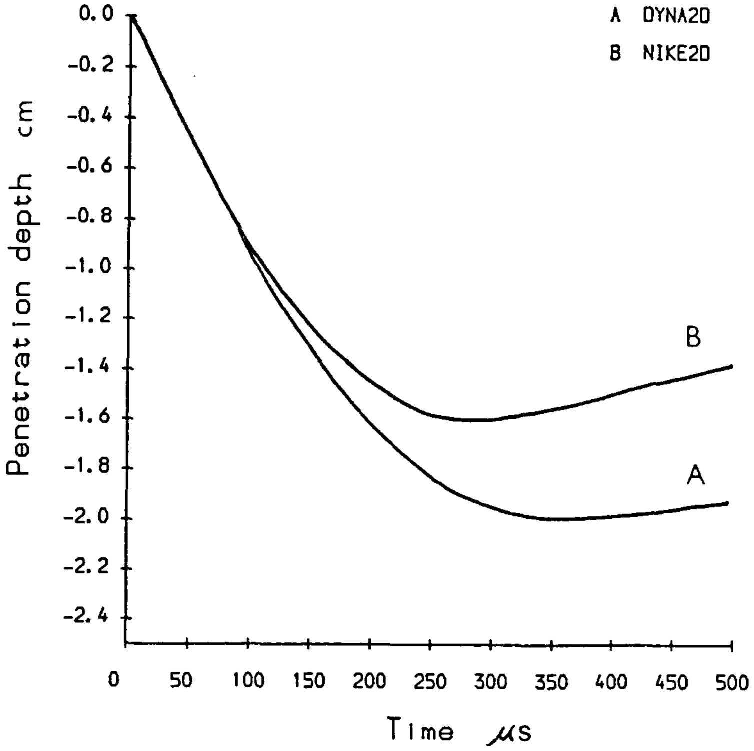

FIGURE 4.53 COMPARISON OF PENETRATION HISTORIES BETWEEN DYNA2D AND NIKE2D

It has been realized that, from the computational point of view, the projectile penetration and pull-out have to form one general process. This implies that a loading curve required to withdraw the projectile after penetration has to be specified in the initial input deck. Since only the initial impact velocity is required to initiate the projectile penetration, thus, the incorporation of the pull-out loading curve (either the displacement or the velocity histories) at this initial stage would interfere with the initial impact velocity to produce erroneous results for reasons which are not clear. Unfortunately, there seems no method of removing this particular hurdle at this time. Thus, no further attempts were made to solve this problem.

Chapter 5 DISCUSSION AND RECOMMENDATIONS

In the preceding chapters, the impact penetration of both projectile and fastener into construction materials such as soils, rocks and concrete, as well as the associated pull-out problem, have been investigated using experimental, analytical and numerical approaches. The efforts made throughout the thesis with respect to all of these three approaches have led to an improved understanding of the phenomena occuring at impact, during penetration and during pull-out, and have provided reasonably accurate predictions as a guide and an insight for further research on this subject. However, because of the complexity and variability of the problem, solutions are far from complete in the context of their relevance to all aspects of the problem. Therefore, the discussions and suggestions which are presented in this chapter aim to emphasize those areas in which further research, leading to improvement of results, can be made.

In Chapter 2, apart from the historical review of the empirical penetration formulae, the major attention has been focused on the development of the analytical penetration theory which is based on cylindrical cavity expansion for the class of locking materials. Because of the complex physical characteristics of the materials considered as well as in the interests of mathematical tractability, a number of the simplifications of the physical situation and of the mathematical manipulation were necessarily assumed. However, this theory is believed to provide a realistic account of the gross features of a non-deforming sharp-nosed cylindrical projectile penetrating porous, compressible locking materials. Its main predictions concern the axial resisting force exerted on the frontal surface of the projectile, the deceleration history, and the penetration depth. The major deficiencies are attributed to the neglect of the stresses on the aft body of the projectile (which is reasonably valid for the penetration of the hemispherical projectile), and to the neglect of the frictional effect which has been shown to be significant in Chapter 4, as well as to the assumption of the radial motion of the target material.

Since no experiments or measurements of projectile penetration other than fastener penetration were conducted, the input parameters required for the quantitative predictions of the theory cannot be evaluated. This deficiency clearly prevents any direct comparison of results from this theory with those of the numerical computations. However, as has been noted and discussed in Chapter 2, the solutions, such as Equations (2.34) and (2.41) have the same form as some of empirical formulae presented in Section 2.2 (for instance, Equations (2.7), (2.10b) and (2.13a)) apart from the incorporation of the nose shape effect in the coupled material constants. This compensation provides some encouragement for attempting comparisons between the analytical and numerical results. To this end, the modified Petry formula in Equation (2.10b) is chosen because it requires fewer material constants, and because it is a widely-used formula, especially in concrete design against projectile impact and penetration (Young, 1969; Sun, Burdette, and Barnett, 1976; Backman and Goldsmith, 1978; and Brown, 1986). Comparison is made with Figure 4.17 over the impact velocity range of 50 m/s to 250 m/s for the projectile having a mass of 3.1 g and a diameter of 4 mm. A constant k is involved, and k is dependent on the nature of the target material. Its variation is governed by many factors, among them, the density, hardness and the compressive strength. Generally, the harder the material is, the lower the value of k. Its range for various materials can be consulted from Table 2 of Sun, Burdette and Barnett (1976), and Backman and Goldsmith (1978) as well as from Table 1 of Brown (1986). For concrete, limestone and sandstone, this constant ranges from 0.0035 (reinforced concrete) to 0.008 (in ft^3/lb). The variation of this constant 0.004 – 0.007 is illustrated in Figure 5.1 in which the impact velocity is plotted against the penetration

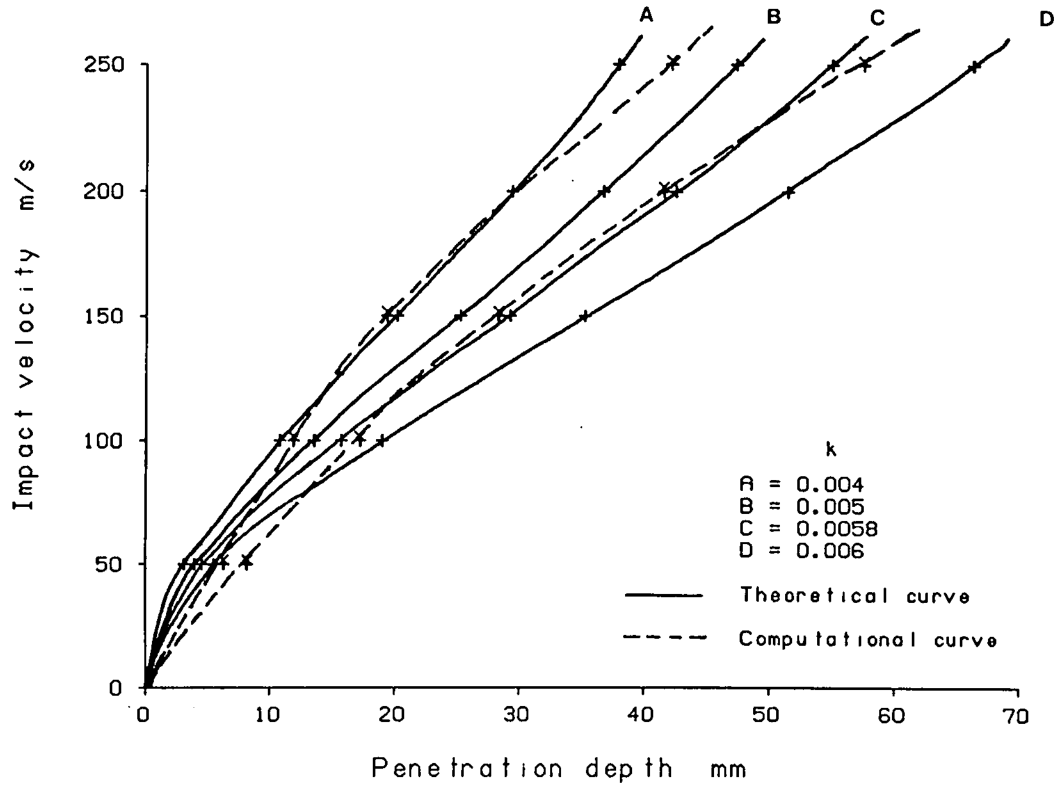

FIGURE 5.1 COMPARISON OF IMPACT VELOCITY-PENETRATION DEPTH RELATIONS

depth. Also plotted is the computational curve indicated by a dashed line. It is seen that none of them fit the computational curve very well throughout the velocity range. Nevertheless, the curve with a k value of 0.0058 appears to give the best correlation. The major disparity occurs at velocities below 100 m/s. Petry's formula seems to predict the existence of a critical velocity on reaching which the target resistance is considerably reduced. However, this feature is not as clearly evident on the computational curve.

As has been shown from the computational results of Chapter 4, in the fastener penetration, the washer does not exert significant resistance on the shank penetration because of the dominant inertia effect of the piston. Thus, the washer behaviour can be ignored without greatly affecting the gross features of the fastener shank penetration in this situation. The direct advantage of this assumption is to compare the results of the fastener penetration into the sandstone targets with both the computational curve and the modified predictions from the Petry formula. However, examination of the modified Petry formula reveals that the formula is independent of the nose shape of the projectile although it is well recognized that sharp noses encounter less resistance than blunt noses. This enables comparison of the results from the experimental, analytical and numerical approaches for the fastener penetration. The prediction, made from the modified Petry's formula with the material constant k of 0.0058 and plotted in Figure 4.48 is now presented in Figure 5.2 which shows an excellent correlation . This comparison, which is made possible under the assumptions discussed in the previous paragraph, is somewhat crude, and the good agreement may be regarded as fortuitous. However, the fact that the same value of this material constant fits both two curves provides hope that the form of this formula may be more general than at first anticipated. Thus, this chosen material constant, k, of 0.0058 may be taken as a rough estimate of the material constant of the

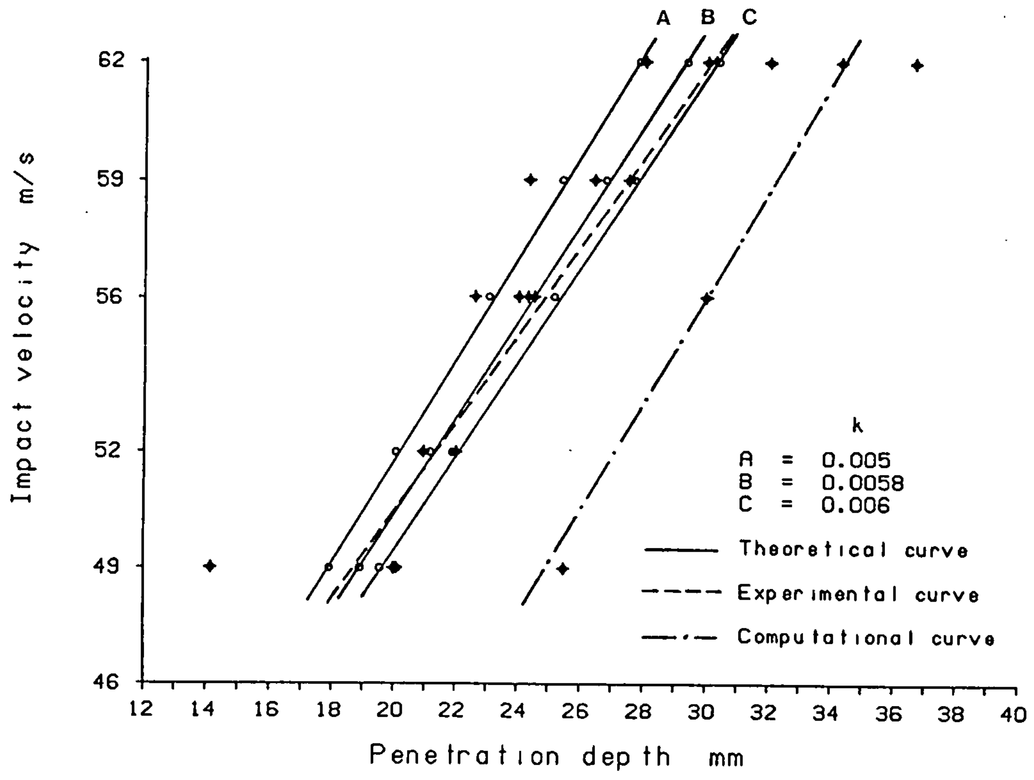

FIGURE 5.2 COMPARISON OF THEORETICAL, EXPERIMENTAL AND COMPUTATIONAL RESULTS

sandstone for this formula in the impact penetration considered.

It should be emphasized that although the experiments conducted in Chapter 3 are quite satisfactory, they are, however, rather simple, and have left quite a few facets requiring further experiments to be performed in order to obtain more information (comprehension and analysis) about the penetration and its associated pull-out phenomena. For instance, investigations can be conducted on the fastener shank penetrations using the fasteners with their washers being moved right to the thresholds of the threads before firing. Given a sufficient numbers of targets, this type of experiment, if performed, may quite easily indicate the actual effect of the washer retardation. Perhaps, the most tempting method to collect the dynamic information rather than pre- and post-impact measurements is to record the target response in terms of the radial and tangential strains using the strain gauge technique. All of these suggested experiments may provide vital information to improve on understanding of the impact penetration phenomena and to compare results with those obtained using other approaches.

It is found, by comparing it with the computed peak pressures which are achieved during the projectile penetrations, that the maximum pull-out force obtained at a constant rate of extraction is extremely low. This suggests that the initial kinetic energy of the fastener-piston combination is primarily dissipated in plastic deformation of the target, in the formation and propagation of cracks, and in the generation of heat. It is believed that the speed of the pull-out plays an important role in these pull-out tests, and may affect the pull-out force. Thus, the validity of the pull-out results that were obtained is restricted to and limited by the constant rate used during the tests. Further experiments are desirable to find out the differences of the pull-out forces required to withdraw the fasteners at the different rates from the targets in which their penetrations are achieved using the same initial kinetic energy (or impact velocity).

In order to understand and predict the damage or failure of the target material subjected to the impact loading,it is often necessary to examine the impacted target using a scanning electron microscope (SEM) and an optical microscope. Although there are some rather advanced high-speed cameras and related image forming devices still being developed which may provide a promising technique to record the impact phenomena directly, they are generally either expensive to use or utterly inaccessible. Thus, the technique used in this thesis for this aspect of the work relies completely on the post-impact examination of the target using microscopes. Efforts made to this end are presented in Section 3.4, in which the damage to the sandstone targets adjacent to the craters has been examined using the optical microscope at magnifications up to 52-times. Sufficient evidence of sandstone crushing, shearing and cracking has been found. Since only two target specimens were prepared, from each of which only a limited number of thin sections cut at the chosen directions could be obtained, the local and structural crackings associated with the damage caused by the impact penetration are only qualitatively examined. The results obtained have indeed improved the understanding to the impact penetration. However, these results are not sufficient to generate a description of the damage in terms of the microstructural quantities for the target examined, and are completely inadequate for establishing any reliable quantitative relation such as the cracking extent - the energy level of the impact loading, even on an empirical basis. To predict or quantify the target damage is even more difficult. The mathematical displines used for this purpose are from either continuum fracture mechanics pioneered by Griffith and Irwin, or a microstatistical internal-state variable approach both of which are somewhat complicated subjects beyond the scope of this thesis. For further information on this subject, a review article by Gilman (1968), two monographs by Lawn and Wilshaw (1975), and by Zukas et al (1982), respectively, may be consulted.

In Chapter 4, the numerical investigations have been carried out using computer programs, and two objectives have been achieved. These comprise the numerical analysis of the projectile penetration and the simulation of the fastener penetration. The majority of this work has been performed using the elastic plastic model to represent the target behaviour. The factors which most affect the penetration process of the projectile such as the impact velocity, the nose shape of projectile, target yield strength and the hardening modulus, as well as the projectile-target friction, have been investigated. Based on the experience gained in modelling the projectile penetration, the fastener penetration has been successfully simulated. Because of lack of the measured input parameters of the frictional coefficient and the hardening modulus, and also because of the static strengths of the target material used in this dynamic process, some variations from actual behaviour may have been introduced. However, a rough estimate of these parameters has provided reasonably accurate predictive calculations. The slightly deeper penetration obtained, as shown in Figure 5.2, may be attributed either to the lower Young's modulus (i.e. the static value) or to the smaller hardening modulus.

In the penetration experiments that were conducted, structural cracks are widely observed as long as the impact velocity is greater than 52 m/s (corresponding to the power regulator setting on the cartridge tool of 1.75). Although there is no information available about the fraction of the initial kinetic energy associated with the formation and propagation of cracks, these cracks clearly absorb a certain amount of the energy. This seems important for an accurate account of the gross features of the target behaviour modelled in the computation. However, the incorporation of such a material characteristic is beyond the capability of a two-dimensional computer code. This deficiency in the present computations undertaken in this thesis may well lead to the deeper penetration since the fraction of the energy which should be absorbed during cracking has to be transformed into the plastic target deformation. Another factor which was not accounted for in this axisymmetric computation was the potential rotation of the penetrator during penetration. Also, it is believed that the washer behaviour, although substantially insignificant, can be better described using a loading curve.

In the present numerical investigation the soil and crushable foam model has also been used. The yield - pressure relation is required for input, apart from the pressure - volumetric strain relation. Because of lack of sufficient experimental data leading to flexibility of the determination of the constants in the former relation throughout the stress range, the quadratic term is set to zero for simplicity. The computational results presented in Figure 4.10 show that the stress level achieved at the penetration condition considered is of the order of the uniaxial compressive strength of the target material. Thus a large departure from the parabolic fitting used in the calculation is not expected to take place. However, in the fastener penetration, the stress level is substantially higher than in the projectile penetration case. Since the maximum pressure in the pressure - volumetric strain relation obtained from the triaxial experiments is only 52 MPa, for the higher pressures which are achieved, no data are available. Therefore, this material model has not been used beyond the projectile penetration.

A final mention about penetration simulation should be made with respect to the assumption made throughout Chapter 4 concerning the small central hole introduced in the target. Ideally, it should be necessary to show that such a hole does not alter the states of either stress or particle velocity in the target. Unfortunately, because of the limitation of the computer resources, this assumption has not been justified in this thesis. However, it has been proved by Schwer, Rosinsky and Day (1988) in their work.

Finally, the pull-out of the embedded fastener has not been successfully simulated using the computer codes.

CHAPTER 6 CONCLUSIONS

The subject of impact penetration into soil, rocks and concrete has been investigated in this thesis. Because of the complexity and variability of this subject which involves various diverse fields, a rather general review has been provided to include the definitions of some phenomenological terms, classification of the impact process, and brief descriptions of some basic principles and related phenomena pertaining to impact and penetration in terms of stress wave propagations. Three analytical approaches have been adopted : theoretical, experimental, and numerical.

In the theoretical work, and in addition to an assembly of empirical penetration formulae, a non-deforming sharp-nosed projectile penetration theory has been developed on the basis of the existing cylindrical cavity expansion theory with the constitutive relations of the target materials idealized by compressible locking behaviour in a hydrostatic state and elastic-plastic, linear strain-hardening behaviour in shear. It is important to re-emphasize simplifying assumptions made in this theory such that (1) the stresses on the aft body of the projectile were neglected, (2) the frictional effect on the projectile-target interface was not taken into account, (3) the motions of the target materials were assumed to be only radial. Since no dedicated experiments were conducted for the determination of the material constants required for input, the predictions of this theory could not be quantified. It was thus not possible to compare this theory with either the experimental results or the numerical results. Despite these limitations, this theory does provide a correct assessment of the general features of the problem considered. It was found that

(1) The axial resisting force was proportional to the projectile radius and impact velocity. Ignorance of target inertia overestimated the resisting force and

underestimated the penetration depth.

(2) Not surprisingly, the penetration depth increased as the impact velocity increased. A denser or a longer projectile penetrated into a target more deeply. An increase in projectile diameter reduced penetration.

In the experimental approach, the penetration tests were conducted using a cartridge-operated tool firing steel fasteners into sandstone and concrete targets. Relationships between the power regulator setting (controlling impact velocity and initial kinetic energy) and the penetration depth were deduced from the measured results. The associated pull-out problem has also been studied. Pull-out tests were conducted to establish the relationships between impact velocity and the pull-out force recorded using an Instron universal testing machine at a constant rate of pull-out. Post-impact examinations of thin sections made from the impacted target specimens were performed. For the range of test conditions considered in the present investigation, the following conclusions may be drawn.

(1) The penetration depth was directly proportional to the impact velocity. A long shank length of fastener was desirable, but an increase of this length also increased the susceptibility to bending failure.

(2) With an originally-adopted pull-out technique, the expected debonding process in the sandstone target did not occur; rather the shear failure took place within the target along the conical plane. Values of the pull-out forces were low. With an improved technique the requisite debonding process did occur and the values of the pull-out forces noticeably increased.

(3) The pull-out force depended little on the penetration depth for the sandstone target, and was independent of the penetration depth for the concrete.

(4) The general damage observed in the sandstone targets covered two re-

gions : (i) a grain-pulverized region and (ii) a cracked region. The distinctive features of these two regions were that, in the former, quartz grains were pulverized, and were detached from the parent sandstone showing no clear preference for a cracking path, while, in the latter, the formation and propagation of cracks were greatly affected by the grain boundaries.

With the present availability of large computer programs such as DYNA2D and NIKE2D suite in the public domain, the fundamental case of projectile (normal) impact penetration, has been studied using both elastic-plastic, and soil and crushable foam models to represent the sandstone target behaviour. The key factors affecting the projectile penetration into the large target, factors such as the initial impact velocity, the nose shape, the projectile-target friction, the yield strength and the hardening modulus at low velocities, have been investigated. Based on the projectile penetration model, the fastener penetration with the piston propellant has been simulated. Computational results from both the projectile and the fastener penetrations have been compared with those obtained either empirically or experimentally, and reasonable agreements have been achieved. For the cases investigated under given impact conditions, it was found that

(1) The penetration depth increased parabolically with increase in the impact velocity. The projectile at low velocities rebounded after reaching the maximum depth of the penetration until the impact velocity was sufficient large.

(2) The frictional force alone, with the frictional coefficient up to 0.1, reduced the penetration depth by 20 % at an impact velocity of 100 m/s.

(3) The initial kinetic energy was primarily transformed into target deformation. Only 4 % of the energy imparted to the target material was associated with the particle motion.

(4) The yield strength had the most significant effect on the penetration compared with the perfectly-plastic model (I). Resistance was directly proportional to this strength parameter. Penetration duration and depth reduced by 150 μs and 40 percent, respectively. The target kinetic energy was increased by a factor of four.

(5) The hardening modulus had a significant effect on the penetration depth. With the value of 0.5 % of Young's modulus the penetration at the impact velocity of 100 m/s was reduced by 25 % compared with the perfectly-plastic case. However, this modulus appeared to have no effect on the penetration duration.

(6) The hemispherical-nosed projectile achieved a penetration depth only 60 % of that obtained with the ogival-nosed projectile (CRH = 2.5) at an impact velocity of 100 m/s. Separation of the projectile-target interface was observed along the aft-body of the hemispherical-nosed projectile, while this feature was absent for the penetration of the ogival-nosed projectile.

(7) The depth of the fastener penetration was constantly greater than indicated by the experimental results by 20 % over the impact velocity range.

(8) The projectile and fastener suffered no gross deformation, and behaved very much like rigid bodies.

The significant capability of the numerical computations is that they provide quantitative information on interior stress, strain and velocity states at any time and any location in system, and that various material properties and parameters can be varied easily, with their effects being noted and compared as presented. For the projectile and fastener penetrations at the low velocities considered, the dynamic stresses generated by the impact were of a similar order to the material strengths. Thus, the response of the target materials in computation was dominated by these material strengths. However, since there were no available dynamic experiments orientated to characterize the candidate materials in the impact penetration environments from which either stress-strain relation or simple strength parameters could be extracted, such a numerical analysis may not be relied upon entirely for quantitative results. If realistic constitutive relations or material properties are provided, then computer programs such as those used in this thesis can be an efficient tool for both developing an approximate method of analysis and supplementing experimental investigations.

The present status of this impact penetration problem is that more work (both experimental and numerical) is needed in order to verify the theory of projectile penetration, and to instill confidence in the outcomes by cross-correlating results from the different approaches.

In the future, it is hoped to continue exploring the penetration process of a fastener both experimentally and numerically. In the former approach, effort should be directly made to collect the dynamic data using a strain gauge technique, so that comparison with the computational results can be made. In the latter approach, study should be pursued to investigate the problem of target dilational effects inevitably associated with the penetration. An attempt should be made to investigate the effect of a central hole in the fastener so that possible controlled collapse mechanisms in the fastener can be assessed in order to reduce rock dilations. Finally, the numerical modelling of the pull-out process should certainly be pursued.

Appendix A DEVELOPMENT OF THE CAVITY EXPANSION THEORY

This appendix presents an exact solution of the dynamic expansion of a cylindrical cavity within the framework of the proposed theory. Major contributions to the development of the theory of cavity expansion were made by Bishop, Hill, and Mott (1945), Hopkins (1960), Goodier (1965), Hanagud and Ross (1971), and Norwood (1974). Bishop, Hill, and Mott proposed static solutions for the expansions of both spherical and cylindrical cavities produced by a indenting punch in a semi-infinite elastic-plastic, linear strain-hardening material, whereas Hopkins presented a dynamic solution for the expansion of a spherical cavity in elastic-perfectly plastic material. Goodier treated a similar problem, and attempted a solution in a semi-infinite, incompressible elastic plastic, linear strain-hardening material. Hanagud and Ross modified this theory to account for the material compressibility by means of an ideal locking approximation under hydrostatic stress. Norwood developed a corresponding analysis for the expansion of a cylindrical cavity under a state of plane strain. The present work developed thereinafter adopts a similar logic to that in the work of the above authors.

A.1 Problem Statement

Consider the sudden application of uniform hydrostatic time-dependent pressure (from projectile loading) to a semi-infinite, homogeneous and isotropic target using a cylindrical polar system of coordinates. A cavity of radius a_0 (≥ 0) is produced on the surface. Under this pressure, the material first experiences the elastic deformation. By additional increase of pressure the yield strength is reached at the expanding surface of the cavity and the cavity has been enlarged to radius $r(t)$ ($\geq a_0$). This process is regarded as an expansion of a cavity and can be imagined as one of a series of expansions which will follow. Thus, the projectile penetration is assumed to be formed by a series of cylindrical expansions initiated at the tip of a projectile nose. As the radius of the projectile is approached the cavity will not expand any further. Thereafter the material experiences plastic locking deformation in dilatation and plastic behaviour in shear. The material is then placed in an expanding state in which the cavity is surrounded by plastic and elastic zones. The physical phenomena so posed suggest that plasticity is confined to a region adjacent to the cavity. Accordingly it can be assumed that the structure of the motion is as follows. This structure is illustrated also in Figure 2.5.

Cavity	$0 < r \leq a(t)$
Plastic region	$a(t) \leq r \leq q(t)$
Elastic region	$q(t) \leq r \leq R(t)$
Undisturbed region	$R(t) < r$

Here, σ_r and σ_θ represent the normal stresses in the radial and tangential directions, σ_z in the vertical direction. Correspondingly, ϵ_r, ϵ_θ represent the strains in the radial and tangential directions. t represents the time coordinate measured from the instant of first application of pressure, r is distance measured from the centre of the cavity having an initial radius a_0. The solid is supposed initially at rest and free from stress. All physical quantities are assumed functions only of the independent variables r, t. Because of cylindrical symmetry

$$\sigma_{r\theta} = \sigma_{\theta z} = \sigma_{zr} = \epsilon_{r\theta} = \epsilon_{rz} = \epsilon_{\theta z} = 0, \quad \epsilon_z = 0$$

and

$$u_r = u_r(r,t), \quad \sigma_r = \sigma_r(r,t), \quad \sigma_\theta = \sigma_\theta(r,t), \quad \sigma_z = \sigma_z(r,t) \tag{A.1}$$

This implies a state of plane strain. Under these coordinates of cylindrical symmetry, the most important objective of this theory is to predict the extent of the disturbed region and the elastic-plastic boundary and the resulting stresses.

The governing equation of motion is*

$$\frac{\partial \sigma_r}{\partial r} + \frac{\sigma_r - \sigma_\theta}{r} = \rho \frac{Dv}{Dt}, \quad v = \frac{\partial u}{\partial t} \tag{A.2}$$

where ρ is the instantaneous density, subscripts 0, 1, 2 will be added to it in the following analysis corresponding to each appropriate region, e.g. ρ_1 for elastic region, v is the particle velocity and $\frac{Dv}{Dt}$ is the total or Eulerian derivative of the particle velocity with respect to time along the particle path :

$$\frac{Dv}{Dt} = \frac{\partial v}{\partial t} + v\frac{\partial v}{\partial r} \tag{A.3}$$

In general, the use of a superior dot, D/Dt, denotes differentiation following the motion of a material point, i.e. $D\mathrm{F}/Dt = \partial \mathrm{F}/\partial t + v(\partial \mathrm{F}/\partial r)$ for any given function F that is attributable to the motion of a material point (see Fung, 1965). Because of the large deformations in the material involved in the present problem, an Eulerian description of the motion is chosen to establish equations sufficient for the determination of the distributions of displacement, velocity, stress and density at all times **. In the following analysis, according to the structure of the motion the development of a solution is split into elastic and plastic regions in addition to the separate consideration for the elastic-plastic interface.

A.2 Elastic Region (I)

As shown in Figure 2.5, this region contains the locked-elastic material behind the advancing shock front $r = R(t)$ where r is the Eulerian radial coordinate. The elastic locking condition requires the material around the cavity to

---

* The subscript r on u will be omitted henceforth because u_r is only non-zero component of displacement.

** However, it should be noted that strictly speaking the use of the convention notation $\dot{\epsilon}_r$,$\dot{\epsilon}_\theta$ to denote strains rates could violate this definition, since these quantities are defined in their own specific way as will be seen in Equation (A.5).

obey the following expression for dilatation on the application of a hydrostatic pressure :

$$\epsilon = \epsilon_r + \epsilon_\theta = \epsilon_{el} \tag{A.4}$$

where ϵ_{el} is the elastic locking strain, and is assumed to be a material constant, $\epsilon_{el} = -\epsilon_1$. The kinetic relations are expressed in terms of the radial outward particle velocity $v(r,t)$. If the displacement undergone by a material point at radius r and t is u, then

$$\dot{\epsilon}_r = \frac{\partial v}{\partial r} = \frac{\partial \dot{u}}{\partial r}, \quad \dot{\epsilon}_\theta = \frac{v}{r} = \frac{\dot{u}}{r}, \quad v = \dot{u} \tag{A.5}$$

Differentiating Equation (A.4) and combining it with Equation (A.5) leads to

$$\dot{\epsilon}_r + \dot{\epsilon}_\theta = \frac{\partial v}{\partial r} + \frac{v}{r} = \frac{1}{r}\frac{\partial(rv)}{\partial r} = 0 \tag{A.6}$$

Integration of Equation (A.6) gives

$$v = \frac{f(t)}{r} \tag{A.7}$$

where f(t) is an unknown function of integration. Stresses and strains in the elastic region are related by Hooke's law as

$$\begin{aligned} \epsilon_r &= \frac{1}{E}[\sigma_r - \nu(\sigma_\theta + \sigma_z)] \\ \epsilon_\theta &= \frac{1}{E}[\sigma_\theta - \nu(\sigma_z + \sigma_r)] \end{aligned} \tag{A.8}$$

Then the stress-strain relationship in shear for an elastic material is obtained upon substitution of Equation (A.8a) and (A.8b) as

$$\sigma_\theta - \sigma_r = 2G(\epsilon_\theta - \epsilon_r) \tag{A.9}$$

It is previously stated that the material in this region is in a locked elastic state which implies that the material allows no further compressibility. Then, G is taken to be $E/3$. Using Equation (A.4) with $\epsilon_{el} = -\epsilon_1$ and $E/3$ in Equation (A.9) it immediately follows that

$$\sigma_\theta - \sigma_r = \frac{2}{3}E(2\epsilon_\theta + \epsilon_1) \tag{A.10}$$

Since the motion is purely radial, ϵ_θ may appropriately be evaluated for large deformations by following Hopkins (1960). This gives

$$\epsilon_\theta = \ln(\frac{r}{r_o}) \qquad (A.11)$$

where r_0 is the initial radial coordinate of a particle that has moved to position r behind the shock front $r = R(t)$ (because of the passage of shock wave). Combining Equations (A.2), (A.3), (A.7), (A.10) and (A.11) leads to

$$\frac{\partial \sigma_r}{\partial r} = \frac{2E}{3r}(2\ln\frac{r}{r_o} + \epsilon_1) + \rho_1(\frac{\dot{f}}{r} - \frac{f^2}{r^3}) \qquad (A.12)$$

Integration of Equation (A.12) results in

$$\sigma_r(r,t) = \sigma_r(q,t) + \rho_1 \dot{f} \ln\frac{r}{q} + \frac{1}{2}\rho_1 f^2(\frac{1}{r^2} - \frac{1}{q^2}) + \frac{2E}{3}\int_q^r (2\ln\frac{r}{r_o} + \epsilon_1)\frac{dr}{r} \qquad (A.13)$$

where q is the interface radius at time t between elastic and plastic regions, and $\sigma_r(q,t)$ is a function of integration which remains to be determined. Considering the jump condition for conservation of mass at $r = R(t)$ provides the condition

$$\rho_o(\dot{R} - v_o) = \rho_1(\dot{R} - v_1) \qquad (A.14)$$

where v_0, v_1 are the particle velocities in the stress free and elastic regions, respectively, and $v_0 = 0, v_1 = \frac{f(t)}{R}$. Thus, Equation (A.14) becomes

$$f(t) = \alpha_1 R\dot{R} \qquad (A.15a)$$

in which

$$\alpha_1 = 1 - \frac{\rho_o}{\rho_1} \qquad (A.15b)$$

where α_1 is the locking compressibility. Likewise, the conservation of momentum at $r = R(t)$ offers

$$\sigma_r(R,t) - \sigma_{r0}(R,t) = -\rho_1(\dot{R} - v_1)v_1 - \rho_0(\dot{R} - v_0)v_0 \qquad (A.16)$$

where σ_{r0} is the normal stress in the stress free region, is zero. Thus, Equation (A.16) becomes

$$\sigma_r(R,t) = -\rho_1(\dot{R} - v_1)v_1 = -\rho_1\frac{f}{R}(\dot{R} - \frac{f}{R}) \qquad (A.17)$$

Substituting Equation (A.15) into (A.17) gives

$$\sigma_r(R,t) = -\rho_o \alpha_1 \dot{R}^2 \tag{A.18}$$

However, in some zone adjacent to the elastic-plastic interface at $r = q(t)$ of elastic region, the elastic stresses are assumed to be in a state of incipient plasticity of the form

$$\sigma_\theta - \sigma_r = Y \tag{A.19}$$

Combining this condition with Equations (A.10) and (A.11) yields

$$\ln\frac{q}{q_0} = \frac{3Y}{4E} - \frac{\epsilon_1}{2} = \beta \tag{A.20}$$

where β is a material constant. Rearranging Equation (A.20) gives

$$q_0 = qe^{-\beta} \tag{A.21}$$

Applying conservation of mass in this region, $q(t) < r \leq R(t)$, offers

$$\rho_1(r^2 - q^2) = \rho_o(r_o^2 - q_o^2) \tag{A.22}$$

Combining Equation (A.22) with Equation (A.21) yields

$$(\frac{r_o}{r})^2 = \frac{\rho_1}{\rho_o}[1 - \frac{q^2}{r^2}(1 - e^{-2\beta})\frac{\rho_o}{\rho_1}] \tag{A.23}$$

It is apparent,as shown in Section 2.3, that the volumetric strain is function of material volume variation, and it is also apparent that $\rho V_v = 1$ for the mass conservation. Therefore,

$$d\epsilon = \frac{dV_v}{V_v} = -\frac{d\rho}{\rho}$$

which is integrated for initial and final values in elastic region to give

$$\epsilon_f - \epsilon_i = -\ln(\frac{\rho_f}{\rho_i}) \tag{A.24}$$

where $\epsilon_i = 0$, $\epsilon_f = -\epsilon_1$; $\rho_i = \rho_0$, $\rho_f = \rho_1$, respectively. Thus, Equation (A.24) becomes

$$\epsilon_1 = \ln(\frac{\rho_1}{\rho_o}) \tag{A.25}$$

A.3 Plastic region (II)

The procedure for analysis in this region is similar to that for the analysis given in the elastic region. The locking condition remains in the same form, that is

$$\epsilon_r + \epsilon_\theta = \epsilon_{pl} = -\epsilon_2 \tag{A.26}$$

where ϵ_{pl} is the plastic locking strain and equals a material constant, $-\epsilon_2$ as shown. However, a change will be made in the stress-strain relation as follows by starting from Equation (A.9). When yielding first occurs, the material behaviour is described by

$$\sigma_\theta - \sigma_r = Y = 2G(\epsilon_\theta - \epsilon_r) = 2G\epsilon_Y = \frac{2}{3}E\epsilon_Y \tag{A.27}$$

where ϵ_Y is the yield strain corresponding to the yield strength. By analogy with with Equation (A.9), the stress-strain relation in shear for the locked plastic material is expressed as

$$\sigma_\theta - \sigma_r = Y + \frac{2}{3}E_t(\epsilon_\theta - \epsilon_r - \epsilon_Y) \tag{A.28}$$

Substituting Equation (A.27) into (A.28) to eliminate ϵ_Y in conjunction with Equation (A.26) yields

$$\sigma_\theta - \sigma_r = \frac{2}{3}E_t(2\epsilon_\theta + \epsilon_2) + Y_1, \quad Y_1 = Y(1 - \frac{E_t}{E}) \tag{A.29}$$

The particle velocity is defined in this region as

$$v = \frac{g(t)}{r} \tag{A.30}$$

The equation of motion then becomes

$$\frac{\partial \sigma_r}{\partial r} = \frac{2E_t}{3r}(2\ln\frac{r}{r_o} + \epsilon_2) + \frac{Y_1}{r} + \frac{\rho_2}{r}(\dot{g} - \frac{g^2}{r^2}) \tag{A.31}$$

At the cavity surface, the applied pressure is supposedly prescribed, i.e.

$$\sigma_r = -p(t), \quad r = a, \quad t \geq 0 \tag{A.32}$$

Thus, integration of Equation (A.31) with the boundary condition of Equation (A.32) gives

$$\sigma_r(r,t) = -P(t) + Y_1 \ln\frac{r}{a} + \rho_2 \dot{g} \ln\frac{r}{s} + \frac{1}{2}\rho_2 g^2 (r^{-2} - s^{-2}) + \frac{2}{3}E_t \int_a^r (2\ln\frac{r}{r_o} + \epsilon_2)\frac{dr}{r} \tag{A.33}$$

The conservation of mass in this region provides

$$\rho_o(r_o^2 - a_o^2) = \rho_2(r^2 - a^2) \tag{A.34a}$$

If $a_o \doteq 0 < a$, this equation becomes

$$\rho_o r_o^2 = \rho_2(r^2 - a^2) \tag{A.34b}$$

Rearranging the above expression gives

$$(\frac{r}{r_o})^2 = \frac{\rho_o}{\rho_2}(\frac{r}{a})^2[(\frac{r}{a})^2 - 1]^{-1} \tag{A.35}$$

For the special case at $r = q$, Equation (A.34b) becomes

$$\rho_o q_o^2 = \rho_2(q^2 - a^2) \tag{A.36}$$

In conjunction with Equation (A.21), Equation (A.36) is expressed as

$$(\frac{q}{a})^2 = (1 - \frac{\rho_o}{\rho_2}e^{-2\beta})^{-1} \tag{A.37}$$

Now, the plastic locking strain is obtained using a similar process to that given by Equations (A.24), (A.25) in the elastic region. Integration must be accomplished in two separate ranges because of a discontinuity in density at the elastic-plastic interface.

$$\begin{aligned} \int_i^f d\epsilon &= \int_i^l d\epsilon + \int_l^f d\epsilon = \epsilon_f - \epsilon_i = -\epsilon_2 \\ = -\int_i^f \frac{d\rho}{\rho} &= -\int_i^l \frac{d\rho}{\rho} - \int_l^f \frac{d\rho}{\rho} = -\ln\frac{\rho_l}{\rho_i} - \ln\frac{\rho_f}{\rho_l} \\ &= -\ln\frac{\rho_f}{\rho_i} = -\ln\frac{\rho_2}{\rho_0} \end{aligned} \tag{A.38}$$

in where $\epsilon_i = 0, \ \rho_i = \rho_0, \ \rho_f = \rho_2$ are implied. That is

$$\epsilon_2 = \ln(\frac{\rho_2}{\rho_o}) \tag{A.39}$$

A.4 Elastic-plastic Interface

At the elastic-plastic interface, mass and linear momentum must be conserved. Mass conservation offers :

$$\rho_2(\dot{q} - v_2) = \rho_1(\dot{q} - v_1), \quad r = q \tag{A.40}$$

where $v_1 = f(t)/q, v_2 = g(t)/q$. Solving for g(t) yields

$$g(t) = \alpha_2 q\dot{q} + \frac{\rho_1}{\rho_2}f(t) \tag{A.41a}$$

where

$$\alpha_2 = 1 - \frac{\rho_1}{\rho_2} \tag{A.41b}$$

The momentum conservation at this interface provides

$$\sigma_{r2}(q,t) - \sigma_{r1}(q,t) = -\rho_2(\dot{q} - v_2)v_2 + \rho_1(\dot{q} - v_1)v_1 \quad \text{at} \quad r = q \tag{A.42}$$

where the second subscripts 1 and 2 on the stress quantities denote the elastic and plastic side of the interface. In conjunction with Equation (A.40), Equation (A.42) becomes

$$\sigma_{r2}(q,t) - \sigma_{r1}(q,t) = -\rho_1(\dot{q} - v_1)(v_2 - v_1) \tag{A.43}$$

Upon substitution of Equation (A.41) with $v_1 = f(t)/q, \quad v_2 = g(t)/q$, Equation (A.43) becomes

$$\sigma_{r2} - \sigma_{r1} = -\rho_1\alpha_2(\dot{q} - \frac{f}{q})^2 \tag{A.44}$$

Combining Equations (A.13) at $r = R$, (A.18) and (A.33) at $r = q$ with Equation (A.44) to solve p(t) yields

$$p(t) = \rho_1 \ln\frac{R}{q}\dot{f} + \frac{\rho_1 f^2}{2}(R^{-2} - q^{-2}) + \frac{2E}{3}\int_q^R (2\ln\frac{r}{r_o} + \epsilon_1)\frac{dr}{r} +$$

$$\rho_0\alpha_1\dot{R}^2 + Y_1\ln\frac{q}{a} + \rho_2\dot{g}\ln\frac{q}{a} + \frac{\rho_2 g^2}{2}(q^{-2} - a^{-2}) +$$

$$\frac{2}{3}E_t\int_a^q(2\ln\frac{r}{r_o} + \epsilon_2)\frac{dr}{r} + \rho_1\alpha_2(\dot{q} - \frac{f}{q})^2 \qquad (A.45)$$

In conjunction with Equations (A.15), (A.41) and their derivatives, Equation (A.45) becomes

$$p(t) = \rho_1\alpha_1\ln\frac{R}{q}(R\ddot{R} + \dot{R}^2) + \frac{1}{2}\rho_1{\alpha_1}^2R^2\dot{R}^2(R^{-2} - q^{-2}) +$$

$$\frac{2}{3}E\int_q^R(2\ln\frac{r}{r_0} + \epsilon_1)\frac{dr}{r} + \rho_0\alpha_1\dot{R}^2 + Y_1\ln\frac{q}{a} +$$

$$[\rho_2\alpha_2(\dot{q}^2 + q\ddot{q}) + \rho_1\alpha_1(\dot{R}^2 + R\ddot{R})]\ln\frac{q}{a} + \frac{1}{2q}(\rho_2\alpha_2 q\dot{q} + \rho_1\alpha_1 R\dot{R})^2(q^{-2} - a^{-2}) +$$

$$\frac{2}{3}E_t\int_a^q(2\ln\frac{r}{r_0} + \epsilon_2)\frac{dr}{r} + \rho_1\alpha_2(\dot{q} - \frac{\alpha_1 R\dot{R}}{q})^2 \qquad (A.46)$$

A.5 Approximate Solution

From Equation (A.46), the complexity of the exact solution for pressure acting on the cavity wall is apparent. In addition to two definite integrals that remain to be evaluated, there are also two boundary relations unknown, i.e. q/a and R/q. Therefore, in order to enable predictions to be made some simplifications of this expression have to be considered. First, if the leading shock front is relatively weak, then the cavity jump between the stress free state and the locked elastic state is supposedly very small. Thus, an approximation can be made as follows :

$$\rho_1 \doteq \rho_0 \qquad (A.47)$$

What follows immediately from Equations (A.15), (A.25) and (A.41) because of Equation (A.47) is

$$\alpha_1 \doteq 0, \quad f(t) \doteq 0 \qquad (A.48)$$

$$\epsilon_1 \doteq 0 \qquad (A.49)$$

$$\alpha_2 = 1 - \frac{\rho_o}{\rho_2}, \quad g(t) \doteq \alpha_2 q\dot{q} \qquad (A.50)$$

It should be noted that Young's modulus is usually far greater than the yield strength of a material, or $Y/E << 1$. In conjunction with Equation (A.49), Equation (A.20) becomes

$$\beta << 1 \qquad (A.51)$$

From Equation (A.23)it gives

$$\frac{r}{r_o} \doteq [1 - (1 - e^{-2\beta})(\frac{q}{r})^2]^{-\frac{1}{2}} \qquad (A.52)$$

Since $r > q$ and $1 - e^{-2\beta}$ is small, according to the binomial theorem, the above equation yields

$$\frac{r}{r_0} \doteq 1 + \frac{1 - e^{-2\beta}}{2}(\frac{q}{r})^2 \qquad (A.53)$$

so that

$$\ln\frac{r}{r_o} = \ln[1 + (1 - e^{-2\beta})(\frac{q}{r})^2] \qquad (A.54)$$

Using Taylor's series, Equation (A.54) can be further approximated to be

$$\ln\frac{r}{r_0} = \frac{1 - e^{-2\beta}}{2}(\frac{q}{r})^2 \qquad (A.55)$$

With these simplifications, the first integral, I_1 in Equation (A.45) becomes

$$I_1 = \frac{2}{3}E\int_q^R (2\ln\frac{r}{r_o} + \epsilon_1)\frac{dr}{r} \doteq \frac{2}{3}E\int_q^R (1 - e^{-2\beta})(\frac{q}{r})^2\frac{dr}{r}$$

which on integration gives

$$I_1 \doteq \frac{E}{3}(1 - e^{-2\beta})[1 - (\frac{q}{R})^2] \qquad (A.56)$$

Since the assumption so made results in Equations (A.47) and (A.49), it is implied that the radial distance may approach infinity, i.e. $R \rightarrow \infty$. Thus, Equation (A.56) becomes

$$I_1 \doteq \frac{E}{3}(1 - e^{-2\beta}) \qquad (A.57)$$

If now Equation (A.37) is reconsidered in conjunction with Equation (A.51), the following expression results

$$\frac{q}{a} \doteq \frac{1}{\sqrt{\alpha_2}}, \quad \dot{q} \doteq \frac{\dot{a}}{\sqrt{\alpha_2}} \qquad (A.58)$$

It is clear that at $r = a$, the particle velocity $v(a,t)$ at the cavity surface must be equal to the time rate of change of cavity radius a. That is, in conjunction with Equations (A.30), (A.50) and (A.58)

$$v(a,t) = \frac{g(t)}{a} = \frac{\alpha_2 q \dot{q}}{a} = \alpha_2 \dot{q}(\frac{q}{a}) = \dot{a} \qquad (A.59)$$

which shows the consistency in the approximations.

Next, consider the second integral, I_2 in Equation (A.45) and use Equations (A.35) and (A.39), then

$$\begin{aligned} I_2 &= \frac{2}{3}E_t \int_a^q (2\ln\frac{r}{r_0} + \epsilon_2)\frac{dr}{r} = \frac{2}{3}E_t \int_a^q \{\ln[\frac{\rho_0}{\rho_2}(\frac{r}{a})^2 \frac{1}{(\frac{r}{a})^2 - 1}] + \ln\frac{\rho_2}{\rho_0}\}\frac{dr}{r} \\ &= \frac{2}{3}E_t \int_a^q \ln[\frac{(\frac{r}{a})^2}{(\frac{r}{a})^2 - 1}]\frac{dr}{r} = \frac{2}{3}E_t \int_a^q 2\ln\frac{r}{a}\frac{dr}{r} - \frac{2}{3}E_t \int_a^q \ln[(\frac{r}{a} - 1)(\frac{r}{a} + 1)]\frac{dr}{r} \\ &= \frac{2}{3}E_t \ln^2(\frac{q}{a}) - \frac{2}{3}E_t \int_a^q \ln(1 + \frac{r}{a})\frac{dr}{r} - \frac{2}{3}E_t \int_a^q \ln(\frac{r}{a} - 1)\frac{dr}{r} \\ &= \frac{2}{3}E_t \ln^2(\frac{q}{a}) - \frac{2}{3}E_t I_3 - \frac{2}{3}E_t I_4 \end{aligned} \qquad (A.60)$$

The integrals I_3 and I_4 defined above can be separately evaluated as follows.

a). $I_3 = \int_a^q \ln(1 + \frac{r}{a})\frac{dr}{r}$

Now a transformation is necessary for the integration of I_3. Let $\ln\frac{r}{a} = \gamma$ then $r = ae^\gamma$, $dr = ae^\gamma d\gamma$, $\ln(1 + \frac{r}{a}) = \ln(1 + e^\gamma)$ and as $r \to a$, $\gamma \to 0$; $r \to q$, $\gamma \to \ln\frac{q}{a}$. Therefore

$$I_3 = \int_0^{\ln\frac{q}{a}} \ln(1 + e^\gamma)d\gamma = \int_0^{\ln\frac{q}{a}} \sum_{n=1}^{\infty}(-1)^{n-1}\frac{e^{n\gamma}}{n}d\gamma = \sum_{n=1}^{\infty}\frac{(-1)^{n-1}}{n^2}[(\frac{q}{a})^n - 1] \qquad (A.61)$$

b). $I_4 = \int_a^q \ln(\frac{r}{a} - 1)\frac{dr}{r}$

It must be noted that the integrand of this integral has infinite discontinuous points at $r = a$, i.e. $\lim_{r\to a}\ln(\frac{r}{a} - 1) = \infty$. Hence, I_4 is a so-called generalized integral and needs a special method of integration. Now take $\omega > 0$, if the limit $\lim_{\omega\to 0}\int_{a+\omega}^q \ln(\frac{r}{a} - 1)\frac{dr}{r}$ exists, then define

$$I_4 = \int_a^q \ln(\frac{r}{a} - 1)\frac{dr}{r} = \lim_{\omega\to 0}\int_{a+\omega}^q \ln(\frac{r}{a} - 1)\frac{dr}{r} \qquad (A.62)$$

Exercise a transformation similar to that above by defining $\frac{r}{a} - 1 = e^{\gamma}$ in Equation (A.62), then $r = a(e^{\gamma} + 1)$, $dr = ae^{\gamma}d\gamma$, $\ln(\frac{r}{a} - 1) = \gamma$ and $r \rightarrow a + \omega$, $\gamma \rightarrow \ln\frac{\omega}{a}$; $r \rightarrow q$, $\gamma \rightarrow \ln(\frac{q}{a} - 1)$. Thus, Equation (A.62) becomes

$$I_4 = \lim_{\omega \rightarrow 0} \int_{\ln\frac{\omega}{a}}^{\ln\frac{q}{a} - 1} \frac{\gamma e^{\gamma}}{(1 + e^{\gamma})} d\gamma$$

$$= \lim_{\omega \rightarrow 0} [\ln(\frac{q}{a} - 1)\ln\frac{q}{a} - \ln\frac{\omega}{a}\ln(1 + \frac{\omega}{a})] - \lim_{\omega \rightarrow 0} \int_{\ln\frac{\omega}{a}}^{\ln(\frac{q}{a} - 1)} \ln(1 + e^{\gamma}) d\gamma$$

$$= \ln(\frac{q}{a} - 1)\ln\frac{q}{a} - \sum_{n=1}^{\infty} \frac{(-1)^{n-1}}{n^2}(\frac{q}{a} - 1)^n - \lim_{\omega \rightarrow 0} \ln\frac{\omega}{a}\ln(1 + \frac{\omega}{a}) \qquad (A.63)$$

where $\lim_{\omega \rightarrow 0} \ln\frac{\omega}{a}\ln(1 + \frac{\omega}{a}) = I_5$ is a indeterminate limit which can be determined by using the L'Hospital rule as follows

$$I_5 = \lim_{\omega \rightarrow 0} \ln\frac{\omega}{a}\ln(1 + \frac{\omega}{a}) = 0 \qquad (A.64)$$

Combining Equations (A.61), (A.63) and (A.64), Equation (A.60) becomes

$$I_2 = -\frac{2}{3}E_t\ln(\frac{q}{a})\ln(1 - \frac{a}{q}) - \frac{2}{3}E_t \sum_{n=1}^{\infty} \frac{(-1)^{n-1}}{n^2}[(\frac{q}{a})^n - (\frac{q}{a} - 1)^n - 1] \qquad (A.65)$$

Finally, Equation (A.45) in conjunction with Equations (A.48), (A.50), (A.57), (A.58) and (A.65) becomes

$$p(t) = \frac{E}{3}(1 - e^{-2\beta}) - \frac{Y_1}{2}\ln\alpha_2 + \frac{E_t}{3}\ln\alpha_2\ln(1 - \sqrt{\alpha_2})$$

$$+\frac{\rho_0}{2}\dot{a}^2 - \frac{1}{2}\rho_2\ln\alpha_2(\dot{a}^2 + a\ddot{a}) - \frac{2}{3}E_t \sum_{n=1}^{\infty} \frac{(-1)^{n-1}}{n^2}[\alpha_2^{-\frac{n}{2}} - (\alpha_2^{-\frac{1}{2}} - 1)^n - 1] \qquad (A.66)$$

where β, Y_1 and α_2 are given by Equations (A.20), (A.29) and (A.50), respectively.

Appendix B NOTATION

$a, \dot{a}, \ddot{a}$	radial position, velocity and acceleration of cylindrical cavity surface, respectively.
a_0	initial cavity radius.
a_n	positive constants, $n = 0, 1, \cdot\cdot, n$
A	projectile cross-sectional area.
b, b_1	constants.
B	inertial coefficient for projectile nose in penetration theory.
c_e	elastic wave velocity.
c_p	plastic wave velocity.
c_s	shock wave velocity.
C	inertial coefficient function of penetration in penetration theory.
C_1, C_2	quasi-static and inertial coefficients for ogival projectile nose in penetration theory, respectively.
d	constant.
D	projectile diameter.
e	specific internal energy.
E	Young's modulus.
E_t	strain-hardening modulus.
$f(t)$	unknown integration function for elastic region in cavity expansion theory.
$f(\epsilon)$	quasi-static stress in rate-dependent uniaxial stress wave theory.
F	axial resisting force.
F_z	axial resisting force along the projectile axis of symmetry in penetration theory.
g	gravity acceleration.
$g(t)$	unknown integration function for plastic region in cavity expansion theory.

$g(\sigma, \epsilon)$	plastic strain rate function in rate-dependent uniaxial stress wave theory.
G	shear modulus.
I_n	determinate integration , $n = 1, \cdot\cdot, 5$.
j	variable used for transformation.
J	variable used for transformation.
k	constant
K	bulk modulus.
L	projectile nose length.
m	projectile mass.
M	effective projectile mass.
N	soil constant in Young's empirical equations.
$p(t)$	compressive normal stress on the projectile surface.
p_s, p_d	quasi-static component and dynamic component of $p(t)$.
P	pressure.
P_c	critical pressure.
q	radius of the elastic-plastic interface.
r	Eulerian radial coordinate.
r_0	initial position of the particle currently at radius r.
R	radius of the stress free-elastic interface.
s	radius of circular sector for ogival nose.
S	surface area of projectile nose.
t	time.
u	displacement.
u_r	radial displacement.
U	plastic work.
v	particle velocity.
v_0, v_1, v_2	particle velocities in stress free, elastic and plastic regions,

	respectively.
v_x	particle velocity in orthogonal coordinates.
V	impact velocity.
V_0	initial impact velocity.
V_v	specific volume.
V_z	instant impact velocity in penetration theory.
W	projectile weight.
x	longitudinal distance in orthogonal coordinates.
Y	yield strength.
Y_0	yield strength in elastic-perfectly plastic material.
Y_1	effective yield strength.
Z	instant penetration depth.
Z_c	critical penetration depth at critical velocity V_c.
Z_f	final penetration depth.
α_1, α_2	locking compressibility.
β	constant.
ϵ	total strain.
ϵ_0	constant strain.
ϵ_1, ϵ_2	constant strains in locked elastic and locked plastic regions, respectively.
$\epsilon_r, \epsilon_\theta$	strains in radial and tangential directions, respectively.
ϵ_x, ϵ_y	strains in orthogonal coordinates.
ϵ_c	critical strain.
ϵ_l	locking strain.
$\epsilon_{el}, \epsilon_{pl}$	elastic and plastic locking strains, respectively.
ϵ_Y	yield strain corresponding to σ_Y.
ϵ_z	strain in the vertical direction.
θ	ogival half-nose angle.

π	3.14159.
ρ	instant density.
ρ_0, ρ_1, ρ_2	densities in stress free, elastic and plastic regions, respectively.
ρ_c	critical density.
ρ_l	locking density.
ρ_{el}, ρ_{pl}	elastic and plastic locking densities, respectively.
σ	stress.
σ_r, σ_θ	stresses in radial and tangential directions, respectively.
σ_x, σ_y	stresses in orthogonal coordinates.
σ_z	normal stress in the vertical direction.
ν	Poisson's ratio.
ϕ	conical half-nose angle.
ψ	nose shape factor in Young's empirical equations.
ω	transformation variable.

REFERENCE

— (1955), *Proc. 1st Hypervelocity and Impact Effects Symp.* , Santa Monica, California.

— (1957), *Proc. 2nd Hypervelocity and Impact Effects Symp.* , Washington, D.C.

— (1959), *Proc. 3rd Symp. on Hypervelocity Impact* , Chicago, Illinois.

— (1960), *Proc. 4th Symp. on Hypervelocity Impact* , Eglin AFB, Florida.

— (1961), *Proc. 5th Symp. on Hypervelocity Impact* , Denver, Colorado.

— (1963), *Proc. 6th Symp. on Hypervelocity Impact* , Cleveland, Ohio.

— (1965), *Proc. 7th Symp. on Hypervelocity Impact* , Tampa, Florida.

— (1969), *Proc. AIAA Hypervelocity Impact Conference* , Cincinnati, Ohio.

— (1983), *Hilti DX450 Tool Operating Instructions* . Publication No. W 1066 483 10-e 1.

— (1966), *Specification for Cartridge-operated Fixing Tools* (British Standard 4078:1966).

Achenbach, J.D. (1973), *Wave propagation in elastic solids* , North Holland, Amsterdam.

Allen, W.A., Mayfield, E.B., and Morrison, H.L. (1957a), *Dynamics of a projectile penetrating sand* , J. Appl. Phys., **28(3)**, 370-376.

Allen, W.A., Mayfield, E.B., and Morrison, H.L. (1957b), *Dynamics of a projectile penetrating sand. Part II* , J. Appl. Phys., **28(11)**, 1331-1335.

Backman, M.E., and Goldsmith, W. (1978), *The mechanics of penetration of projectiles into targets* , Int. J. Eng. Sci., **16(1)**, 1-99.

Bancroft, D. (1941), *The velocity of longitudinal waves in cylindrical bars* , Physical Review, **59**, 588-598.

Bell, J.F. (1951), *Propagation of plastic waves in pre-stressed bars* , Tech. Rep. No.5, Johns Hopkins University, Baltimore.

Benson, D.J., and Hallquist, J.O. (1986), *A simple rigid body algorithm for structural dynamics programs* , Int. J. Num. Meth. Eng., **22**, 723-749.

Bernard, R.S., and Hanagud, S.V. (1975), *Development of a projectile penetration theory , Report 1* , US Army Engineer Waterways Experiment Station, Vicksburg, Mississippi, U.S.A..

Bernard, R.S. (1976), *Development of a projectile penetration theory, Report 2* , US Army Engineer Waterways Experiment Station, Vicksburg, Mississippi, U.S.A..

Bertholf, L.D. (1967), *Numerical solution for two-dimensional elastic wave propagation in finite bars* , J. Appl. Mech., **34(Series E)** 725-734.

Birkhoff, G., MacDougall, D.P., Pugh, E.M., and Taylor, G.I. (1948), *Explosives with lined cavities* , J. Appl. Phys., **19**, 563.

Bishop, R.F., Hill, R., and Mott, N.F. (1945), *The theory of indentation and hardness tests* , Proc. Phys. Soci. London, **57**, 147-159.

Brown, S.J. (1986), *Energy release protection for pressurized systems. Part II. Review of studies into impact/terminal ballistics* , Appl. Mech. Rev., **39(2)**, 177-201.

Burke, J., and Weiss, V. (editors) (1971), *Shock waves and mechanical properties of solids* , Proc. 17th Army materials research conference, Syracuse University Press.

Butler, D.K. (1975), *An analytical study of projectile penetration into rock* , Technical Report S-75-7, U.S. Army Engineer Waterways Experiment Station, Vicksburg, Miss., U.S.A..

Byers, R.K., Yarrington, P., and Chabai, A.J. (1978), *Dynamic penetration* *of soil media by slender projectiles* , Int. J. Eng. Sci., **16(11)**, 835-844.

Campbell, J.D. (1973), *Dynamic plasticity : macroscopic and microscopic aspects* , Mater. Sci. Eng., **12**, 3-21.

Chadwick, P. (1959), *The quasi-static expansion of a spherical cavity in metals and ideal soils* , Quart. J. Mech. Appl. Math., **12(1)**, 52-71.

Chandra, J., and Flaherty, J.E. (editors) (1983), *Computational aspects of penetration mechanics* , Vol. 3, Lecture Notes in Engineering (C.A. Brebbia, and S.A. Orzag, eds.), Springer-Verlag, Berlin.

Chisholm, P.B., Peleze, R.M., and Pugh, F.L. (1962), *An earth trajectory model for subsurface ballistic and thrusted vehicles* , TDR AFSWC-TDR-62-106, Air Force Special Weapons Centre, Kirtland Air Force Base, Albuquerque, New Mexico, U.S.A.

Chou, P.C., and Hopkins, A.R. (editors) (1972), *Dynamic response of materials to intense impulsive loading* , Air Force Materials Laboratory, Wright-Patterson Air Force Base, Ohio, USA.

Chree, C. (1889), *The equations of an isotropic elastic solid in polar and cylindrical coordinates, their solution and application* , Trans. Cambridge Phil. Soci., **14**, 251-369.

Conway, H.D., and Jakubowski, M. (1969), *Axial impact of short cylindrical bars* , J. Appl. Mech., **36**, 809-813.

Cristescu, N. (1967), *Dynamic plasticity* , North Holland, Amsterdam.

Cristescu, N. (1968), *Dynamic plasticity* , Appl. Mech. Rev., **21(7)**, 659-668.

Cristescu, N. (1972), *A procedure for determining the constitutive equations for materials exhibiting both time-dependent and time-independent plasticity* , Int. J. Solids Struct., **8**, 511-531.

Davies, R.M. (1948), *A critical study of the Hopkinson pressure bar* , Trans.

Royal Phil. Society. London, Series A, **240**, 375-475.

Davison, L., and Graham, R.A. (1979), *Shock compression of solids* , Phys. Reports, **55(4)**, 255-379.

Donnell, L.H. (1930), *Longitudinal wave transmission and impact* , Trans. ASME, **52**, 153-167.

Doran, D.G., and Lindre, R.K. (1966) *Shock effects in solids* , Solid State Phys., **19**, 229-290.

Dremin, A.N., and Adadurov, G.A. (1964), *The behaviour of glass under dynamic loading* , Soviet Phys.-Solid State, **6**, 1379.

Duvall, G.E. (1962), *Shock waves in the study of solids* , Appl. Mech. Rev., **15(11)**, 849-854.

Duwez, P.E., and Clark, D.S. (1947), *An experimental study of the propagation of plastic deformation under conditions of longitudinal impact* , Proc. ASME, **47**, 502-532.

Forrestal, M.J., Longcope, D.B., and Norwood, F.R. (1981), *A model to estimate forces on conical penetrators into dry porous rock* . J. Appl. Mech., **48**, 25-29.

Forrestal, M.J., Norwood, F.R., and Longcope, D.B. (1981), *Penetration into targets described by locked hydrostats and shear strength* , Int. J. Solids Structures **17**, 915-924.

Fowles, G.R. (1961), *Shock wave compression of hardened and annealed 2024 aluminum* , J. Appl. Phys., **32(8)**, 1475-1487.

Fuchs, O.P. (1963), *Impact phenomena* , J. Amer. Inst. Aeronautics Astronautics (or J. AIAA), **1(9)**, 2124-2126.

Gilman, J.J. (1968), *Dislocation dynamics and the response of materials to impact* , Appl. Mech. Rev., **21(8)**, 767-783.

Goldsmith, W. (1960), *Impact* , Arnold, London.

Goldsmith, W. (1963), *Impact: the collision of solids* , Appl. Mech. Rev., **16(11)**, 855-866.

Goodier, J.N. (1965), *On the mechanics of indentation and cratering in solid targets of strain-hardening metal by impact of hard and soft spheres* , Proc. 7th Symp. Hypervelocity Impact, **3**, J. AIAA, New York, 215-259.

Grimminger, G. (1948), *Probability that a meteorite will hit or penetrate a body situated in the vicinity of the earth* , J. Appl. Phys., **19**, 947.

Hallquist, J.O. (1983a), *MAZE - An input generator for DYNA2D and NIKE2D* , University of California, Lawrence Livermore National Laboratory, Rept. UCID-19029, Rev. 2, USA.

Hallquist, J.O. (1983b), *NIKE2D - A vectorized, implicit, finite deformation, finite element code for analysing the static and dynamic response of 2-D solids* , University of California, Lawrence Livermore National Laboratory, Rept. UCID-19677, USA.

Hallquist, J.O. (1984), *User's manual for DYNA2D - An explicit two-dimensional hydrodynamic finite element code with interactive rezoning* , University of California, Lawrence Livermore National Laboratory, Rept. UCID-18756, Rev. 2, USA.

Hallquist, J.O. (1985), *ORION - An interactive colour post-processsor for two-dimensional finite element codes* , University of California, Lawrence Livermore National Laboratory, Rept. UCID-19310, Rev. 2, USA.

Hanagud, S., and Ross, B. (1971), *Large deformation, deep penetration theory for a compressible strain-hardening target material* , J. AIAA, **9(5)**, 905-911.

Hopkins, H.G. (1960), *Dynamics expansion of spherical cavities in metals,* Progress in Solid Mechanics, **1**, R. Hill and I.N. Sneddon, eds., Pergamon Press, 84-164.

Hopkins, H.G. (1961), *Dynamic anelastic deformation of metals* , Appl.

Mech. Rev., **14(6)**, 417-431.

Johnson, G.R. (1977), *High velocity impact calculations in three dimensions* , J. Appl. Mech., **44**, 95-100.

Johnson, G.R. (1979a), *Three-dimensional computer code for dynamic response of solids to intensive impulsive loads* , Int. J. Num. Meth. Eng., **14**, 1865-1871.

Johnson, G.R. (1979b), *Dynamic response of axisymmetric solids subjected to impact and spin* , J. AIAA, **17(9)**, 975-979.

Johnson, G.R. (1986), *Dynamic Lagrangian computations for solids, with variable nodal connectivity for severe distortions* , Int. J. Num. Meth. Eng., **23**, 509-522.

Johnson, K.L.(1985), *Contact mechanics* , Cambridge University Press, Cambridge.

Johnson, W. (1972), *Impact strength of materials* , Arnold, London.

Jonas, G.H., and Zukas, J.A. (1978), *Mechanics of penetration : analysis and experiment* , Int. J. Eng. Sci., **16**, 879-903.

Jones, O.E., and Norwood, F.R. (1967), *Axially symmetric cross-sectional strain and stress distribution in suddenly loaded cylindrical elastic bars* , J. Appl. Mech., **34**, 718-724.

Karman, T.von, and Duwez, P.E. (1950), *On the propagation of plastic deformation in solids* , J. Appl. Phys., **21**, 987-994.

Kinslow, R. (editor) (1970), *High velocity impact phenomena* , Tennessee Technological University, Academic Press, New York.

Kolsky, H. (1953), *Stress waves in solids* , Clarendon Press, Oxford.

Lawn, B.R., and Wilshaw, T.R. (1975), *Fracture of brittle solids* , Cambridge University Press, Cambridge.

Lee, E.H. (1952), *A boundary value problem in the theory of plastic wave* *propagation* , Quart. J. Appl. Math., **10**, 335-346.

Lee, E.H., and Liu, D.T. (1967), *Finite strain elastic-plastic theory particularly for plane wave analysis*, J. Appl. Phys., **38(1)**, 19-27.

Longcope, D.B., and Forrestal, M.J. (1983), *Penetration of targets described by a Mohr-Coulomb failure criterion with a tension cutoff* , J. Appl. Mech., **50**, 327-333.

Longcope, D.B., and Grady, D.E. (1978), *Initial response of a rock penetrator* , J. Appl. Mech., **45**, 559-564.

Lubliner, J. (1964), *A generalized theory of strain-rate-dependent plastic wave propagation in bars* , J. Mech. Phys. Solids, **12**, 59-65.

Ludwik, P. (1909), *Uber den Einfluss der deformationsgeschwindigkeit bei bleibenden defo mationen mit besonderer beruecksichtigung der nachwirkung serchcinungen*, Phys. Zeitschrift, **10**, 411-417.

Malvern, L.E. (1951a), *The propagation of longitudinal waves of plastic deformation in a bar of material exhibiting a strain-rate effect* , J. Appl. Mech., **18**, 203-208.

Malvern, L.E. (1951b), *Plastic wave propagation in a bar of material exhibiting a strain-rate effect* , Quart. J. Appl. Math., **8**, 405-411.

Miklowitz, J. (1960), *Recent developments in elastic wave propagation* , Appl. Mech. Rev., **13(12)**, 865-878.

Misey, J.J. (1977), *Analysis of long rod penetration at hypervelocity impact* , J. AIAA, **15(12)**, 1696-1698.

Morland, L.W. (1959), *The propagation of plane irrotational waves through an elastoplastic medium* , Phil. Trans. Roy. Soc. London, **A251**, 341-383.

Murff, J.D., and Coyle, H.M. (1973), *Prediction method for projectile penetration* , J. Soil Mech. Foundations Div.. ASCE, **99(SM11)**, 1033-1037.

Nicholas, T. (1982), *Elastic-plastic stress waves* , in *Impact dynamics* , 4th chapter, Zukas et al (Ed.).

Norwood, F.R. (1974), *Cylindrical cavity expansion in a locking soil* , Report SLA-74-0201, Sandia Laboratories, Albuquerque, N.M., U.S.A..

Nowacki, W.K. (1978), *Stress waves in non-elastic solids* , Pergamon Press, Oxford.

Öpik, E. (1936), *Researches on the physical theory of meteor phenomena : Part I Theory of the formation of meteor craters* , Acta et Commentaris University Tartuensis, **28(6)**, A30.

Pack, D.C., and Evans, W.M. (1951), *Penetration by high velocity jets* , Proc. Phys. Soc. London, **64**, 298-302; 303-310.

Pidsley, P.H. (1984), *A numerical study of long rod impact onto a large target* , J. Mech. Phys. Solids, **32(4)**, 315-333.

Pochhammer, L. (1876), J. fur Mathematik (Creele), Bd. 81, 324 (see Love, The Mathematical Theory of Elasticity, Dover, New York, 1944, pp. 289).

Rakhmatulin, H.A. (1945), *On plastic waves of loading (*In Russian*)*, Prikl. Mat. Mekh., **9**, 91-100.

Rohani, B. (1975), *Analysis of projectile penetration into concrete and rock targets* , MISC-PAPER-S-75-25, US Army Engineer Waterways Experiment Station, Vicksburg, Mississippi, U.S.A.

Schwer, L., Rosinsky, R., and Day, J. (1988), *An axisymmetric Lagrangian technique for predicting earth penetration including penetrator response* , Int. J. Num. Anal. Meth. Geom., **12**, 235-262.

Sedgwick, R.T., Hageman, L.J., Herrman, R.G., and Waddell, J.L. (1978), *Numerical investigations in penetration mechanics* , Int. J. Eng. Sci., **16(11)**, 859-869.

Skalak, R. (1957), *Longitudinal impact of a semi-infinite circular elastic bar* , J. Appl. Mech., **24(1)**, 59-64.

Sokolovsky, V.V. (1948), *The propagation of elastic viscoplastic waves in bars (*in Russian*)* , Prikl. Mat. Mekh.,**12**, 261-280.

Sun, C., Burdette, E.G., and Barnett, R.O. (1976), *Missile penetration* , J. Structural Div., ASCE, **102(ST5)**, 1141-1146.

Swift, H.F. (1982), *Hypervelocity impact mechanics* , in *Impact dynamics* , 6th chapter, Zukas et al (Ed.).

Tate, A. (1967), *A theory for the deceleration of long rods after impact* , J. Mech. Phys. Solids, **15**, 387-399.

Tate, A. (1969), *Further results in the theory of long rod penetration* , J. Mech. Phys. Solids, **17**, 141-150.

Taylor, G.I. (1946), *The testing of materials at high rates of loading* , J. Inst. Civil. Eng., **26**, 486-518.

Taylor, J.W. (1965), *Dislocation dynamics and dynamic yielding* , J. Appl. Phys., **36(10)**, 3146-3150.

Tennant, P.W. (1987), *Stud velocity measurements using an Hilti DX450 gun* , Mechanical Engineering (A.M. Division) Report, UMIST.

Tennant, P.W. (1988), *Further investigation of stud velocities using an Hilti DX450 piston tool* , Mechanical Engineering (A.M. Division) Report, UMIST.

Thigpen, L. (1974), *Projectile penetration of elastic-plastic earth media*, J. Geotech. Eng., ASCE, **100(GT3)**, 279-294.

Wang, W.L. (1971), *Low velocity projectile penetration* , J. Soil Mech. Foundations Div., ASCE, **97(SM12)**, 1635-1655.

Wasley, R.J. (1973), *Stress wave propagation in solids : An introduction* , Marcel Dekker, New York.

Wilkins, M.L. (1978), *Mechanics of penetration and perforation* , Int. J. Eng. Sci., **16(11)**, 793-807.

Wood, D.S. (1952), *On longitudinal plane waves of elastic-plastic strain in solids* , J. Appl. Phys., **19**, 521-525.

Wood, E.R. and Philips, A., (1967), *On the theory of plastic wave propagation in a bar* , J. Mech. Phys. Solids, **15(4)**, 241-254.

Young, C.W. (1969), *Depth prediction for earth-penetrating projectiles* , J. Soil Mech. Foundations Div., ASCE, **95(SM3)**, 803-817.

Zaid, A.I.O., El-Kalay, A., and Travis, F.W. (1973), *An examination of the perforation of a mild steel plate by a flat-ended cylindrical projectile* , Int. J. Mech. Sci., **15**, 129-143.

Zukas, J.A., Nicholas, T., Swift, H.F., Greszczuk, L.B., and Curran, D.R. (1982), *Impact dynamics* , John Wiley and Sons, New York.

Alekseevskii, V.P. (1966), *Penetration of a rod into a target at high velocity* , Comb. Expl. Shock Waves, **2**, 63-66 (trans. from Russian).

Forrestal, M.J. (1983), *Forces on conical-nosed penetrators into targets with constant shear strength* , Mech. Materials, **2**, 173-177.

Forrestal, M.J. (1986), *Penetration into dry porous rock* , Int. J. Solids Structures, **22(12)**, 1485-1500.

Forrestal, M.J., Longcope, D.B. (1982), *Closed-form solutions for forces on conical-nosed penetrators into geological targets with constant shear strength* , Mech. Materials, **1**, 285-295.

Fung, Y.C. (1965), *Foundations of solid mechanics* , Prentice-Hall, Inc., Englewood Cliffs, New Jersey, USA.

Hanagud, S. (1964), *Spherical waves in a simple locking medium* , Bull. Seis. Soci. Amer., **54(2)**, 737-754.

Hanagud, S. (1966), *Finite amplitude spherical waves in a locking-relaxing solid* , Proc. 5th US National Cong. Appl. Mech., 63-77.

Hill, R. (1950), *The mathematical theory of plasticity* , Oxford University Press, Oxford.

Johnson, K.L. (1982), *One hundred years of Hertz contact* , Proc. Inst. Mech. Eng., **196**, 363-377.

Longcope, D.B., and Forrestal, M.J. (1981), *Closed-form approximations for forces on conical penetrators into dry porous rock* , J. Appl. Mech., **48**, 971-972.

Miles, J.M. (1961), *The propagation of an impulsive into a visco-locking medium* , J. Appl. Mech., **28**, 21-24.

Norwood, F.R., and Sears, M.P. (1982), *A nonlinear model for the dynamics of penetration into geological targets* , J. Appl. Mecch., **49**, 26-30.

Prager, W. (1957a), *Elastic solids of limited compressibility* , Proc. IX Int. Cong. Appl. Mech., **5**, 205-211.

Prager, W. (1957b), *On ideal locking materials* , Trans. Soci. Rheology, **1**, 169-175.

Salvadori, M.G., Skalak, R., and Weidlinger, P. (1960), *Waves and shocks in locking and dissipative medium* , J. Eng. Mech. Div., ASCE, **86(EM2)**, 77-105.

Scott, R.A., and Pearce, R.W. (1975), *Soil compaction by impact* , Geotechnique, **25**, 19-30.

Sun, C.T., and Philips, A. (1969), *Finite deformation of an ideal locking medium* , Developments in Mechanics Vol.5, Proc. 11th Midwestern Mech. Conf., 689-700.

White, M.P., and Griffis, LeVan, (1948) *The propagation of plasticity in uniaxial compression* , J. Appl. Mech., **15**, 256-260.

Zvolinskii, N.V. (1960), *On the emission (radiation) of an elastic wave from a spherical explosion in the ground* , Prikl. Mat. Mekh., **24(1)**, 166-176.

Zvolinskii, N.V., Pod"Yapol'skiy, G.S., and Flitman, L.M. (1973), *Theoretical aspects of the problem of an explosion in the ground* , Physics Solid Earth : USSR, **1** , 16-27.